

TECHNISCHE UNIVERSITÄT MÜNCHEN

Physik-Department  
Lehrstuhl für Experimentalphysik - Astroteilchenphysik E15

**Development of Cryogenic Light Detectors  
with Neganov-Luke Amplification  
for the Dark Matter Experiments CRESST and EURECA**

Christian Isaila

Vollständiger Abdruck der von der Fakultät für Physik der Technischen Universität München zur Erlangung des akademischen Grades eines

Doktors der Naturwissenschaften (Dr. rer. nat.)

genehmigten Dissertation.

Vorsitzender: Univ.-Prof. Dr. Alejandro Ibarra

Prüfer der Dissertation: 1. Univ.-Prof. Dr. Franz von Feilitzsch  
2. Univ.-Prof. Dr. Rudolf Gross

Die Dissertation wurde am 27.05.2010 bei der Technischen Universität München eingereicht und durch die Fakultät für Physik am 09.06.2010 angenommen.



# Abstract

One of the main objectives of contemporary astroparticle physics is solving the Dark Matter enigma. Among several hypothetical particles that might account for Dark Matter, WIMPs (Weakly Interacting Massive Particles) play a key role. The neutralino is a well-motivated WIMP candidate provided by supersymmetric extensions of the Standard Model of particle physics. An extended Dark Matter discussion can be found in chapter 2.

The aim of the CRESST (Cryogenic Rare Event Search with Superconducting Thermometers) experiment is the direct detection of WIMPs via coherent elastic scattering off the nuclei in a terrestrial target. To provide a high sensitivity for nuclear recoils, detectors capable of an active event-by-event discrimination of the background induced by electron recoils (due to  $\gamma$ 's and  $\beta$ 's) are required. The detection scheme employed in the second phase of CRESST is based on cryogenic detectors using the phonon-light technique, i.e. the simultaneous measurement of the phonons and the scintillation light induced by incident particles in a  $\text{CaWO}_4$  target crystal operated at mK temperatures. The phonons are measured by a transition edge sensor (TES), the scintillation light by a cryogenic light detector based on high-purity silicon or silicon-on-sapphire (SOS) absorbers also equipped with a TES. The combination of a phonon and a scintillation light detector is referred to as a detector module. Due to the different light yields of electron and nuclear recoils a very efficient suppression of the background induced by  $\gamma$ 's and  $\beta$ 's is achieved in this way. A detailed description of the experimental setup in CRESST together with the main results can be found in chapter 3.

With the phonon-light technique the remaining background in CRESST originates from neutrons. In the energy region of interest for Dark Matter search neutrons in a  $\text{CaWO}_4$  crystal mainly scatter off oxygen and calcium whereas WIMPs are expected to induce mainly tungsten recoils. Thus, a large part of the background originating from neutrons can be actively rejected if the slightly different light yields associated with O, Ca and W recoils in the nuclear recoil band can be resolved. However, the fraction of the deposited energy in a  $\text{CaWO}_4$  crystal due to electron recoils detected as light is at the percent level and this fraction is further reduced for nuclear recoils by a factor (Quenching Factor, QF) of  $\gtrsim 10$ . In addition,

the energy resolution of the light channel for nuclear recoils is dominated by noise due to the small number of photons absorbed in the light detector. Therefore, to improve the energy resolution of the light channel in this energy region, more sensitive light detectors are needed.

A promising technique for increasing the sensitivity of the light detectors is based on the Neganov-Luke effect. This effect describes the generation of additional phonons by drifting photon-induced electron-hole pairs in the semiconducting absorber of the light detectors by an applied electric field. The main aim of this thesis was the development of cryogenic light detectors with Neganov-Luke amplification. The light detectors developed here are based on the composite detector design (CDD), i.e. the TES is evaporated onto a small silicon substrate which is coupled to a high-purity silicon absorber by gluing. The TESs consist of Ir/Au bilayers evaporated onto the small silicon substrates using a shadow mask. For the application of the electric field, aluminum electrodes are directly evaporated onto the Si absorber. A detailed description of the operation principle of a TES is given in chapter 4. The processes involved in the fabrication of the cryogenic light detectors are discussed in chapter 5. More details on the working principle of a light detector with Neganov-Luke amplification can be found in chapter 6.

For the characterization of the light detectors a new method based on photon statistics has been developed (see chapter 6). Here, the light pulses used for the detector calibration are provided by a pulsed blue InGaN light-emitting diode (LED) and are injected via optical fibres into the detector. The results obtained by this method are consistent with those from the common calibration scheme based on a  $^{55}\text{Fe}$  source. The calibration with light from the LED, however, has the advantage that multiple peaks with energies covering a range of several keV down to the energy threshold of the detector can be used. In this way, non-linearities of the detector response can also be taken into account. The  $5\sigma$  energy threshold of the light detectors based on the CDD range between  $\sim 100$ - $200$  eV and are thus comparable with the light detectors based on directly evaporated TESs.

For the operation of light detectors in Neganov-Luke mode, a new method for the application of the voltage has been developed. Prior to operating the detector with the nominal voltage, a higher voltage is applied for  $\sim 30$  min to erode the shallow traps present in the silicon absorber. Otherwise charge carriers escaping from such traps cause an additional noise reducing the achieved improvement of the signal-to-noise ratio. Since space charges build up with time in the absorber and lead to a reduction of the amplification, a new procedure to efficiently remove the space charges (regeneration) has been developed. In this way, stable long-term operation conditions as required for the integration into the CRESST experiment are achieved. For detector regeneration, the Neganov-Luke voltage is turned off and the absorber is flushed for  $\sim 10$  s by light provided by the LED. Thus, most space charges accumulated in the detector are removed. Details on the regeneration

procedure can be found in chapter 6.

The Neganov-Luke effect has improved the signal-to-noise ratio of the light detectors by a factor of  $\sim 10$ . Considering initial  $5\sigma$  energy thresholds of  $\sim 100$ - $200$  eV of the light detectors with no applied Neganov-Luke voltage this improvement corresponds to energy thresholds of  $\sim 10$ - $20$  eV (see chapter 6). To investigate the effect of the Neganov-Luke amplification on the performance of a detector module a neutron calibration has been performed in the neutron-scattering facility at the Maier-Leibnitz-Laboratorium (MLL). Here, an improvement of the signal-to-noise ratio of the light detector by a factor of  $\sim 2.4$  could be achieved due to the Neganov-Luke effect. This reduced the discrimination threshold between the electron and nuclear recoil bands from  $\sim 30$  keV to  $\sim 10$  keV which is the best performance of a detector module ever achieved at our institute.



# Überblick

Das Rätsel der Dunklen Materie ist eine der zentralen Fragestellungen der heutigen Astroteilchenphysik. Unter den zahlreichen Teilchenkandidaten als Hauptkomponente der Dunklen Materie spielen schwach wechselwirkende massive Elementarteilchen, sogenannte WIMPs (Weakly Interacting Massive Particles) eine zentrale Rolle. Im Rahmen supersymmetrischer Erweiterungen des Standardmodells der Teilchenphysik existiert mit dem Neutralino ein gut motivierter Teilchenkandidat für WIMPs. Eine ausführliche Diskussion über Dunkle Materie findet man in Kapitel 2.

Das Ziel von CRESST (Cryogenic Rare Event Search with Superconducting Thermometers) ist der direkte Nachweis von WIMPs über die kohärente elastische Streuung an Atomkernen in einem erdgebundenen Detektor. Um besonders sensitiv für diese Art von Ereignissen zu sein, benötigt man Detektoren, die eine aktive Untergrundunterdrückung auf einer Event-by-Event Basis ermöglichen, d.h. Elektronrückstöße (durch  $\gamma$ s und  $\beta$ s) von Kernrückstößen diskriminieren können.

Die in der zweiten Phase von CRESST angewandte Nachweismethode basiert auf der Phonon-Licht-Technik mit kryogenen Detektoren. Diese beruht auf der simultanen Messung der Phononen und des Szintillationslichts, die in einem  $\text{CaWO}_4$ -Kristall bei Temperaturen im mK-Bereich durch einfallende Teilchen erzeugt werden. Die Phononen werden dabei mit Hilfe eines supraleitenden Phasenübergangsthermometers (TES) gemessen, während das Szintillationslicht mit Hilfe eines kryogenen Lichtdetektors basierend auf hochreinen Silizium- oder Silicon-Sapphire (SOS)-Absorbern ebenfalls mit einem TES nachgewiesen wird. Die Kombination aus einem Phonon- und einem Szintillationslichtdetektor wird als Detektormodul bezeichnet. Durch die unterschiedliche Lichtausbeute von Elektronrückstößen im Vergleich zu Kernrückstößen kann dadurch der Untergrund durch Elektronen und Gammastrahlung sehr effizient unterdrückt werden. Eine detaillierte Beschreibung des Aufbaus des CRESST-Experiments und eine Zusammenfassung der wichtigsten Resultate findet man in Kapitel 3.

Durch Anwendung der Phonon-Licht-Technik wird der verbleibende Untergrund in CRESST im wesentlichen auf Neutronen reduziert. Im für die WIMP-Suche relevanten Energiebereich erwartet man Neutronenstreuung hauptsächlich

an Sauerstoff und Kalzium in einem  $\text{CaWO}_4$ -Kristall, während WIMPs vermutlich überwiegend Wolframrückstöße induzieren. Dadurch würde sich auch der Neutronenuntergrund diskriminieren lassen, wenn man die leicht unterschiedlichen Lichtausbeuten der Sauerstoff-, Kalzium- und Wolfram-Rückstöße im Kernrückstoßband auflösen könnte. Da für Elektronrückstöße in einem  $\text{CaWO}_4$ -Kristall nur wenige Prozent der deponierten Energie als Szintillationslicht im Lichtkanal nachgewiesen werden und dieser Anteil für Kernrückstöße um einen Faktor (Quenching Faktor, QF)  $\gtrsim 10$  niedriger ist, wird die Energieauflösung des Lichtdetektors im Kernrückstoßband hauptsächlich durch elektronisches Rauschen bestimmt. Um die Energieauflösung des Lichtdetektors in diesem Energiebereich zu verbessern, benötigt man deshalb sensitivere Lichtdetektoren.

Eine vielversprechende Möglichkeit zur Steigerung der Sensitivität der Lichtdetektoren bietet der Neganov-Luke-Effekt. Er basiert auf der Erzeugung zusätzlicher Phononen durch lichtinduzierte Elektron-Loch Paare, die im halbleitenden Absorber des Lichtdetektors in einem angelegten elektrischen Feld gedriftet werden. Das Hauptziel dieser Arbeit war die Entwicklung von kryogenen Lichtdetektoren mit Neganov-Luke-Verstärkung. Diese Detektoren basieren auf dem Composite Detector Design (CDD), d.h. das TES wird auf ein kleines Substrat aufgedampft, das dann auf den Absorber aufgeklebt wird. Das TES besteht aus einer Ir/Au-Doppelschicht und wird mit Hilfe einer Schattenmaske aufgedampft. Zum Anlegen der elektrischen Spannung werden Aluminium-Elektroden direkt auf den Silizium-Absorber aufgedampft. Eine detaillierte Darstellung der Funktionsweise eines Phasenübergangsthermometers findet man in Kapitel 4. Die einzelnen Prozesse, die zur Herstellung der Lichtdetektoren notwendig sind, werden in Kapitel 5 beschrieben. Mehr Details zu Lichtdetektoren mit Neganov-Luke-Verstärkung findet man in Kapitel 6.

Zur Charakterisierung der Lichtdetektoren wurde eine neuartige Methode basierend auf der Photonenstatistik entwickelt (siehe Kapitel 6). Hierbei werden zur Kalibrierung des Detektors Lichtsignale aus einer gepulsten blauen InGaN LED über eine Glasfaser in den Detektor injiziert. Die Ergebnisse dieser Methode sind dabei mit der herkömmlichen Kalibrierung durch eine  $^{55}\text{Fe}$ -Quelle konsistent. Der Vorteil dieser Methode liegt allerdings darin, dass mehrere Linien im Energiebereich von einigen keV bis hin zur Energieschwelle des Detektors zur Kalibrierung herangezogen werden können. Damit kann auch eine nichtlineare Detektorantwort berücksichtigt werden. Die auf diesem Design basierenden Detektoren weisen mit  $5\sigma$ -Energieschwellen zwischen 100-200 eV eine vergleichbare Sensitivität auf wie Lichtdetektoren mit direkt aufgedampften Phasenübergangsthermometern.

Zum Anlegen der Neganov-Luke-Spannung wurde eine neue Methode entwickelt. Hierbei wird vor dem Betrieb mit der nominellen Spannung eine um 20-30 V höhere Spannung für ca. 30 Minuten angelegt. Dadurch werden die an flachen Störstellen schwach gebundenen Ladungsträger entfernt, die sonst zusätzliches Rauschen

verursachen und die erzielbare Sensitivität reduzieren. Da Raumladungen, die im Neganov-Luke-Betrieb im Absorber entstehen, die erzielte Verstärkung verringern, wurde eine neue Methode zur Beseitigung dieser Raumladungen (Regeneration) entwickelt. Dadurch kann ein stabiler Langzeitbetrieb, wie bei der Implementierung in CRESST erforderlich, gewährleistet werden. Zur Regeneration des Lichtdetektors wird die Neganov-Luke-Spannung abgeschaltet und der Absorber für ca. 10 s mit Licht aus der LED bestrahlt. Dadurch werden die meisten angesammelten Ladungsträger aus dem Detektor entfernt. Details zur Regeneration findet man in Kapitel 6.

Mit Hilfe des Neganov-Luke-Effekts konnte das Signal-zu-Rausch-Verhältnis der Lichtdetektoren um einen Faktor  $\sim 10$  verbessert werden. Ausgehend von einer  $5\sigma$ -Energieschwelle von  $\sim 100$ - $200$  eV im nichtverstärkten Betrieb, entspricht diese Verbesserung einer Energieschwelle von  $\sim 10$ - $20$  eV (siehe Kapitel 6). Um die Auswirkung des Neganov-Luke-Effekts auf die Performance eines Detektormoduls zu untersuchen wurde eine Neutronenkalibration am Maier-Leibnitz-Laboratorium (MLL) durchgeführt. Hierbei konnte die Energieschwelle des Lichtdetektors um einen Faktor  $\sim 2.4$  durch den Neganov-Luke-Effekt verbessert werden. Dadurch konnte die Trennschwelle zwischen dem Elektron- und dem Kernrückstoßband des Detektormoduls von  $\sim 30$  keV auf  $\sim 10$  keV reduziert werden. Eine derartig gute Trennschwelle wurde mit herkömmlichen Lichtdetektoren niemals zuvor an unserem Institut erreicht.



# Contents

<b>1</b>	<b>Introduction</b>	<b>1</b>
<b>2</b>	<b>Dark Matter</b>	<b>5</b>
2.1	The Need for Dark Matter . . . . .	5
2.1.1	Dynamical Evidence . . . . .	5
2.1.2	Cosmological Indications . . . . .	9
2.2	Dark Matter Candidates . . . . .	20
2.2.1	Baryonic Dark Matter . . . . .	20
2.2.2	Non-Baryonic Dark Matter . . . . .	20
2.2.3	Modified Newtonian Dynamics (MOND) . . . . .	24
2.3	Indirect Detection of Dark Matter . . . . .	24
2.3.1	Indirect Search with Neutrinos . . . . .	24
2.3.2	Indirect Search with $\gamma$ -Rays . . . . .	25
2.3.3	Charged Cosmic Rays from WIMP Annihilation . . . . .	26
2.3.4	The WMAP Haze . . . . .	26
2.4	Direct Detection of Cold Dark Matter . . . . .	27
2.4.1	Halo Model . . . . .	27
2.4.2	Scattering Rates . . . . .	28
2.4.3	Experimental Requirements . . . . .	30
2.4.4	WIMP Signatures . . . . .	32
2.5	WIMP Direct Detection Experiments . . . . .	34
2.5.1	The DAMA/LIBRA Annual Modulation . . . . .	35
2.5.2	Liquid Noble Gas Experiments . . . . .	36
2.5.3	Cryogenic Dark Matter Experiments . . . . .	38
2.6	Perspectives of Dark Matter Searches . . . . .	45
<b>3</b>	<b>The CRESST Experiment</b>	<b>47</b>
3.1	The CRESST Experimental Setup . . . . .	47
3.2	Detection Principle . . . . .	50
3.2.1	CRESST Detector Modules . . . . .	51
3.2.2	Readout Scheme . . . . .	53

3.3	Background . . . . .	54
3.4	Quenching Factors . . . . .	57
3.5	CRESST Dark Matter Limits . . . . .	63
3.6	Perspectives . . . . .	67
<b>4</b>	<b>Detector Physics</b>	<b>69</b>
4.1	Basic Principle . . . . .	69
4.2	Signal Generation . . . . .	70
4.2.1	Phonon Excitation and the Neganov-Luke Effect . . . . .	70
4.2.2	Phonon Down-Conversion and Thermalization . . . . .	71
4.2.3	Thermal Detector Model . . . . .	73
4.2.4	Thermal Model for Composite Detectors . . . . .	78
4.3	Transition Edge Sensors . . . . .	80
4.3.1	Basic Principle . . . . .	80
4.3.2	Electrothermal Feedback . . . . .	82
<b>5</b>	<b>Experimental Techniques</b>	<b>85</b>
5.1	Detector Fabrication . . . . .	85
5.1.1	Ir/Au Films . . . . .	85
5.1.2	Aluminum Electrodes . . . . .	87
5.2	Experimental Setup . . . . .	89
5.2.1	The $^3\text{He}/^4\text{He}$ Dilution Refrigerator . . . . .	89
5.2.2	Detector Operation . . . . .	91
5.2.3	LED and High Voltage System . . . . .	93
5.2.4	Read-Out Electronics . . . . .	95
5.2.5	Data Acquisition (DAQ) . . . . .	97
<b>6</b>	<b>Results and Discussion</b>	<b>101</b>
6.1	Composite Light Detectors with Neganov-Luke Amplification . . . . .	101
6.2	Light Detector Si518 . . . . .	102
6.2.1	Setup . . . . .	102
6.2.2	Calibration . . . . .	103
6.2.3	Neganov-Luke Amplification . . . . .	117
6.2.4	Relevance of the Neganov-Luke Effect for the Phonon-Light Technique . . . . .	136
6.3	Light Detector Si519 . . . . .	142
6.3.1	Setup . . . . .	142
6.3.2	Calibration . . . . .	143
6.3.3	Neganov-Luke Amplification . . . . .	146
6.4	Light Detector Si521 - Measurements at the Maier-Leibnitz-Laboratorium (MLL) with a Neganov-Luke Detector . . . . .	147

6.4.1	Setup . . . . .	147
6.4.2	Calibration of the Light Detector . . . . .	151
6.4.3	Performance of the Light Detector in Neganov-Luke Mode .	153
<b>7</b>	<b>Conclusions and Outlook</b>	<b>157</b>
	<b>Appendix A</b>	<b>161</b>
	<b>Appendix B</b>	<b>165</b>
	<b>Bibliography</b>	<b>167</b>
	<b>Danksagung</b>	<b>177</b>



# Chapter 1

## Introduction

Several experiments in nuclear and astroparticle physics require detectors with excellent energy resolution and sensitivity. When restricted to conventional detection schemes the choices are limited to Ge and Si semiconductor detectors fabricated as p-i-n diodes. Since the energy  $\epsilon$  needed to create an electron-hole pair is 2.99 eV in Ge [1] and 3.64 eV in Si [1] only about 30% of the energy  $E$  of incident charged particles and photons is deposited in the detection channel. For particles that do not interact via the electromagnetic interaction like neutrons this yield is further reduced by a factor of  $\sim 3$  [2]. The missing energy is converted into lattice vibrations (phonons) and is therefore lost in the detection channel.

The fluctuation of the number of generated charge carriers for a given energy deposition is expressed in terms of the Fano factor  $F$  [3] and puts a fundamental limit on the energy resolution obtainable with semiconductor detectors [4]:

$$\Delta E_{FWHM} = 2.35\sqrt{\epsilon FE}. \quad (1.1)$$

The shortcomings of conventional semiconductor detectors can be overcome with cryogenic particle detectors based on the detection of particle-induced phonons using transition edge sensors (TES) or neutron transmutation doped (NTD) thermistors. As the energies needed to generate these excitations are of the order of meV and thus orders of magnitudes smaller than the electron-hole pair creation energy in semiconductor detectors, it is evident that they achieve better performance with respect to energy resolution and sensitivity since the fluctuating number of phonons is negligible compared to the total number of phonons generated. The fundamental energy resolution is only limited by the thermodynamic fluctuation of the energy content of the detector [5]:

$$\Delta E_{FWHM} = 2.35\sqrt{k_B CT^2}. \quad (1.2)$$

Here  $k_B$  is the Boltzmann constant,  $C$  the heat capacity of the detector and  $T$

the operation temperature. The energy resolution of cryogenic detectors using semiconducting or dielectric absorbers, however, is mainly limited by trapping of charge carriers by localized states in the band gap.

Furthermore, the sensitivity attainable with cryogenic detectors is so large that even nuclear recoils can be efficiently detected. For this reason, cryogenic detectors are potentially suitable for the detection of low-energy neutrinos via coherent scattering off nuclei as well as the detection of Weakly Interacting Massive Particles (WIMPs) which may account for the missing mass in our galaxy. Here, the energy transferred to the nuclei is only a few keV and thus not efficiently detectable with common detectors. In addition, there are virtually no restrictions on the absorber materials of cryogenic detectors. Therefore, the mass number of the target nuclei can be varied to cover large mass ranges and to have targets with different spins. This would allow to identify a possible WIMP signal by comparing the rates measured in different target materials.

With respect to Dark Matter searches the only limitation for cryogenic detectors arises from the radioactive background originating from both electron recoils ( $\gamma$ 's and  $\beta$ 's) and nuclear recoils (neutrons). By measuring a second particle-induced excitation in the target material in addition to phonons, cryogenic detectors offer a very efficient technique for the active suppression of the background induced by electron recoils. This additional excitation is, e.g. charge in a semiconducting absorber (Si, Ge) or light in a scintillating target crystal such as  $\text{CaWO}_4$ , LiF or BGO. Charge is measured by common FET-based electronics, whereas the light is detected by a second cryogenic detector based on Si or SOS (silicon-on-sapphire) absorbers. Due to the different light and ionization yields of nuclear recoils relative to electron recoils, the background induced by  $\gamma$ 's and  $\beta$ 's can be efficiently suppressed in this way. Here, the discrimination threshold sets the threshold of the detector used for Dark Matter analysis which is  $\sim 10\text{-}20$  keV for the cryogenic detectors currently employed for WIMP searches.

When using scintillating absorber crystals consisting of different nuclei such as  $\text{CaWO}_4$  as employed by the CRESST (Cryogenic Rare Event Search with Superconducting Thermometers) experiment even a discrimination of the neutron-induced background can be achieved. Since neutrons mainly scatter off oxygen and calcium and WIMPs are expected to mainly induce tungsten recoils the neutron background can be actively suppressed when the contributions of the different nuclei to the nuclear recoil band can be resolved. Since, however, only a small fraction of the energy deposited in the crystal via nuclear recoils is detected as light, the separation of electron and nuclear recoil band is mainly determined by photon statistics and electronic noise. Therefore, it can be improved with more sensitive light detectors.

A very promising technique, referred to as the Neganov-Luke effect, for improving the sensitivity of cryogenic detectors based on semiconducting absorbers

---

has been proposed by Neganov, Trofimov [6] and Luke [7]. It is based on the amplification of the phonon signal by drifting the photon-induced electron-hole pairs by an applied field. The application of the Neganov-Luke effect for scintillation light detection was the main objective of this thesis. Employing high-purity silicon absorbers together with the Neganov-Luke effect has helped to improve the sensitivity of cryogenic light detectors by a factor of about ten.

*1. Introduction*

---

# Chapter 2

## Dark Matter

There are several astrophysical and cosmological considerations indicating that most of the matter in the Universe is invisible, that is, it neither absorbs nor emits electromagnetic radiation of any frequency. Its existence can most directly be inferred from the gravitational interaction with luminous matter. A well-motivated candidate for particle Dark Matter is the neutralino, a weakly interacting, supersymmetric relic particle [8]. Among several techniques aiming at Dark Matter detection, cryogenic detectors have reached the sensitivity to test the supersymmetric parameter space. This chapter reviews some of the facts suggesting the existence of Dark Matter and introduces the best motivated candidates as well as the most important detection techniques.

### 2.1 The Need for Dark Matter

#### 2.1.1 Dynamical Evidence

##### 2.1.1.1 Rotation Curves of Spiral Galaxies

The flat rotation curves of spiral galaxies provide the most direct evidence for the existence of Dark Matter on galactic scales. The circular velocity profile is obtained by measuring the Doppler shift of spectral lines. The combination of different methods based on optical tracers and the 21 cm emission line of neutral hydrogen allows the measurement of the rotational velocity profile far beyond the optical disk. The typical rotation curve of a spiral galaxy is depicted in Fig. 2.1. There is an increase of the orbital velocity up to about 100 km/s at a distance of approximately 5 kpc from the galactic center, remaining then constant out to large radii. This velocity profile has been observed in many spiral galaxies [9].

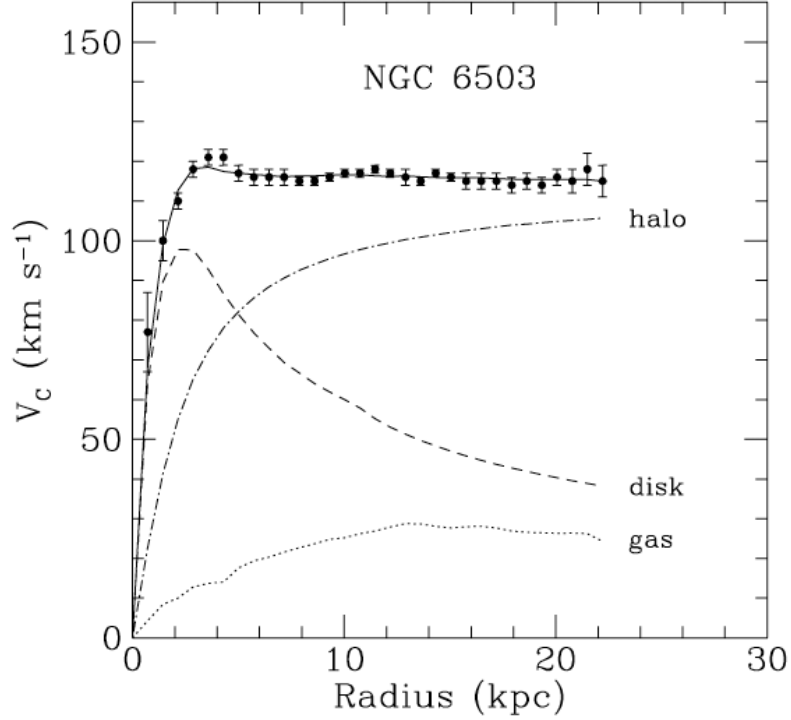


Figure 2.1: Rotational curve of the galaxy NGC 6503 together with the contributions of halo, optical disk and gas, respectively [10].

Assuming that the total matter content of the galaxy is luminous this behaviour, however, is unexpected as the observed surface luminosity exhibits an exponential decrease [11].

According to Newtonian dynamics the orbital velocity  $v(r)$  is given by

$$v(r) = \sqrt{\frac{GM(r)}{r}}, \quad (2.1)$$

where  $G$  is the gravitational constant and  $M(r)$  the mass enclosed by the orbit with radius  $r$ :

$$M(r) = 4\pi \int_0^r \rho(R)R^2 dR. \quad (2.2)$$

Thus, from the observed density profile  $\rho(r)$  the orbital velocity should decrease  $\propto 1/\sqrt{r}$ . The discrepancy between observed and expected rotation curves implies the existence of a Dark Matter halo with  $\rho(r) \propto 1/r^2$ , i.e.  $M(r) \propto r$ .

### 2.1.1.2 Galaxy Clusters

#### The Virial Theorem

Galaxy clusters and superclusters are the largest self-gravitating structures in the Universe containing several hundreds of galaxies. They have typical extents of several Mpc and masses up to  $10^{15} M_{\odot}$ . The first to derive the mass of a cluster and to point at the existence of large amounts of non-luminous matter was the Swiss astronomer Fritz Zwicky (1933) [12]. Assuming that the galaxies in a cluster are gravitationally bound and that their distribution is stationary he made use of the virial theorem which states that

$$2 \langle E_{kin} \rangle = - \langle E_{pot} \rangle . \quad (2.3)$$

$\langle E_{kin} \rangle$  is the average kinetic energy and for a cluster containing  $N$  galaxies it is given by

$$\langle E_{kin} \rangle = \frac{1}{2} N \langle mv^2 \rangle . \quad (2.4)$$

The potential energy  $\langle E_{pot} \rangle$  due to the mutual gravitational attraction of the galaxies can be expressed as

$$\langle E_{pot} \rangle = -\frac{1}{2} GN(N-1) \frac{\langle m^2 \rangle}{\langle r \rangle} . \quad (2.5)$$

Under the assumption that  $N \approx (N-1)$  the total mass  $M = N \langle m \rangle$  is then given by

$$M \approx \frac{2 \langle r \rangle \langle v^2 \rangle}{G} . \quad (2.6)$$

Knowing  $\langle v^2 \rangle$  from Doppler shift measurements of spectral lines and estimating the extent  $\langle r \rangle$  of the cluster, Zwicky obtained a mass-to-luminosity ratio  $M/L$  of about 300 for the Coma cluster providing the first evidence for the existence of non-luminous matter in the Universe.

The identification of galaxy clusters as the most powerful X-ray emitters in the Universe revealed the presence of larger amounts of luminous matter on cluster scales in the form of a hot gas ( $T \approx 10^8 \text{K}$ ) which emits X-rays by electron bremsstrahlung. Assuming the gas to be in hydrostatic equilibrium its mass fraction can be estimated using the virial theorem. It turns out, however, that it only makes up 10-20% of the virial mass of the cluster [13] without resolving the missing mass problem.

## Gravitational Lensing

The deflection of light rays passing massive objects can be described by general relativity. In the most symmetric case where a source lies exactly behind a lens with spherical mass distribution the source is imaged into a ring ('Einstein Ring') [14]. In the more general case of galaxy clusters these ideal conditions are not given so that slightly distorted images of background galaxies in the form of arcs and arclets curved around the cluster center are observed (Fig. 2.2).

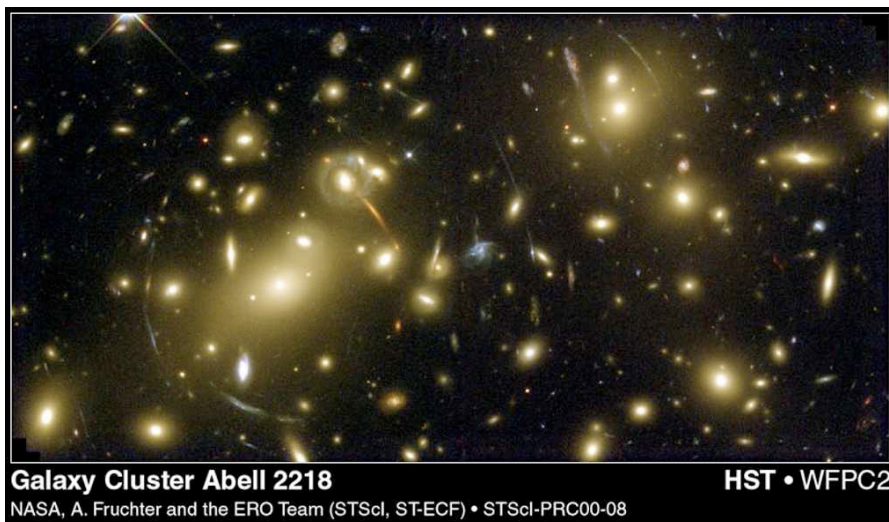


Figure 2.2: Gravitational lensing in the cluster Abell 2218 (NASA Archive).

The analysis of the arcs obtained by gravitational lensing provides a tool for studying the mass distribution of the lensing cluster. Mass estimates based on this method also reveal large amounts of Dark Matter on cluster scales in rough agreement with the results based on the virial theorem [15].

## The Bullet Cluster

A unique, direct evidence for the existence of Dark Matter is provided by the galaxy cluster 1E0657-558 ('Bullet Cluster') [16, 17]. It is composed of two colliding subclusters moving with a relative velocity of about  $4500 \text{ km s}^{-1}$  [16]. In the course of the collision process the hot X-ray emitting intracluster gas is spatially separated from the galaxies which behave like collisionless particles whereas the plasma experiences ram pressure and slows down.

The distribution of the collisionless galaxies and the plasma can be derived from observations with optical and X-ray telescopes, respectively. The overall

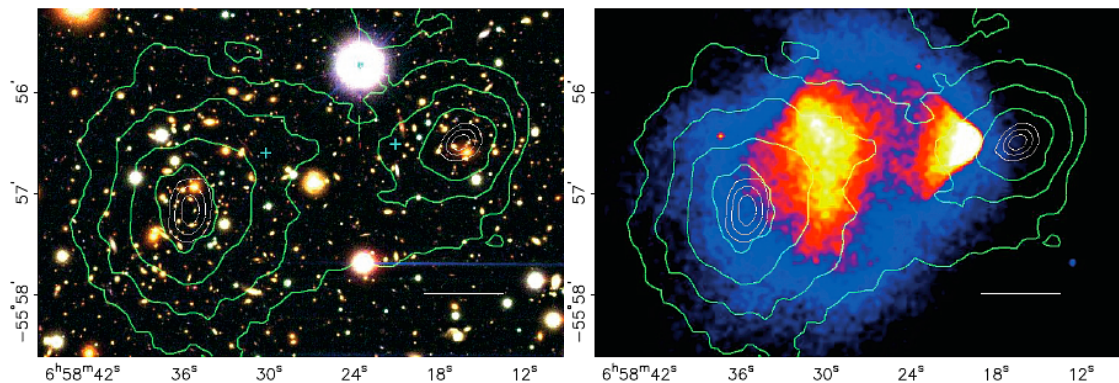


Figure 2.3: *Left*: Image from the 'Magellan' telescope of the colliding cluster 1E 0657-558. *Right*: X-ray image of the 'Bullet Cluster' ('Chandra' telescope). The lensing mass distribution is indicated by the green contours. The white bars in both images correspond to 200 kpc. Figure from [17].

mass distribution has been probed by weak gravitational lensing. Comparing these results, it turns out that the mass distribution does not trace the intracluster gas, which is the dominant luminous component, but the distribution of the galaxies (Fig. 2.3), indicating that the cluster mass is dominated by collisionless Dark Matter.

## 2.1.2 Cosmological Indications

The gravitational interplay with luminous matter is the most direct evidence for the existence of Dark Matter on galaxy and cluster scales. In the framework of modern cosmology, however, the need for Dark Matter arises in a more general way. Great advances in observational cosmology have helped fixing the parameters of the Standard Cosmological Model putting stringent constraints on the density of Dark Matter.

### 2.1.2.1 Standard Cosmology

The evolution of the Universe is described by the solution of Einstein's field equation [18]:

$$\mathcal{R}_{\mu\nu} - \frac{1}{2}g_{\mu\nu}\mathcal{R} = 8\pi GT_{\mu\nu} + \Lambda g_{\mu\nu}. \quad (2.7)$$

$\mathcal{R}_{\mu\nu}$  and  $\mathcal{R}$  are the Ricci tensor and scalar, respectively.  $T_{\mu\nu}$  denotes the energy-momentum tensor,  $g_{\mu\nu}$  the metric tensor,  $G$  the gravitational constant and  $\Lambda$  the cosmological constant. The terms on the left-hand-side describe the geometry of

the Universe which is related to the energy content represented by the first term on the right-hand side. This relation is the key concept of general relativity. The term containing the cosmological constant represents a vacuum energy acting as a possible source of gravity even in the absence of matter.

The Standard Model of Cosmology is the solution of the Einstein field equation proposed by Friedmann, Lemaître, Robertson and Walker, which assumes the Universe to be homogeneous and isotropic on large scales. This is equivalent to the Cosmological Principle stating that there is no preferred spatial position in the Universe. The most general metric of a 4D space-time with a maximally symmetric 3D subspace is the Robertson-Walker metric giving a line-element squared of the form

$$ds^2 = dt^2 - R^2(t) \left[ \frac{dr^2}{1 - kr^2} + r^2 d\theta^2 + r^2 \sin^2\theta d\Phi^2 \right]. \quad (2.8)$$

Here  $r$ ,  $\theta$  and  $\Phi$  denote the spherical coordinates.  $R(t)$  is the scale factor and  $k$  the curvature parameter taking one of the values  $k = -1, 0, +1$  corresponding to open, flat or closed geometries.

Under the assumption that matter and radiation behave like a perfect fluid the energy-momentum tensor,  $T_{\mu\nu}$ , can be written in diagonal form

$$T_{\mu\nu} = \text{diag}(\rho, \vec{p}), \quad (2.9)$$

with the energy density  $\rho$  and the isotropic pressure  $\vec{p}$ . With these approximations, the different components of the field equation (2.7) yield the Friedmann-Lemaître-Robertson-Walker (FLRW) equations:

$$\left( \frac{\dot{R}}{R} \right)^2 = \frac{8\pi G}{3} \rho - \frac{k}{R^2} + \frac{\Lambda}{3} \quad (2.10)$$

$$\frac{\ddot{R}}{R} = -\frac{4\pi G}{3}(\rho + 3p) + \frac{\Lambda}{3}. \quad (2.11)$$

The first of these equations is also referred to as the Friedmann equation.  $\dot{R}/R$  defines the Hubble parameter  $H(t)$  that governs the local expansion of the Universe according to Hubble's law [19]:

$$v = Hd, \quad (2.12)$$

with the recession velocity  $v$  and the distance  $d$ .

The present value of the Hubble parameter  $H_0$ , called Hubble constant, is given by

$$H_0 = h_0 \cdot 100 \text{ km Mpc}^{-1} \text{ s}^{-1}, \quad (2.13)$$

with the scaled Hubble constant  $h_0 = 0.701 \pm 0.013$  [20]. The evolution of the scale factor within the time interval  $t_2 - t_1$  is usually expressed in terms of the redshift  $z$ :

$$1 + z = \frac{R(t_2)}{R(t_1)}. \quad (2.14)$$

Assuming  $\Lambda = 0$ , it follows from the Friedmann equation that the Universe is flat ( $k = 0$ ) when the energy density equals the critical density

$$\rho_c \equiv \frac{3H^2}{8\pi G}. \quad (2.15)$$

Its present numerical value is  $\rho_{c,0} = 1.05 \cdot 10^{-5} h_0^2 \text{ GeV cm}^{-3}$  [21]. Expressing the energy density  $\rho$  in terms of the critical density:

$$\Omega \equiv \frac{\rho}{\rho_c} \quad (2.16)$$

the Friedmann equation can be written in the form

$$\frac{k}{R^2} = H^2(\Omega - 1) = H^2(\Omega_r + \Omega_m + \Omega_\Lambda - 1), \quad (2.17)$$

with the contributions to the overall density by relativistic particles  $\Omega_r$ , pressureless matter  $\Omega_m$  and the vacuum  $\Omega_\Lambda = \Lambda/3H^2$ . This means that the overall geometry of the Universe is completely determined by the density parameter  $\Omega$ :

$\rho > \rho_c$	$\Omega > 1$	$k=+1$	Closed Universe
$\rho = \rho_c$	$\Omega = 1$	$k=0$	Flat Universe
$\rho < \rho_c$	$\Omega < 1$	$k=-1$	Open Universe

The second FLRW equation (2.11) describes the dynamics of the Universe as an interplay of accelerating and decelerating effects due to vacuum energy on the one hand, matter and radiation on the other hand. As there is no general solution for an arbitrary composition of the energy density, the time evolution of the scale factor is usually delineated for only one dominant component. Here a simple relation, referred to as the equation of state, between  $\rho$  and  $p$  is assumed [18]:

$$p = \alpha\rho, \quad (2.18)$$

where  $\alpha$  is a constant. Making the ansatz  $R(t) \sim t^\beta$  equation 2.11 can be solved yielding [18]:

$$R(t) \sim t^{1/2} \text{ (Radiation domination)} \quad (2.19)$$

$$R(t) \sim t^{2/3} \text{ (Matter domination)} \quad (2.20)$$

$$R(t) \sim e^{\sqrt{\Lambda/3}t} \text{ (Vacuum energy domination)}. \quad (2.21)$$

The high predictive power of the Standard Model made it the prime candidate to describe our Universe. It has created the theoretical framework to explain the synthesis of the light elements, structure formation and the radiation remnants of the early Universe. Accurate measurements of the abundance of the light elements as well as the analysis of the anisotropies of the Cosmic Microwave Background (CMB) have helped fixing the parameters of the Standard Cosmological Model indicating that the Universe is flat and most of the matter is dark (see section 2.1.2.3).

### 2.1.2.2 Big-Bang Nucleosynthesis

Big-Bang Nucleosynthesis (BBN) is the synthesis of the light elements Deuterium (D),  $^3\text{He}$ ,  $^4\text{He}$  and  $^7\text{Li}$  during the first few minutes after the Big Bang. BBN is a very sensitive probe of the physics in the early radiation-dominated era of the Universe about 1 second after the Big Bang at temperatures  $T \sim 1\text{MeV}$ . At higher temperatures protons and neutrons were kept in equilibrium by reactions like [18]



The ratio of neutron and proton number densities is given by:  $n_n/n_p = e^{-\Delta m/T}$ , where  $\Delta m = 1.29\text{MeV}$  is the neutron-proton mass difference. Thus at high temperatures, this ratio is close to unity. As the reactions 2.22 - 2.24 are governed by the weak interaction, their inter-conversion rate is given by  $\Gamma_{n \leftrightarrow p} \propto T^5$  [18]. It falls faster than the Hubble expansion rate  $H \propto T^2$  leading to a suppression of the neutron number density. Thus thermal equilibrium could not be maintained leading to a "freeze-out" of the neutron and proton number densities fixing their ratio  $n_n/n_p$  to a value of about 1/6 at  $T \sim 1\text{MeV}$ . Although the freeze-out temperature is below the binding energy of Deuterium ( $\Delta D = 2.23\text{ MeV}$ ) its synthesis via  $p(n, \gamma)D$  is not efficient since the photo-dissociation rate  $\sim n_\gamma e^{-\Delta D/T}$  is much larger than the production rate  $\sim n_B$  due to the low baryon-to-photon ratio

$\eta \equiv n_B/n_\gamma \sim 10^{-9}$ . At temperatures of about 0.1 MeV, Deuterium became stable against photo-dissociation increasing its abundance which led to a fast fusion to  ${}^4\text{He}$  consuming nearly all neutrons through one of the following chains [18]:



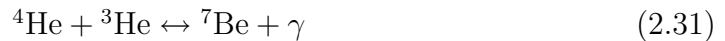
or:



Taking into account that by this time the  $n_n/n_p$  ratio dropped to 1/7 due to the  $\beta$ -decay of unbound neutrons, the mass fraction of  ${}^4\text{He}$  can be approximated by

$$Y_p({}^4\text{He}) = \frac{2n_n/n_p}{1 + n_n/n_p} \sim 0.25. \quad (2.29)$$

The primordial abundances of D and  ${}^3\text{He}$  result from the reactions 2.25 - 2.28 after dropping out of equilibrium.  ${}^7\text{Li}$  is produced through [18]



Heavier elements are not produced in significant quantities because of the absence of stable nuclei with  $A=5$ , 6 or 8. The synthesis of heavier elements with more than three protons, such as  ${}^{12}\text{C}$ , is suppressed by the high Coulomb barrier.

The primordial abundances depend mainly on two parameters. First, the expansion rate relative to the rates of the weak interaction determines the freeze-out temperature and thus the neutron-to-proton ratio  $n_n/n_p$ . Second, the baryon-to-photon ratio  $\eta$  sets the temperature at which nucleosynthesis begins. Larger values of  $\eta$  correspond to higher initial temperatures so that more neutrons get bound in  ${}^4\text{He}$  leading to a decrease of the abundances of D and  ${}^3\text{He}$  (Fig. 2.4). It is therefore possible to infer the density of baryonic matter  $\Omega_b$  in the Universe from the primordial abundances. The evolution of the light-nuclei mass fractions with temperature for  $\eta = 5.1 \cdot 10^{-10}$  is depicted in Fig. 2.5.

In later epochs of the Universe, nucleosynthesis occurs only in stellar fusion reactions at high temperatures. These processes, however, also alter the abundances of

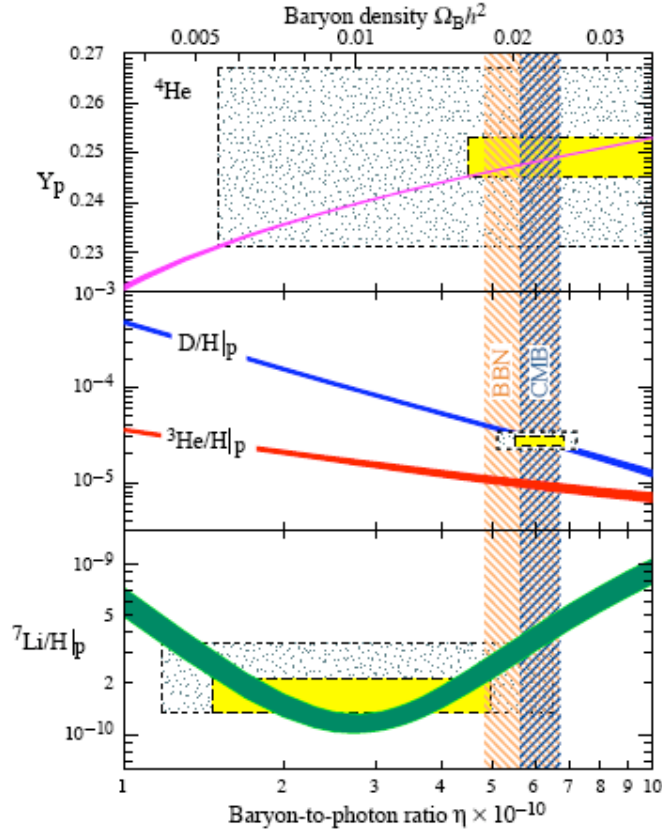


Figure 2.4: The primordial abundances of D,  ${}^3\text{He}$ ,  ${}^4\text{He}$ ,  ${}^7\text{Li}$  as predicted by BBN together with experimental data. The small boxes contain the  $2\sigma$  statistical errors; the larger boxes  $\pm 2\sigma$  statistical and systematic errors. The predictions of the baryon density by CMB and BBN are indicated by the vertical bands [21].

the light elements. Therefore, primordial mass fractions are estimated from measurements in astrophysical sites with low metallicities. The measured abundancies are depicted in Fig. 2.4<sup>1</sup> indicating a baryon-to-proton ratio  $\eta$  of [21]

$$4.7 \cdot 10^{-10} \leq \eta \leq 6.5 \cdot 10^{-10} \quad (95 \% \text{ CL}) \quad (2.33)$$

yielding a baryon density of [21]

$$0.017 \leq \Omega_b h^2 \leq 0.024 \quad (95 \% \text{ CL}). \quad (2.34)$$

<sup>1</sup>The primordial abundancies (denoted by the subscript 'p') of deuterium ( $\text{D}/\text{H}|_p$ ),  ${}^3\text{He}$  ( ${}^3\text{He}/\text{H}|_p$ ) and lithium ( ${}^7\text{Li}/\text{H}|_p$ ) are given with respect to hydrogen (H), whereas  $Y_p$  is the primordial abundance of  ${}^4\text{He}$ .

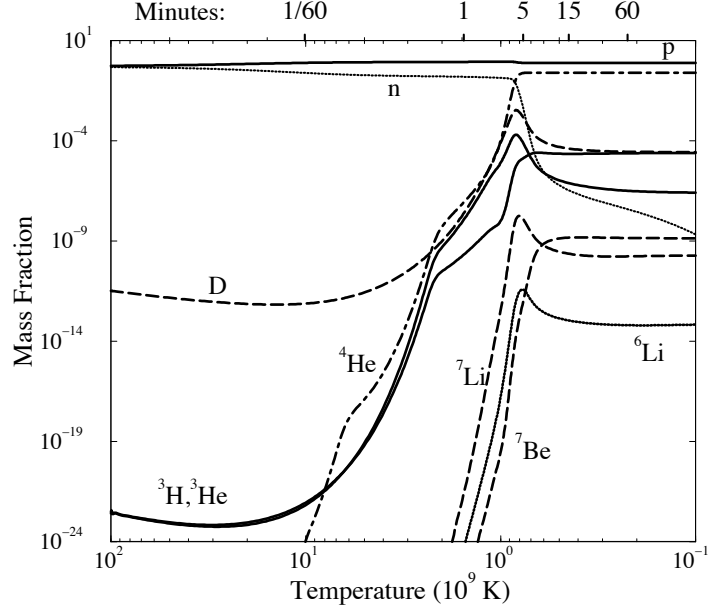


Figure 2.5: The evolution of mass fractions of the light nuclei with temperature for  $\eta = 5.1 \cdot 10^{-10}$  [22].

Thus, the baryonic matter content is too low to close the Universe. Furthermore, as luminous matter makes up only  $0.0024h^{-1}$  of the overall matter density [23] it becomes evident that most of the baryonic matter is optically dark.

### 2.1.2.3 Cosmic Microwave Background

The Cosmic Microwave Background (CMB) is one of the main pillars of Big-Bang cosmology. Its existence has been predicted by Gamow, Alpher and Herman [24], [25] as part of their model for nucleosynthesis. It was first observed by Penzias and Wilson [26] as a source of excess noise in a radio receiver. The origin of the CMB dates back to the early hot phases of the Universe. For about 300000 years after Nucleosynthesis, baryons were found in the form of a hot plasma. In this phase matter and radiation were kept in equilibrium mainly by reactions such as [27]

$$\gamma + e^- \rightarrow \gamma + e^- \quad (2.35)$$

$$\gamma + e^- \leftrightarrow e^- + \gamma + \gamma \quad (2.36)$$

$$e^- + X \leftrightarrow e^- + X + \gamma. \quad (2.37)$$

These are Compton scattering (2.35), double Compton scattering (2.36) and thermal bremsstrahlung (2.37), where X denotes an ion. The link between electrons and protons was maintained by the electromagnetic interaction. As the Universe expanded and the temperature fell below the ionization energy of hydrogen (H), the reaction



dropped out of equilibrium and radiation decoupled from matter as all free electrons were bound by protons producing hydrogen (Recombination). The background radiation cooled to about 2.7 K due to the subsequent expansion of the Universe and is now referred to as the Cosmic Microwave Background (CMB). The Planck distribution that has been established during the equilibrium era has been preserved as the expansion affects both frequency and temperature in the same way [27]. The measured CMB spectrum is depicted in Fig. 2.6. It is in good agreement with a black-body distribution with a maximum at about 2.73 K. The most accurate value of the CMB temperature  $T_\gamma = 2.725 \pm 0.002$  K has been provided by the FIRAS ('Far InfraRed Absolute Spectrophotometer') instrument on the COBE satellite [28].

Observations have shown that the CMB is isotropic at a level of  $10^{-5}$  [30]. These anisotropies can be interpreted as fluctuations of the gravitational potential at the time radiation decoupled from matter. Their analysis provides a test of cosmological models and a method of fixing cosmological parameters.

The temperature anisotropy at a fixed point  $(\theta, \phi)$  in the sky can be expanded in a series of spherical harmonics  $Y_{lm}(\theta, \phi)$  [18]:

$$\frac{\Delta T}{T}(\theta, \phi) = \sum_{l,m} a_{lm} Y_{lm}(\theta, \phi). \quad (2.39)$$

For two different directions in the sky denoted by the unit vectors  $\vec{n}$  and  $\vec{m}$  an auto-correlation function  $C(\theta)$  can be defined as

$$C(\theta) \equiv \left\langle \frac{\Delta T(\vec{n})}{T}, \frac{\Delta T(\vec{m})}{T} \right\rangle = \frac{1}{4\pi} \sum_l (2l+1) C_l P_l(\cos \theta), \quad (2.40)$$

with  $\vec{n} \cdot \vec{m} = \cos \theta$ . A multipole  $l$  can be related to an angular scale  $\theta$  by the approximate relationship  $\theta \sim \pi/l$ . Most of the cosmological information is contained in the coefficients  $C_l$  of the Legendre polynomials  $P_l$ . Assuming the anisotropies to be gaussian, they can be expressed in terms of the variance of the  $a_{lm}$ :

$$C_l = \langle |a_{lm}|^2 \rangle = \frac{1}{2l+1} \sum_{m=-l}^{m=+l} |a_{lm}|^2. \quad (2.41)$$

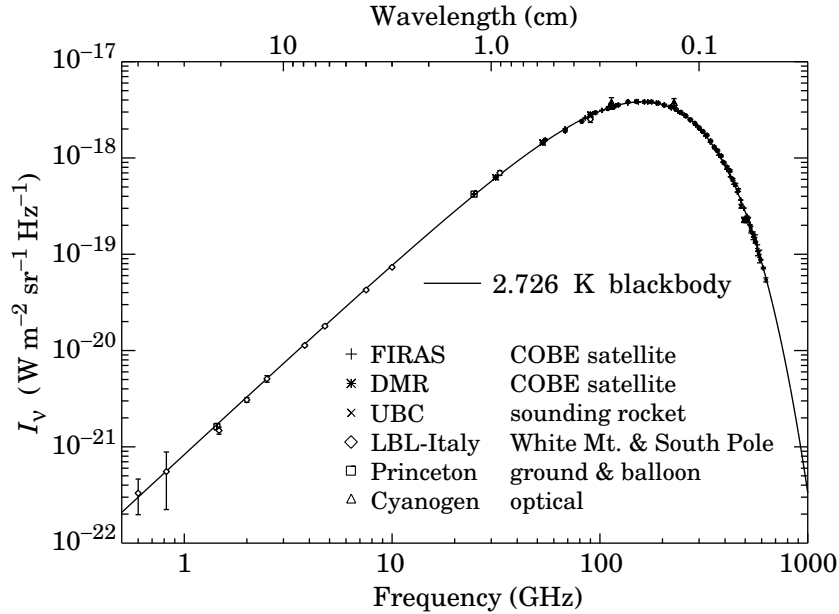


Figure 2.6: Precision measurements of the Cosmic Microwave Background fitted by a black-body distribution with a maximum at 2.726 K [29].

The monopole component ( $l=0$ ) can be associated with the mean temperature  $T_\gamma$  of the CMB. It can only be measured by absolute temperature devices like the FIRAS instrument on the COBE satellite. The largest anisotropy with an amplitude of  $3.358 \pm 0.017$  mK [31] is the first spherical harmonic (dipole,  $l=1$ ) which is dominated by the Doppler shift due to the motion of the solar system relative to the blackbody field. The theoretical power spectrum of the higher multipoles ( $l > 1$ ) is shown in Fig. 2.7. It can be subdivided into three main regimes [21]:

- **The Sachs-Wolfe Plateau ( $l \lesssim 100$ ):** At large angular scales (low  $l$ ) the dominant source of CMB anisotropies is gravitational redshift occurring on the surface of last scattering as well as by potentials CMB photons pass through on their way to the observer. These are referred to as the Sachs-Wolfe and the Integrated Sachs-Wolfe (ISW) effect, respectively.
- **The Acoustic Peaks ( $100 \lesssim l \lesssim 1000$ ):** Prior to Recombination baryons and photons were tightly coupled to each other behaving like a baryon-photon fluid. Perturbation of the gravitational potential mainly caused by Dark Matter drove oscillations in the baryon-photon plasma with the photon pressure acting as a repulsive, harmonic force. The first acoustic peak at  $l \approx 200$

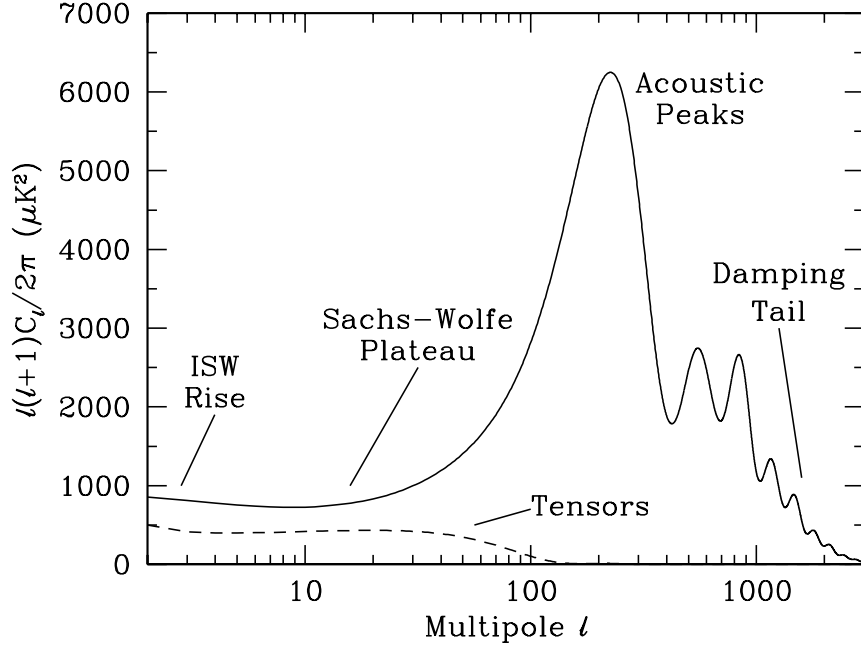


Figure 2.7: The theoretical CMB power spectrum. The different features denoted in the figure are explained in the text. Figure from [21].

can be related to the mode of the oscillating baryon-photon fluid that just reached its first maximum (compression) at the surface of last scattering. The ensuing acoustic peaks correspond to the modes reaching their second, third, fourth etc. antinodes of oscillation representing a series of alternating compressions and rarefactions of the baryon-photon fluid.

- **The Damping Tail ( $l \gtrsim 1000$ ):** Since the recombination process is not an instantaneous process, the surface of last scattering has a finite thickness. This can result in an imperfect baryon-photon coupling allowing for interdiffusion of both components leading to damped oscillations of the higher modes. This is referred to as Silk damping [32].

The tensor contribution depicted in Fig. 2.7 corresponds to gravity wave modes.

Comparing the coefficients  $C_\ell$  with those predicted by theoretical models provides a way of determining basic cosmological parameters. The most accurate values have been obtained by the satellite experiment WMAP (Wilkinson Microwave Anisotropy Probe). The power spectrum measured by WMAP and other balloon (Boomerang) and ground-based (Acbar, CBI) experiments is shown in Fig. 2.8.

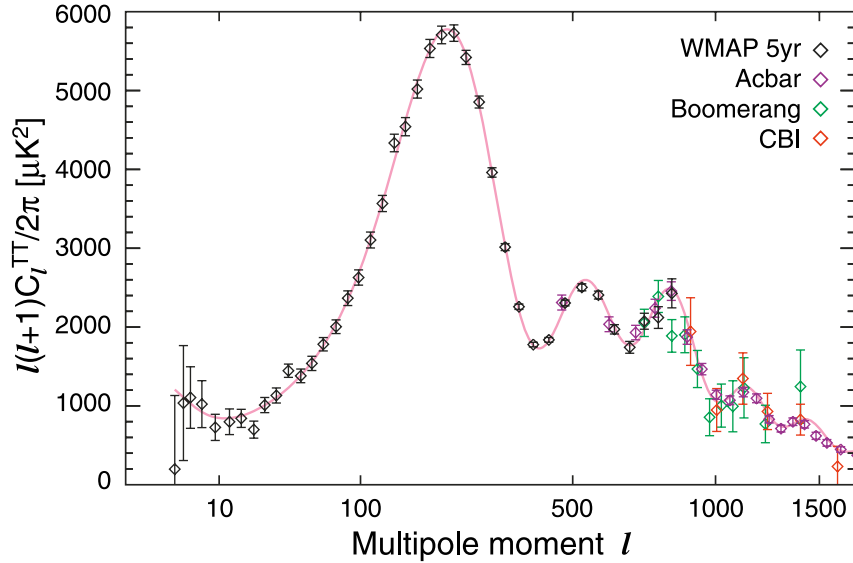


Figure 2.8: The WMAP 5-year temperature (TT) power spectrum with the results from Acbar, Boomerang and CBI. The full (red) curve is the best-fit six parameter  $\Lambda$ CDM model applied to the whole data set [33].

Some basic cosmological parameters derived from WMAP data combined with measurements of Type Ia supernovae (SN) and Baryon Acoustic Oscillations (BAO) in the galaxy distribution are depicted in Table 2.1 (68% CL) [20].

Table 2.1: Basic cosmological parameters

Parameter	Value
Age of Universe $t_0$	$13.73 \pm 0.12$ Gyr
Scaled Hubble constant $h_0$	$0.701 \pm 0.013$
Baryon density $\Omega_b$	$0.0462 \pm 0.0015$
Dark matter density $\Omega_{dm}$	$0.233 \pm 0.013$
Dark energy density $\Omega_\Lambda$	$0.721 \pm 0.015$
Total density $\Omega_{tot}$	$1.0052 \pm 0.0064$

According to this data set our Universe seems to be flat and dark. Its overall density is mainly dominated by Dark Energy and Dark Matter, whereas the contribution by radiation and neutrinos is insignificant. At the age of Recombination, however, photons made up 15% and neutrinos 10% of the Universe density. The baryonic density obtained from these measurements is in excellent agreement

with predictions from Big-Bang Nucleosynthesis. This is even more remarkable since these values have been obtained from different epochs of the Universe with very different physics. Due to this concordance, Nucleosynthesis and the Cosmic Microwave Background have become the cornerstones of the Standard Model of Cosmology.

## 2.2 Dark Matter Candidates

As shown in the previous section there is overwhelming evidence for Dark Matter. Several candidates have been proposed to account for it including baryonic and non-baryonic matter. The best motivated candidates will be presented in the following.

### 2.2.1 Baryonic Dark Matter

As already pointed out, even most of the baryonic matter is dark. Thus it cannot be found in the form of gas since then it would emit electromagnetic radiation either as microwaves from neutral hydrogen or UV thermal bremsstrahlung radiation from clouds of ionized hydrogen and helium. Neutron stars or black holes that are created in supernovae explosions would have ejected heavy elements that are also spectroscopically detectable.

The most popular candidates for baryonic dark matter are MAssive Compact Halo Objects (MACHOs). This is a generic term for any dark massive compact halo objects. Brown dwarfs are the most popular MACHO candidates. They are too light to develop the temperature and pressure needed for hydrogen burning ( $M < 0.08 M_{\odot}$ ). The most common MACHO detection technique is based on gravitational lensing. Measurements by the MACHO and EROS collaborations [34, 35] revealed that a standard halo contains less than  $\sim 15\%$  of dark objects in the mass range  $2 \cdot 10^{-7} - 1 M_{\odot}$ .

### 2.2.2 Non-Baryonic Dark Matter

Besides the results from Big-Bang Nucleosynthesis and WMAP especially arguments from structure formation [36] indicate that most of the matter in the Universe is non-baryonic. The most common hypothesis favours non-baryonic particle Dark Matter that has been created in the early hot stages of the Universe and, being stable enough, survived until present day.

### 2.2.2.1 Neutrinos

The only non-baryonic candidate which is known to exist is the neutrino. In the early Universe it was kept in equilibrium by reactions governed by the weak interaction and decoupled at a temperature of about 1 MeV. At this time neutrinos were relativistic and are hence an example for hot Dark Matter. Their total relic density is predicted to be [37]

$$\Omega_\nu h^2 = \sum_{i=1}^3 \frac{m_i}{93 \text{ eV}}, \quad (2.42)$$

where  $m_i$  denotes the mass of the  $i$ -th neutrino. Direct kinematic measurements based on tritium  $\beta$ -decay give a limit of  $m_\nu < (2.0 - 2.2) \text{ eV}$  [38], [39] implying a relic density of

$$\Omega_\nu h^2 \lesssim 0.07. \quad (2.43)$$

The precision measurements of WMAP put more stringent constraints on the neutrino relic density, yielding  $\Omega_\nu h^2 < 0.0065$  (95 % CL) [20]. These results suggest that neutrinos are not abundant enough to solve the Dark Matter enigma. Arguments from structure formation confirm these results. In a Universe dominated by hot Dark Matter large objects like superclusters form first, while smaller structures such as galaxies are then formed via fragmentation processes. This top-down scenario, however, disagrees with observations indicating that most of the Dark Matter must be cold.

### 2.2.2.2 Axions

Quantum Chromodynamics (QCD) is the gauge theory of the strong interaction. The QCD Lagrangian contains a term which, depending on an angular parameter  $\theta$ , can produce CP violating effects. A vanishing electric dipole moment of the neutron, however, indicates that  $\theta$  is close to zero, meaning that the strong interaction is not CP violating, although there is no a-priori argument against a value of order unity. This is referred to as the strong CP problem. The solution proposed by Peccei and Quinn [40] introduces a new global U(1) symmetry that is spontaneously broken. The pseudo-Golstone boson associated with this symmetry-breaking is the axion. Laboratory searches, stellar cooling and the dynamics of supernovae 1987A constrain the axion mass  $m_a < 0.01 \text{ eV}$  [41]. Due to their weak coupling to matter, axions never were in equilibrium in the early Universe so that they might account for the cold Dark Matter today [41]. The most promising axion detection scheme is based on the inverse Primakoff effect, i.e., the conversion of solar axions

into X-ray photons in strong magnetic fields. The best experimental upper limit on the axion-photon coupling of  $g_{a\gamma} < 8.8 \cdot 10^{-11} \text{ GeV}^{-1}$  (95 % CL) for  $m_a \lesssim 0.02 \text{ eV}$  has been set by the CAST ('CERN Axion Solar Telescope') experiment [42].

### 2.2.2.3 Supersymmetric Candidates

#### Weakly Interacting Massive Particles (WIMPs)-The Neutralino

Weakly Interacting Massive Particles are a generic class of electrically neutral, massive ( $m_\chi \sim \text{GeV-TeV}$ ) relic particles that interact only via weak interaction and gravity. They decoupled from equilibrium in the early Universe at a temperature  $T \sim m_\chi/20$ , so that they were non-relativistic at decoupling. Since this temperature is nearly independent of other WIMP properties they are natural candidates for cold Dark Matter. The WIMP relic density is given by [41]

$$\Omega h^2 \sim \frac{3 \times 10^{-27} \text{ cm}^3/\text{s}}{\langle \sigma_{ann} v \rangle}, \quad (2.44)$$

with the WIMP annihilation cross section  $\sigma_{ann}$  and the relative velocity  $v$  of the annihilating WIMPs. Annihilation cross sections of the order of the electroweak scale reveal relic densities that are cosmologically relevant. This coincidence has singled out WIMPs as the most favoured Dark Matter candidates.

Supersymmetric extensions of the Standard Model of particle physics provide well motivated WIMP candidates. Supersymmetry (SUSY) is a fundamental symmetry between fermions and bosons. It predicts for each Standard Model particle a supersymmetric partner which differs by half a unit of spin. These are the sleptons (superpartners of leptons, spin 0), the squarks (superpartners of quarks, spin 0), the gauginos (superpartners of the gauge bosons, spin 1/2) and the higgsinos (superpartners of the higgs bosons, spin 1/2). Most supersymmetric models contain a conserved multiplicative quantum number, referred to as R-parity:

$$R = (-1)^{3(B-L)+2S}, \quad (2.45)$$

with the baryon number  $B$ , the lepton number  $L$  and the spin  $S$ . The conservation of R-parity implies that the lightest supersymmetric particle (LSP) is stable. In the minimal supersymmetric extension of the Standard Model of particle physics (MSSM), the LSP is constituted by the lightest neutralino  $\chi$  which is a superposition of photino  $\tilde{\gamma}$ , zino  $\tilde{Z}^0$  and the neutral higgsinos  $\tilde{H}_1^0$  and  $\tilde{H}_2^0$ :

$$\chi = a_1 \tilde{\gamma} + a_2 \tilde{Z}^0 + a_3 \tilde{H}_1^0 + a_4 \tilde{H}_2^0. \quad (2.46)$$

A particular MSSM configuration is specified by several parameters. There is a wide range of parameter space with production and annihilation rates in the early Universe such that  $\Omega_\chi \sim \Omega_{DM}$  [43]. The neutralino mass ranges from 35 GeV

up to 2 TeV. The lower bound is constrained by accelerator experiments such as LEP [44]. The upper bound results from the requirement of Supersymmetry to maintain the mass hierarchy between the GUT scale and the electroweak scale.

### Superweakly Interacting Massive Particles (SWIMPs)-The Gravitino

Besides WIMPs whose interaction strength is set by the weak scale  $\sigma_{weak}$ , another species of supersymmetric particles, referred to as Superweakly Interacting Massive Particles (SWIMPs), is also known to possibly provide the observed cold DM relic density. Their interaction strength, however, is strongly suppressed compared to WIMPs by some large mass scale  $m_\Lambda$  [45]:

$$\sigma_{SWIMP} \sim \left( \frac{m_W}{m_\Lambda} \right)^2 \sigma_{weak}. \quad (2.47)$$

A well motivated SWIMP candidate is the Gravitino, the spin-3/2 supersymmetric partner of the Graviton [46]. Its interaction is suppressed by the reduced Planck scale  $M_p=2.4 \times 10^{18}$  GeV [45]. If the Gravitino is the lightest supersymmetric partner (LSP), its relic density is given by [47]

$$\Omega_{3/2} h^2 \sim 0.27 \left( \frac{T_R}{10^{10} \text{ GeV}} \right) \left( \frac{100 \text{ GeV}}{m_{3/2}} \right) \left( \frac{m_{\tilde{g}}}{1 \text{ TeV}} \right)^2, \quad (2.48)$$

where  $T_R$  is the reheating temperature of the Universe,  $m_{3/2}$  the Gravitino mass and  $m_{\tilde{g}}$  the Gluino mass.

A LSP with such a weak interaction, however, spoils the predictions of the Standard Cosmological Model with respect to Big-Bang Nucleosynthesis, since the Next-To-Lightest Supersymmetric Partner (NLSP) then becomes so longlived that it decays during or after nucleosynthesis. This problem can be overcome by introducing a small breaking of R-parity [48] leading to a decay of the NLSP into Standard Model particles long before nucleosynthesis by R-parity violating interactions could take place. If R-parity is not conserved, the neutralino becomes too short-lived to account for DM, in contrast to the Gravitino whose decay is suppressed by the Planck scale and the small R-parity violating couplings [49]. Assuming the Gravitino to be heavier than the gauge bosons, its primary decay channels are [50, 51, 52]:  $\Psi_{3/2} \rightarrow \gamma\nu, W^\pm l^\mp, Z^0\nu$ . Although the lifetime of a Gravitino with a mass of 100 GeV ranges between  $10^{23}$  and  $10^{37}$  s [53], which is orders of magnitudes larger than the age of the Universe, it might be decaying at rates large enough to make it indirectly detectable via its decay products.

### 2.2.3 Modified Newtonian Dynamics (MOND)

As long as no particle Dark Matter has been found another attempt can be made to explain a large variety of Dark-Matter phenomena. This is based on a modification of gravity such that no Dark Matter is needed.

In one phenomenological approach proposed by M. Milgrom [54] gravitational accelerations  $a$  below a certain limit  $a_0$  are given by

$$\frac{a^2}{a_0} = \frac{GM}{r^2}, \quad (2.49)$$

with  $a_0 \approx 10^{-8} \text{cm/s}^2$  and the gravitational constant  $G$ . This approach was very successful in explaining various phenomena related to dwarf galaxies, spiral galaxies and galaxy clusters [54, 55, 56, 57]. Like all theories based on modified gravity, however, the MOND approach lacks a relativistic formulation. Therefore it cannot be applied on cosmological scales.

## 2.3 Indirect Detection of Dark Matter

The indirect DM detection scheme aims at the detection of annihilation or decay products of particle Dark Matter. These particles are mainly neutrinos,  $\gamma$ 's and charged particles.

### 2.3.1 Indirect Search with Neutrinos

Due to their weak interaction neutrinos constitute the only particle species that is able to escape from very dense astronomical sites such as the Sun or the Earth where WIMPs are believed to accumulate [58, 59]. They furthermore retain information on their source since neutrinos are not deflected by the magnetic fields present in the galaxy. Up to now, existing experiments only set limits on the neutrino flux from DM annihilation. These experiments employ either multipurpose detectors in underground laboratories (BAKSAN [60], MACRO [61] and Super-Kamiokande [62]) or neutrino telescopes operated in deep water or ice (BAIKAL [63, 64] and AMANDA [65, 66]). Future neutrino-telescope based experiments are planned to complement the sky-coverage (ANTARES [67], NESTOR [68]) and to increase the sensitive volume (ICECUBE [69]) of current searches. All existing experiments search for neutrinos from DM annihilation within a certain cone of the target source by comparing the observed events with the expected background events. The major background for neutrino telescopes results from neutrinos induced in the atmosphere by cosmic-ray interactions.

Although current neutrino indirect DM searches suffer from low count rates, this approach is very promising due to the clear signature expected from neutrinos emitted by a pointlike source with an energy spectrum characteristic for the decaying or annihilating DM particles.

### 2.3.2 Indirect Search with $\gamma$ -Rays

Like neutrinos,  $\gamma$ -rays are not deflected by the galactic magnetic fields so that they point back to their source and possibly provide angular information. Furthermore, since gamma rays are not redshifted over galactic distances, they retain their spectral information.

The spectrum of photons expected from DM annihilation strongly depends on the WIMPs being considered. Neutralinos, for example, typically annihilate to final states consisting of heavy fermions ( $b\bar{b}$ ,  $t\bar{t}$ ,  $\tau^+\tau^-$ ) or bosons such as  $ZZ$  or  $W^+W^-$  [8]. Each of these annihilation modes results in a continuous spectrum of  $\gamma$  rays. In addition, the neutralino can also annihilate directly to  $\gamma$ 's via:  $\chi\chi \rightarrow \gamma\gamma$  [70] or  $\chi\chi \rightarrow \gamma Z$  [71] leading to a clear spectral signature. Such photons, however, are produced only in a very small fraction of neutralino annihilations.

Space-based experiments searching for  $\gamma$ 's from DM annihilations focus on low energies, those on ground at high energies. To date, several gamma-ray observatories have reported excess signals that can be ascribed to DM annihilations.

**1. The EGRET galactic spectrum:** During the 1990s the EGRET instrument on the Compton Gamma Ray observatory provided the first  $\gamma$ -ray survey in an energy range between a few MeV and about 20 GeV. When compared to galactic models an increased gamma-ray flux has been observed at energies above 1 GeV. This has been ascribed to DM annihilations in the galactic halo [72]. This interpretation, however, requires significant departures from standard galactic models such as DM halo profiles and galactic diffusion models. This excess flux is expected to be quickly clarified by the Fermi gamma ray space telescope.

**2. The EGRET extragalactic spectrum:** In addition to the galactic emission, a significant fraction of the extragalactic  $\gamma$  ray background is also expected to originate from DM annihilations [73]. The origin of the diffuse extragalactic gamma ray background observed by EGRET is not yet known. Besides several astrophysical sources such as blazars, a large fraction of the gammas with energies in the 1-20 GeV range might result from annihilating WIMPs [74]. The observed spectrum reasonably fits with predictions for a WIMP mass of roughly 500 GeV, even though large annihilation rates are required for this scenario. It has also been suggested that EGRET's extragalactic spectrum can be explained by a gravitino

with a mass of  $m_{3/2} \sim 150$  GeV and a lifetime of  $\tau_{3/2} \sim 10^{26}$  s [75].

**3. The INTEGRAL 511 keV line:** A very bright emission of 511 keV photons from the galactic center has been observed by the SPI (SPectrometer on INTEGRAL) spectrometer on board of the INTEGRAL satellite [76]. Assuming this signal to originate from DM annihilations a WIMP mass in the MeV range is required [77]. This can only be constituted by some exotic Dark Matter candidates such as fermionic or scalar DM particles annihilating through a vector mediator that must also be very light in order to avoid overabundance today [78].

To date, none of these signals have been positively confirmed. New results from more precise experiments such as the Fermi gamma ray space observatory (formerly known as GLAST) will help clarify their origins.

### 2.3.3 Charged Cosmic Rays from WIMP Annihilation

In addition to neutrinos and gamma rays, WIMPs are expected to decay into charged particles such as electrons, positrons, protons or antiprotons. In contrast to neutrinos and  $\gamma$ 's they are influenced by the galactic magnetic fields resulting in a diffuse spectrum at Earth.

Up to now several experiments have reported excess fluxes of electrons and positrons in the galactic halo. The space-based PAMELA experiment launched in June of 2006 reported an anomalous rise in the cosmic ray positron fraction above 10 GeV [79] confirming earlier results from HEAT [80]. In addition, an excess in the electron flux between 300 and 800 GeV has been observed by the ATIC balloon experiment [81]. Taken together, these observations indicate the presence of a local (within  $\sim 1$  kpc) source of electrons and positrons. Even though the origin of this source is not yet clear, two possibilities are likely: the emission from pulsars [82] or Dark Matter annihilations [83, 84]. The latter scenario, however, requires WIMPs with special properties, i.e. annihilation dominantly to charged leptons at rates orders of magnitudes higher than expected for a thermal relic.

### 2.3.4 The WMAP Haze

The Wilkinson Microwave Anisotropy Probe (WMAP) has observed an excess of microwave emission in the inner  $20^\circ$  around the center of the Milky Way, known as WMAP Haze [85]. Among several possible origins that may account for this emission, it has been suggested that it could result from annihilating WIMPs [86]. These produce relativistic electrons and positrons which when travelling under the influence of galactic magnetic fields produce synchrotron radiation which can be measured by WMAP.

In contrast to the other signals, the WMAP Haze neither requires unexpected particle properties nor special astrophysics to be a possible product of annihilating WIMPs. The observed angular distribution, intensity and spectrum are consistent with a particle thermally produced in the early Universe with interaction strengths on the electroweak scale.

Since from the DM profile and the annihilation cross sections needed to generate the Haze a prompt gamma ray flux is expected, these results can be checked by the upcoming Fermi gamma ray space telescope [87]. Improved measurements of the spectrum and angular distribution are further expected from the Planck satellite.

## 2.4 Direct Detection of Cold Dark Matter

The basic idea underlying the direct detection technique is that if WIMPs are gravitationally bound in our galactic halo there must be a substantial flux on Earth. Since the interaction strength with ordinary matter is assumed to be given by the weak coupling there is a non-negligible chance of detecting them in low-background experiments [88]. The most promising detection scheme is based on elastic scattering of neutralinos off atomic nuclei.

### 2.4.1 Halo Model

The calculation of the scattering rates expected in a direct detection experiment depends on several parameters which are subject to considerable uncertainty, including the WIMP mass, the scattering cross section, the local density as well as the velocity distribution. A commonly used model for the Dark Matter distribution that produces flat rotation curves at large radii is the cored spherical isothermal halo [89]:

$$\rho(r) = \rho_0 \frac{a^2 + r_0^2}{a^2 + r^2}, \quad (2.50)$$

where  $a$  denotes the core radius,  $r_0$  the radius of the Sun's orbit around the galactic center and  $\rho_0 \approx 0.3 \text{ GeVcm}^{-3}$  [8] the local WIMP density. The corresponding velocity distribution in the galactic rest frame is given by a Maxwellian distribution:

$$f(\vec{v}, \vec{v}_E) \sim \exp\left(-\frac{(\vec{v} + \vec{v}_E)^2}{v_0^2}\right), \quad (2.51)$$

where  $v_0 \approx 220 \text{ km/s}$  [90] is the circular speed of the Sun around the galactic center.  $\vec{v}_E$  denotes the Earth velocity in the motionless halo, which is a sum of the Earth's orbital velocity around the Sun  $v_{orb} \approx 30 \text{ km/s}$ , the Sun's velocity  $v_0$  with respect to the galactic disk and the velocity of the disk itself  $v_{disk} \approx 12 \text{ km/s}$  [91]:

$$v_E = v_\odot + v_{orb} \cos\gamma \cos[\omega(t - t_0)], \quad (2.52)$$

where  $v_\odot = v_0 + v_{disk} \approx 232$  km/s and  $\omega = 2\pi/1\text{yr}$ . The angle  $\gamma \approx 60^\circ$  denotes the inclination of the Earth's orbital plane with respect to the galactic plane. The phase is given by  $t_0 = \text{June 2nd} \pm 1.3$  days. This distribution is furthermore truncated by an escape velocity  $v_{esc} \approx 650$  km/s [92]. WIMPs with velocities larger than  $v_{esc}$  escape the gravitational potential, so that they do not contribute to the total flux.

### 2.4.2 Scattering Rates

The differential WIMP scattering rate off nuclei can be written as [8]

$$dR = N_T \frac{\rho_0}{m_\chi} f(v, v_E) v \frac{d\sigma}{dE_R} dE_R dv. \quad (2.53)$$

Here,  $N_T$  denotes the number of target nuclei,  $\rho_0$  the local WIMP density,  $m_\chi$  the WIMP mass,  $v$  and  $f(v, v_E)$  the WIMP velocity and the velocity distribution, respectively. Since WIMP velocities are non-relativistic the nuclear recoil energy  $E_R$  is given by

$$E_R = \frac{\mu_N^2 v^2}{m_N} (1 - \cos\theta), \quad (2.54)$$

with the nuclear mass  $m_N$ , the WIMP-nucleus reduced mass  $\mu_N = m_\chi m_N / (m_\chi + m_N)$  and the scattering angle  $\theta$  in the center-of-mass frame.

The differential WIMP-nucleus cross section  $d\sigma/dE_R$  has a spin-independent (scalar) and a spin-dependent (axial) component [8]:

$$\frac{d\sigma}{dE_R} = \left( \frac{d\sigma}{dE_R} \right)_S + \left( \frac{d\sigma}{dE_R} \right)_A = \frac{\sigma_N^{S0}}{E_R^{max}} F_S^2(E_R) + \frac{\sigma_N^{A0}}{E_R^{max}} F_A^2(E_R), \quad (2.55)$$

where  $E_R^{max} = 2\mu_N^2 v^2 / m_N$  is the maximum recoil energy.  $\sigma_N^{S0}$  and  $\sigma_N^{A0}$  denote the WIMP-nucleus cross sections in the limit of zero momentum transfer for scalar and axial coupling, respectively. The total spin-dependent cross section at zero momentum transfer  $\sigma_N^{A0}$  is given by [8]

$$\sigma_N^{A0} = \frac{32}{\pi} G_F^2 \mu_N^2 \Lambda^2 J(J+1), \quad (2.56)$$

where  $J$  is the total angular momentum of the nucleus and  $G_F$  Fermi's constant.  $\Lambda$  is given by

$$\Lambda = (1/J)[a_p \langle S_p \rangle + a_n \langle S_n \rangle]. \quad (2.57)$$

Here  $\langle S_p \rangle$  and  $\langle S_n \rangle$  denote the expectation values of the spin content of the proton and neutron group in the nucleus, respectively, whereas  $a_p$  and  $a_n$  are the corresponding axial couplings.

The total scalar cross section at zero momentum transfer  $\sigma_N^{S0}$  is [8]

$$\sigma_N^{S0} = \frac{4\mu_N^2}{\pi} [Zf_p + (A - Z)f_n]^2, \quad (2.58)$$

where  $Z$  is the nuclear charge,  $A - Z$  the number of neutrons,  $f_p$  and  $f_n$  the effective couplings of neutralinos to protons and neutrons, respectively. In most cases  $f_p$  equals  $f_n$  so that  $\sigma_N^{S0} \propto A^2$ . For target masses with  $A \geq 30$  the scalar part is in general dominant [8].

When the wavelength  $\lambda = h/q$  associated with the momentum transfer  $q = \sqrt{2m_N E_R}$  is no longer large compared to the nuclear radius, both scalar and axial cross sections begin to fall with increasing  $q$ . This is usually described by multiplicative form factors  $F_S(E_R)$  and  $F_A(E_R)$  for the scalar and axial interaction, respectively. An analytic expression for the spin-independent interaction is provided by the Helm form factor [93]:

$$F(qr_n) = 3 \frac{\sin(qr_n) - qr_n \cos(qr_n)}{(qr_n)^3} e^{-(qs)^2/2}, \quad (2.59)$$

where  $r_n = \sqrt{c^2 + 7/3\pi^2 a^2 - 5s^2}$  is an effective nuclear radius with  $s \approx 0.9$  fm,  $a \approx 0.52$  fm and  $c \approx 1.23A^{1/3} - 0.6$  fm [94].

The Helm form factors for different nuclei commonly used in terrestrial targets are depicted in Fig. 2.9. For heavier nuclei such as Xe and W the influence of the form factors becomes significant at larger momentum transfers. The differential scattering rates for spin-independent interaction are obtained by integrating over all incoming velocities. Ignoring the Earth velocity  $v_E$ , one gets [94]

$$\frac{dR}{dE_R} = \frac{k_\infty}{k_{esc}} \frac{\sigma_N^{S0} \rho_0}{\sqrt{\pi} v_0 m_\chi \mu_N^2} F_S^2(E_R) \left[ \exp\left(-\frac{E_R m_N}{2\mu_N^2 v_0^2}\right) - \exp\left(-\frac{v_{esc}^2}{v_0^2}\right) \right]. \quad (2.60)$$

Here,  $k_{esc}$  denotes the scale factor of the truncated Maxwellian velocity distribution given by equation 2.51, whereas  $k_\infty$  corresponds to a distribution with  $v_{esc} \rightarrow \infty$ . The need to compare results from different target materials requires to refer the recoil spectra to nucleons rather than to a specific nucleus. Since the WIMP-nucleus cross section in the zero-momentum transfer for spin-independent interaction,  $\sigma_N^{S0}$ , scales as  $A^2 \mu_N^2$  [94], it can be written in terms of the WIMP-nucleon cross section  $\sigma_n^{S0}$  as [94]

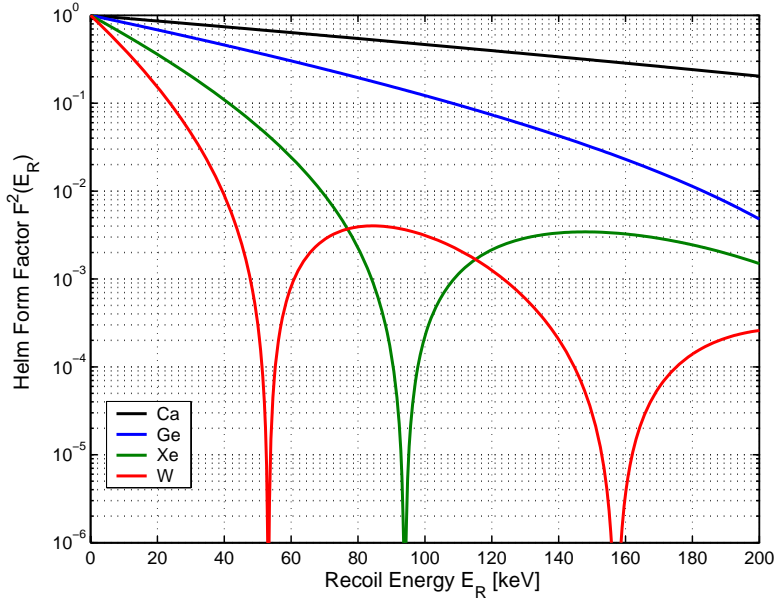


Figure 2.9: Helm form factors for Ca, Ge, Xe and W nuclei.

$$\sigma_N^{S0} = \sigma_n^{S0} \left( \frac{\mu_N}{\mu_n} \right)^2 A^2, \quad (2.61)$$

where  $\mu_n$  is the WIMP-nucleon reduced mass.

The differential WIMP recoil spectra for different nuclei is shown in Fig. 2.10 assuming spin-independent interaction for a WIMP mass of 100 GeV and a WIMP-nucleon cross section  $\sigma_n^{S0}=10^{-43}$  cm<sup>2</sup>.

The total rates for a given interaction (scalar or axial) are obtained by integrating the differential rates over deposited energies above the energy threshold  $E_{thr}$  of the detector (Fig. 2.11).

### 2.4.3 Experimental Requirements

From the theoretical event rates depicted in Fig. 2.10 and Fig. 2.11 several important conclusions concerning direct Dark Matter experiments become evident:

1. **Target Mass:** The expected WIMP-nucleus scattering rates range below 1/kg/day, therefore target masses up to the tonne scale are needed to gain sufficient statistical accuracy in a reasonable time.
2. **Energy Threshold:** Since the WIMP signal originates from a featureless

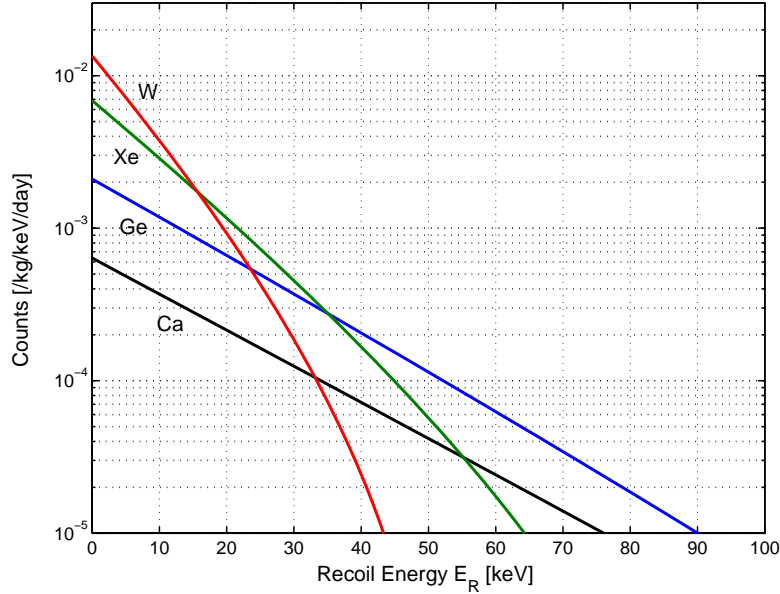


Figure 2.10: Differential WIMP scattering rates for spin-independent interaction for Ca, Ge, Xe and W for a WIMP mass of 100 GeV and a WIMP-nucleon cross section of  $10^{-43} \text{ cm}^2$ .

quasi-exponentially decreasing energy spectrum, low energy thresholds are mandatory. This is a key requirement especially for experiments using targets consisting of heavier nuclei such as Xe and W. Despite their advantage due to the  $A^2$  dependence of the scattering cross section in the limit of zero momentum transfer, they become less optimal at higher energies ( $\gtrsim 20 \text{ keV}$ ) due to the Helm form factor suppression.

**3. Background:** Due to the low WIMP scattering rates, a basic requirement of direct Dark Matter experiments is understanding and suppressing the various types of background. The significant sources of background in a rare-event experiment can be roughly subdivided into [95]: (a) environmental radioactivity (mainly  $\gamma$ 's from the U and Th decay chains as well as from  $^{40}\text{K}$  decay), (b) radioimpurities in detector and shielding materials ( $^{210}\text{Pb}$  in lead shields, e.g.), (c) Rn and its progenies, (d) cosmic rays (mainly neutrons, muons, and secondaries), and (e) neutrons from fission and  $(\alpha, n)$  reactions.

A low background can be achieved in both passive and active ways. Passive rejection techniques involve shieldings against the different types of environmental radioactivity, a high material selection of detector components and setting up the experiment in an underground facility in order to reduce the effect of cosmic rays.

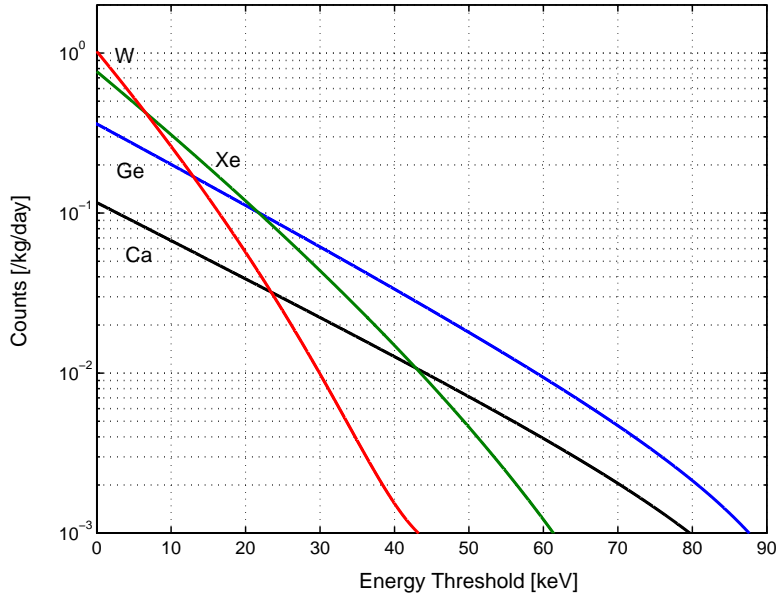


Figure 2.11: WIMP scattering rates for spin-independent interaction for Ca, Ge, Xe and W for a WIMP mass of 100 GeV and a WIMP-nucleon cross section of  $10^{-43}$  cm<sup>2</sup>.

Since the WIMP signal is expected to originate from nuclear recoils, the main background is constituted by electron recoils induced by  $\gamma$ 's and  $\beta$ 's. This type of background can be actively rejected using hybrid detectors providing a twofold signature of the particle interaction such as a phonon-charge or phonon-light signal allowing for an event-by-event discrimination of electron recoils. Highly granular hybrid detectors furthermore offer the opportunity to reject multiple scattering events which can be ascribed to neutrons. Further active background rejection techniques range from active shields (plastic/liquid scintillators or water Cherenkov shields) surrounding the detector and acting as muon vetos, to position sensitive detectors allowing for the discrimination of surface events mainly caused by electron recoils. The latter one is a mandatory requirement for all hybrid detectors based on the phonon-charge technique, since near-surface electron recoils mimic nuclear recoils due to insufficient charge collection [96].

#### 2.4.4 WIMP Signatures

Since the events induced by electron recoils can be effectively discriminated using hybrid detectors, the remaining background is constituted mainly by neutrons and heavy nuclear recoils associated with radon surface contamination [97]. Due to the featureless shape of the WIMP energy spectrum, it cannot be distinguished from the

remaining background. Therefore, for convincing Dark Matter detection a unique signature is needed.

Assuming a non-rotating spherical halo, an annual modulation of the direct scattering rates is expected since the Earth's motion in the galactic frame (see section 2.4.1) induces a variation of the relative velocity between the galactic halo and the earth's trajectory (Fig. 2.12, left panel) [98, 99].

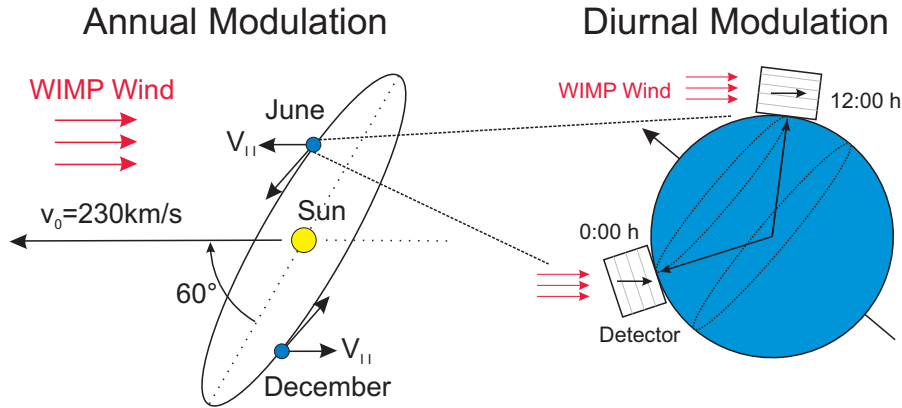


Figure 2.12: Annual modulation of the expected WIMP direct detection rates due to the Earth's movement around the Sun (left panel). Directional modulation on a daily basis (right panel).

The expected scattering rates can be approximated by a cosine function with a period of 1 year and a phase of  $t_0 \approx \text{June}^{2\text{nd}}$ :

$$R(t) = R_0 + R_m \cos[\omega(t - t_0)]. \quad (2.62)$$

Here  $R_0$  and  $R_m$  denote the amplitudes of the constant and modulated signals, respectively, whereas the background rates are not considered. Since the expected modulation effect is of the order of  $\sim 0.07$ , its detection requires large detector masses, a high long-term stability and a background that is not subject to the same modulation effects.

A much stronger signature is provided by the Earth motion around its axis leading to a diurnal modulation of the recoil direction (Fig. 2.12, right panel) [100, 101]. The resulting forward-backward asymmetry is expected to be of the order of  $\sim 1$  so that fewer events are needed to see this effect. A mandatory prerequisite, however, is the ability to detect the recoil direction. This represents an ambitious objective. The by now most promising directional detection technique is developed in the context of the DRIFT (Directional Recoil Identification From Tracks) experiment using low density gas targets such as  $\text{CS}_2$  at room temperature [102].

A third signature is provided by the dependence of the scattering rates ( $\sim A^2$ ) on the target material, i.e., on the target-nucleus mass ( $A$ ). Therefore, operating detectors consisting of different target materials under similar background conditions, offers the opportunity to compare the interaction rates, thus providing a test of the WIMP hypothesis.

## 2.5 WIMP Direct Detection Experiments

Despite the stringent constraints set by the experimental requirements mentioned in section 2.4.3, i.e., energy threshold, target mass and low background, many experiments currently search for WIMP Dark Matter. The techniques employed in these experiments are mainly based on ionization, scintillation or phonon detection as well as on combinations of them in order to meet the requirement of an active suppression of the background induced by electron recoils. A classification scheme of the most important current direct DM experiments is shown in Fig. 2.13.

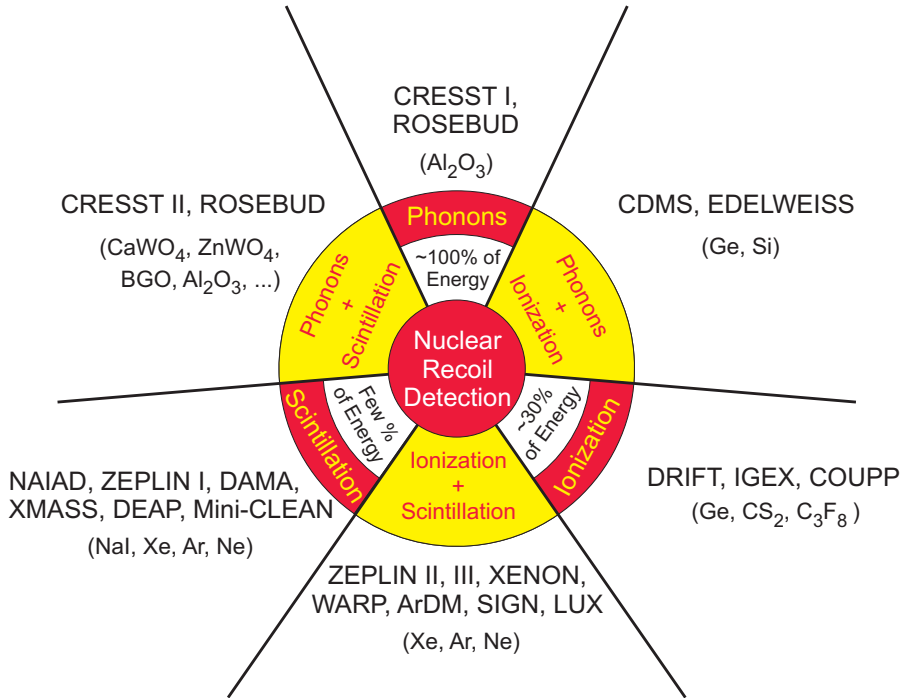


Figure 2.13: Classification of current direct Dark Matter experiments according to their detection schemes.

In the following the most important Dark Matter detection schemes and the corresponding experiments will be outlined.

### 2.5.1 The DAMA/LIBRA Annual Modulation

The DAMA (DARK MATTER) experiment operated at the Gran Sasso National Laboratory of the I.N.F.N. aims at the detection of particle DM exploring the annual modulation signature (eq. 2.62). In its first phase (DAMA/NaI) DAMA employed a total of nine radiopure NaI(Tl) scintillators each of 9.70 kg and read out by two PMTs working in coincidence with an energy threshold of  $\sim 2$  keV. DAMA/NaI has been operated over seven full annual cycles between 1996 and 2002 providing a total exposure of 0.29 ton years.

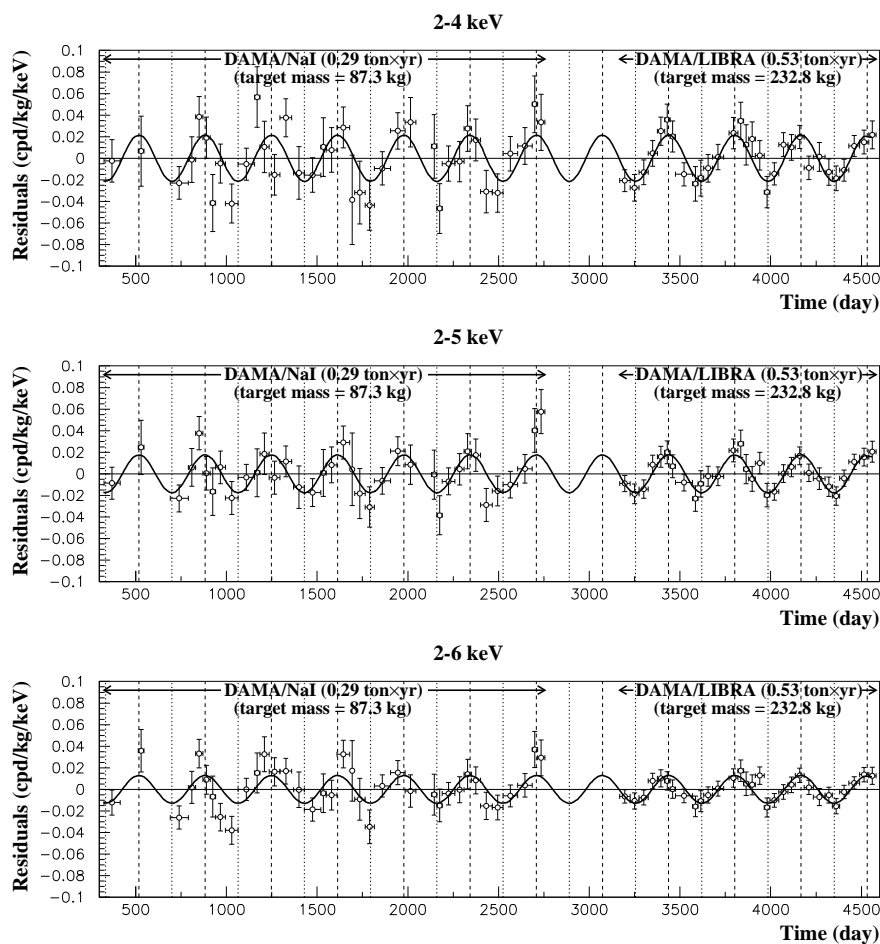


Figure 2.14: Residual rate of single-hit events in the (2-4), (2-5), (2-6) keV energy intervals measured by DAMA/NaI and DAMA/LIBRA. The solid lines represent the superimposed cosinoidal functions  $A\cos[\omega(t-t_0)]$  with a period of one year and a phase  $t_0=152.5$  days (June<sup>2nd</sup>). The zero of the time scale is January 1<sup>st</sup> [103].

The investigation of the annual modulation signature is claimed to be realized model independent by analyzing the time dependence of the residual rates of single hit events. The residual rates are derived from the measured event rates by subtracting the constant part corresponding to the average rate of all detectors and energy bins over the cycles. This analysis exhibits the presence of a modulated cosine-like behaviour at  $6.3\sigma$  C.L. with a period of  $1.00 \pm 0.01$  year and a phase consistent with June<sup>2nd</sup> [104]. Assuming standard halo parameters this modulation corresponds to a WIMP mass of  $\sim 50$  GeV and a WIMP nucleon cross section for spin-independent interaction of  $\sim 10^{-6}$ pb.

The second phase of DAMA (DAMA/LIBRA) has started 2003 with a similar setup and a total mass of  $\sim 250$  kg. The analysis of the data from an exposure of 0.53 ton years confirm the results of DAMA/NaI exhibiting the same modulation effects at  $8.2\sigma$  C.L. [103]. The combined results from DAMA/NaI and DAMA/LIBRA are depicted in Fig. 2.14.

Up to now all WIMP mass regions and cross sections related to elastic scattering models that have been found to reconcile DAMA's annual modulation with the negative results of other direct Dark Matter experiments such as CDMS, EDELWEISS or CRESST have been rejected. New studies, however, taking the ion channeling effect [105],[106] into account revive the possibility of DAMA's compatibility with other direct DM experiments, especially at low WIMP masses. This effect describes the enhancement of the scintillation light yield for nuclear recoils along the characteristic axes or planes of the crystal particularly for small energies. All channelled events are considered to have the same ionization yield as electron recoils of the same energy providing an energy threshold of roughly 2 keV. Even if considering the ion channeling effect, the most preferred DAMA regions for spin-independent interaction of any WIMP mass are ruled out at  $3\sigma$  [107]. Only for WIMP masses of  $\sim 10$  GeV, reasonable fits outside of these preferred regions are compatible with all upper limits from negative searches, considering ion channeling [107], [108], [109], [110], [111]. For spin-dependent interaction, WIMP masses below 10 GeV provide compatibility with other searches when ion channeling is included [107].

### 2.5.2 Liquid Noble Gas Experiments

Hybrid Dark Matter detectors employing the charge-light technique are currently based on liquid noble gases. The main target materials are neon (CLEAN [112]), argon (ArDM [113], WARP [114], DEAP [115]) and xenon (XENON10 [116], ZEPLIN [117], XMASS [118]). Some of their properties relevant for the employment as targets in a Dark Matter detector are summarized in table 2.2.

Liquid neon (LNe), argon (LAr) and xenon (LXe) have excellent properties as Dark Matter targets. They are intrinsic scintillators with high light yields

Element	Operating Temperature	Wavelength	Ionization Energy
Ne	22 K	85 nm	21.56 eV
Ar	87 K	128 nm	15.75 eV
Xe	165 K	175 nm	12.13 eV

Table 2.2: Main properties of the liquid noble gases neon, argon and xenon that are relevant for their employment as targets in Dark Matter detectors based on the charge-light technique [119].

and owing to the low ionization potentials also high ionization yields. They are furthermore available in large quantities and can be easily purified to 1 ppt-levels. While neon is free of any radioactive isotopes, natural argon contains  $\sim 1$  Bq/kg of  $^{39}\text{Ar}$  ( $\beta$ -emitter,  $T_{1/2}=269$  yr, endpoint energy 565 keV) yielding an integrated event rate of 1 kHz per ton. The operation of large LAr detectors requires therefore a low  $^{39}\text{Ar}$  content. Besides the double beta emitter  $^{136}\text{Xe}$  ( $T_{1/2} \sim 10^{21}$  yr) natural xenon does not contain other radioactive isotopes. The only radioactive impurity originates from  $^{85}\text{Kr}$  ( $\beta$ -emitter,  $T_{1/2}=10.76$  yr, endpoint energy 687 keV) that has to be reduced to few 100 ppt levels for a 100 kg detector. This can be achieved by distillation [118] or adsorption on a charcoal column [119].

Due to its high atomic number ( $A=131.3$ ) xenon is favorable as a target for scalar WIMP-nucleon interaction and the presence of two isotopes with an odd number of nucleons ( $^{129}\text{Xe}$  (spin-1/2, 26.4%) and  $^{131}\text{Xe}$  (spin-3/2, 21.2%)) yields significant sensitivity to the WIMP spin-dependent interaction. Due to its high density ( $3 \text{ g/cm}^3$ ) and high atomic number ( $Z=54$ ) it allows furthermore to build self-shielding detectors and in contrast to Ar and Ne no wavelength shifters are needed.

All detectors employing noble liquid gases are currently operated in dual-phase mode consisting of a liquid target and a gas phase above the liquid. A particle interaction in the liquid generates both scintillation light and ionization. The primarily generated photons (prompt light) are detected by an array of UV-sensitive PMTs. When a high electric field ( $\sim 1 \text{ kV/cm}$ ) is applied the particle-induced electrons in the liquid can be extracted into the gas phase where additional photons (proportional light) and charge are generated. The simultaneous measurement of the light and charge signals allows a discrimination of the background induced by electron recoils. The proportional light is also detected and from the time delay of both light signals the event depth ( $z$ ) can be reconstructed. Since the x-y position can be inferred from the relative size of the signals in the PMTs, a full 3D reconstruction of the event position in the detector can be achieved allowing for fiducial volume cuts for a better background discrimination.

**XENON10:** Up to now the most successful liquid noble gas DM experiment is XENON10 [116]. It has operated a 15 kg dual phase time projection chamber in the Gran Sasso Underground Laboratory (L.N.G.S.) during the period between October 2006 and February 2007. Two UV-sensitive PMT arrays are used to measure the prompt and proportional light. The bottom array (41 PMTs) is in the liquid and measures mainly the prompt light signal. The bottom array in the gas consists of 48 PMTs and detects the proportional light. From the relative size of the signals in the top array the x-y position can be reconstructed with a resolution of a few mm. The z-coordinate can be inferred from the electron drift time with a resolution of less than 1 mm. With the position reconstruction a fiducial volume with a mass of 5.4 kg can be defined in the central part of the detector. Here the  $\gamma$  background is at a level of 0.6 events/kg/day/keV mainly due to self-shielding effects.

Based on calibration measurements with  $\gamma$  and neutron sources a region of interest for the WIMP analysis could be defined. It ranges between 4.5 and 29.6 keV ( $3\sigma$ ) below the mean of the nuclear recoil band. The logarithmic ionization/scintillation (S2/S1) ratios of the events recorded during the 58.6 live-days are depicted in Fig. 2.15. The region of interest is marked by the vertical (black) lines and the horizontal (blue) lines.

From a total of 1800 observed events during this run, 10 events are found in the WIMP acceptance region. Seven of them are expected from statistical leakage assuming a Gaussian distribution of the electron recoil band. In order to set conservative limits on the spin-independent WIMP-nucleon cross section all 10 events are considered as WIMP candidates. In this way, an upper limit of  $5.6 \cdot 10^{-8}$  pb could be set for a WIMP mass of 30 GeV [120] (see Fig. 3.15 in section 3.5).

The XENON collaboration aims at increasing the target mass up to 1 tonne. With an increased target mass and a strongly reduced background a sensitivity to spin-independent WIMP-nucleon cross section of  $<10^{-9}$  pb is expected [121].

### 2.5.3 Cryogenic Dark Matter Experiments

Cryogenic phonon detectors meet the basic requirements of Dark Matter experiments due to their unprecedented energy resolutions and sensitivities. In addition, they allow the employment of absorbers with masses of several 100 g each. Dielectric materials are used because of their  $T^3$  dependence of the specific heat at low temperatures. The hybrid detection scheme (see Fig. 2.13) offers the opportunity to actively discriminate the background induced by electron recoils. This hybrid detection scheme based on cryogenic phonon sensors has been realized in two different ways, as phonon-charge and phonon-light detectors.

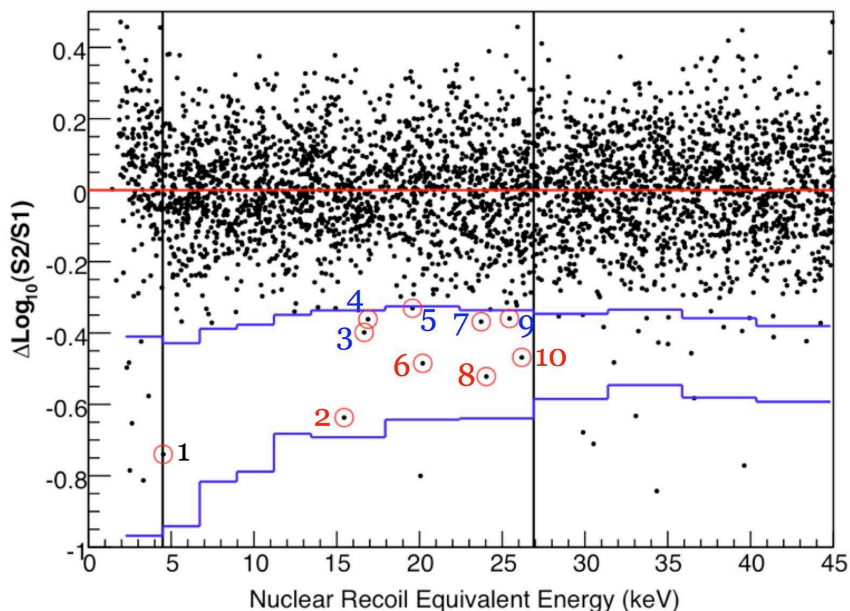


Figure 2.15: XENON10 results from 58.6 live-days with a fiducial volume of 5.4 kg. The vertical lines mark the region of interest (4.5 to 26.9 keV nuclear recoil equivalent energy). The (blue) horizontal lines indicate the nuclear recoil acceptance region. S2/S1 denote the ionization/scintillation ratios of the events. Figure from [116].

### 2.5.3.1 Phonon-Charge Detection

The phonon-charge technique was the first one to provide active discrimination of electron recoil events using cryogenic detectors [122, 123]. The detector materials of choice employed in this detection scheme are high-purity germanium and silicon single crystals. Ge, however, is preferred, mainly due to the higher scattering rates expected from the  $A^2$  dependence of the spin-independent cross section in the limit of zero-momentum transfer.

The principle underlying this discrimination scheme is based on the different ionization efficiencies of electron and nuclear recoils. Germanium has a bandgap of  $\sim 0.7$  eV [4] and the mean electron recoil energy needed for the generation of an electron-hole pair is  $\sim 2.9$  eV [4]. The ionization efficiency of nuclear recoils is about a factor of 3 lower than for electron recoils providing an efficient technique for the discrimination of electron recoils down to 10 keV recoil energy (Fig. 2.16). The quenching factor corresponding to the reduced ionization efficiency of nuclear recoils can be determined experimentally using neutron sources and tagged neutron beams [2, 124].

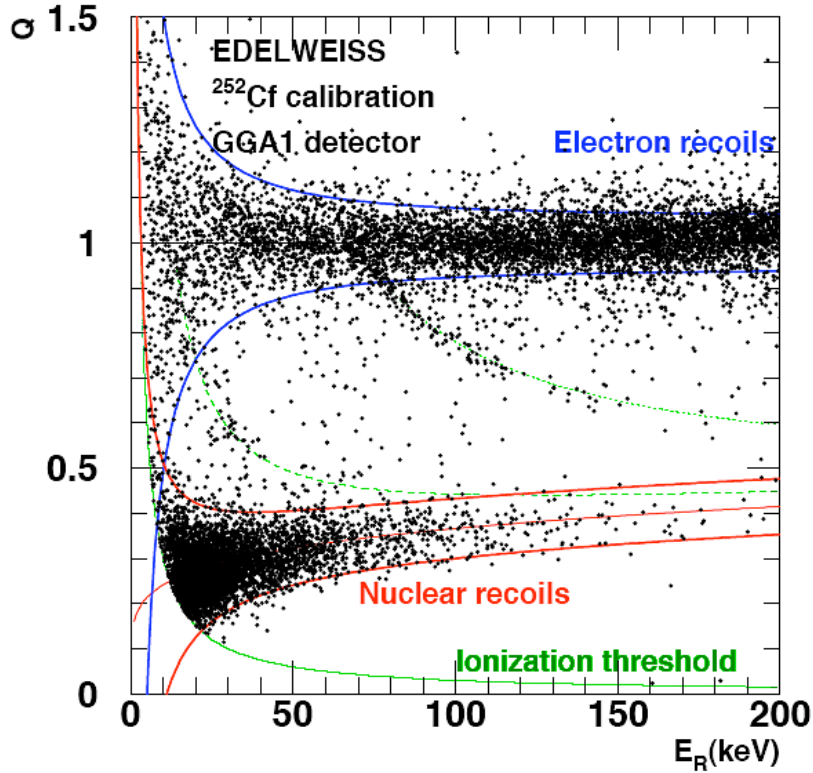


Figure 2.16:  $^{252}\text{Cf}$  calibration of a Ge detector (EDELWEISS experiment) [124].

The response of a  $\sim 320$  g Ge detector to electron and nuclear recoils is depicted in Fig. 2.16 [124]. The quenching factor  $Q$  is defined as the ratio of ionization to phonon signal amplitude and is set to 1 for electron recoils. For nuclear recoils this ratio is approximately 0.3. The solid blue and red lines represent the 90% electron and nuclear recoil zones, respectively. The curve corresponding to the ionization threshold is also indicated. The dashed lines are due to the 13.26 and 68.75 keV levels excited in  $^{73}\text{Ge}$  by inelastic neutron scattering.

One of the major drawbacks of the phonon-charge technique is the insufficient charge collection of near-surface events which degrades the discrimination capability of such detectors. This mainly results from the screening of the external collection field inside the electron-hole plasma generated by the particle interaction. The screened charge carriers can then diffuse to the wrong electrode where they get trapped being thus removed from the detection channel. This shortcoming has been partially overcome by introducing a thin layer of sputtered amorphous Ge beneath the Al electrodes. The physics of these structures is not known with

certainty but following the most common hypothesis the amorphous layers act as repulsive barriers thus preventing the collection of charge carriers that would be otherwise trapped due to diffusion processes. Charge carriers of the correct species that are drifted to the electrodes and accumulate at the layer are still sufficiently collected since the contacts exhibit a non-zero conductivity ( $\sim \text{G}\Omega/\text{cm}^2$ ) due to hopping conduction [125]. Further discrimination schemes of near surface events are based on pulse shape analysis and the timing difference between the phonon and charge signals.

It has furthermore turned out that trapping of charge carriers due to localized states in the band gap of the semiconductor leads to the creation of space charges compensating the collection field. Therefore, a periodical regeneration of the detectors either by LED illumination or by irradiation by an external  $\gamma$ -ray source ( $^{137}\text{Cs}$ ,  $^{60}\text{Co}$ ) is necessary to provide stable operation conditions.

Two of the leading direct DM experiments are based on the phonon-charge technique: CDMS (Cryogenic Dark Matter Search) and EDELWEISS (Expérience pour DEtecter Les Wimps En Site Souterrain).

**CDMS and SuperCDMS:** The Cryogenic Dark Matter Search experiment in its second phase operates a total of 30 low-temperature high-purity Ge and Si detectors at  $\sim 40$  mK in the Soudan Underground Laboratory in Minnesota beneath an overburden of 2090 meters water equivalent (m.w.e.). The detectors are disks with a thickness of 1 cm and a diameter of 7.6 cm (Fig. 2.17, left panel). The masses of the Ge and Si disks are 250 g and 100 g, respectively [126]. A stack of six detectors together with their cold electronics are collectively referred to as a tower. The phonon signal is measured by four transition edge sensors photolithographically patterned onto the detector surface. Each of them covers a quadrant of one planar face of the absorber. The sensors are read out independently which allows for a reconstruction of the x-y event position with a resolution of  $\sim 1$  mm. The charge is collected by a small electric field (3 V/cm) on two concentric electrodes. The outer electrode is used for rejecting events near the edges of the crystal which can be ascribed to background interactions. The simultaneous measurement of phonons and charge provides discrimination of background photons above 10 keV with  $>99.99\%$  efficiency [126]. Near-surface events can be rejected with  $>96\%$  efficiency using additional information from the pulse shape [126].

The CDMS collaboration recently published the results of the analysis of the data from a total raw exposure of 612 kg days [127]. Here, two events were observed in the region of interest. According to background estimates, the probability of observing two or more background events is 23%. Together with all previous CDMS data acquired in the second phase of the experiment an upper limit on the WIMP-nucleon spin-independent cross-section of  $3.8 \times 10^{-44} \text{ cm}^2$  could be set for a WIMP mass of 70 GeV.

The SuperCDMS-25 experiment aims at the improvement of existing best limits by more than two orders of magnitudes with lower absolute background and improved background rejection operating 42 Ge detectors (640 g, 1" thick) at SNO-Lab. It will be the first step towards the ton-scale experiment SuperCDMS [128].

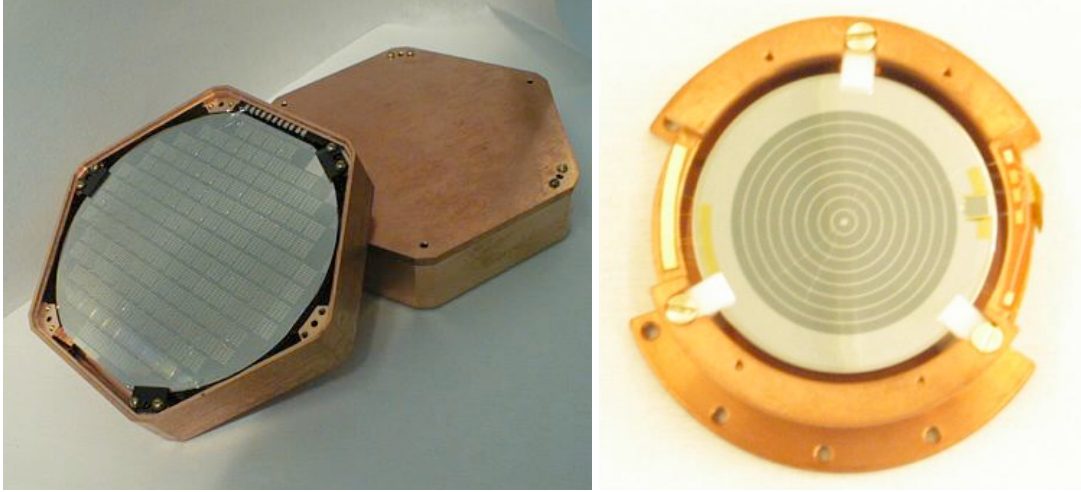


Figure 2.17: *Left:* Photograph of a Z-sensitive ionization-phonon (ZIP) detector employed in the CDMS experiment. Figure from [129]. *Right:* Photograph of a Ge/NTD/INTERDIGIT detector operated in the second phase of the EDELWEISS experiment. Figure from [130].

**EDELWEISS:** The EDELWEISS experiment is located in the Laboratoire Souterrain de Modane at 4800 m.w.e. In its first phase, EDELWEISS performed four physics runs with five 320 g Ge detectors operated at  $\sim 17$  mK accumulating a total of 62 kg days [131]. The detectors are disks with a diameter of 7 cm and a thickness of 2 cm. The edges are beveled at an angle of  $45^\circ$ . The phonon signal is read out by neutron transmutation doped (NTD) Ge sensors glued on the detectors [131]. The charge is collected by two electrodes where one is segmented into an inner region and a guard ring for rejecting events originating from the edges of the detector. The collection voltage is either +6.34 V or -4.0 V. Four of the detectors are equipped with layers of amorphous Si or Ge for a better charge collection. The analysis of the data resulted in an upper limit on spin-independent WIMP-nucleon cross section of  $\sim 2 \times 10^{-42} \text{cm}^2$  for a WIMP mass of 100 GeV [131].

EDELWEISS I ceased running in 2004 to allow for an upgrade. Since the sensitivity in the first phase was mainly limited by the inability to distinguish between low-yield near-surface events and nuclear recoils due to the slow NTD sensors, the collaboration has developed two new detector designs. The first one

(Ge/NbSi) is based on NbSi thin films evaporated on each side of a cylinder-shaped Ge crystal. These films show a strong difference in pulse shape depending on the interaction depth, providing thus a powerful technique for the rejection of near-surface events [132]. The second approach (Ge/NTD/INTERDIGIT) is based on Ge absorbers with NTD readout of the phonon signal, whereas the charge is measured by a set of four interleaved electrodes deposited on both sides of the detector (Fig. 2.17, right panel). Here near-surface events can be efficiently discriminated using the relative signal amplitudes in the different readout channels [133].

End of 2009, the EDELWEISS collaboration published the results of the analysis of the data acquired with nine 400 g Ge detectors equipped with interleaved electrodes from an effective total exposure of 144 kg days [134]. With one event in the region of interest, an upper limit on the spin-independent WIMP-nucleon cross section of  $1.0 \times 10^{-43} \text{ cm}^2$  at 90% CL for a WIMP mass of 80 GeV could be set.

### 2.5.3.2 Phonon-Light Detection

The second hybrid detection scheme based on cryogenic detectors relies on the simultaneous measurement of phonons and light generated in a scintillating crystal by incident particles. Since the light output per unit energy for electron and nuclear recoils is significantly different, the background induced by  $\gamma$ 's and  $\beta$ 's can efficiently be discriminated in this way.

Like the massive Si and Ge detectors employing the phonon-charge technique, detectors based on scintillating absorbers with masses of several hundred grams now routinely achieve thresholds of few keV in the phonon channel. The phonon-light technique, however, benefits from the fact that a large variety of materials such as  $\text{CaWO}_4$ , BGO or  $\text{ZnWO}_4$  exhibit scintillating properties at low temperatures. Consequently, nuclear elements other than silicon and germanium can be used as WIMP targets. This provides a test of the WIMP hypothesis due to the  $A^2$  dependence of the spin-independent WIMP-nucleon cross section in the limit of zero-momentum transfer. Furthermore no surface effects have been observed up to now, in contrast to the detectors based on the simultaneous measurement of phonons and charge which suffer from insufficient charge collection of near-surface events.

The major drawback of the phonon-light detection scheme arises from the low light yield. Only  $\sim 1\%$  of the energy deposited in the crystal is effectively detected as light and this fraction is further diminished for nuclear recoils particularly for heavy nuclei such as tungsten in  $\text{CaWO}_4$ , where a reduction of the light yield by a factor of  $\sim 40$  [135] is expected. For this reason nuclear recoils from heavy radon disintegration products may represent an important background for these detec-

tors since they induce low-light recoils that are indistinguishable from recoils of the heavier nuclei in the crystals such as bismuth in BGO or tungsten in  $\text{CaWO}_4$  (s. chapter 3). A key requirement for the phonon-light technique are therefore crystals with high light yields at low temperatures as well as an efficient light detection. The latter includes both the light collection and the sensitivity of the light detector. A powerful technique for improving the sensitivity of the light detector is the Neganov-Luke effect. Using semiconducting absorbers, the threshold can be significantly improved by drifting the light-induced electron-hole pairs in an electric field. More details on this technique can be found in chapter 6.

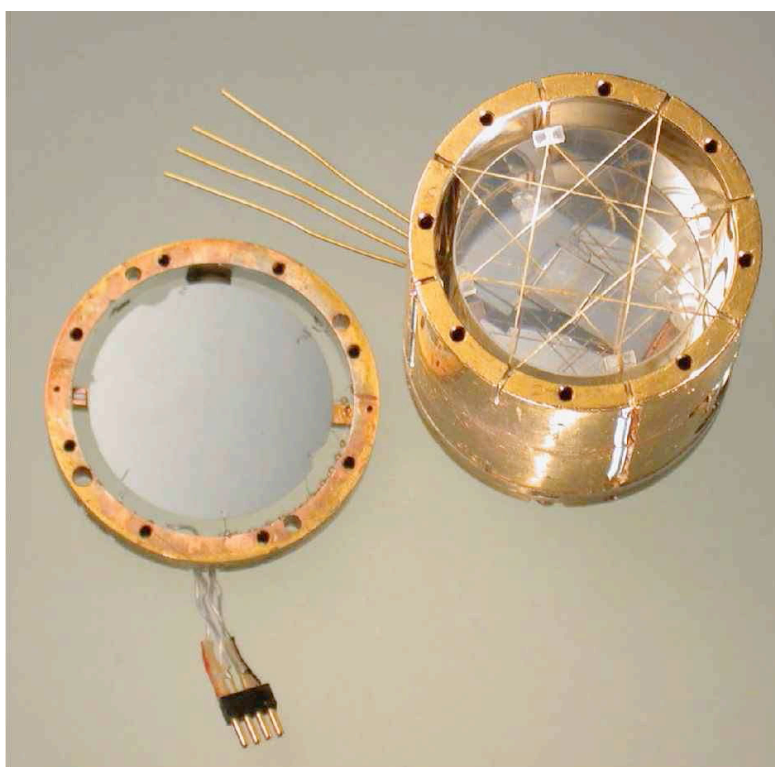


Figure 2.18: Photograph of a detector module employed in the ROSEBUD experiment. Here a 91g BGO crystal is used as a target (right), whereas the light induced by incident particles is detected by a Ge light detector (diameter=25 mm) (left). For a efficient light collection the module is mounted in a reflective housing (Fig. from [96]).

The phonon-light technique is currently employed by two direct DM experiments, ROSEBUD (Rare Objects SEarch with Bolometers Underground) [136, 137, 138] and CRESST (Cryogenic Rare Event Search with Superconducting Thermometers) [139, 140]. The ROSEBUD experiment operates a multielement target in the Canfranc Underground Laboratory. The scintillating crystals employed in this

experiment are mainly BGO, doped  $\text{Al}_2\text{O}_3$ , LiF and  $\text{CaWO}_4$ . The light induced in the scintillators is measured by light detectors based on Ge absorbers. The temperature increase of the crystals and the light detectors are both read out by NTD (Neutron Transmutation Doped) sensors. A typical detector module employed in the ROSEBUD experiment is depicted in Fig. 2.18.

The CRESST experiment hosted at the Gran Sasso National Laboratory, aims at the operation of 33 detector modules each consisting of a 300 g  $\text{CaWO}_4$  detector and a light detector with a silicon-on-sapphire (SOS) absorber. The phonon signals in both detectors are read out by superconducting transition edge sensors (TES). A detailed description of the CRESST experiment can be found in chapter 3.

## 2.6 Perspectives of Dark Matter Searches

It is by now well-established that most of the matter in the Universe is dark. Among several candidates that have been proposed to account for it, WIMPs play a central role with the neutralino as a well-motivated WIMP candidate provided by Supersymmetry. One of the most promising detection schemes is based on the direct measurement of the nuclear recoils induced by WIMPs in a terrestrial target. Most direct DM experiments currently employ hybrid detectors providing an efficient discrimination of the electromagnetic background by simultaneously measuring two types of excitation (e.g. phonon-charge, phonon-light, light-charge) induced by incident particles in the target. The significant improvement of sensitivity due to this technique, currently allows to explore the supersymmetric parameter space.

With the present detection schemes sensitivities of the order of  $\sim 10^{-10}$  pb for the spin-independent interaction can be achieved with target masses at the ton scale and with an improved background control. A challenging aspect remains, however, the identification of the nature of DM in case of a signal. Here, a promising strategy is the employment of a multi-element target which allows to explore the  $A^2$  dependence of the spin-independent scattering rate. Furthermore, target nuclei with and without spin will allow to distinguish between different theoretical models. Here results from indirect searches may help to determine the DM distribution in the galactic halo.



# Chapter 3

## The CRESST Experiment

The CRESST (Cryogenic Rare Event Search with Superconducting Thermometers) experiment aims at the direct detection of particle Dark Matter. The detectors employed in Phase I of the CRESST experiment consisted of  $\sim 262$  g sapphire absorbers ( $\text{Al}_2\text{O}_3$ ) equipped with tungsten transition edge sensors (TESs) operated at  $\sim 15$  mK. Due to the low energy threshold ( $\sim 600$  eV) of one of these detectors, up to now the best limits on both spin-dependent and spin-independent interaction for WIMPs with masses below 5 GeV could be set in a 138 h run in 2001 [141].

In its second phase (CRESST II), the CRESST experiment is now employing the phonon-light technique. The sapphire detectors have been replaced by detector modules each consisting of a  $\sim 300$  g scintillating  $\text{CaWO}_4$  absorber crystal and an additional light detector. The simultaneous measurement of both phonons and light induced by particle interactions in the crystal allows for an event-by-event discrimination of the background originating from electron recoils due to the higher light output as compared to nuclear recoils of the same energy. In CRESST II, 33 modules with a total mass of  $\sim 10$  kg can be installed aiming at a sensitivity for the WIMP spin-independent interaction of  $\sim 10^{-8}$  pb.

This chapter is focused on the CRESST experimental setup as well as the detector modules employed in Phase II. Furthermore, the most important results will be presented.

### 3.1 The CRESST Experimental Setup

The CRESST experiment is hosted in the Laboratori Nazionali del Gran Sasso (L.N.G.S.), presently the largest laboratory for particle astrophysics worldwide. The underground facilities are located on one side of the 10 km long freeway tunnel crossing the Gran Sasso Mountain. The laboratory consists of three experimental halls each about 100 m long, 20 m wide and 18 m high. A sketch is shown in

### 3. The CRESST Experiment

---

Fig. 3.1. The CRESST experiment in its second phase is set up in Hall A, which provides a shielding of  $\sim 3500$  meter water equivalent (m.w.e.) rock overburden [142].

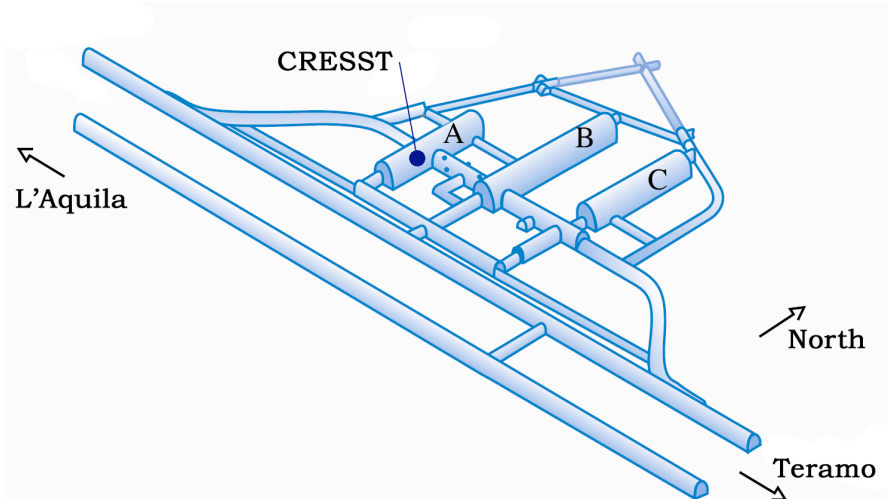


Figure 3.1: Sketch of the L.N.G.S. underground laboratory located on one side of the freeway tunnel crossing the Gran Sasso Mountain. The CRESST experiment is located in Hall A, which provides  $\sim 3500$  m water equivalent rock overburden. Figure taken from [143].

The central part of the CRESST experimental setup consists of a  $^3\text{He}/^4\text{He}$  dilution refrigerator (cooling power at 100 mK  $\approx 1$  mW) which cools the detectors to their operating temperature of roughly 10 mK (Fig. 3.2). Since the cryostat does not entirely consist of radiopure materials the detectors are mounted in a separate volume ("Cold Box") made of radiopure copper which is thermally coupled to the mixing chamber via a copper rod ("Cold Finger", CF). The experimental volume of the "Cold Box" can hold up to  $\sim 10$  kg of detector material. The inner shield against gamma radiation consists of a double layer of 14 cm of radiopure copper and 20 cm of lead. These shields are surrounded by an air-tight stainless steel box ("Radon Box", RB) flushed with boil-off nitrogen gas and maintained at small overpressure in order to keep radon away from the proximity of the detectors.

The Cu/Pb shielding is surrounded by 20 plastic scintillator panels each with an area of  $\sim 1\text{-}1.2$  m<sup>2</sup> acting as an active muon veto (MV). A total solid angle coverage of 98.7 % is achieved by using three types of panels. Only a circular opening of 0.27 m<sup>2</sup> remains due to the feedthrough of the cold box. The photomultiplier signals are read out via optical fibers in order to avoid electromagnetic interference.

The outer layer consists of 45 cm of polyethylene (PE) plates installed to moderate ambient neutrons below threshold or to thermal energies where they can then

be captured on hydrogen. With a capture range of 4.3 cm in  $\text{CH}_2$  materials [144] incoming neutrons are effectively shielded.

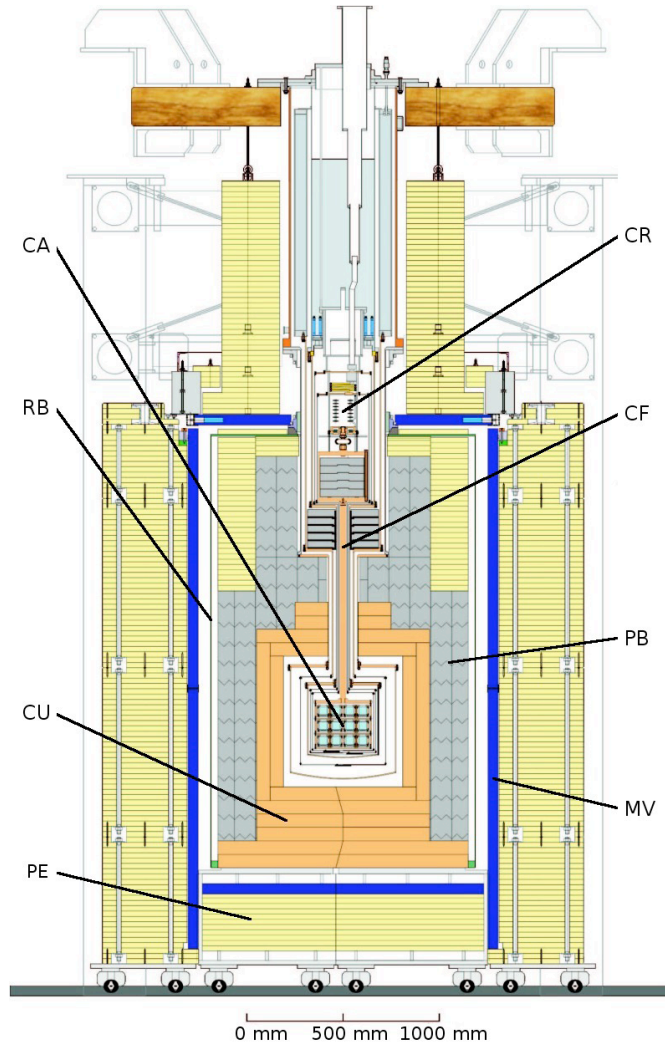


Figure 3.2: Schematic drawing of the CRESST cryostat. The detector carousel (CA) is connected via the coldfinger (CF) to the mixing chamber (CR). The shielding against gamma rays consists of a copper (CU) and a lead (PB) layer. The inner shielding is surrounded by the radon box (RB) and the muon veto (MV). The outer shielding consists of a 45 cm thick polyethylene (PE) neutron moderator. Figure taken from [140].

In order to reduce electromagnetic interference the whole setup is placed in a Faraday cage (Fig. 3.3) which itself is located in a three-level building. The lower

level, where the detectors and the shieldings are located, is equipped with a class-100 clean room [141]. The upper level of the cage which is outside the clean room hosts the electronics and allows access to the cryostat for servicing, e.g., for refilling cryoliquids. The data acquisition computers are located on the third floor of the CRESST building.

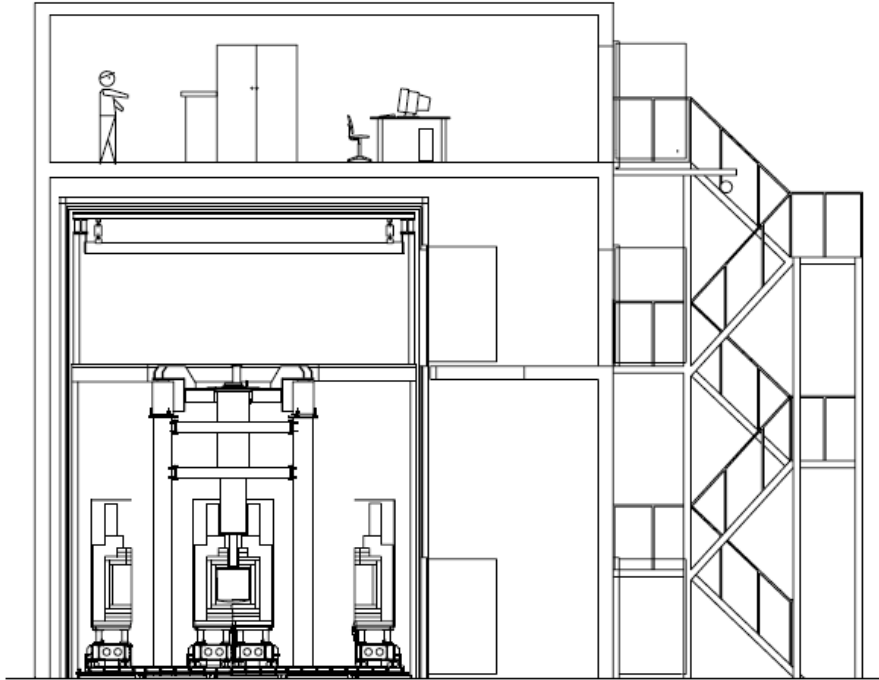


Figure 3.3: Schematic view of the CRESST building at L.N.G.S. (Fig. from [141]). The two lower levels host the experimental setup, whereas the third floor hosts the data acquisition.

## 3.2 Detection Principle

For a further improvement of the sensitivity, the detectors employed in CRESST II are now based on the phonon-light technique. The simultaneous measurement of phonons and scintillation light induced by incident particles in a  $\text{CaWO}_4$  absorber provides an efficient discrimination of the background due to electron recoils.  $\text{CaWO}_4$  was chosen due to its relatively high light output at low temperatures and in order to take advantage of the  $A^2$  dependence of the spin-independent cross section related to the high atomic mass of tungsten ( $A=183.84$ ). The simultaneous measurement of phonons and light with detectors based on  $\text{CaWO}_4$  (a so-called

detector module) was first demonstrated by P. Meunier *et al.* [145]. In this proof-of-principle experiment a 6 g  $\text{CaWO}_4$  absorber and a light detector based on silicon on sapphire (SOS) were employed. Both detectors were equipped with tungsten TESs operated at  $\sim 12$  mK.

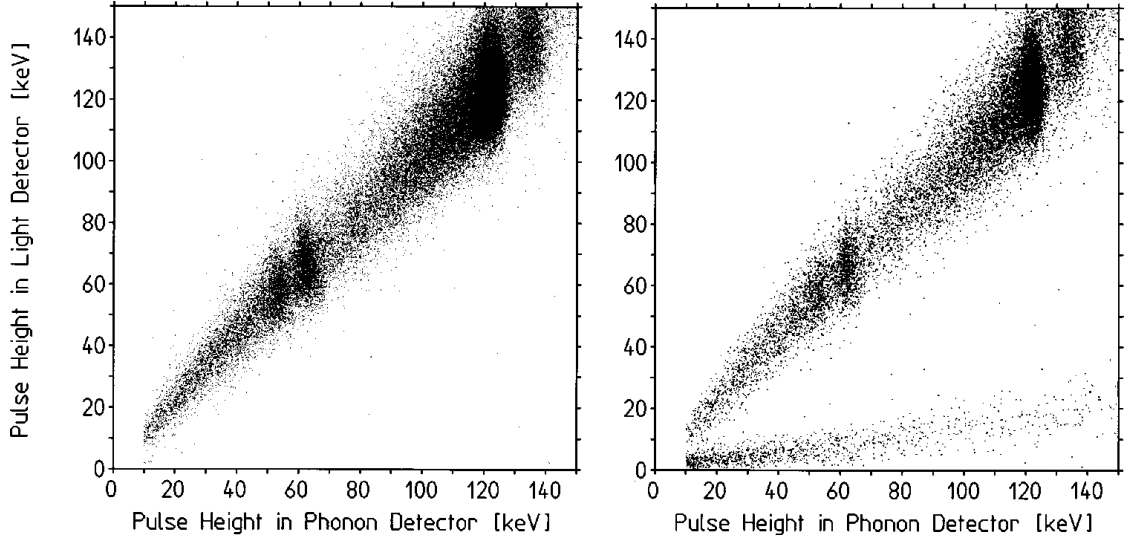


Figure 3.4: Response of a prototype detector module to electron recoils induced by a  $^{57}\text{Co}$   $\gamma$  source and a  $^{90}\text{Sr}$   $\beta$  source on the left panel and in addition to neutrons emitted by an AmBe source on the right panel. Due to the higher light yield of electron recoils, events induced by  $\gamma$ 's and  $\beta$ 's can efficiently be discriminated from neutron events down to  $\sim 10$  keV of recoil energy. Figure taken from [145].

The response of this detector module to electron and nuclear recoils is depicted in Fig. 3.4. The left panel shows the pulse-height spectrum in the light detector relative to the phonon signal in the  $\text{CaWO}_4$  absorber due to  $\gamma$ 's from a  $^{57}\text{Co}$  source and to electrons from a  $^{90}\text{Sr}$   $\beta$  source, both inducing electron recoils. In addition, the detector module was exposed to an AmBe neutron source inducing nuclear recoils (Fig. 3.4, right panel). Due to the different light yields of electron and nuclear recoils of the same energy a detector module is able to clearly discriminate these two classes of events down to  $\sim 10$  keV of recoil energy proving its suitability as a direct Dark Matter detector with the ability to actively reject the background induced by electron recoils.

### 3.2.1 CRESST Detector Modules

The detector modules now employed in the CRESST experiment consist of a  $\sim 300$  g  $\text{CaWO}_4$  absorber crystal providing the measurement of the energy of incident

### 3. The CRESST Experiment

particles. The light induced in the crystal is measured by a second cryogenic detector. A photograph of an open detector module used in CRESST II together with the corresponding schematic view are depicted in Fig. 3.5.

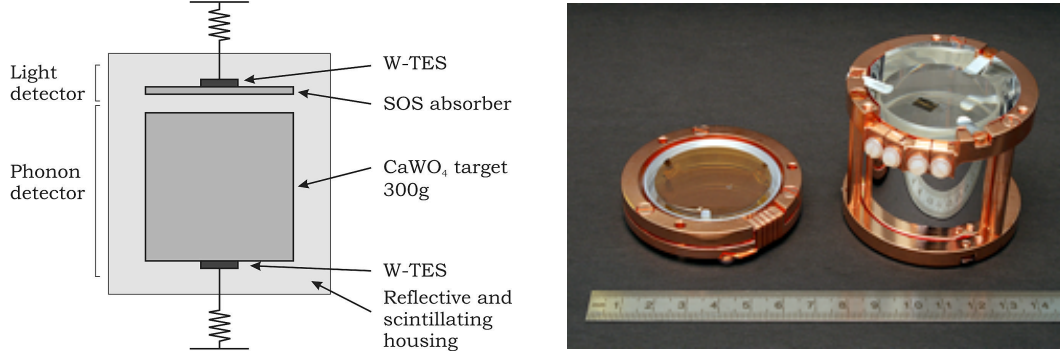


Figure 3.5: *Left panel:* Schematic view of a detector module employed in the second phase of the CRESST experiment (CRESST II). Each module consists of a  $\sim 300$  g  $\text{CaWO}_4$  absorber crystal and a light detector based on silicon on sapphire (SOS). Both detectors are equipped with superconducting tungsten TESs and are housed in a reflective cavity. (Figure from [140]). *Right panel:* Photograph of an open detector module as used in CRESST II.

The cylindrical crystals (height=4 cm, diameter=4 cm) with masses of about 300 g are equipped with transition edge sensors (TESs) consisting of tungsten metal which, in its  $\alpha$  phase, becomes superconducting at  $\sim 15$  mK. The light detectors are based on sapphire absorbers (thickness=0.4 mm, diameter=4 cm, mass=3.2 g) with an epitaxially grown  $1 \mu\text{m}$  thick silicon layer on one side in order to improve the scintillation light absorption. This material, also referred to as silicon-on-sapphire (SOS), benefits from the excellent phonon properties of  $\text{Al}_2\text{O}_3$ . The resolution of the light channel can substantially be improved by roughening the flat surface of the  $\text{CaWO}_4$  crystal to a roughness of  $\sim 10 \mu\text{m}$ . The light-induced phonon signal in the SOS substrate is also read out by a tungsten TES. In contrast to the sensor on the  $\text{CaWO}_4$  crystal, the tungsten film on the light detector is connected to aluminum phonon collectors to improve the phonon-collection efficiency without increasing the heat capacity [146]. The TESs of both the  $\text{CaWO}_4$  crystal and the light detector are furthermore equipped with Au heaters which are needed for temperature stabilization and calibration via heater pulses. For an efficient light collection the whole module is enclosed in a reflective housing. The reflector consisting of 3M foil [139] was furthermore chosen to be scintillating in order to reject low-light events induced by the alpha decay of Po (s. sect. 3.3).

The detector modules are mounted in a support structure ("carousel") (Fig. 3.6) capable of carrying 33 modules which can be mounted and dismantled individually corresponding to a total target mass of  $\sim 10$  kg. The carousel is made of

ultrapure copper and is weakly coupled to the cold finger resulting in a relaxation time of high-frequency temperature variations of the mixing chamber of roughly 30 min. In this way, stable operation conditions are provided for the detectors.

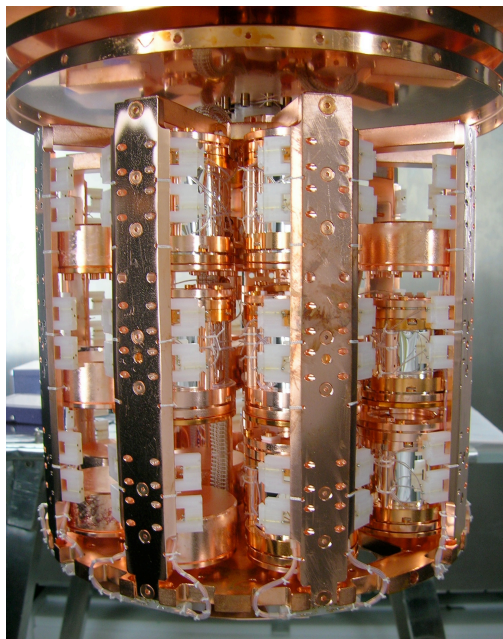


Figure 3.6: Support structure ("carousel") accommodating the CRESST II detector modules [140].

### 3.2.2 Readout Scheme

The tungsten TESs of both the phonon and the light channel are read out by DC SQUIDs. The readout circuit of a TES implemented in CRESST II is depicted in Fig. 3.7. Here, in contrast to the setup described in chap. 4, the sensor (W-TES) is mounted in parallel to the SQUID input coil which is in series with two reference resistors (R). The circuit is biased with a constant current which is shared between both branches. A change of the TES resistance alters the current through the SQUID input coil providing the electrical signal. For the operation of 33 detector modules a multichannel SQUID system is employed. This consists of 66 SQUID units providing the readout for two sensors per module.

Besides the readout lines depicted in Fig. 3.7, each sensor has an additional heater-line pair for temperature control and calibration pulses. The TES temperature is monitored by injecting heater pulses via the heater lines with a rate of  $\sim 0.3$  Hz. The online evaluation of these heater pulses provides a method to stabilize the

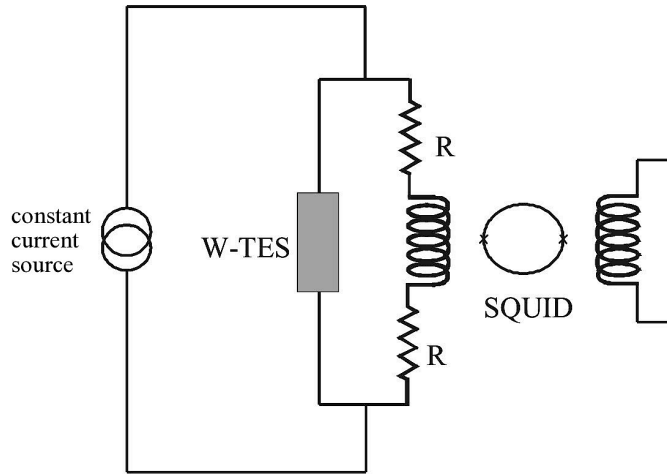


Figure 3.7: Readout circuit implemented in CRESST II. The circuit is biased with a constant current which is shared between both branches. A change of the TES resistance alters the current through the SQUID input coil providing the electrical signal. Figure taken from [140].

TES temperature via the heating current. In addition, pulses of known energy are injected every 30 s which are used for the calibration of the pulse height spectrum.

### 3.3 Background

The setup of the CRESST experiment has to meet the basic requirement of a low radioactive background which is mandatory for any direct Dark Matter experiment. In the following, the different sources of background relevant for the CRESST setup at L.N.G.S. will be discussed.

#### Cosmic Rays

The operation in an underground facility provides a very efficient shielding against cosmic rays, especially against muons which are the most penetrating component. Due to a rock overburden of  $\sim 1400$  m corresponding to  $\sim 3500$  meter water equivalent (m.w.e) the muon flux is reduced by six orders of magnitude to about  $1 \text{ h}^{-1}\text{m}^{-2}$  in Hall A [142]. For an active rejection of the background induced by muons, a muon veto consisting of 20 plastic scintillator panels each with an area of  $\sim 1\text{-}1.2 \text{ m}^2$  is employed (see section 3.1).

### Beta/Gamma Background

The integral gamma flux from the ambient rock for all natural decay chains is  $\sim 1 \text{ cm}^{-2}\text{s}^{-1}$  [147]. The detailed activities of rock samples from the different halls of the Gran Sasso underground laboratory are given in Table 3.1. The observed differences between the values for the halls A, B and C result from the different local compositions of the rock.

Location	$\gamma$ Activity [ $\text{Bq}\cdot\text{kg}^{-1}$ ]			
	$^{232}\text{Th}$	$^{238}\text{U}$	$^{40}\text{K}$	$^{214}\text{Bi}$
Hall A	$8.8 \pm 0.3$	$84.7 \pm 8.4$	$224 \pm 6$	$41.9 \pm 0.6$
Hall B	$0.25 \pm 0.08$	$5.2 \pm 1.3$	$5.1 \pm 1.3$	$4.2 \pm 0.3$
Hall C	$0.27 \pm 0.10$	$8.2 \pm 1.7$	$2.9 \pm 1.4$	$5.1 \pm 0.2$

Table 3.1:  $\gamma$  activity of rock samples from the different halls in the Gran Sasso laboratory [147].

The background induced by  $\beta$ 's and  $\gamma$ 's is suppressed in both active and passive ways in the CRESST setup. The passive shielding consists of a Cu/Pb double layer (see section 3.1) whereas active suppression is achieved by a simultaneous measurement of phonons and scintillation light induced by incident particles in the  $\text{CaWO}_4$  absorber crystals. The active suppression of the background originating from electron recoils is limited by the light output at low energies which sets a lower boundary of  $\sim 10 \text{ keV}$  of the energy interval (ranging up to  $40 \text{ keV}$ ) used for WIMP analysis.

### Neutron Background

There are several sources contributing to the overall neutron flux present in the CRESST setup:

1. Low-energy neutrons originating from fission and  $(\alpha, n)$  reactions in the rock and the concrete walls of the laboratory.
2. Low-energy neutrons induced by fission in the shielding material and the setup.
3. Muon-induced high energetic neutrons in the rock which can produce additional neutrons by spallation in the experimental setup.
4. High-energy neutrons induced by muons in the shielding material.

### 3. The CRESST Experiment

The measured neutron fluxes in Hall A of the L.N.G.S for different energy intervals are given in Table 3.2. Thermal neutrons with energies below 1 MeV are dominant. They constitute a serious background since they mainly scatter elastically off the target nuclei and can therefore mimic a WIMP signal.

Energy Interval [MeV]	Neutron Flux [ $10^{-6}\text{cm}^{-6}\text{s}^{-1}$ ]
$< 50 \cdot 10^{-9}$	$1.07 \pm 0.05$
$50 \cdot 10^{-9} - 10^{-3}$	$1.99 \pm 0.05$
$10^{-3} - 2.5$	$0.530 \pm 0.008$
2.5 - 5	$0.18 \pm 0.04$
5 - 10	$0.04 \pm 0.01$
10 - 15	$(0.7 \pm 0.2) \cdot 10^{-3}$
15 - 20	$(0.1 \pm 0.3) \cdot 10^{-6}$

Table 3.2: Integral muon fluxes measured for different energy intervals in Hall A of the L.N.G.S. [148].

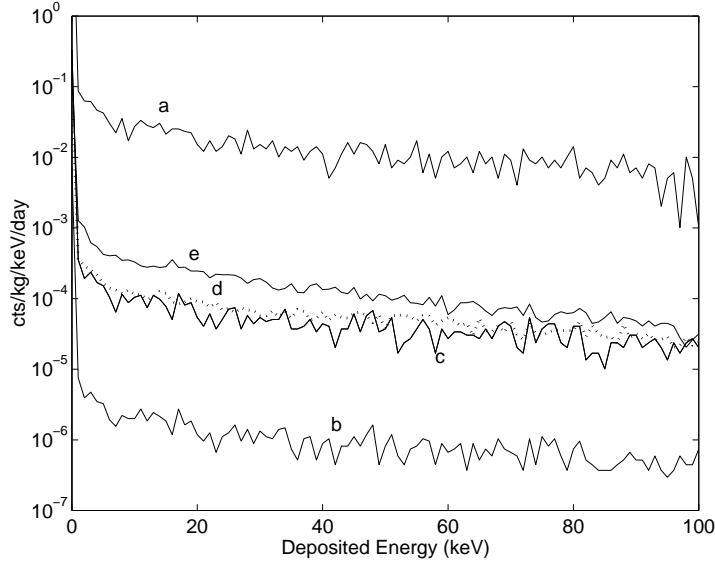


Figure 3.8: Simulated neutron recoil spectra in  $\text{CaWO}_4$  originating from different sources: (a) Low-energy neutrons from the surrounding rock/concrete without neutron moderator, (b) Low-energy neutrons from the surrounding rock/concrete with a 50 cm polyethylene neutron moderator, (c) Low-energy neutrons from  $^{238}\text{U}$  in the lead shield, (d) High-energy neutrons induced by muons in the rock, (e) High-energy neutrons induced by muons in the CRESST setup [149].

The expected signals due to the various sources of neutrons depending on different shielding materials have been studied by Monte-Carlo simulations [150]. It has been shown that the neutron flux in the relevant energy range depends on the humidity of the concrete of the walls in the laboratory since wet concrete acts as a moderator. The simulated recoil spectra in  $\text{CaWO}_4$  assuming dry concrete are depicted in Fig. 3.8.

According to these results the installed PE shield in the CRESST setup is expected to reduce the low-energy neutron background from the surrounding rock by more than three orders of magnitude. High energetic muon-induced neutrons in the rock are less efficiently moderated. With a 50 cm PE shield a reduction by only one order of magnitude is expected [150]. Events from muon-induced neutrons in the inner shield can be rejected via a coincident event in the muon veto.

With the installed PE shield and the muon veto, the remaining neutron background originates from fission of  $^{238}\text{U}$  in the lead shielding. These neutrons cannot be eliminated since there is no moderator between the Pb shield and the detectors. Therefore, the  $^{238}\text{U}$  content of the lead shield might be the limiting element for the experiment's sensitivity.

### Surface $\alpha$ Decays

A further background source arises from the Rn progeny  $^{210}\text{Po}$  which is a common contamination on or slightly below surfaces where it can be implanted by  $\alpha$  decays.  $^{210}\text{Po}$  decays to a  $^{206}\text{Pb}$  nucleus of 104 keV recoil energy and a 5.3 MeV  $\alpha$  particle. When the decaying Po nucleus is on the reflective foil surrounding the crystal and the alpha particle moves away from the detector the  $^{206}\text{Pb}$  nucleus will be detected as a low-light event. If the Po nucleus is implanted in the reflective foil it might lose some energy on the way out generating nuclear recoil-like events with energies below 40 keV limiting therefore the experimental sensitivity. A detailed discussion of this type of background can be found in [151, 97]. A possible solution to this problem is provided by scintillating reflective foils. Alpha particles moving away from the detector will produce light in the reflector turning this type of events into electron recoil-like events. In this way they can be removed from the region of interest [139].

## 3.4 Quenching Factors

The discrimination principle of events due to electron recoils in the phonon-light technique is based on the reduced light output of nuclear recoils relative to electron recoils of the same energy. The lower light yield associated with nuclear recoils is referred to as quenching and is expressed by the quenching factor  $Q$  defined as

$$Q = \frac{\text{Signal Amplitude in Phonon Channel}}{\text{Signal Amplitude in Light Channel}}. \quad (3.1)$$

$Q$  is usually normalized to 1 for electron recoils at 122 keV.  $1/Q$  is referred to as the light yield. In compound target materials such as  $\text{CaWO}_4$  the light quenching furthermore depends on the nucleus the incident particle is scattered off. Therefore these materials are characterized by several quenching factors.

The knowledge of these quenching factors might improve the rejection capability of the detector with respect to background events induced in the nuclear recoil band which are supposed to originate essentially from neutrons. For kinematical reasons, in the region of interest (10-40 keV), neutrons mainly scatter off oxygen and calcium in  $\text{CaWO}_4$ , whereas WIMPs are expected to induce mainly tungsten recoils due to the  $A^2$  dependence (where  $A$  is the atomic mass number) of the scalar cross section.

Several experiments using different techniques have been carried out to measure the quenching factors of the elements in  $\text{CaWO}_4$ . The most important schemes will be presented in the following.

### Ion Impinging Experiment

This experiment, set up at the Max-Planck Institut für Physik in München, is based on the measurement of the scintillation light generated by ions impinging on a  $\text{CaWO}_4$  crystal [135]. The setup is depicted in Fig. 3.9.

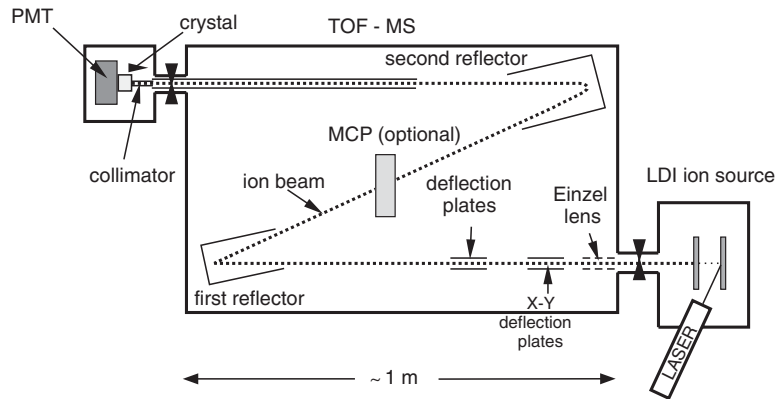


Figure 3.9: Schematic drawing of the setup of the ion impinging experiment. Ions produced with a Laser Desorption/Ionization (LDI) source are accelerated towards a  $\text{CaWO}_4$  target crystal. The mass and the kinetic energy of the ions can be selected in a time-of-flight mass spectrometer (TOF-MS). The scintillation light generated in the crystal by the incident ions is detected by a photomultiplier (PMT) [135].

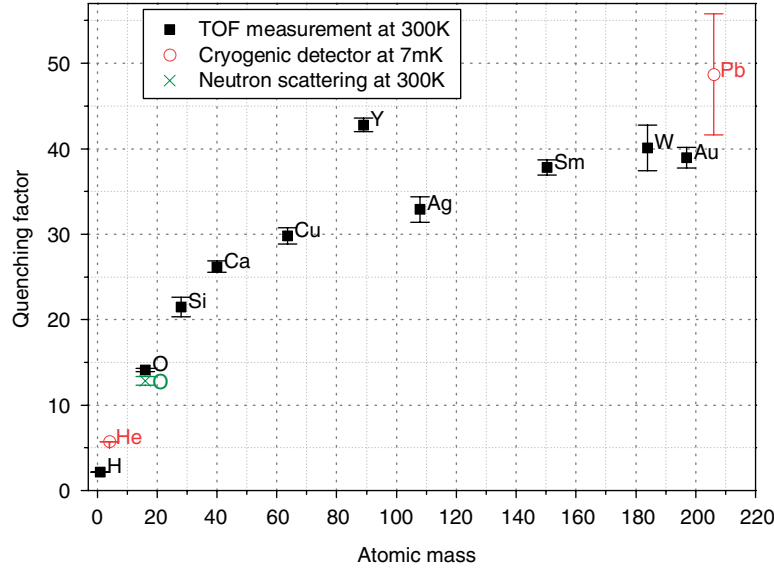


Figure 3.10: Dependence of the quenching factor of  $\text{CaWO}_4$  on the atomic mass of the selected ions. The squares denote the results obtained with the ion impinging experiment. The circles are the quenching factors derived from Dark Matter data [139]. The result for oxygen denoted by the cross has been measured in a neutron scattering experiment at room temperature [152, 153]. Figure from [135].

The ions are produced in a Laser Desorption/Ionization source (LDI) by irradiating the source material with a pulsed laser. They are then accelerated by a voltage of  $\sim 18$  kV towards the  $\text{CaWO}_4$  crystal. In a time-of-flight mass spectrometer (TOF-MS) ions with a certain mass and kinetic energy are selected to hit the crystal where they generate scintillation light which is then detected by a photomultiplier tube (PMT). From a comparison with a  $^{55}\text{Fe}$  X-ray reference source quenching factors can be determined.

The results for the quenching factors obtained in this way with different sources covering a mass range from hydrogen ( $A=1$ ) up to gold ( $A=197$ ) are depicted in Fig. 3.10. From the results relevant for the CRESST experiment, i.e. oxygen ( $Q_O=14.3 \pm 0.5$ ), calcium ( $Q_{Ca}=27.4 \pm 1$ ) and tungsten ( $Q_W=41 \pm 3$ ), it becomes obvious that a discrimination between the different nuclear recoils in  $\text{CaWO}_4$  is achievable due to the significantly different light yields.

Due to the low penetration depth of the impinging ions in  $\text{CaWO}_4$ , the measured scintillation light is generated close to the surface. This might be a limiting aspect for the accuracy of the quenching factors determined in this way. A second systematic error might arise from the room-temperature operation of this experiment that could yield different results compared to cryogenic temperatures, where

the DM experiment itself is performed.

#### Neutron Scattering Experiment

The drawbacks of the ion impinging experiment can be overcome in a neutron scattering experiment operated at cryogenic temperatures. The only setup that allows the measurement of the quenching factors of target materials for DM search, e.g., of the elements in  $\text{CaWO}_4$  at mK temperatures has been installed at the Maier-Leibnitz-Accelerator Laboratory (MLL) in Garching. Its design also allows the characterization of other target materials such as  $\text{ZnWO}_4$ , BaF, LiF or BGO which will become relevant in the framework of the future multitarget tonne-scale experiment EURECA (European Underground Rare Event Calorimeter Array).

An accurate determination of the quenching factors is achieved by using monoenergetic neutrons scattered under a fixed angle. The neutron energy can then be determined either with the cryogenic detector or by a time-of-flight (ToF) measurement. In this way, the recoiling nucleus can be determined via the recoil energy. The signals from the different elements form distinct, well-separated populations in the data.

First measurements at the neutron scattering facility have been carried out at room temperature [152, 153] employing a beam of pulsed neutrons produced via the reaction  $p(^{11}\text{B},n)^{11}\text{C}$ . In this scheme, still used in the present setup, 60 MeV boron ions from the accelerator are directed onto a hydrogen target producing monoenergetic neutrons with an energy of 11 MeV. The reference time for the time-of-flight measurement is provided by the pulsed  $^{11}\text{B}$  beam. The neutron detectors are based on the liquid scintillator NE213, read out by a PMT. A total of 40 neutron detectors have been employed covering a certain range of scattering angles with respect to the beam line. The liquid scintillator NE213 allows a discrimination between neutron and gamma events due to different pulse shapes.

To obtain the quenching factor, the light output of the target crystal has to be determined. This light was measured by two photomultiplier tubes optically coupled to the  $\text{CaWO}_4$  target crystal. With this setup only the quenching factors for oxygen ( $Q_O=12.8 \pm 0.5$ ) and calcium ( $Q_{Ca}=16 \pm 4$ ) could be determined. An accurate value for tungsten could not be obtained due to the low light yield.

Since the light output of  $\text{CaWO}_4$  is expected to be temperature dependent, the setup has been modified to allow the measurement of the quenching factors at cryogenic temperatures. A schematic view of the present experimental setup is depicted in Fig. 3.11. The  $\text{CaWO}_4$  target crystal is now operated as a cryogenic detector in a  $^3\text{He}/^4\text{He}$  dilution refrigerator. The size of the cylindrical crystal with a diameter of 20 mm and 5 mm height was chosen to be smaller than those usually employed in the CRESST experiment [151]. In this way, the double scattering rate of neutrons in the crystal is reduced which is a key requirement for an accurate

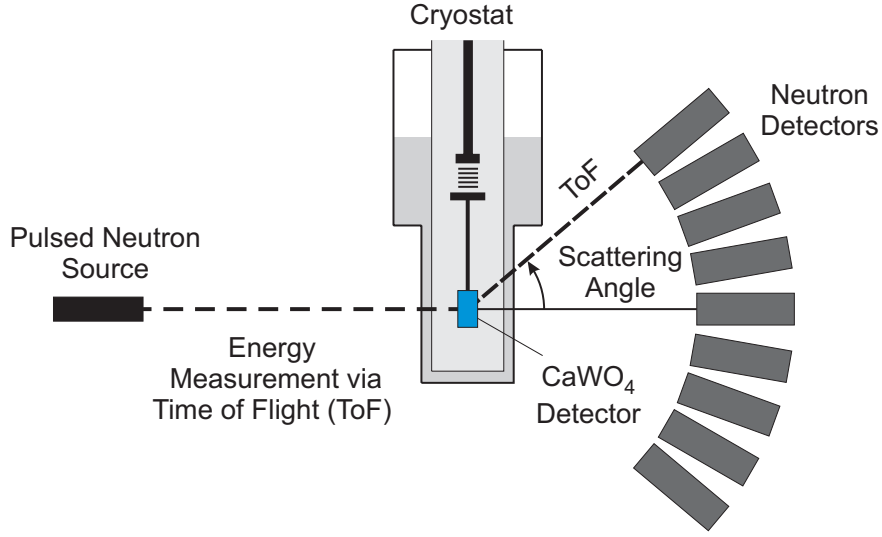


Figure 3.11: Schematic view of the neutron scattering facility. It features a pulsed neutron beam, a cryogenic detector with a  $\text{CaWO}_4$  absorber crystal mounted in a  $^3\text{He}/^4\text{He}$  dilution refrigerator and an array of 40 neutron detectors for the time-of-flight (ToF) measurement.

measurement of quenching factors. The small size of the  $\text{CaWO}_4$  target further reduces the background rate due to the ambient radioactivity and cosmic rays. This is important, since the scattering facility is set up above ground and no shielding is used. Despite the small size of the absorber, the detector has to be fast in order to deal with count rates of the order of 10 Hz. This has been achieved by using an Ir/Au TES equipped with Al phonon collectors providing an efficient collection of athermal phonons [151]. The scintillation light is measured by a second cryogenic detector using a  $20 \times 20 \text{ mm}^2$  Si absorber also equipped with an Ir/Au TES.

The first measurements performed at cryogenic temperatures at the MLL did not employ a time-of-flight measurement [154, 155]. The pulse-height spectrum for each nucleus is therefore continuous ranging from zero up to a maximum energy which depends on the neutron energy and the mass of the recoiling nucleus. Due to the different light yields associated with a specific nucleus in the crystal, the nuclear recoil band actually consists of three bands: the oxygen, the calcium and the tungsten recoil band. Since these slightly overlapping bands exhibit a Gaussian distribution it is possible to fit them in a given energy range in order to derive the corresponding quenching factors.

In this way, a quenching factor of  $Q_O = 10 \pm 1$  and  $Q_{Ca} = 17.9 \pm 0.2$  could be derived in the energy range between 100-500 keV for oxygen (O) and calcium (Ca), respectively. In the same way, the quenching factor for tungsten  $Q_W = 35_{-9}^{+19}$  has

been determined in the energy interval 160-180 keV [154]. The large error of the quenching factor of tungsten results from the overlapping bands and the poor statistics associated with tungsten recoils.

A separation of the contributions of the different nuclei to the nuclear recoil band is expected when exploiting the triple coincidence between the signals from the accelerator, the cryodetector and the neutron detectors. For an accurate determination of the triple-coincidence events the setup has been upgraded with a DAQ system based on the VME standard [155]. Due to its fast bus systems all cryodetector and PMT events can be recorded with this system. The coincident events are then evaluated in an offline analysis. Here, a hardware coincidence search is not feasible due to the different time constants of the cryodetector ( $\tau_{CRYO} \sim 2$  ms) and the PMTs ( $\tau_{PMT} \sim 10$  ns) that differ by several orders of magnitude.

With this technique a total of 62 triple-coincidence neutron events have been found in the data taken during the beamtime in August of 2009. The recoil energy of these events is plotted versus their ToF in Fig. 3.12 [156, 155].

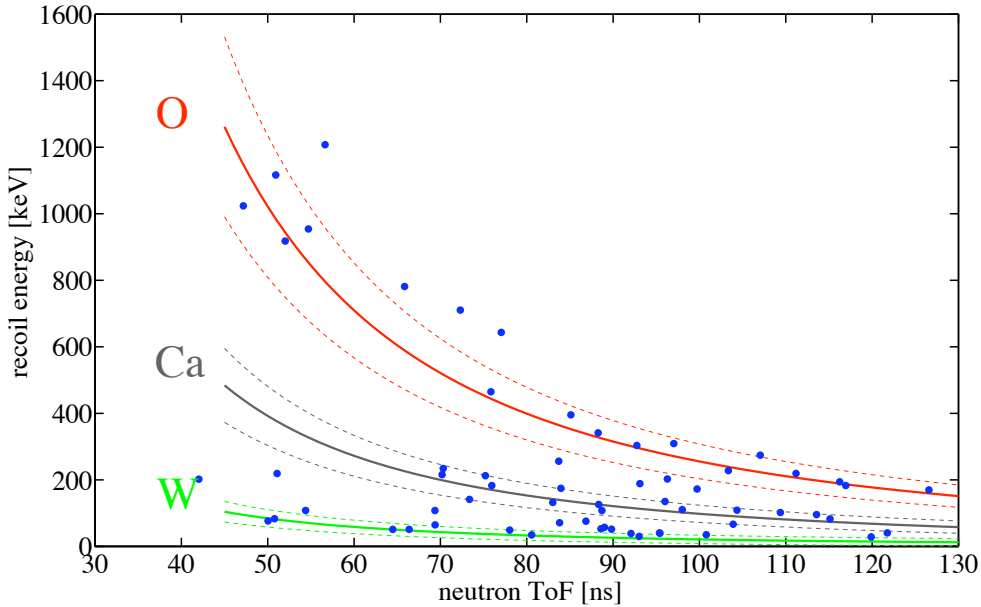


Figure 3.12: Recoil energy versus ToF of the triple-coincidence neutron events found in the data taken during August of 2009. The full lines indicate the calculated recoil energies for different ToFs for the different nuclei in  $\text{CaWO}_4$ . The dashed lines correspond to the estimated errors due to geometrical and timing uncertainties. Figure taken from [156].

After cuts, 14 events can be identified as oxygen recoils, 14 as calcium recoils and 7 as tungsten recoils. Even though the statistics is too poor to accurately determine

the quenching factors of the three elements, the data seem to agree, at least for oxygen and tungsten, with the results obtained with other experiments proving the ToF technique to be a reliable tool for quenching factor measurements. It furthermore offers the opportunity to measure quenching factors at energies less than 100 keV since the contributions of the different nuclei can be clearly separated with the ToF technique (Fig. 3.12). This, however, requires better statistics and an improved light detector. Here, light detectors with Neganov-Luke amplification can play a significant role (see chapter 6).

### 3.5 CRESST Dark Matter Limits

CRESST started its second phase employing the phonon-light technique in 2002. After a few runs needed to optimize the prototype detectors, a total net exposure of 20.5 kg days could be achieved in spring 2004 with two 300 g detectors. During this run neither a polyethylene neutron shield nor a muon veto were employed. The low-energy event distribution of the data taken in this run is depicted in Fig. 3.13 showing the light yield versus energy in the phonon channel of the crystals labelled "Julia" and "Daisy".

For the nuclear recoil acceptance region a quenching factor of 7.4 was used. With this value the region below the upper dashed curve contains 90% of the nuclear recoils whereas the lower dashed curve corresponds to the 10% boundary. With a quenching factor of 40 for tungsten, 90% of the tungsten recoils are expected to be found below the solid black curve.

The region used for the WIMP analysis indicated by the vertical lines in Fig. 3.13 ranges from 12 to 40 keV. The lower bound was set to be well above the intersection region of the electron and nuclear recoil bands. Due to the Helm form-factor suppression of the coherent scattering rates on tungsten, 95% of the tungsten recoils are expected below the upper bound of 40 keV.

In this acceptance region a total of 16 events have been obtained with both detectors corresponding to a rate of  $0.87 \pm 0.22$ /(kg day). Since most of these events were found between the 10% and 90% boundaries they were most likely due to neutrons which is consistent with Monte-Carlo simulations yielding a rate of 0.6/(kg day) [149] in this energy range when no shielding against neutrons is employed.

The detector module with the crystal labelled "Daisy" exhibited a better resolution in the light channel (bottom in Fig. 3.13) allowing a reasonable discrimination of tungsten recoils. In the data taken with this module no events were found below the solid curve where 90% of the tungsten events are expected indicating that the nuclear recoils in this region were indeed due to neutrons.

Due to the absence of tungsten events in the energy region used for the Dark

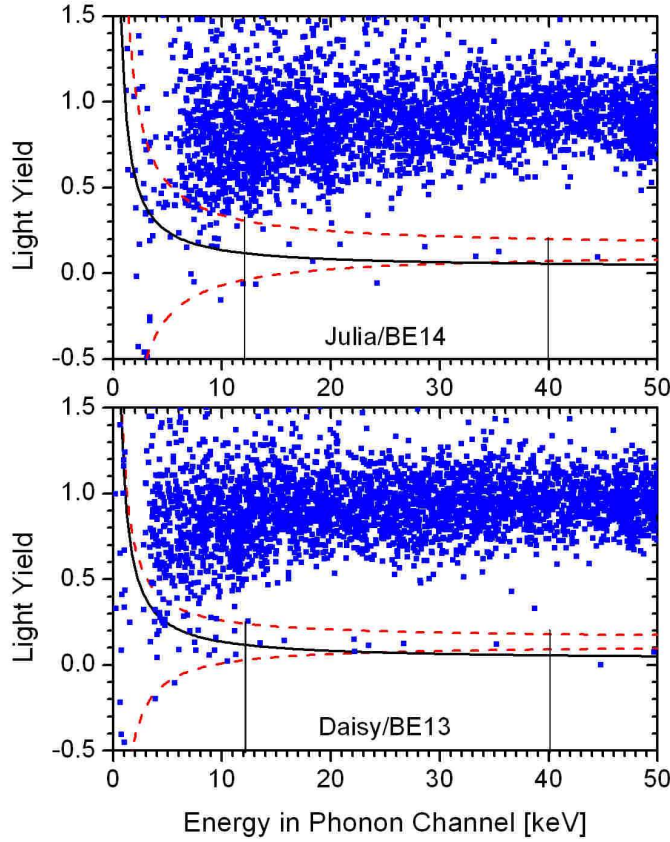


Figure 3.13: Low-energy event distribution of the data taken with two 300 g detectors in spring 2004. In this run no neutron shield and no muon veto were present. The dashed lines indicate the nuclear recoil acceptance region. The energy interval used for WIMP analysis is marked by the vertical black lines. Below the solid curve 90% of the tungsten recoils are expected assuming a quenching factor of 40 for W recoils [139].

Matter analysis, a much stronger limit on the spin-independent WIMP-nucleon cross section could be deduced from the data acquired with this module alone. An upper limit of  $1.6 \cdot 10^{-6}$  pb for the spin-independent WIMP-nucleon cross section for a WIMP mass of 60 GeV was obtained [139].

Judging from these results, the sensitivity of CRESST is mainly limited by the neutron background when the resolution of the light channel is not sufficient to discriminate the events resulting from tungsten recoils. For this reason a polyethylene shield with a thickness of 45 cm as well as a muon veto were installed during a major upgrade phase between 2004 and 2006 after which an extended commissioning run was carried out. The data taken with two of the modules operated in this run could be used to set new Dark Matter limits [140]. The low-energy event

distribution is depicted in Fig. 3.14.

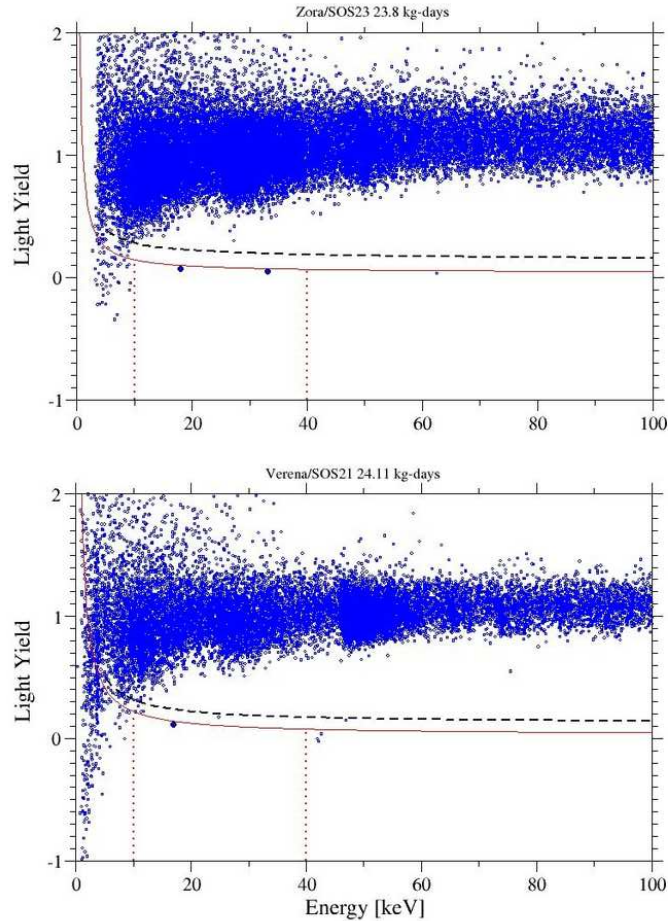


Figure 3.14: Low-energy event distribution measured with two detector modules during the commissioning run. The plots show the light yield versus total energy as measured by the phonon channel. Below the dashed black curve 90% of the nuclear recoils are expected. The solid red curve indicates the corresponding 90% region of tungsten recoils. The vertical lines mark the energy region used for the WIMP analysis. Figure taken from [140].

The cumulative exposure of the detector modules labelled "Zora/SOS23" (top panel in Fig. 3.14) and "Verena/SOS21" (bottom panel) was 47.9 kg days corresponding to a total tungsten exposure of 30.6 kg days. Below the black dashed lines in Fig. 3.14, 90% of the nuclear recoils are expected. The solid red curves mark the corresponding 90% regions for the tungsten recoils. The energy region from 10 to 40 keV used for the Dark Matter analysis can be found between the vertical

lines. In this energy interval a total of 3 events are found in the tungsten recoil acceptance region corresponding to a rate of 0.063 per kg day. Using standard halo parameters, an upper limit on the spin-independent WIMP-nucleon cross section of  $4.8 \times 10^{-7}$  pb for a WIMP mass of  $\sim 50$  GeV could be set from this data. This limit is depicted in Fig. 3.15 together with the current limits set by EDELWEISS II [134], ZEPLIN III [157], XENON10 [120] and CDMS [127]. The filled red area corresponds to the DAMA/LIBRA results when ion channeling is included [107]. The filled green area indicates the supersymmetric parameter space predicted by E. A. Baltz and P. Gondolo [158].

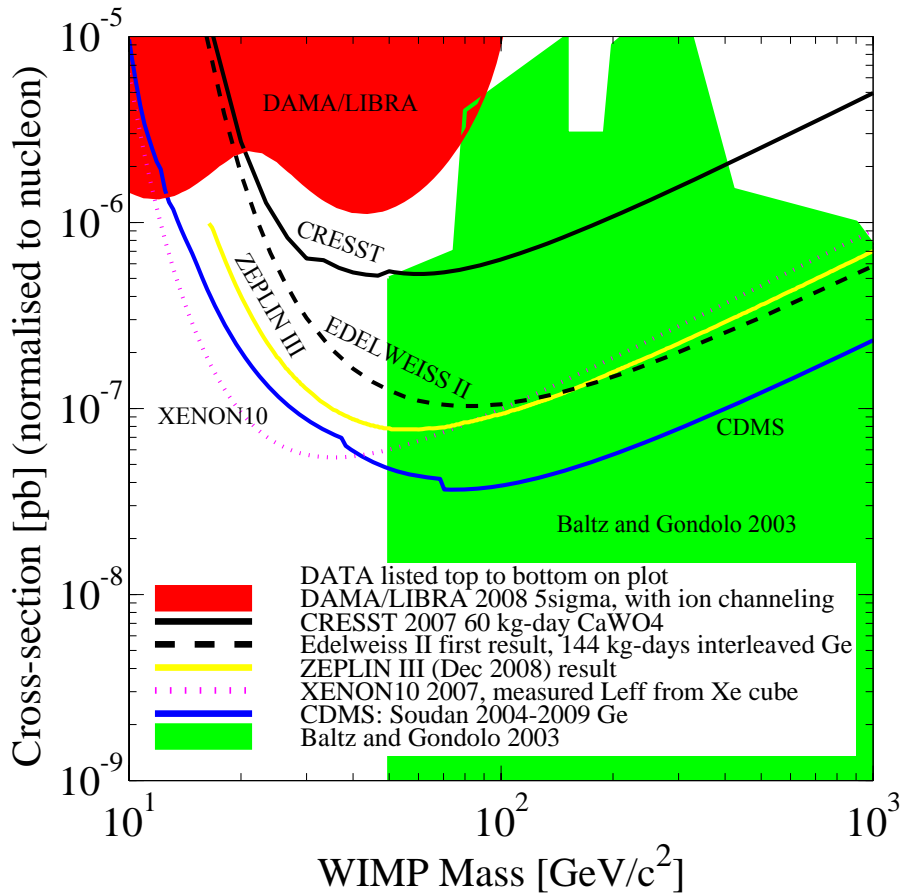


Figure 3.15: CRESST II limit (black solid line) on the coherent WIMP-nucleon cross section obtained from the data taken during the commissioning run (s. Fig. 3.14) together with the results of other direct DM experiments as well as predictions of supersymmetric models (green area). Figure generated by [159].

When compared to the results of the run in 2004 [139], only 4 events are found in

the same acceptance region of the nuclear recoil band corresponding to a rate of  $\sim 0.083$  per kg day. This is an improvement by a factor of  $\sim 10$  and can be mainly attributed to the presence of the polyethylene neutron shield.

The origin, however, of the 3 events compatible with tungsten recoils that limit the present sensitivity has not yet been resolved with certainty [140]. They can possibly be ascribed to a small leakage in the neutron shield above the muon veto that has been fixed only after data taking was finished. Other possible sources are muon-induced neutrons from non-operational modules and events induced by nuclear recoils from surface alpha decays that could not be vetoed due to an incomplete coverage of the inner surface of the module with scintillator. Further details are given in Ref. [140].

### 3.6 Perspectives

The present CRESST II setup is able to hold a total target mass of  $\sim 10$  kg corresponding to 33 modules. In the present run started in July 2009, a total of 18 modules are installed. Ten of them are taking data corresponding to a total target mass of 3 kg and up to now to a total exposure of several 100 kg days. The upper limit on the spin-independent WIMP-nucleon cross section that will be set from the data taken in this run is expected to be in the  $10^{-8}$ pb range.

Besides the improvement of the last CRESST-II limits, one of the major purposes of this run is the identification of the origin of the events observed during the commissioning run in the tungsten acceptance region. Since these events are mainly related to the low light yield, attempts have been made to improve the light emission and detection. This includes the employment of other scintillators such as  $\text{ZnWO}_4$ , the light detection with two light detectors in one of the installed modules as well as absorbers with glued TESs (composite detectors) [160, 161] in order to prevent the degradation of the light emitting properties of the absorber crystal due to the manufacturing processes involving high temperatures.

Once fully equipped, CRESST II will be able to reach a sensitivity of  $\sim 10^{-8}$ pb. For a further improvement of the sensitivity larger targets and a better background suppression will be needed. The exploration of the range between  $10^{-8}$ - $10^{-10}$ pb which is currently most favoured by supersymmetric models, is the goal of the new Dark Matter project EURECA (European Underground Rare Event Calorimeter Array) mainly based on CRESST, EDELWEISS and ROSEBUD expertise [162]. The aim of EURECA is to operate a calorimeter array at the tonne scale consisting of different targets as well as an improved background control. The multi-elemental target will provide a signature due to the  $A^2$  dependence of the WIMP-nucleon scattering rates which is essential for an unambiguous identification of the signals induced by particle Dark Matter.



# Chapter 4

## Detector Physics

### 4.1 Basic Principle

The detectors focused on in this work, rely on the detection of phonons by a transition edge sensor (TES). The phonons are excited by incident particles in a semiconducting or dielectric absorber at mK temperatures. A TES is a superconducting film operated in its narrow transition region between the normal and the superconducting state (see section 4.3) thus making the film resistance highly sensitive to temperature. In this operation mode, phonons absorbed in the TES heat the sensor and change its resistance which is converted into an electrical signal by a SQUID. Equilibrium conditions are reestablished due to a weak thermal link between the TES and a heat sink. A schematic view of a cryogenic detector is shown in Fig. 4.1.

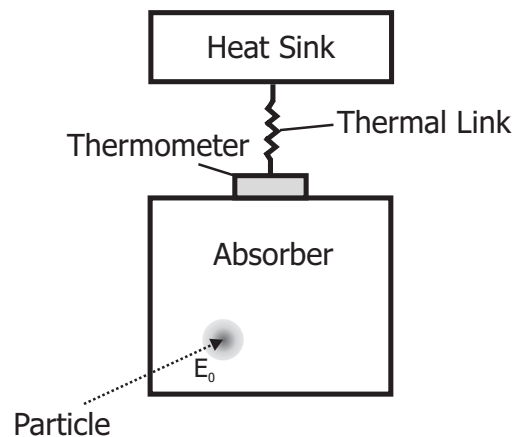


Figure 4.1: Schematic view of a cryogenic detector consisting of an absorber equipped with a thermometer (TES) which is connected via a weak thermal link to a heat sink.

In the following the different processes involved in the formation of the signal of a cryogenic detector will be described. It includes an amplification scheme of the phonon signal proposed by Neganov and Luke which is based on the additional phonons generated by drifted charge carriers in a semiconducting absorber [6, 7].

## 4.2 Signal Generation

### 4.2.1 Phonon Excitation and the Neganov-Luke Effect

At the low operating temperatures of cryogenic detectors the phonons excited by particle interactions greatly differ with respect to their energy spectra and transport properties. The primarily generated phonons strongly depend on the type of interaction which can be roughly subdivided into nuclear and electron recoils.

The energy deposited via nuclear recoils is quickly converted into acoustic phonons by collisions of the recoiling nucleus with other atoms. The phonons generated in these processes populate the whole phonon spectrum. Their average energy is on the scale of the Debye energy [163].

In interactions involving electron recoils, the deposited energy is converted into high energetic electrons. Requiring energy and momentum conservation and assuming equal effective masses for electrons and holes the minimum energy required to create a secondary electron-hole pair is  $E_{eh}=1.5E_g$  [4], where  $E_g$  is the bandgap energy. For energies higher than  $E_{eh}$ , the interactions of the primarily excited electrons are dominated by electron-electron scattering creating secondary electron-hole pairs. For energies lower than  $E_{eh}$  the relaxation to the band edge occurs mainly via phonon emission [164]. On a time scale of the order of 100 ps, optical phonons decay into acoustic phonons of about half the Debye frequency  $\nu_D$  yielding a nearly monochromatic phonon spectrum [165]. The energy of the thermalized electron-hole pairs at the band edge can be converted into phonons by recombination. Here, localized states in the band gap, referred to as traps, play an important role since they can be occupied by the thermalized electrons or holes. At the low operating temperatures considered here, these states can be long lived so that the energy of trapped charge carriers is lost in the detection channel. This effect might be a limiting factor for the energy resolution when using dielectric or semiconducting absorbers if the density of the localized states is high.

Following Neganov, Trofimov [6] and Luke [7], additional optical phonons can be generated in a semiconducting absorber by drifting the particle-induced electron-hole pairs in an applied electric field (Fig. 4.2). Provided that no charge carriers are lost, the thermal gain  $G_t$  is given by  $G_t=1+eV/\epsilon$ , where  $e$  is the charge of an electron,  $V$  the applied voltage and  $\epsilon$  the energy required on average to create an

electron-hole pair. A more detailed discussion on cryogenic light detectors with Neganov-Luke amplification can be found in sect. 6.2.3.

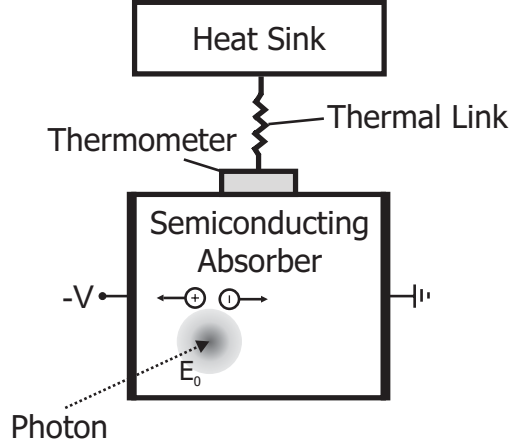


Figure 4.2: Schematic drawing of a cryogenic detector employing a semiconducting absorber equipped with two electrodes. The particle-induced electron-hole pairs are drifted by the applied voltage ( $V$ ) generating additional phonons.

Since mobilities of electrons and holes in high-purity silicon and germanium at low temperatures are of the order of  $10^4$ - $10^5$   $\text{cm}^2/\text{Vs}$  [166] the time needed to drift the charge carriers to the electrodes ranges up to  $\sim 1\mu\text{s}$ . This sets the time scale relevant for the conversion of the energy deposited in the detector into acoustic phonons.

#### 4.2.2 Phonon Down-Conversion and Thermalization

Disregarding the different time scales, the energy deposited in a dielectric or semiconducting absorber at low temperatures is always converted into high-energetic acoustic phonons, however, with a spectrum strongly dependent on the type of interaction. These acoustic phonons can be found in longitudinal (LA) and transversal (TA) modes. The down-conversion of acoustic phonons is dominated by the anharmonic decay of LA phonons via:  $\text{LA} \rightarrow \text{TA} + \text{TA}$  or  $\text{LA} \rightarrow \text{TA} + \text{LA}$ , with a highly frequency-dependent decay rate  $\Gamma_d \propto \nu^5$  [167]. Since TA phonons occupy the lowest branch of the dispersion curve their decay is strongly inhibited in isotropic media [168]. In real crystalline solids, however, TA phonons are expected to decay. The corresponding decay rate is found to have a high spatial anisotropy [169].

Another process which affects the high-energetic acoustic phonons is elastic isotope scattering with a frequency dependent rate  $\Gamma_{\text{isotope}} \propto \nu^4$  [170]. It induces

conversions between the transversal and longitudinal modes creating an effective decay channel for TA phonons [169].

Due to the strong frequency dependence of the anharmonic decay rate, there is a rapid initial down-conversion of the phonon energy. In a silicon crystal, starting with a phonon population at half the Debye frequency  $\nu_D$  ( $\nu_D=13.5$  THz in Si) the average frequency rapidly decreases to about 300 GHz remaining then nearly constant on a ms time scale [171] during which the phonons spread ballistically over the entire absorber. This frequency, however, corresponds to the maximum of a 5 K Planck distribution, i.e. the phonons would not thermalize on this time scale in an ideal non-conducting crystal absorber. In a real crystal, adsorbates on the surface [172] and surface defects induced in manufacturing processes cause a further down-conversion of the phonon energy leading to a thermalization in the absorber on a ms time scale.

The down-conversion of the ballistic phonons in the absorber competes with their absorption in the thermometer film where their energy is quickly thermalized due to the strong electron interaction leading to a temperature rise of the electron system. The resulting time constant  $\tau_n$  for the thermalization of the non-thermal phonon population in the absorber is given by [171]

$$\tau_n = \left( \frac{1}{\tau_{film}} + \frac{1}{\tau_{crystal}} \right)^{-1}, \quad (4.1)$$

where  $\tau_{film}$  and  $\tau_{crystal}$  denote the time constants for the thermalization in the film and the crystal, respectively. With the effective absorption probability  $\eta$ ,  $\tau_{film}$  is given by

$$\tau_{film} = \frac{\tau_0}{\eta}. \quad (4.2)$$

Here,  $\tau_0$  denotes the ideal thermalization time corresponding to the case that all phonons transmitted into the thermometer are absorbed. It is given by [171]

$$\tau_0 = \frac{2V_a}{A \langle v_{\perp} \alpha \rangle}. \quad (4.3)$$

Here,  $V_a$  is the absorber volume,  $A$  the area of the absorber-thermometer interface,  $v_{\perp}$  the phonon group velocity normal to the interface and  $\alpha$  the transmission probability.  $\langle \dots \rangle$  denotes an average over modes and wave vectors of incident phonons at the absorber-thermometer interface.

The fraction  $\epsilon$  of the phonons thermalized in the thermometer is given by

$$\epsilon = \frac{\tau_n}{\tau_{film}} = \frac{\tau_{crystal}}{\tau_{crystal} + \tau_{film}}. \quad (4.4)$$

The fraction  $(1 - \epsilon)$  of the phonons not absorbed in the thermometer thermalizes in the absorber heating it up. This induces an additional temperature rise of the electron system of the thermometer due to the thermal coupling to the phonon system of the absorber. Therefore, the pulses observed with cryogenic detectors employing dielectric absorbers, exhibit two time constants corresponding to the different thermalization processes. For an accurate description of the pulse shape of these detectors the different components and their couplings must be taken into account.

### 4.2.3 Thermal Detector Model

In this subsection a thermal model (based on [171]) of a cryogenic detector employing dielectric absorbers with directly evaporated thermometer films will be presented.

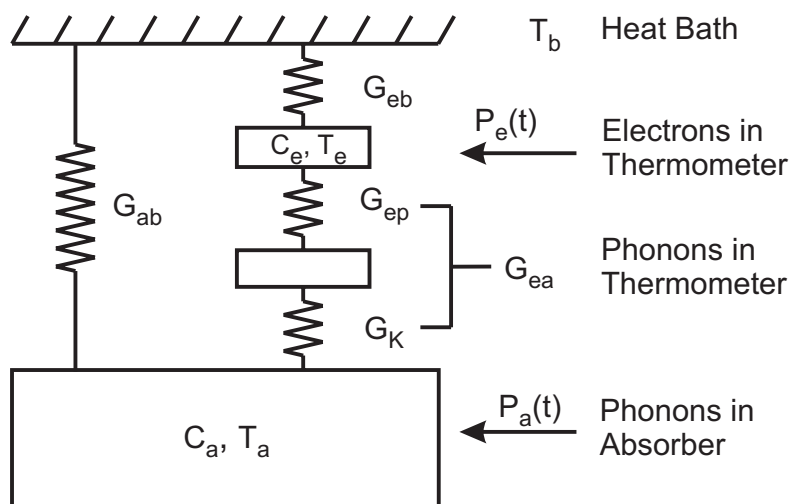


Figure 4.3: Thermal model of a phonon-mediated cryogenic detector employing dielectric absorbers with directly evaporated thermometer films.

A schematic view of the detector model is depicted in Fig. 4.3. Its key components are the electron and the phonon system of the thermometer as well as the phonon system of the absorber. Each component is characterized by its heat capacity  $C$  and its temperature  $T$ .  $P_a(t)$  denotes the power input into the thermal phonon population of the absorber after thermalization of high-frequency phonons. The time-dependent power input into the electron system of the thermometer due to the absorption of non-thermal phonons is given by  $P_e(t)$ .

#### 4.2.3.1 The Power Inputs $P_e(t)$ and $P_a(t)$

For the calculation of the power inputs  $P_e(t)$  and  $P_a(t)$ , one assumes that the energy deposited by an incident particle  $\Delta E$  is instantaneously converted into high-frequency phonons that fill the absorber uniformly. The thermalization rate is independent of their frequency. Taking into account that a fraction  $\epsilon$  of the phonons is thermalized in the thermometer, the initial power input  $P_0$  into the thermometer is then given by

$$P_0 = \frac{\epsilon \Delta E}{\tau_n}, \quad (4.5)$$

with the time constant  $\tau_n$  for the thermalization of the non-thermal phonon population (s. subsect. 4.2.2). Under these assumptions, the power inputs  $P_e(t)$  and  $P_a(t)$  can be written as

$$P_e(t) = \Theta(t) P_0 \exp\left(-\frac{t}{\tau_n}\right) \quad (4.6)$$

$$P_a(t) = \frac{1-\epsilon}{\epsilon} P_e(t). \quad (4.7)$$

The assumption of an immediate conversion of the deposited energy  $\Delta E$  into high-frequency phonons that fill the absorber uniformly is expressed here by the  $\Theta$  function.

#### 4.2.3.2 Thermal Couplings

The electrons and phonons in the thermometer are considered as subsystems weakly coupled by  $G_{ep} \propto T^5$  [171]. The thermal conductance between the phonon systems of thermometer and absorber is given by a Kapitza coupling  $G_K \propto T^3$  [171]. Since the heat capacity of the phonon system of the thermometer can be neglected compared to the heat capacity  $C_e$  of the electrons, an effective coupling  $G_{ea}$  between electrons in the thermometer and thermal phonons in the absorber can be introduced:

$$G_{ea} = \left( \frac{1}{G_{ep}} + \frac{1}{G_K} \right)^{-1}. \quad (4.8)$$

The coupling  $G_{ab} \propto T^3$  [171] of the phonon system of the absorber to the heat bath is provided by the mechanical mounting of the crystal. The thermal link  $G_{eb}$  of the electron system of the thermometer to the heat bath is mediated by the heat conductance of the electrons across the film and a gold bond wire. Its thermal conductance  $G_{Au}$  can be derived from the Wiedemann-Franz law:

$$G_{Au} = \frac{LT}{R_{Au}}, \quad (4.9)$$

where  $R_{Au}$  denotes the resistance at the temperature  $T$  and  $L$  is the Lorentz number ( $L=24.5 \text{ nW}\Omega\text{K}^{-2}$ ).

### 4.2.3.3 Heat Capacities

The heat capacities play an important role in the detector model since they determine the actual temperature rise caused by thermalized phonons. At the low operating temperatures of cryogenic detectors, the heat capacities of dielectrics and semiconductors are dominated by the lattice specific heat  $c_{ph}$ . The Debye theory predicts a  $T^3$  dependence of  $c_{ph}$  at these temperatures [173]:

$$c_{ph} = \frac{12\pi^4}{5} N k_B \left( \frac{T}{\Theta_D} \right)^3, \quad (4.10)$$

where  $N$  denotes the number of lattice atoms per mole,  $k_B$  the Boltzmann constant and  $\Theta_D$  the Debye temperature.

At low temperatures the heat capacities of normal metals are mainly determined by the electronic specific heat and are thus linear in temperature [173]:

$$c_{el} = \frac{\pi^2}{2} N_e k_B \frac{T}{T_F} \equiv \gamma T. \quad (4.11)$$

Here,  $N_e$  denotes the number of conduction electrons per mole,  $T_F$  the Fermi temperature and  $\gamma$  the Sommerfeld constant.

The heat capacity of superconductors is more complicated since there are both phonon and electronic contributions with different temperature dependences. According to BCS theory, at the critical temperature  $T_c$  the heat capacity of a superconductor is 2.43 times the normal-metal value  $c_{el}$  [174]. The value of the heat capacity at the working point can be estimated by taking the ratio of the resistance  $R_{wp}$  at the working point to the normal conducting resistance  $R_n$  as a measure for the fraction of the film in the superconducting phase. Under this assumption, the heat capacity  $c_{wp}$  at the operating point can be written as

$$c_{wp} = c_{el} \left( 2.43 - 1.43 \frac{R_{wp}}{R_n} \right). \quad (4.12)$$

The actual value of the heat capacity within the superconducting transition can be derived from complex impedance measurements [175].

#### 4.2.3.4 Pulse Shape

Having defined all the parameters of the thermal model, the time evolution of the temperature of the absorber  $T_a$  and of the electrons of the thermometer  $T_e$  can now be described by two coupled differential equations [171]:

$$C_e \frac{dT_e}{dt} + (T_e - T_a)G_{ea} + (T_e - T_b)G_{eb} = P_e(t) \quad (4.13)$$

$$C_a \frac{dT_a}{dt} + (T_a - T_e)G_{ea} + (T_a - T_b)G_{ab} = P_a(t), \quad (4.14)$$

where  $T_b$  is the temperature of the heat sink,  $C_e$  and  $C_a$  are the heat capacities of the electrons in the thermometer and the phonons in the absorber. With the initial conditions  $T_a(t=0) = T_e(t=0) = T_b$ , these equations have the following solution for the thermometer signal  $\Delta T_e(t)$ :

$$\Delta T_e(t) = \Theta(t)[A_n(e^{-t/\tau_n} - e^{-t/\tau_{in}}) + A_t(e^{-t/\tau_t} - e^{-t/\tau_n})]. \quad (4.15)$$

The solution consists of two components  $A_n$  and  $A_t$ .  $A_n$  results from the absorption of non-thermal phonons in the thermometer film and is given by

$$A_n = \frac{P_0 \left( \frac{1}{\tau_{in}} - \frac{G_{ab}}{C_a} \right)}{\epsilon \left( \frac{1}{\tau_t} - \frac{1}{\tau_{in}} \right) \left( \frac{1}{\tau_{in}} - \frac{1}{\tau_n} \right)} \left( \frac{\frac{1}{\tau_t} - \frac{G_{ab}}{C_a}}{G_{eb} - \frac{C_e}{C_a} G_{ab}} - \frac{\epsilon}{C_e} \right). \quad (4.16)$$

$A_t$  corresponds to the temperature rise of the absorber as measured by the thermometer:

$$A_t = \frac{P_0 \left( \frac{1}{\tau_t} - \frac{G_{ab}}{C_a} \right)}{\epsilon \left( \frac{1}{\tau_t} - \frac{1}{\tau_{in}} \right) \left( \frac{1}{\tau_t} - \frac{1}{\tau_n} \right)} \left( \frac{\frac{1}{\tau_{in}} - \frac{G_{ab}}{C_a}}{G_{eb} - \frac{C_e}{C_a} G_{ab}} - \frac{\epsilon}{C_e} \right). \quad (4.17)$$

The three time constants in 4.15 are the intrinsic thermal relaxation time of the thermometer  $\tau_{in}$ , the effective thermalization time of non-thermal phonons  $\tau_n$  (eq. 4.1) and the thermal relaxation time  $\tau_t$  of the absorber.  $\tau_{in}$  and  $\tau_t$  can be expressed by the heat capacities and thermal couplings of the system:

$$\tau_{in} = \frac{2}{a + \sqrt{a^2 - 4b}} \quad (4.18)$$

$$\tau_t = \frac{2}{a - \sqrt{a^2 - 4b}}, \quad (4.19)$$

where  $a$  and  $b$  are given by

$$a = \frac{G_{ea} + G_{eb}}{C_e} + \frac{G_{ea} + G_{ab}}{C_a} \quad (4.20)$$

$$b = \frac{G_{ea}G_{eb} + G_{ea}G_{ab} + G_{eb}G_{ab}}{C_e C_a}. \quad (4.21)$$

#### 4.2.3.5 Operation Modes

Since for the detectors this work is focused on,  $C_e \ll C_a$ ,  $\tau_{in}$ ,  $\tau_t$  and  $A_n$  can be simplified as

$$\tau_{in} \approx \frac{1}{a} \approx \frac{C_e}{G_{ea} + G_{eb}} \quad (4.22)$$

$$\tau_t \approx \frac{a}{b} \approx \frac{C_a}{\frac{G_{eb}G_{ea}}{G_{eb} + G_{ea}} + G_{ab}} \quad (4.23)$$

$$A_n \approx \frac{P_0}{(G_{ea} + G_{eb}) \left(1 - \frac{\tau_{in}}{\tau_n}\right) \left(1 - \frac{\tau_{in}}{\tau_t}\right)} = \frac{-\epsilon \Delta E}{C_e \left(1 - \frac{\tau_n}{\tau_{in}}\right) \left(1 - \frac{\tau_{in}}{\tau_t}\right)}. \quad (4.24)$$

From the last equation it becomes evident that the sign of  $A_n$  is determined by the ratio of  $\tau_{in}$  and  $\tau_n$  defining two different modes of operation. At low operating temperatures, where  $G_{ea} \ll G_{eb}$ ,  $\tau_{in}$  is controlled by the thermal conductance of the sensor to the heat sink  $G_{eb}$ .

A TES sensor with  $\tau_{in} \gg \tau_n$  integrates the power input  $P_e(t)$ . The amplitude of the non-thermal component which is then given by

$$A_n \approx -\frac{\epsilon \Delta E}{C_e} \quad (4.25)$$

measures the total energy of the high-frequency phonons absorbed in the thermometer. Therefore, this operation mode is referred to as 'calorimetric'. In this mode  $\tau_n$  defines both the thermal and non-thermal rise times, whereas  $\tau_{in}$  and  $\tau_n$  determine the decay times of the non-thermal and the thermal components.

For a detector with  $\tau_{in} \ll \tau_n$  the amplitude of the non-thermal component is proportional to the power input:

$$A_n \approx \frac{P_0}{G_{ea} + G_{eb}}. \quad (4.26)$$

In this mode the thermometer measures the flux of non-thermal phonons. Therefore, it is also referred to as 'bolometric mode'. In this mode the rise and decay times of the non-thermal component are given by  $\tau_{in}$  and  $\tau_n$ . The corresponding decay times of the thermal component are  $\tau_n$  and  $\tau_t$ .

Due to the long times needed for the thermalization of the high-frequency phonons in the  $\text{CaWO}_4$  crystals employed in the CRESST experiment, the thermometers, they are equipped with, are working in bolometric mode.

#### 4.2.4 Thermal Model for Composite Detectors

The thermal model presented in the previous subsection describes detectors with thermometers directly evaporated onto the absorber. For some applications, however, it turns out to be favorable to evaporate the TES onto a small crystalline substrate which is then coupled to the absorber by gluing (see chapter 6). For an accurate description of the signal of composite detectors the additional component of the glued interface has to be considered.

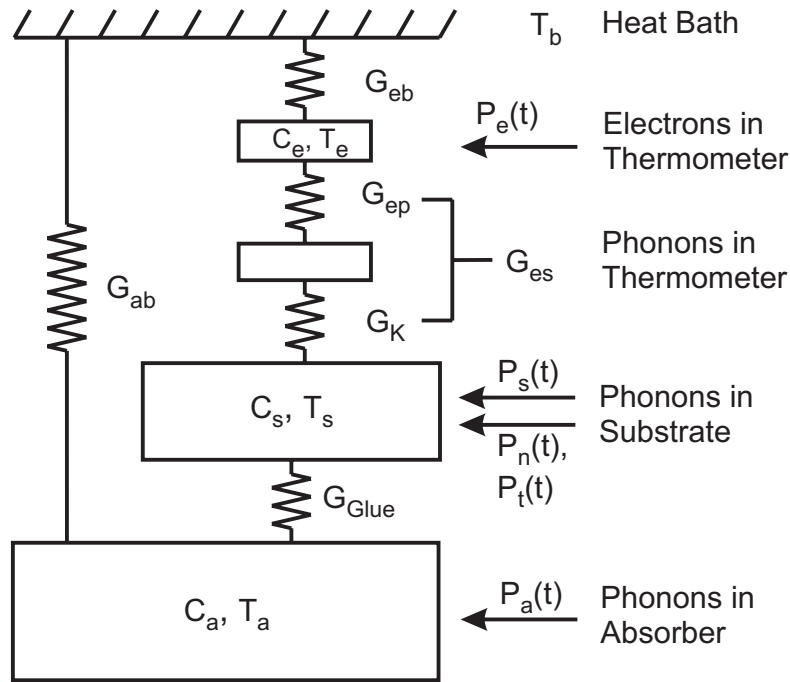


Figure 4.4: Thermal model of a phonon-mediated cryogenic detector employing dielectric absorbers based on the composite design.

A schematic view of the thermal model of a cryogenic composite detector is depicted in Fig. 4.4. As compared to the thermal model of a 'traditional' cryogenic

detector (Fig. 4.3), the crystalline substrate carrying the thermometer film has been added. It is characterized by the heat capacity  $C_s$  and the temperature  $T_s$  whereas its coupling  $G_{glue}$  to the absorber is provided by the glue spot which does not contribute as a thermal component to the system [176, 177]. The effective coupling  $G_{es}$  of the electrons in the thermometer and the thermal phonons in the substrate is again a combination of the electron-phonon coupling in the thermometer  $G_{ep}$  and the Kapitza coupling  $G_K$  of the film to the substrate:

$$G_{es} = \left( \frac{1}{G_{ep}} + \frac{1}{G_K} \right)^{-1}. \quad (4.27)$$

The couplings to the heat bath of phonons in the absorber and electrons in the thermometer are given by  $G_{ab}$  and  $G_{eb}$ , respectively.

In such a system, there are many different ways that non-thermal phonons excited in the absorber can evolve [176, 177]. They can either thermalize in the absorber inducing the heating power  $P_a(t)$  or pass through the glue giving rise to a time-dependent power input  $P_n(t)$  into the non-thermal phonon population of the substrate. The non-thermal phonons in the substrate can then be absorbed in the thermometer film (power input  $P_e(t)$ ), thermalize in the substrate inducing the power input  $P_s(t)$  into its thermal phonon population or propagate back into the absorber. The temperature rise of the substrate due to thermalized non-thermal phonons induces in analogy to a common cryogenic detector a slow signal component since electrons in the thermometer and the phonon system of the substrate are coupled via  $G_{es}$ .

For a quantitative analysis of the signal of a composite cryogenic detector, the thermometer and the TES substrate can be treated as a 'traditional' cryogenic detector described by the thermal model presented in the last subsection. The energy input, however, cannot be treated as an instantaneous process any longer since both the thermal and non-thermal power inputs,  $P_t(t)$  and  $P_n(t)$  from the absorber are time-dependent. The injection of non-thermal phonons depends on their thermalization rate and their collection time defined by the glue spot area relative to the absorber volume. The thermal power input into the substrate mainly depends on the thermalization time of non-thermal phonons, the heat capacity of the absorber as well as the thermal couplings, i.e.  $G_{Glue}$  and  $G_{ab}$ .

The actual signal of a composite detector is therefore obtained by a convolution of the time-dependent power inputs from the absorber with the response of the detector system consisting of substrate and thermometer. The pulse shape analysis of different cryogenic composite detectors employing different absorbers and gluing areas reveals that depending on the exact detector design, i.e. the TES-to-glue-area ratio, either only non-thermal phonons or both non-thermal and thermal phonons significantly contribute to the signal in the TES [177, 176]. A thermal component

is only significant, when the TES-to-glue-area ratio is smaller than 1. In this case non-thermal phonons entering the substrate are not substantially absorbed in the TES since due to the large gluing area a significant fraction can propagate back into the absorber where they thermalize inducing a slow signal component.

## 4.3 Transition Edge Sensors

### 4.3.1 Basic Principle

The key component of the cryogenic detectors this work is focused on, are the thermometers which convert the phonon energy into an electrical signal. The thermometers employed here are transition edge sensors (TES) consisting of a thin superconducting film biased in the narrow transition region between the normal and superconducting state making thus its resistance highly sensitive to temperature. In this way, even small variations of the temperature of the TES result in significant variations of its resistance (Fig. 4.5).

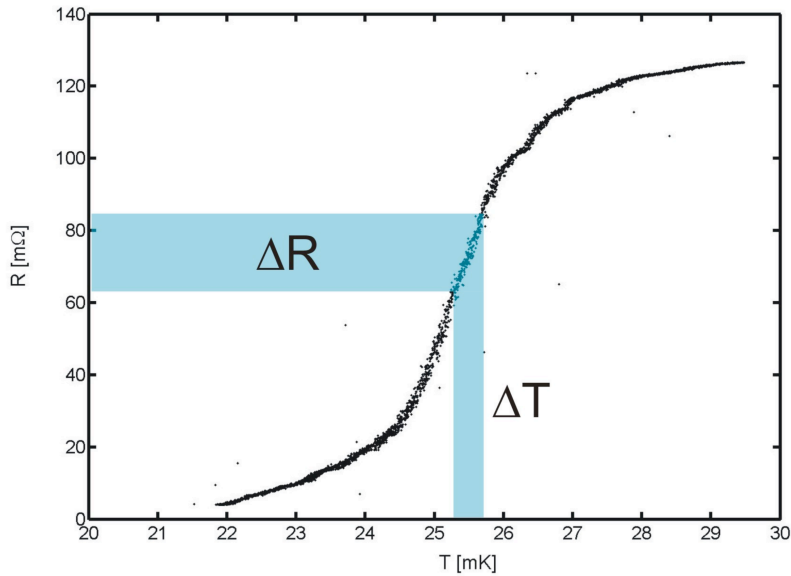


Figure 4.5: Working principle of a transition edge sensor (TES): A thin superconducting film is biased in its narrow transition region between the normal and superconducting state. The resistance becomes highly sensitive to temperature. Therefore, small changes  $\Delta T$  of temperature induced by incident particles alter the TES resistance by  $\Delta R$  providing an electrical signal.

A typical readout circuit to convert a resistance change into an electrical signal is depicted in Fig. 4.6.

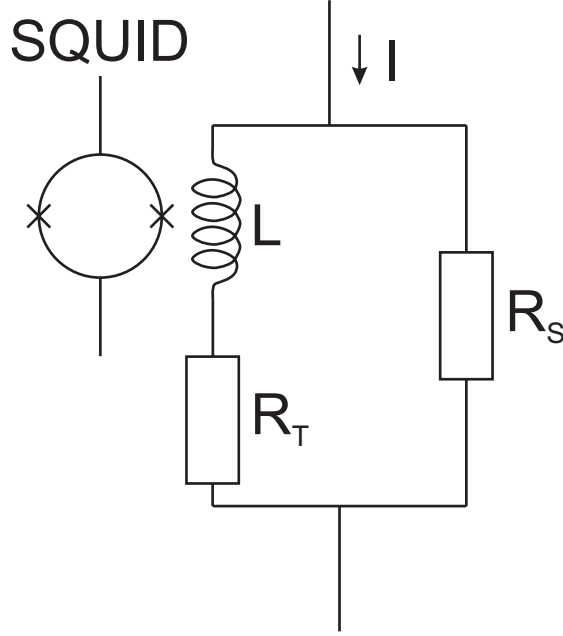


Figure 4.6: Readout circuit of a transition edge sensor. The TES ( $R_T$ ) is in parallel with a reference (shunt) resistor  $R_S$  and in series with the input coil  $L$  of a SQUID. The circuit is biased with a constant current  $I$ . Small changes of  $R_T$  alters the current in the TES branch changing the magnetic field in the coil which is detected by the SQUID.

Here, the TES characterized by its resistance  $R_T$  is in series with a superconducting coil  $L$  and in parallel with a reference (shunt) resistance  $R_S$ . The whole circuit is biased with a constant current  $I$ . A variation of the TES resistance alters the current in the thermometer branch and therefore also the magnetic field of the coil which then can be measured by a Superconducting Quantum Interference Device (SQUID) providing the electrical signal.

The current  $I_T$  in the thermometer branch is given by the TES resistance  $R_T$  and the reference resistance  $R_S$ :

$$I_T = I \frac{R_S}{R_T + R_S}. \quad (4.28)$$

The power  $P_T$  dissipated in the TES due to this current is:  $P_T = I_T^2 R_T$ . Taking this Joule power into account, the thermometer resistance becomes a function of both the temperature  $T$  and the bias current  $I$ . For small signals, the resistance of the TES can be expanded around the steady-state value  $R_0 \equiv R(T_0, I_0)$ :

$$R(T, I) \approx R_0 + \left. \frac{\partial R}{\partial T} \right|_{I_0} \Delta T + \left. \frac{\partial R}{\partial I} \right|_{T_0} \Delta I = R_0 + \alpha \frac{R_0}{T_0} \Delta T + \beta \frac{R_0}{I_0} \Delta I, \quad (4.29)$$

where  $\Delta T \equiv T - T_0$  and  $\Delta I \equiv I - I_0$ .  $\alpha$  and  $\beta$  denote the unitless logarithmic temperature and current sensitivities, respectively:

$$\alpha \equiv \left. \frac{\partial \log R}{\partial \log T} \right|_{I_0} = \left. \frac{T_0}{R_0} \frac{\partial R}{\partial T} \right|_{I_0} \quad (4.30)$$

$$\beta \equiv \left. \frac{\partial \log R}{\partial \log I} \right|_{T_0} = \left. \frac{I_0}{R_0} \frac{\partial R}{\partial I} \right|_{T_0}. \quad (4.31)$$

Including the readout circuit and the Joule power dissipated in the thermometer, the TES response is then determined by the following differential equations governing the state variables, temperature and current:

$$C_e \frac{dT_e}{dt} + (T_e - T_a)G_{ea} + (T_e - T_b)G_{eb} - P_T = P_e(t) \quad (4.32)$$

$$C_a \frac{dT_a}{dt} + (T_a - T_e)G_{ea} + (T_a - T_b)G_{ab} = P_a(t) \quad (4.33)$$

$$L \frac{dI_T}{dt} + R_T I_T - R_S (I - I_T) = 0. \quad (4.34)$$

### 4.3.2 Electrothermal Feedback

The thermal and electrical circuits of a TES described by the differential equations 4.32 - 4.34 are not independent of each other. A temperature signal in the thermometer is transduced into an electrical signal by the change of resistance which in turn alters the current through the TES. This is fed back into a temperature signal by the Joule power dissipated in the TES. This behaviour is referred to as "electrothermal feedback" (ETF) [178]. It can be best described by the dependency of the Joule power on the temperature of the electron system  $T_e$  which can be expressed in terms of the unitless logarithmic temperature sensitivity  $\alpha$ :

$$\frac{\partial P_t}{\partial T_e} = \alpha \frac{P_T}{T_e} \left( \frac{R_S - R_T}{R_S + R_T} \right) = -\alpha_{eff} \frac{P_T}{T_e}, \quad (4.35)$$

where  $\alpha_{eff}$  is given by

$$\alpha_{eff} = \alpha \left( \frac{R_T - R_S}{R_T + R_S} \right). \quad (4.36)$$

Depending on the magnitude of  $R_T$  relative to  $R_S$  the system behaves in different ways. A TES in a readout circuit with  $R_S \ll R_T$  is effectively voltage-biased. Since  $\alpha$  is positive, the Joule power decreases with increasing temperature for such a system and the electrothermal feedback is negative. Under current-bias conditions, i.e.  $R_T \ll R_S$ , the Joule power increases with increasing temperature and the feedback is positive. When the resistances are matched ( $R_S = R_T$ ) the Joule power is independent of temperature for small signals and there is no electrothermal feedback.

There are several advantages in operating a TES in negative electrothermal feedback. The most obvious one is the increased stability against thermal runaway since the decrease in Joule power with increasing temperature acts as a restoring force. The response of a TES under voltage bias conditions will be outlined in the following.

When an event heats the sensor, the reestablishment of the equilibrium temperature is made faster by electrothermal feedback. In the small signal limit, changes of the heating power  $\Delta P_T$  can be treated as linear:

$$\Delta P_T = \frac{\partial P_T}{\partial T_e} \Delta T_e = -\alpha_{eff} \frac{P_T}{T_e} \Delta T_e, \quad (4.37)$$

where  $\alpha_{eff}$  was defined by eq. 4.36 and  $\Delta T_e$  denotes a small deviation from the steady state temperature. The return to equilibrium is then given by

$$C_e \frac{d(\Delta T_e)}{dt} + (\Delta T_e - \Delta T_a) G_{ea} + \Delta T_e G_{eb} + \alpha_{eff} \frac{P_T}{T_e} \Delta T_e = 0. \quad (4.38)$$

From this equation it becomes evident that the electrothermal feedback acts like an additional thermal coupling:

$$G_{etf} \equiv \alpha_{eff} \frac{P_T}{T_e}. \quad (4.39)$$

Ignoring the temperature rise of the absorber  $\Delta T_a$ , eq. 4.38 can then be written as

$$\frac{d(\Delta T_e)}{dt} = - \left( \frac{G_{ea} + G_{eb}}{C_e} + \frac{G_{etf}}{C_e} \right) \Delta T_e \equiv - \left( \frac{1}{\tau_{in}} + \frac{1}{\tau_{etf}} \right) \Delta T_e, \quad (4.40)$$

where  $\tau_{in}$  is the intrinsic relaxation time of the TES (eq. 4.22) and  $\tau_{etf} \equiv C_e/G_{etf}$  the relaxation time due to electrothermal feedback. The solution of this differential equation is:

$$\Delta T_e \propto \exp \left( -\frac{t}{\tau_{etf}} \right), \quad (4.41)$$

where  $\tau_{eff}$  denotes an effective relaxation time given by

$$\frac{1}{\tau_{eff}} = \frac{1}{\tau_{in}} + \frac{1}{\tau_{etf}}. \quad (4.42)$$

For a voltage-biased TES (i.e.  $\alpha_{eff} > 0$ ),  $\tau_{eff}$  is shorter than both the intrinsic time constant  $\tau_{in}$  and the relaxation time due to electrothermal feedback  $\tau_{etf}$ . The latter can be made significantly shorter than  $\tau_{in}$  by choosing large values for  $\alpha_{eff}$  and  $P_T$ .  $\alpha_{eff}$  can be adjusted via the transition steepness  $\alpha$  and by using a small shunt resistance relative to the resistance at the operating point ( $R_S \ll R_T$ ). A high Joule power dissipation  $P_T$  in the TES is obtained by cooling the bath temperature to well below the transition temperature and biasing then the TES into its transition with a high current  $I_T$ .

When the intrinsic time constant becomes much larger than the pulse duration, the system relaxation is dominated by a reduction in Joule heating instead of an increased heat flow to the heat sink. The total energy deposited in the TES is then given by [179]

$$E = \int \Delta P_T dt = V_0 \int \Delta I_T dt. \quad (4.43)$$

Here,  $\Delta P_T$  denotes the change in the Joule power and  $\Delta I_T$  the corresponding change of the current in the TES branch.  $V_0 = (I - I_T)R_S$  is the effective voltage bias of the TES. For  $R_S \ll R_T$  this voltage can be assumed to be constant for small signals since  $I - I_T \gg I_T$ . Due to the relationship given by equation 4.43, the response of the TES for  $\tau_{in} \ll \tau_{etf}$  becomes insensitive to nonlinearities in the transition and nonuniformities of the film. It furthermore increases the dynamic range as the energy is measured even if an event drives the film completely normal [179].

Even under voltage-bias conditions, the TES can become unstable due to oscillations of the system caused by the inductivity  $L$  and the heat capacity of the sensor  $C_e$  [180, 181]. These "electrothermal oscillations" occur when the intrinsic time constant  $\tau_{in}$  becomes shorter than  $\sim 5.8\tau_{el}$ , where the characteristic time constant of the readout circuit  $\tau_{el}$  is given by

$$\tau_{el} = \frac{L}{R_S + R_T}. \quad (4.44)$$

When operated in negative electrothermal feedback, electrothermal oscillations set a limit for the stabilization of the TES.

# Chapter 5

## Experimental Techniques

### 5.1 Detector Fabrication

All detectors presented in this work are based on the composite detector design (CDD), i.e. the superconducting films consisting of Ir/Au bilayers are evaporated onto small crystalline substrates which are then coupled to the absorber by gluing. Light detectors employing Neganov-Luke amplification are additionally equipped with Al electrodes which are directly evaporated onto the absorber. In this section the main experimental techniques involved in the fabrication of detectors based on this design will be described.

#### 5.1.1 Ir/Au Films

With respect to their employment as TESs, the most important properties of superconductors are their transition temperature and transition width. Because of the strong temperature dependence of heat capacities and thermal noise, low transition temperatures are needed for sensors. Here, pure materials such as tungsten can be used. Tungsten exhibits in its  $\alpha$ -phase a transition temperatures of  $\sim 10$  mK [182]. Another method is based on proximity multilayers. Here, a tunable superconductor is produced by depositing several layers of both a superconductor and a normal metal. When the layers are thinner than the superconducting coherence length and the interface between the layers is sufficiently clean, the multilayer film exhibits a reduced transition temperature compared to the pure superconductor due to the proximity effect (see e.g. [183]). This method offers the opportunity to tune the transition temperature via the relative layer thicknesses.

The films produced in this work are based on Ir/Au bilayers produced in an ultra high vacuum (UHV) system by electron beam evaporation. A photograph of this system is depicted in Fig. 5.1. The UHV system consists of two chambers (load lock and main chamber) separated by a gate valve. Samples are inserted into

## 5. Experimental Techniques

---

the system via the load lock which can be vented and pumped independently of the main chamber. Iridium and gold are evaporated in the main chamber by a *Telemark* electron beam gun (MODEL 528) [184]. During evaporation the temperature of the substrate can be controlled between  $\sim 0$ -500 °C by means of a boron nitride heater and a thermometer mounted on the substrate holder. During operation the walls of the main chamber are cooled by liquid nitrogen to freeze out the residual gas. In this way, an average pressure of  $\sim 10^{-10}$  mbar can be achieved.

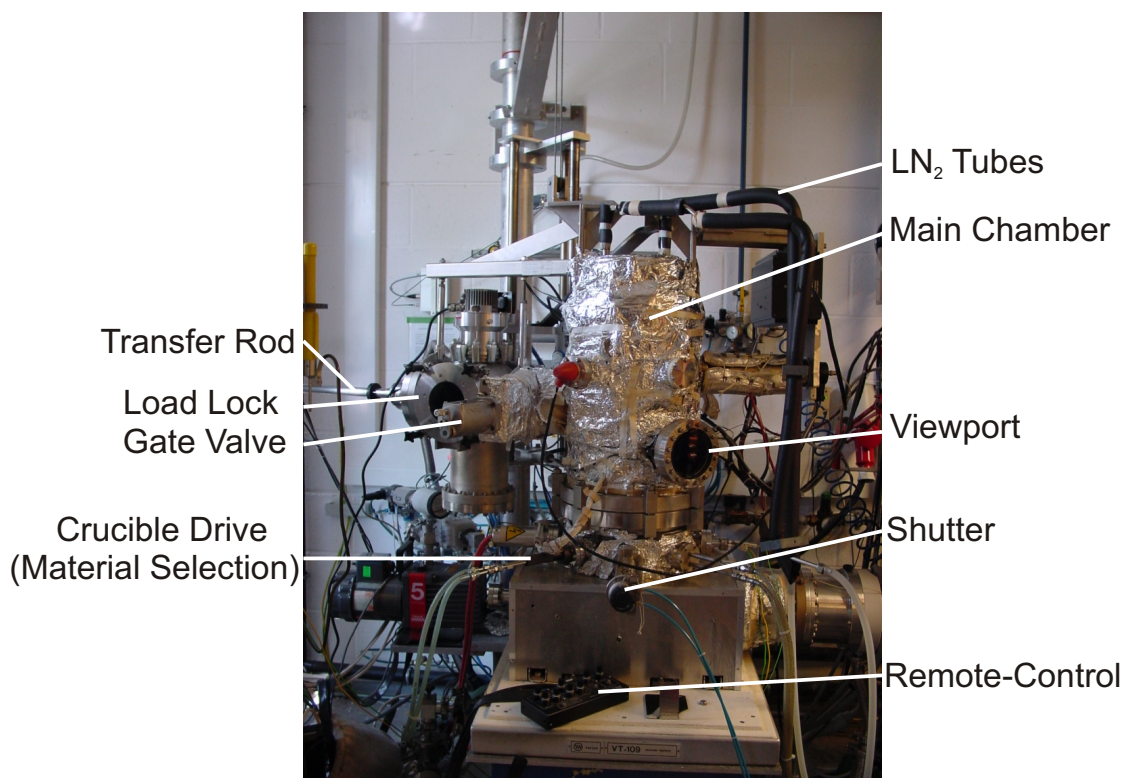


Figure 5.1: Photograph of the Ir/Au evaporation system. In the main chamber iridium and gold are deposited by electron beam evaporation. The sample is introduced into the system via the load lock separated by a gate valve from the main chamber. In this way, it can be pumped and vented independently of the main chamber.

The TESs fabricated for the composite light detectors are evaporated onto small ( $3 \times 5$  mm<sup>2</sup>) silicon substrates using a tantalum shadow mask (Fig. 5.2). In this way, 8 substrates can be evaporated simultaneously.

For proximity effect multilayers based on iridium and gold, it turns out to be favorable to deposit the iridium film on top of the gold layer. Here, an additional thin (50 Å) layer of iridium is evaporated directly onto the substrate acting as a

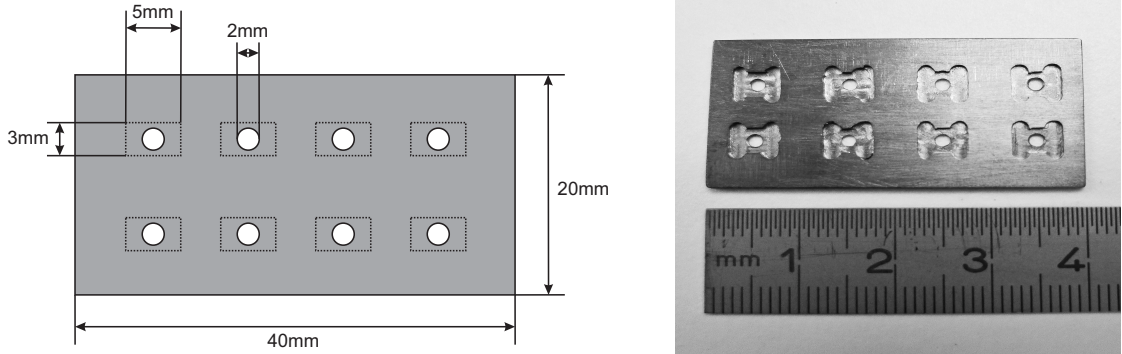


Figure 5.2: *Left Panel:* Schematic drawing of the tantalum shadow mask. It is designed for the simultaneous evaporation of eight thermometers with an area of  $3 \times 5 \text{ mm}^2$  each. *Right Panel:* Photograph of the shadow mask.

'sticking' layer. On top of this layer the Ir/Au bilayer is deposited. The transition temperature can be adjusted via the relative layer thicknesses. For all sensors produced in this work, a gold/iridium layer thickness ratio of  $80\text{\AA}/30\text{\AA}$  has been chosen. After film deposition, the sample is annealed at  $200^\circ\text{C}$  for 2 hours. In this way transition temperatures of  $\sim 30 \text{ mK}$  have routinely been achieved. The deposition parameters are summarized in table 5.1.

Layer Number	Material	Rate [ $\text{\AA}/\text{s}$ ]	Thickness [ $\text{\AA}$ ]	Temperature [ $^\circ\text{C}$ ]
1.	Iridium	0.3	10	300
2.	Gold	1.4	800	150
3.	Iridium	0.3	300	30
Annealing at $200^\circ\text{C}$ for 2 hours				

Table 5.1: Deposition parameters used for the production of Ir/Au transition edge sensors. After film deposition, the sample is annealed at  $200^\circ\text{C}$  for 2 hours.

### 5.1.2 Aluminum Electrodes

The aluminum electrodes are directly evaporated onto the absorber using a lift-off mask. This is created by a negative photolithographic process using the photoresist ma-N 420 obtained from *micro resist*[185]. Here, the following steps are involved:

- Substrate coverage with the photoresist ma-N 420 and spinning at 3000 rpm for 30 s.
- Baking the photoresist at  $100^\circ\text{C}$  for 5 min.

## 5. Experimental Techniques

---

- UV illumination of the photoresist for 120 s patterning the desired structure.
- Development of the photoresist for  $\sim 1$  min using the developer ma-D 330.
- Substrate rinsing with ultrapure water and flushing with nitrogen to dry it.

The aluminum electrodes are deposited onto the absorber by electron beam evaporation in an ultra high vacuum system. A schematical drawing of the system is depicted in Fig. 5.3. It consists of three independent vacuum chambers connected to each other by ultra high vacuum valves. The sample is inserted into the system via the load lock which has to be pumped down to  $\sim 10^{-5}$  mbar prior to opening the vacuum valves to the other chambers. The sample can then be transferred to the other chambers using the magnetic transfer devices the load lock is equipped with.

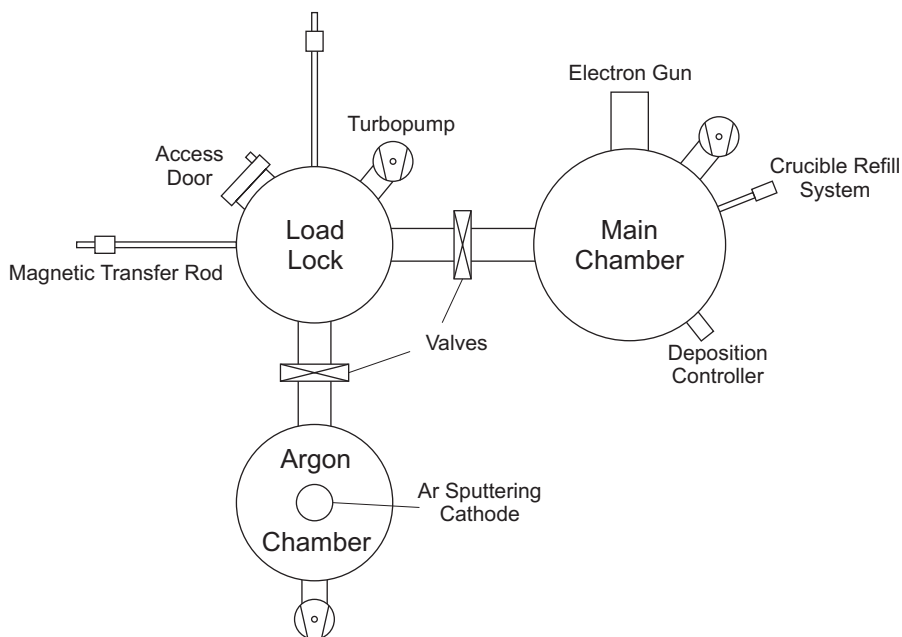


Figure 5.3: Schematic top view of the UHV system for aluminum evaporation. It consists of three chambers separated by vacuum valves: load lock, argon chamber and main chamber. The sample is inserted into the system via the load lock. From the load lock it can be transferred to the other chambers via magnetic transfer rods.

Prior to the aluminum deposition, the sample is ion-etched for roughly 90 s in an argon plasma generated by the argon sputtering cathode in the 'argon chamber'. The aluminum electrodes are finally evaporated in the main chamber that is equipped with an electron beam gun. The main chamber is operated at a pressure

of  $10^{-8}$ - $10^{-9}$  mbar. To stay evacuated for long periods of time, a refill system with a storage for several refills is employed for the crucible. During evaporation the sample can be heated via radiation by a heater installed above the substrate holder. The aluminum films are evaporated at a rate of  $\sim 10$  Å/s. The electrodes have a final thickness of 2 kÅ. After evaporation the lift off mask is removed with acetone.

## 5.2 Experimental Setup

### 5.2.1 The $^3\text{He}/^4\text{He}$ Dilution Refrigerator

The low temperatures needed for the operation of the detectors developed in this work have been provided by a  $^3\text{He}/^4\text{He}$  dilution refrigerator TLE200 manufactured by Oxford Instruments [186]. With this cryostat a base temperature of  $\sim 15$ - $20$  mK is routinely achieved. A schematical view of the refrigerator is shown in Fig. 5.4.

The cooling effect in a  $^3\text{He}/^4\text{He}$  refrigerator is based on the finite solubility of  $^3\text{He}$  in  $^4\text{He}$  at low temperatures. When a mixture of  $^3\text{He}$  and  $^4\text{He}$  with a  $^3\text{He}$  concentration exceeding 6.6% is cooled below 0.87 K, the liquid separates into a  $^4\text{He}$ - and a  $^3\text{He}$ -rich phase with the  $^3\text{He}$ -rich phase floating on top due to its lower density. If the temperature is reduced close to absolute zero, the  $^3\text{He}$ -rich phase will become pure  $^3\text{He}$  while the  $^3\text{He}$  content in the  $^4\text{He}$ -rich phase approaches a constant value of roughly 6.6 %. Since the heat capacity of  $^3\text{He}$  is higher in the dilute phase, cooling can be achieved by transferring  $^3\text{He}$  atoms from the pure to the dilute phase.

The two-phase mixture is contained in the mixing chamber that is connected via a superleak to the still which is operated at  $\sim 750$  mK (see Fig. 5.4). At this temperature the vapour pressure of  $^3\text{He}$  is significantly higher than the vapour pressure of  $^4\text{He}$  providing a way to selectively remove  $^3\text{He}$  from the still by pumping. This in turn reduces the  $^3\text{He}$  concentration in the still that is compensated by  $^3\text{He}$  from the mixing chamber driven by osmotic pressure. Since the  $^3\text{He}$  concentration in the dilute phase in the mixing chamber is constant, the  $^3\text{He}$  going to the still passes across the phase boundary providing a cooling effect. Continuous operation is achieved by circulating the  $^3\text{He}$ . Here, the  $^3\text{He}$  has to be precooled before reentering the mixing chamber. This is achieved in several steps including a  $^4\text{He}$  refrigerator (1K pot) and several heat exchangers (see Fig. 5.4). A more detailed discussion on  $^3\text{He}/^4\text{He}$  dilution refrigerators can be found in [182].

For the cooldown of the TLE 200 dilution refrigerator the following steps are involved:

- Evacuation of the inner vacuum chamber (IVC) to a pressure of  $\sim 10^{-6}$  mbar. The IVC is then filled with  $\sim 5$  mbar of He exchange gas which provides

## 5. Experimental Techniques

thermal contact between the insert of the cryostat and the liquid helium bath.

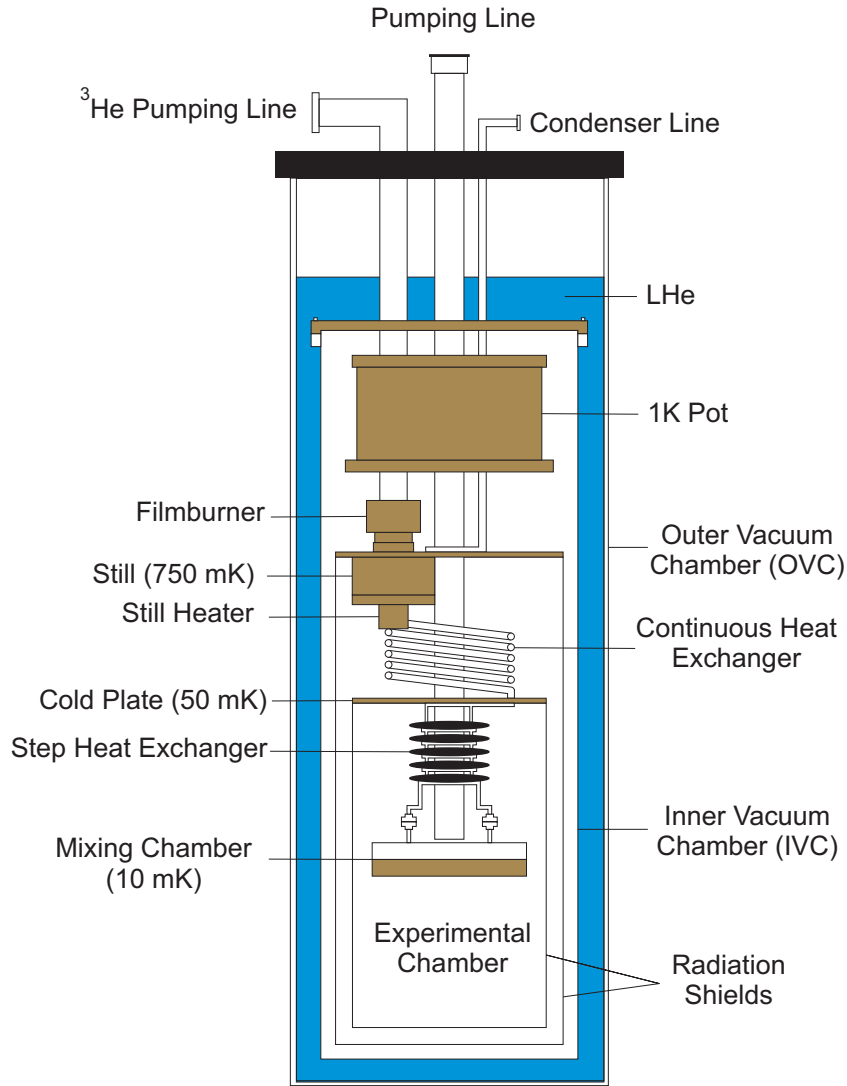


Figure 5.4: Schematic view of the  $^3\text{He}/^4\text{He}$  dilution refrigerator. In operation the mixing chamber has a temperature of  $\sim 15\text{--}20$  mK. Pumping on the 1K pot provides a temperature of  $\sim 1.4$  K at 2-4 mbar. The still temperature is about 750 mK. The temperature of the cold plate is  $\sim 50$  mK.

- Precooling with liquid nitrogen down to  $\sim 100$  K and with He gas boiled off from the liquid He storage tank from  $\sim 100$  K down to  $\sim 10$  K. The He exchange gas is then removed by pumping the IVC (down to  $\sim 10^{-6}$  mbar).

- Filling the dewar with liquid He. Pumping on the 1 K pot further reduces the temperature to  $\sim 1.4$  K.
- Condensation of the  $^3\text{He}/^4\text{He}$  mixture. In operation, the still is kept at a temperature of  $\sim 750$  mK by means of a heater mounted on the still. At this temperature  $^3\text{He}$  and  $^4\text{He}$  can be efficiently separated.

### 5.2.2 Detector Operation

The light detectors operated in this cryostat are placed on small sapphire spheres (1 mm in diameter) in annealed copper holders. For larger crystals such as  $\text{CaWO}_4$  teflon or  $\text{CuSn}_6$  clamps are used. The copper holder acts as the heat sink of the TES. A defined thermal link of the TES to the heat sink is provided by thin gold bond wires (25  $\mu\text{m}$  in diameter) connected via ultrasonic bonding. For the electrical connection of the TES either aluminum bond wires (25  $\mu\text{m}$  in diameter) or aluminum clamps can be used (see chapter 6). The holder is thermally weakly coupled to the mixing chamber via a copper wire with a  $\sim 1.5$  mm<sup>2</sup> cross section. The mechanical connection is provided by a sintimid rod whose thermal conductance can be neglected. This allows the stabilization of the copper holder above the base temperature of the mixing chamber by means of a thermometer and a heater mounted on the holder. A schematical view of the detector setup in the dilution refrigerator is depicted in Fig. 5.5.

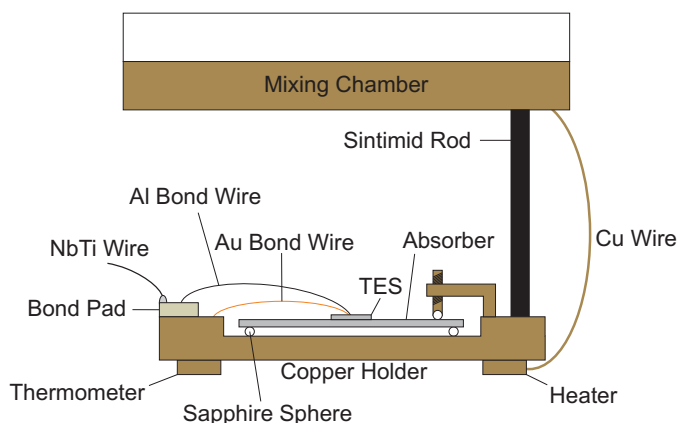


Figure 5.5: Schematic drawing of the detector setup in a  $^3\text{He}/^4\text{He}$  dilution refrigerator. The detector holder consisting of annealed copper is weakly coupled to the mixing chamber via a sintimid rod. A defined thermal link is provided by a copper wire. For temperature control, the holder is equipped with a thermometer and a heater. The detector is placed on small sapphire spheres (diameter=1 mm). Electrical and thermal connections are provided by thin aluminum and gold bond wires, respectively.

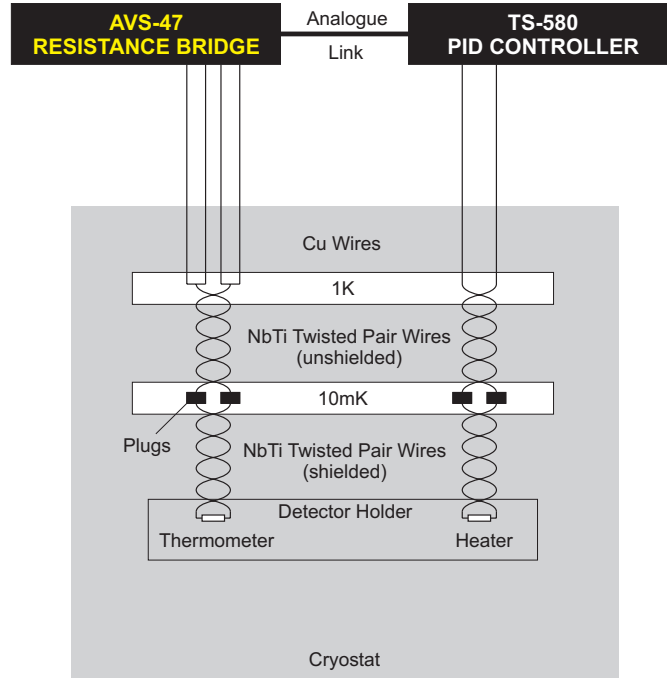


Figure 5.6: Schematical drawing of the temperature control system installed in the cryostat. The resistance of the thermometer is measured by a Picowatt AVS-47 resistance bridge. The measured value is fed as an analogue signal into a Picowatt TS-580A PID controller, which regulates the power dissipated in the heater. For the electrical connection of heater and thermometer copper wires are used down to the 1K-stage. For the lower temperature stages, superconducting NbTi twisted pair wires are employed.

Resistors of the type Speer and ruthenium oxide ( $\text{RuO}_2$ ) are used as thermometers. The resistance is measured by a Picowatt [187] AVS-47 resistance bridge. Typical thermometers have resistances ranging between 30-50  $\text{k}\Omega$  at base temperature. The measured resistance is fed as an analogue signal into a Picowatt TS-580A PID controller that regulates the power dissipated in the heater. As heater resistors, strain gages by Vishay Micro-Measurements [188] glued onto small copper plates are used. At room temperature the resistance of the gages is 120  $\Omega$ . The power dissipated is less than 1  $\mu\text{W}$  per channel. A schematical drawing of the temperature control system installed in the cryostat is shown in Fig. 5.6. Copper wiring provided by the manufacturer was used for both thermometer and heater down to the 1K stage. For the lower temperature stages superconducting NbTi twisted pair wires are employed. Plugs on the mixing chamber allow the individual connection of heaters and thermometers. In this way, wires not needed can be easily removed from the experimental chamber.

### 5.2.3 LED and High Voltage System

The high voltage needed for the operation of light detectors with Neganov-Luke amplification is provided by an *Iseg* [189] EHQ F605x.105K-F 16-channel high-voltage power supply. Each single channel is independently software controllable via a CAN interface and all channels are floating against each other and against module ground.

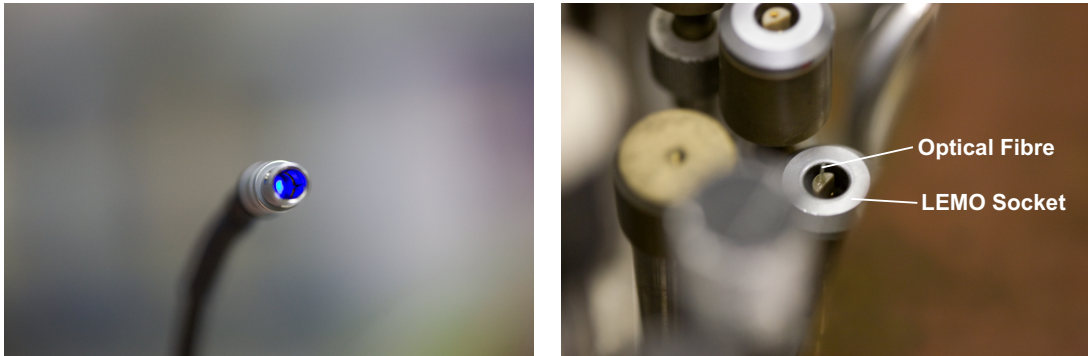


Figure 5.7: *Left Panel:* Blue InGaN LED mounted in a LEMO plug. *Right Panel:* The corresponding LEMO socket equipped with an optical fibre.

When operating a cryogenic light detector in Neganov-Luke mode two light sources with tunable intensity are needed for detector regeneration and for monitoring the pulse height drift, respectively (see chapter 6). These light sources are provided by two blue InGaN LEDs. As their light output furthermore matches the spectral output of a  $\text{CaWO}_4$  crystal ( $\lambda \sim 420\text{nm}$ ), they can also be used for detector calibration exploiting photon statistics (see chapter 6). Here, the LEDs can be operated both at room temperature and on the 4K stage of the cryostat. The light pulses are injected via optical fibres (0.5 mm in diameter) onto the Si absorber of the light detector. For room-temperature operation, the LEDs are mounted in LEMO plugs, while the optical fibres are attached to the corresponding LEMO sockets. Fig. 5.7 shows photographs of a LED mounted in a LEMO plug (left panel) and of the corresponding LEMO socket (right panel). For the operation at 4K, a light-tight copper housing attached to the 4K-stage of the cryostat is used for both LEDs. A photograph of the LEDs mounted on the 4K stage is depicted in Fig. 5.8. The optical fibres are attached to the copper coverage (not shown in Fig. 5.8).

A schematical view of the setup needed for the operation of cryogenic light detectors with Neganov-Luke amplification including the high voltage power supply, the light sources (LEDs) and a *Rohde & Schwarz* [190] AM300 dual channel waveform generator used for the activation of the LEDs is depicted in Fig. 5.9.

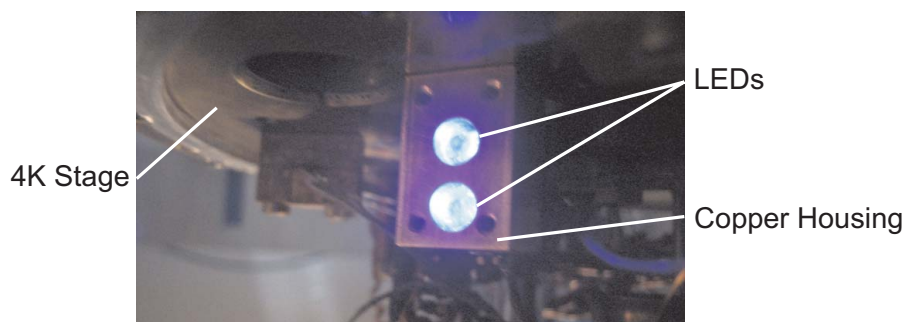


Figure 5.8: Blue InGaN LEDs mounted in a copper block attached to the 4K stage of the cryostat.

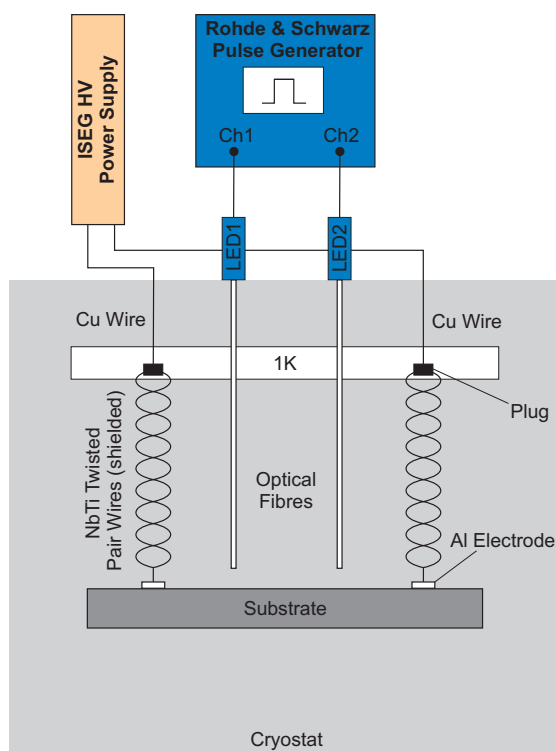


Figure 5.9: Schematic view of the setup needed for light detectors operated in Neganov-Luke mode. The voltage is provided by an *Iseg* high-voltage power supply. The InGaN LEDs are operated at room temperature or at 4K and light pulses are injected via optical fibres into the cryostat. The LEDs are activated by a dual channel *Rhode & Schwarz* pulse generator.

The high-voltage wires down to the 1K stage in the cryostat are copper wires provided by the manufacturer. For the lower temperature stages shielded twisted

pair NbTi wires are employed, which are connected via plugs to the copper lines on the 1K stage. For each channel, two twisted-pair wires are used.

### 5.2.4 Read-Out Electronics

The TESs developed in this work exhibit resistances ranging up to  $\sim 100$  m $\Omega$  which are too low to match the impedance of conventional preamplifier readout electronics with field-effect transistor (FET) input stages. The detection of the small particle-induced changes of the TES resistance is therefore based on Superconducting Quantum Interference Devices (SQUIDs) which are low-impedance devices and very sensitive to small variations of magnetic fields. By means of an input coil connected in series with the TES (see Fig. 4.6), small changes of the TES bias current are translated into magnetic field variations which are then converted into a voltage by the SQUID.

Due to the Josephson effect, the DC voltage across the device depends periodically on the magnetic flux across the input coil of the SQUID, where the period is given by one flux quantum  $\Phi_0 = h/2e \approx 2.07 \times 10^{-15}$  Vs [173]. To enhance the dynamic range and to linearize the response of the SQUID, an additional feedback coil is used to compensate the magnetic field in the input coil. This mode is referred to as the Flux-Locked-Loop (FLL) mode. Fig. 5.10 shows the schematic of the FLL unit of one of the SQUIDs installed in the cryostat.

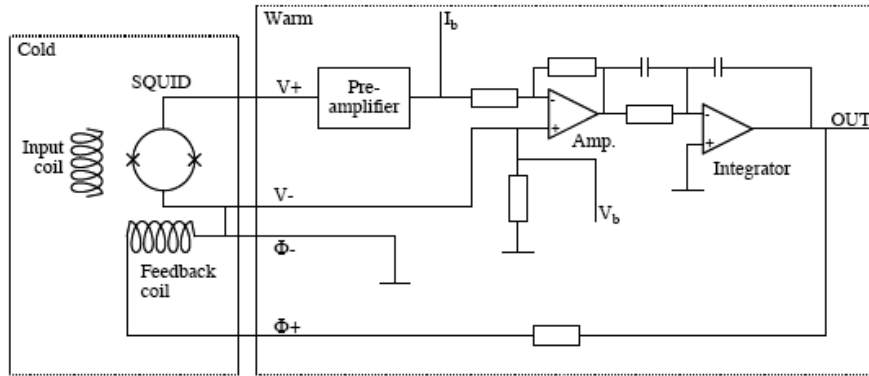


Figure 5.10: Schematic of the FLL unit of the Supracon SQUID. The input coil is connected in series with the TES. The SQUID is biased with a constant current  $I_b$ . Changes of the magnetic flux alter the voltage across the SQUID. These voltage deviations from the equilibrium voltage  $V_b$  are then amplified and integrated providing the output signals. In the FLL mode, the integrated output signal is sent back to the feedback coil. Figure taken from [151].

## 5. Experimental Techniques

In this work two different SQUID systems have been used: one manufactured by Supracon [191] and one by Applied Physics Systems [192]. In table 5.2 the selectable amplifications of both SQUIDs together with the shunt resistors  $R_S$  are listed.

SQUID	Shunt Resistor $R_S$ [ $m\Omega$ ]	Amplification
Applied Physics	30.0	$4.5 \cdot 10^4$ , $4.5 \cdot 10^5$ , $4.5 \cdot 10^6$ , $4.5 \cdot 10^7$
Supracon	56.7	$1.0 \cdot 10^5$ , $10.1 \cdot 10^5$ , $20.1 \cdot 10^5$ , $49.7 \cdot 10^5$

Table 5.2: SQUIDs installed in the TLE200 dilution refrigerator together with the main parameters relevant for data acquisition.

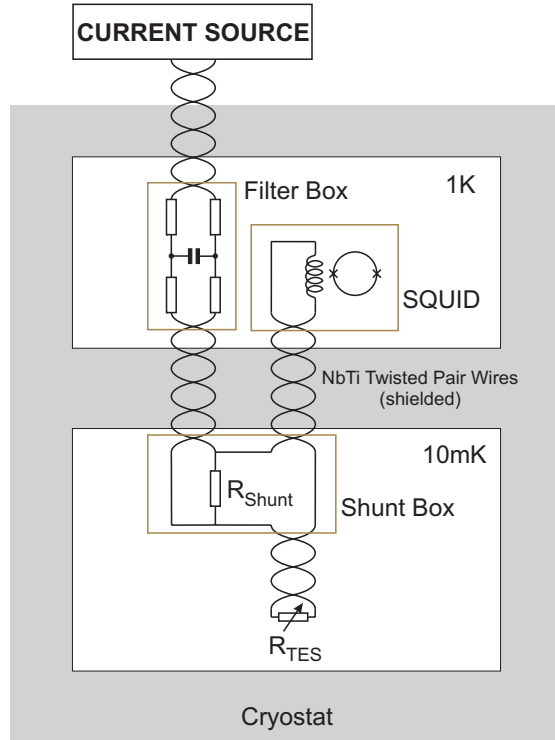


Figure 5.11: Schematic of the readout system in the TLE200 dilution refrigerator. The wiring is provided by shielded twisted pair NbTi wires. The SQUIDs are mounted on the 1K stage together with the filter box housing a symmetrical lowpass filter with a 3dB cutoff frequency of  $\sim 30$  kHz installed in the bias current line. The bias current of the detector is provided by a floating point current source operated at room temperature. The shunt resistor is mounted in a copper box on the mixing chamber.

A schematical drawing of the readout system in the cryostat is depicted in Fig. 5.11. Both SQUIDs are mounted on the 1K stage of the cryostat. The shunt resistors are mounted on the mixing chamber. To minimize electromagnetic interference, they are enclosed in a copper box ('Shunt Box'). The entire wiring is provided by shielded twisted pair NbTi wires thermally coupled to the different temperature stages of the cryostat in order to reduce thermal load on the mixing chamber. The constant current bias is provided by a custom-made floating-point current source operated at room temperature. It provides continuously adjustable bias currents in the range between few nA up to 10 mA. In the bias current line a symmetrical lowpass filter is installed in a copper box on the 1K stage of the cryostat. The 3dB cutoff frequency of the filter is  $\sim 30$  kHz.

### 5.2.5 Data Acquisition (DAQ)

The DAQ system is based on a PXI-Bus system with a controller type 8186 from National Instruments [193]. The controller is based on Windows XP and is equipped with a 40 GByte hard disk. For DAQ two National Instruments ADC (analogue-to-digital converter) cards are used. The 16 bit PXI-6250 card is equipped with 16 multiplexed channels. The maximum sampling rate is 1 MS/sec (1 million samples per second). This card is mainly used as a digital voltmeter, e.g. for temperature measurements. Detector pulses are recorded by a second 12 bit PXI-6115 card with a maximum sampling rate of 10 MS/sec. Each of the four channels of this card is equipped with its own ADC.

The trigger module is based on a PXI prototyping board of the PX2000-107 type from PXIT. The board provides the basic interface to the PXI bus. On the board an additional custom circuit consisting of a simple trigger logic has been added. It is equipped with four input and two output channels - one with an AND gate and one with an OR gate. All settings of the module, including the coupling (AC or DC) and the trigger level are performed via the on-board computer interface with a LabView-based program.

The DAQ system is mainly used for recording detector events and superconducting transitions. The different acquisition schemes and the corresponding settings of the DAQ system will be described in the following.

#### 5.2.5.1 Recording Superconducting Transitions

The temperature and the steepness (i.e. the width) of the superconducting transition of a TES are crucial parameters for the performance of the detector. Therefore, for an accurate characterization of the TES the superconducting transition is measured. The typical setup used in most transition measurements is depicted in Fig. 5.12.

## 5. Experimental Techniques

A rough estimation of the transition temperature range is obtained by varying the holder temperature manually via the TS-580 PID controller while applying a sine wave (or an arbitrary time varying signal) to the detector. The time varying signal is needed to monitor the detector response since the SQUID is only sensitive to changes of the magnetic flux. Once the transition temperature is known, the bath temperature can be slowly ( $\sim 10$  mK/hour) swept through the temperature range of interest. The temperature sweep is controlled by LabView-based software via the GPIB interface of the PXI controller. The temperature of the holder is measured by the AVS-47 resistance bridge and recorded by the 6250 ADC card.

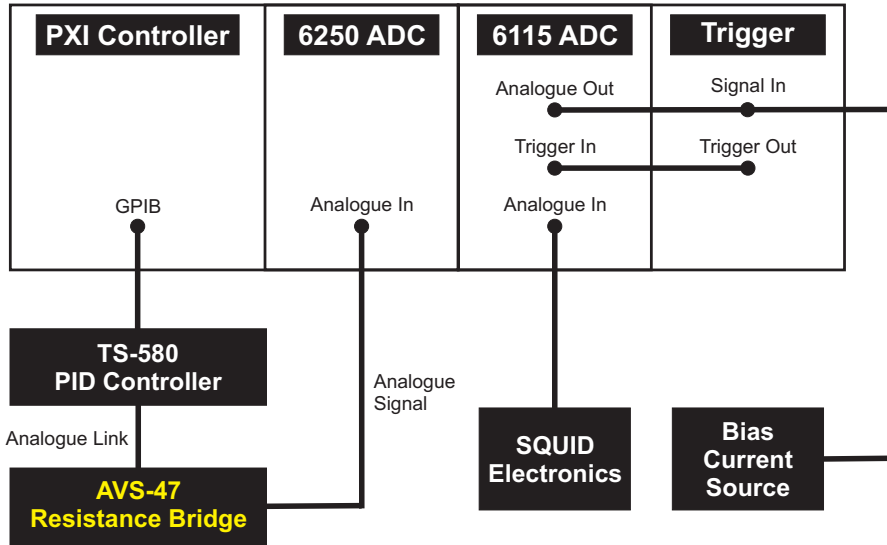


Figure 5.12: Setup used for the acquisition of superconducting transitions. The bath temperature is varied by the TS-580 controlled via the GPIB interface. The temperature is recorded by the 6250 ADC card. Voltage steps provided by the analogue output of the 6115 ADC card are converted by the bias current source into current steps which are injected into the detector bias line. The voltage steps provide the trigger for the acquisition of the detector response by the 6115 ADC card.

The response of the TES is monitored by injecting current steps of height  $I_0$  and alternating polarity into the bias current line. This induces a current change  $\Delta I_T$  in the TES branch (see Fig. 4.6) and the resistance  $R_T$  of the TES can be determined from

$$R_T = R_S \left( \frac{2I_0}{\Delta I_T} - 1 \right), \quad (5.1)$$

where  $R_S$  is the shunt resistor connected in parallel to the TES and the SQUID input coil (see Fig. 4.6). The current steps are generated via the analogue output

of the 6115 ADC card. This provides voltage steps of alternating polarity which are fed into the external voltage input of the current source, where they are converted into current steps. In most measurements a pulse height  $I_0=1\mu\text{A}$  is chosen. The voltage steps provide, furthermore, the trigger signal for the acquisition of the detector response by the PXI-6115 ADC card.

### 5.2.5.2 Recording Detector Events

When operating a cryogenic detector, a constant bath temperature is required. In our setup, the copper holder of the detector acts as the heat bath. Its temperature is controlled by the TS-580 PID controller and the AVS-47 resistance bridge via a thermometer and a heater mounted on the holder. Here, the temperature setpoint is selected manually.

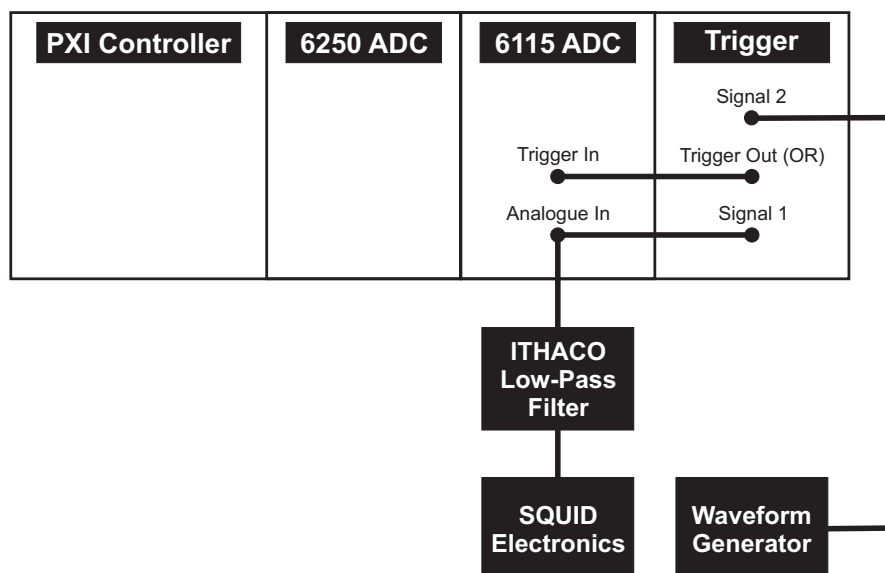


Figure 5.13: Schematical view of the setup of the DAQ system for recording detector events. Triggering is performed on the detector pulses and on TTL pulses injected by a waveform generator at a frequency of  $\sim 0.5$  Hz. In this way, additional noise samples can be recorded, which are needed for an estimation of the detector threshold. To prevent aliasing an ITHACO low-pass filter is used to filter the analogue signal from the SQUID electronics.

A schematical view of the setup of the DAQ system used for the acquisition of detector events is depicted in Fig. 5.13. In this scheme, triggering is performed on the pulses. Therefore, the analogue output of the SQUID electronics is fed into both the trigger input and the analogue input of the PXI-6115 ADC card.

The trigger is operated in AC mode, while the ADC channels are operated in DC mode to monitor the stability of the detector for a given working point. Prior to recording detector events, the analogue signal is filtered by a Bessel low-pass filter to prevent aliasing. The typical cutoff frequency is chosen to be 1/4 of the sampling frequency.

For an estimation of the detector threshold additional noise samples are acquired by a random trigger provided by TTL pulses fed into the second trigger channel at a frequency of  $\sim 0.5$  Hz. Using the OR logic of the trigger card both noise samples and detector pulses can be recorded in this way. More details on the DAQ system can be found in [151].

# Chapter 6

## Results and Discussion

### 6.1 Composite Light Detectors with Neganov-Luke Amplification

All cryogenic light detectors developed in this work employ semiconducting absorbers consisting of high-purity germanium or silicon single crystals. Like all real crystals they contain various types of imperfections which might have great influence on both the phonon and the electrical properties of the semiconductor. These imperfections include both structural and chemical defects.

The structural defects present in a semiconductor can be roughly classified as point defects, line defects and surface defects. Due to the low penetration depth ( $\sim 1 \mu\text{m}$ ) of optical photons in semiconductors, especially surface defects can have great influence on the mobility and the recombination of excess electrons and holes generated by photo-absorption. In covalent semiconductors, such as germanium and silicon, surface defects consist mainly of vacancies leaving unsaturated bonds at the neighbouring atoms. These unsaturated bonds tend to capture electrons from the valence band giving rise to localized acceptor states in the band gap. Other structural defects are easily introduced in manufacturing processes. One such process involved in the fabrication of transition edge sensors with phonon collectors is the structuring of Ir/Au films. This process is based on ion etching in an argon sputtering system, where surface defects are very likely to be introduced by the high energetic argon ions [194].

Chemical defects consist of foreign atoms in substitutional and interstitial sites which introduce localized levels in the energy gap. According to the electronic configuration of these atoms they are able to become ionized acting either as donors or acceptors. For silicon and germanium, many elements are known to introduce impurity levels in the energy gap. With respect to the Ir/Au bilayers used here as TESs, gold plays a crucial role, since it introduces deep levels located at the center

of the bandgap [195], acting therefore as efficient traps.

To avoid the introduction of both chemical and surface defects, the detectors developed in this work are based on the composite design [160, 161], i.e. the Ir/Au bilayers are evaporated onto small crystalline substrates which are then coupled to the absorber by gluing. Furthermore, this design offers the opportunity to test the TES prior to detector fabrication. With respect to light detectors with Neganov-Luke (NL) amplification (see section 4.2 and subsection 6.2.3) the TES can also be electrically decoupled from the drift device (absorber) reducing electromagnetic interference.

## 6.2 Light Detector Si518

### 6.2.1 Setup

The setup of the light detector Si518 with NL amplification is depicted in Fig. 6.1.

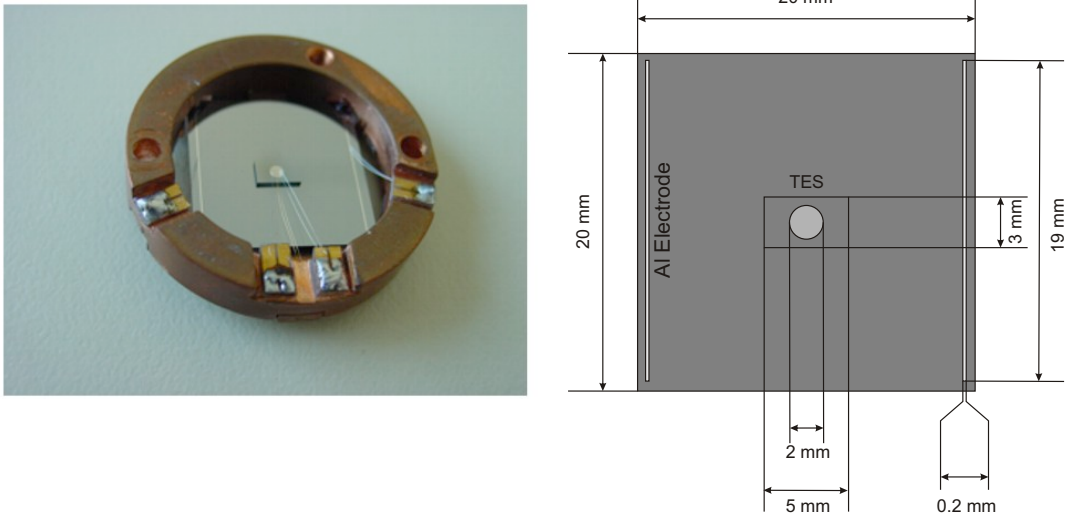


Figure 6.1: *Left panel:* Photograph of the composite light detector Si518 mounted in a copper holder. *Right panel:* Schematic view of the composite light detector Si518. It consists of a  $20 \times 20 \times 0.5 \text{ mm}^3$  silicon absorber and a small  $(3 \times 5 \times 0.5 \text{ mm}^3)$  Si substrate carrying the Ir/Au TES. The thermometer is coupled to the absorber by gluing. The absorber is equipped with two  $(19 \times 0.2) \text{ mm}^2$  Al electrodes for the application of the NL voltage.

The TES ( $\sim 2 \text{ mm}$  in diameter) is evaporated onto a small  $(3 \times 5 \times 0.5 \text{ mm}^3)$  Si substrate using a tantalum shadow mask (see chapter 5). The absorber is a  $20 \times 20 \times 0.5$

mm<sup>3</sup> Si disk with a room-temperature resistivity of  $>10$  k $\Omega$ cm. The Si substrates used here have been bought from *CrysTec* [196]. The small substrate carrying the TES is attached to the absorber using a special cryo-resin (EPO-TEK 301-2) from *EPO-TEK* [197]. For the application of the Neganov-Luke voltage, the absorber is equipped with two aluminum electrodes ( $19 \times 0.2$  mm<sup>2</sup>) directly evaporated onto the Si absorber. The thickness of the electrodes is  $\sim 2$  k $\text{Å}$ .

### 6.2.2 Calibration

In this section the different techniques used for the calibration of the light detector will be presented. Different sources have been employed: <sup>55</sup>Fe (Mn X-rays), light from LEDs and the scintillation light emitted by a CaWO<sub>4</sub> crystal excited by external sources. A typical setup is depicted in Fig. 6.2. Here, the light detector (2) is attached to a CaWO<sub>4</sub> crystal which is mounted in a reflective housing (1). The <sup>55</sup>Fe source (4) and the optical fibre (3) needed for the injection of the light pulses from the LED are positioned below the light detector.

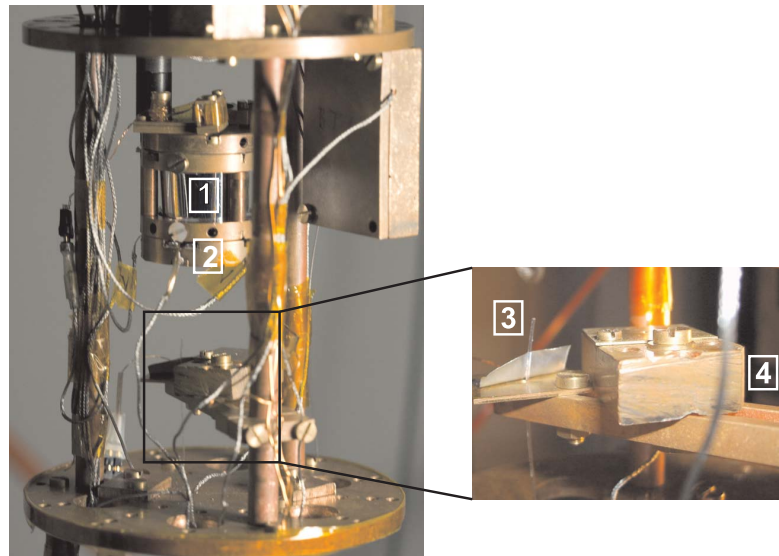


Figure 6.2: Photograph of a detector module mounted in the cryostat showing the reflective housing (1) containing the CaWO<sub>4</sub> crystal, the light detector (2) with Neganov-Luke amplification, the fiber optics (3) and the <sup>55</sup>Fe source (4).

#### 6.2.2.1 Search for the Optimal Working Point

Transition edge sensors benefit from the fact that being operated in electrothermal feedback they self-stabilize in the transition leading to an improved performance.

The TES is operated in a mode where the bath temperature  $T_{\text{Bath}}$  is stabilized slightly below the transition temperature  $T_c$  whereas the TES is biased at its superconducting transition by a DC current  $I_{\text{Bias}}$ . This means, however, that there is a wide  $T_{\text{Bath}}-I_{\text{Bias}}$  parameter space that strongly affects the performance of the detector.

In order to find the optimal working point a new method has been developed to probe the  $T_{\text{Bath}}-I_{\text{Bias}}$  parameter space. For this procedure a well-defined energy input (reference signal) into the TES is needed and the response of the sensor has to be monitored while continuously varying the bath temperature and the bias current. This reference signal can be provided by heater pulses directly injected into the TES or by any other source with a defined energy. Here a pulsed blue LED (s. subsect. 6.2.2.3) was employed (pulse frequency  $f \sim 11$  Hz, pulse duration  $\tau_{\text{pulse}} \sim 3 \mu\text{s}$ ). It is also suitable for the optimization of the working point of a Neganov-Luke amplified signal since the energy is deposited in the absorber that acts as a drift device.

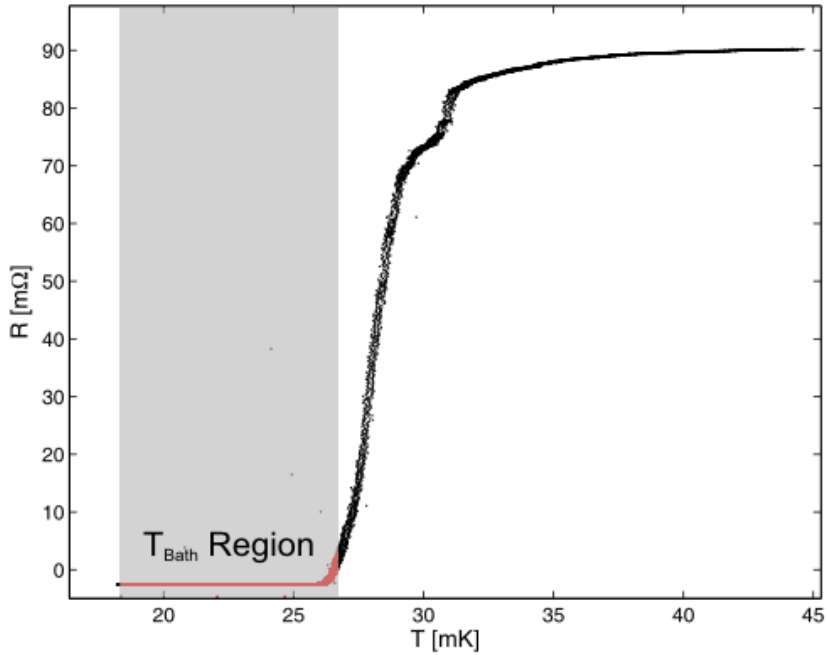


Figure 6.3: Superconducting transition curve of the light detector Si518 recorded with  $I_{\text{Bias}}=1 \mu\text{A}$ . The transition temperature  $T_c$  is at  $\sim 30$  mK. The transition width is  $\sim 4$  mK. The shaded area represents the region of the bath temperature used to find the optimal working point.

In the following the principle of this procedure will be illustrated on the basis of

the light detector Si518. Its transition curve recorded with a current of  $I_{\text{Bias}}=1 \mu\text{A}$  is depicted in Fig. 6.3. The shaded area between  $\sim 18$  and  $\sim 27$  mK marks the region the bath temperature  $T_{\text{Bath}}$  was swept with a period of  $\sim 4.5$  h to find the optimal working point. The lower bound of this region is mainly set by the base temperature of the cryostat of  $\sim 16$  mK. While sweeping the bath temperature, a triangular signal with a frequency of 2 mHz was applied to the TES, thus varying the bias current between 0-150  $\mu\text{A}$ . With these slow variations of the bath temperature  $T_{\text{Bath}}$  and the bias current  $I_{\text{Bias}}$ , the working point of the TES was well-defined for each recorded light pulse.

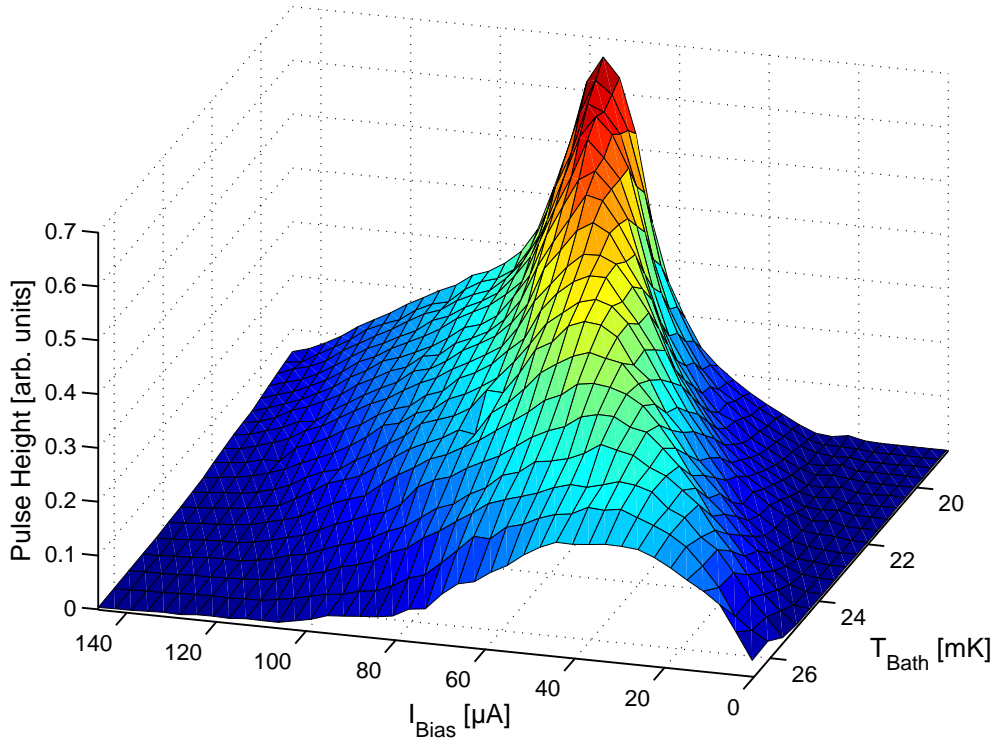


Figure 6.4: Surface plot showing the dependence of the detector response (pulse height) on bath temperature  $T_{\text{Bath}}$  and bias current  $I_{\text{Bias}}$ . A fixed energy input was provided by a pulsed LED.

For recording the light pulses, a trigger signal was provided by an external trigger output of the pulse generator. In this way samples could be recorded even if the TES was outside its transition. For each pulse, both the bath temperature  $T_{\text{Bath}}$  and the bias current  $I_{\text{Bias}}$  were recorded acquiring 1024 samples for each

pair  $(T_{\text{Bath}}, I_{\text{Bias}})$ .  $T_{\text{Bath}}$  and  $I_{\text{Bias}}$  were determined by taking the average of these samples which helped eliminating the influence of bit noise. For the acquisition of the light pulses a 1 kHz Bessel filter was used to prevent aliasing. The pulse height of the light pulses was determined by a template-fit procedure [151]. In order to find the optimal working point the  $T_{\text{Bath}}-I_{\text{Bias}}$  plain has been segmented into  $18 \times 40$  bins. For each bin the average of the pulse heights of the light pulses was calculated. A surface plot showing the dependence of the pulse height on bath temperature and bias current is depicted in Fig. 6.4. The corresponding contour plot is shown in Fig. 6.5.

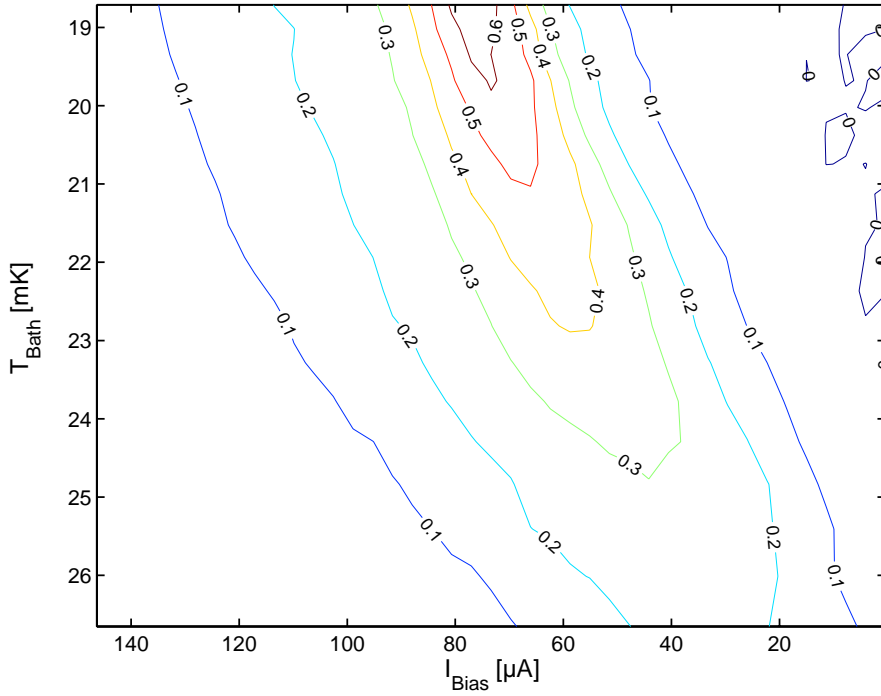


Figure 6.5: Contour plot showing the dependence of the pulse height on the bath temperature  $T_{\text{Bath}}$  and the bias current  $I_{\text{Bias}}$ . This contour plot corresponds to the surface plot depicted in Fig. 6.4.

To investigate the dependence of the pulse height on the bias current, the bath temperature was stabilized at  $\sim 19$  mK while  $I_{\text{Bias}}$  was swept between  $\sim 0-190$   $\mu\text{A}$  (Fig. 6.6, top panel). The asymmetry of the observed pulse height with respect to the alternating bias current results from non-linearities in the superconducting transition and different voltage-bias conditions associated with the varying resistance of the TES (see chapter 4). A maximum of the pulse height has been obtained for a bias current of  $I_{\text{Bias}} \sim 80$   $\mu\text{A}$  (Fig. 6.6, bottom panel).

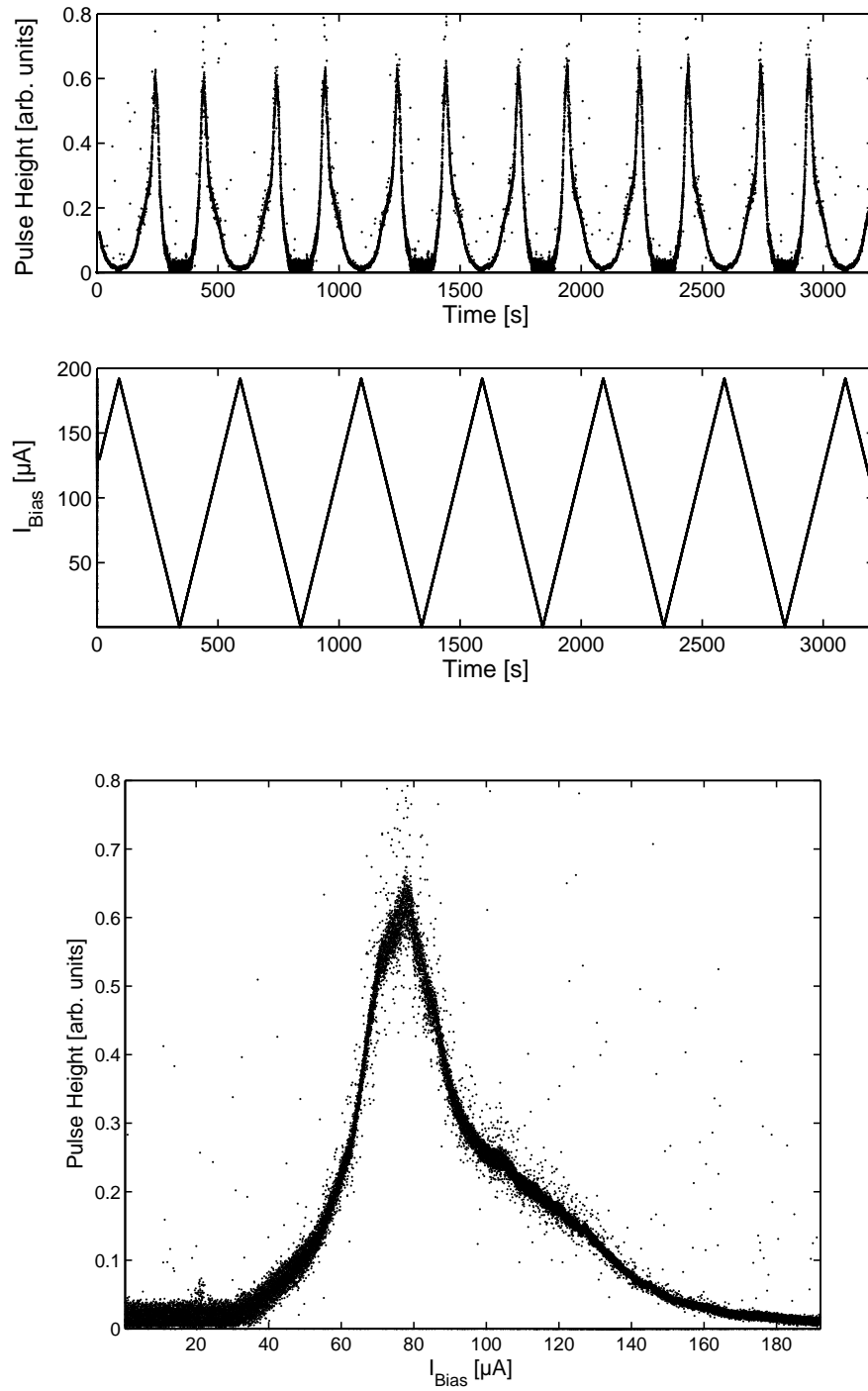


Figure 6.6: *Top*: Variation of the pulse height with  $I_{\text{Bias}}$  while the bath temperature was held constant at  $\sim 19$  mK. *Bottom*: Dependence of the pulse height on the bias current at  $T_{\text{Bath}} \sim 19$  mK.

A possible drawback of this procedure is that only the pulse height is monitored. An optimal working point, however, is characterized by an optimal signal-to-noise ratio (S/N) which is difficult to monitor in this way since only few pulses are acquired for a given  $T_{\text{Bath}}-I_{\text{Bias}}$  parameter set and no noise samples are recorded. This procedure, however, allows an estimation of the optimal base temperature which is assumed to be found at the maximal pulse height.

### 6.2.2.2 Calibration with $^{55}\text{Fe}$

For a further optimization of S/N a  $^{55}\text{Fe}$  source was used. The bath temperature was stabilized at  $\sim 19$  mK while varying the bias current between 70-140  $\mu\text{A}$  in decimal steps and recording for each bias current 5000 pulses provided by a  $^{55}\text{Fe}$  source. For the estimation of S/N, pretrigger samples were used to determine the width of the baseline. The dependence of S/N on the bias current between 70-140  $\mu\text{A}$  at  $T_{\text{Bath}} \sim 19$  mK is depicted in Fig. 6.7.

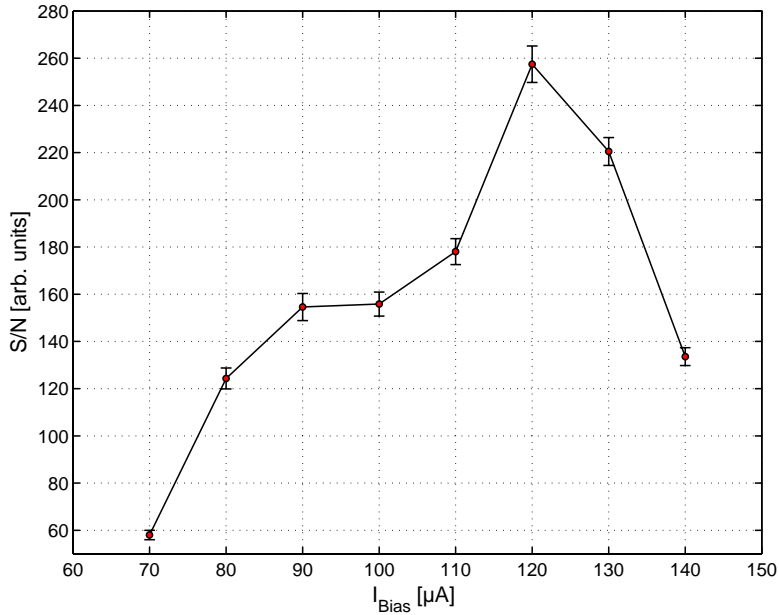


Figure 6.7: Dependence of the signal-to-noise ratio (S/N) on the bias current at  $T_{\text{Bath}} \sim 19$  mK. The error bars correspond to the  $2\sigma$  error (95% C.L.).

Even though the pulse height is maximal at  $I_{\text{Bias}} \sim 80 \mu\text{A}$ , the best S/N is achieved with a current of  $\sim 120 \mu\text{A}$ . This effect can be explained in terms of negative electrothermal feedback (ETF). A TES is operated in this mode when it is voltage biased, i.e.  $R_S \ll R_T$  (s. chapt. 4), where  $R_S$  denotes the shunt resistance and

$R_T$  the resistance of the TES at the working point. By increasing the bias current from  $80 \mu\text{A}$  to  $120 \mu\text{A}$ , the resistance of the TES rises too (since the TES is operated in its transition), providing more efficient voltage bias conditions (see subsection 4.3.2) of the TES leading to a significant improvement of the noise level. This overcompensates the loss in pulse height leading to a net improvement of the signal-to-noise ratio (S/N) by a factor of  $\sim 2$  (s. Fig. 6.7). Fig. 6.8 shows two Mn- $K_\alpha$  pulses acquired with bias currents of  $80 \mu\text{A}$  and  $120 \mu\text{A}$  as well as the noise spectra obtained by averaging the current spectral densities (see Appendix B) of 1000 noise samples recorded at both working points.

Since the performance of a transition edge sensor is mainly determined by electrothermal feedback (see subsection 4.3.2), a good working point can be found by stabilizing the bath temperature well below the transition temperature and varying the bias current over a wide range in small steps. For a given bias current a few thousands of pulses and noise samples have to be recorded in order to determine the corresponding signal-to-noise ratio. For this purpose a pulsed LED is more suitable than a  $^{55}\text{Fe}$  source since the pulse period can be adjusted for a quick scan of the relevant bias-current range.

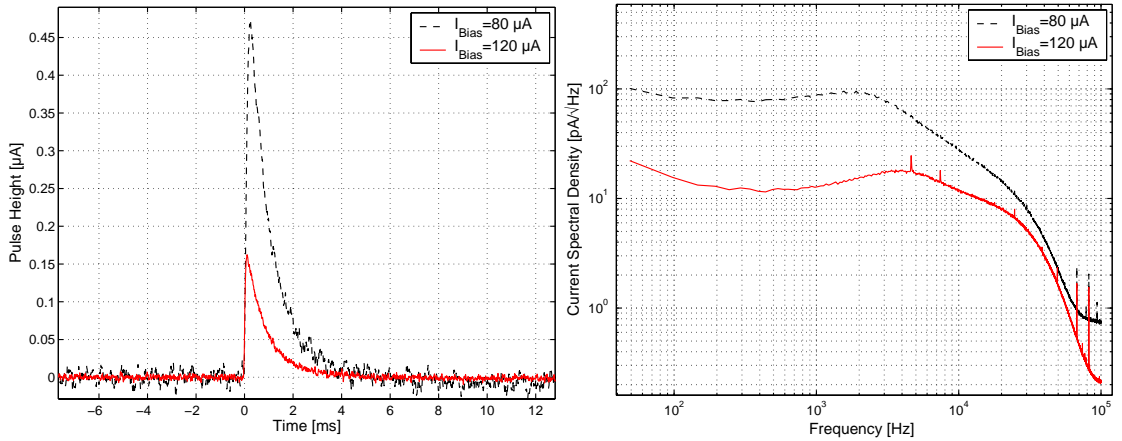


Figure 6.8: *Left panel:* Mn- $K_\alpha$  pulses acquired with bias currents of  $80 \mu\text{A}$  and  $120 \mu\text{A}$ . *Right panel:* Averaged current spectral densities obtained from noise samples recorded at  $80 \mu\text{A}$  and  $120 \mu\text{A}$ .

In Fig. 6.9 the averaged current spectral densities obtained from 1000 Mn- $K_\alpha$  events and noise samples are shown. The samples with a record length of 4096 channels have been acquired at a sampling rate of  $F_S=200 \text{ kHz}$  using a Bessel filter with a cutoff frequency of  $50 \text{ kHz}$  as an anti-aliasing filter. The highest frequency that can be acquired at this sampling rate is  $(F_S/2)-(F_S/4096)=99951.2 \text{ Hz}$  [198], whereas the lowest frequency is given by  $F_S/4096=48.8 \text{ Hz}$  [198]. From Fig. 6.9 it becomes evident that the entire information of a pulse is contained in the frequency

## 6. Results and Discussion

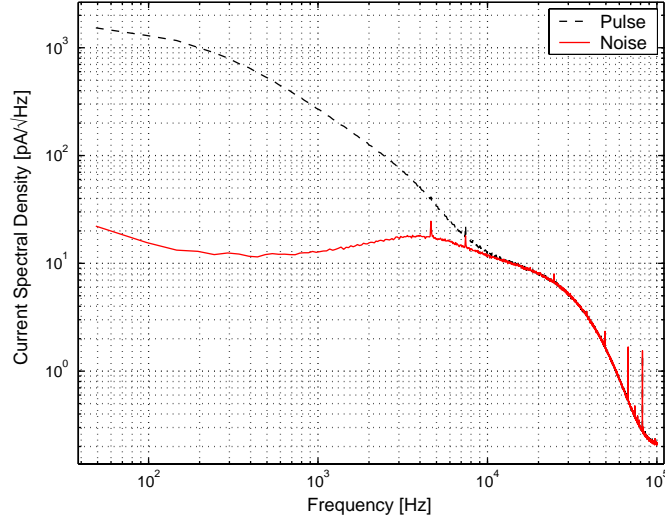


Figure 6.9: Averaged current spectral densities calculated from noise and pulse samples ( $T_{\text{Bath}} \sim 19$  mK,  $I_{\text{Bias}}=120$   $\mu\text{A}$ ).

region below  $\sim 10$  kHz. Above this frequency, the signal is dominated by noise. Below 10 kHz, the current spectral density at  $I_{\text{Bias}}=80$   $\mu\text{A}$  is roughly one order of magnitude higher than at  $I_{\text{Bias}}=120$   $\mu\text{A}$  (Fig. 6.8, *right panel*) which explains the better performance at the higher bias current.

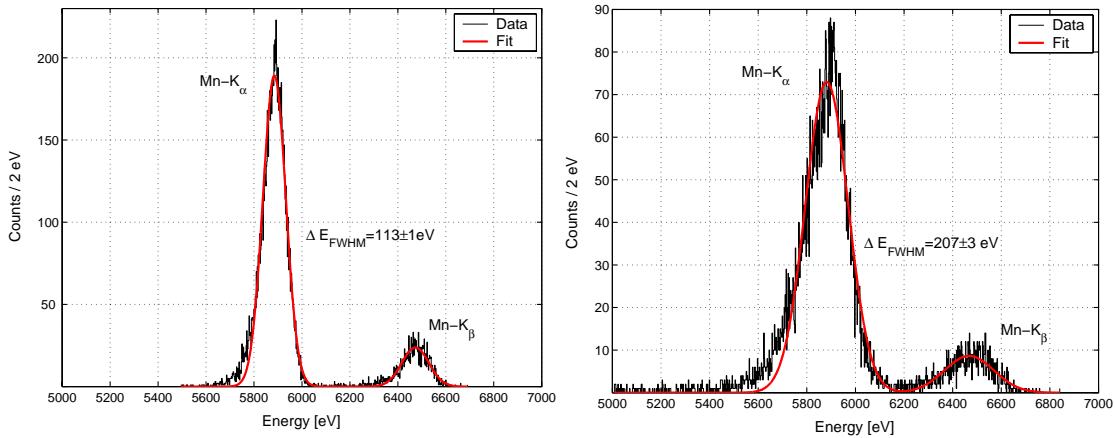


Figure 6.10: Histogram of the Mn- $K_{\alpha}$  (5.9 keV) and Mn- $K_{\beta}$  (6.4 keV) lines of a  $^{55}\text{Fe}$  source with (*left panel*) and without (*right panel*) aperture.

The spectra obtained from  $^{55}\text{Fe}$  irradiation of the light detector with and without a 1 mm aperture are shown in Fig. 6.10. The amplitudes of the pulses are determined

in off-line analysis by fitting the pulses with a template obtained from averaged good pulses. The resolution of the Mn-K lines has been obtained from a fit with two Gaussians yielding a FWHM energy resolution at 5.9 keV of 113 eV (with aperture) and 207 eV (no aperture). Although the spectrum using the aperture was acquired at a slightly different working point, this significant difference can be mainly ascribed to a position dependence of the light detector response caused by the large surface-to-volume ratio of the absorber. This causes a high surface scattering rate of non-thermal phonons and therefore an increased down-conversion rate (see section 4.2.2) due to the higher defect density expected at the surface. Since the number of surface scattering events varies with the event position on the absorber, a deterioration of the energy resolution is expected.

To estimate the energy threshold of the light detector, noise samples have been acquired by a random trigger. Fig. 6.11 shows the amplitude histogram obtained by fitting these noise samples with the template pulse. The FWHM of the noise peak is  $\Delta E_{\text{FWHM}}=37.6$  eV corresponding to a  $5\sigma$  threshold of  $\Delta E_{5\sigma}=80$  eV, where  $\Delta E_{5\sigma}$  is given by

$$\Delta E_{5\sigma} = \frac{5\Delta E_{\text{FWHM}}}{2\sqrt{2 \ln 2}} \approx 2.12\Delta E_{\text{FWHM}}. \quad (6.1)$$

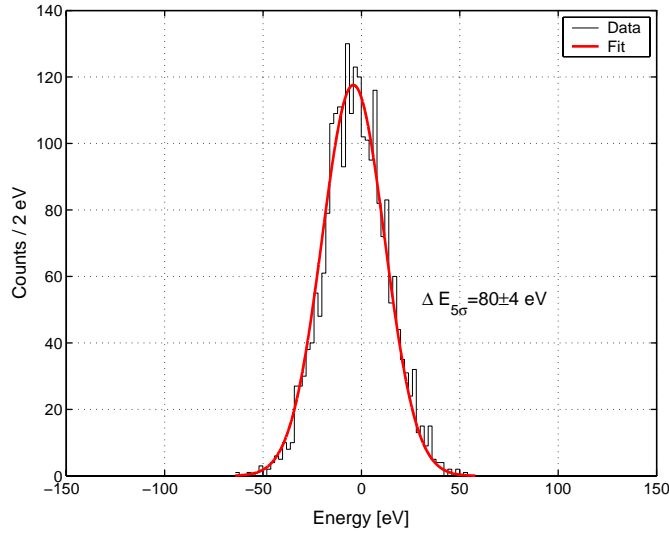


Figure 6.11: Histogram of the amplitudes obtained by template fitting of the noise samples.

This energy threshold defines the smallest signal that can be discriminated from noise in an off-line analysis by a template fit. This definition of the energy thresh-

old, however, is only valid if the trigger information is provided by other sources. In the phonon-light detection scheme (see subsection 2.5.3.2), a cryogenic light detector is always operated in coincidence with a phonon signal generated at the same time as the light signal. This phonon signal usually provides the trigger information. Therefore, the  $5\sigma$  width of the noise peak obtained for light detectors in off-line analysis can indeed be considered as their relevant energy threshold.

### 6.2.2.3 Calibration with Light

The main advantage using  $^{55}\text{Fe}$  sources for the calibration of light detectors arises from the well-defined energy of the X-ray photon. Assuming, however, that only about 1% of the energy deposited in a  $\text{CaWO}_4$  crystal is detected as light the energy deposited by a 6 keV photon in the light detector corresponds to electron recoils of roughly 600 keV in the crystal. This is far beyond the region of interest ( $\sim 10\text{-}40$  keV) in a Dark Matter experiment using  $\text{CaWO}_4$  target crystals, particularly with regard to the high quenching factor of  $\sim 35$  associated with tungsten recoils. The estimation of the threshold based on the energy information from the  $^{55}\text{Fe}$  source furthermore implies a high degree of linearity and a constant pulse shape down to the lowest energies of interest ( $\sim 3$  eV). These assumptions might not be valid.

For a more accurate characterization of the light detectors a new calibration scheme based on a pulsed blue-light signal of an InGaN light-emitting diode (LED) ( $\lambda \sim 430$  nm) was developed in the present thesis. The wavelength of the light emitted by the LED was chosen to match the spectral output ( $\sim 420$  nm) of the  $\text{CaWO}_4$  crystals. The spectral output of the LED transmitted through the optical fibre used here to inject photons into the cryostat is depicted in Fig. 6.12.

In this calibration scheme the energy of a given light peak is inferred from the peak width and the corresponding peak position. The width  $\sigma$  of a light peak induced in a cryogenic light detector depends on several parameters, in particular on electronic noise  $\sigma_{el}$ , position dependence of the detector response  $\sigma_{pos}$ , charge trapping  $\sigma_{tr}$ , photon statistics  $\sigma_{ph}$  etc. Since these contributions can be assumed to be independent of each other, the total observed resolution  $\sigma$  can be written as

$$\sigma^2 = \sigma_{ph}^2 + \sigma_{el}^2 + \sigma_{tr}^2 + \sigma_{pos}^2 + \dots \equiv \sigma_{ph}^2 + \sigma_0^2, \quad (6.2)$$

where  $\sigma_0$  denotes all the parameters affecting the resolution besides  $\sigma_{ph}$ . Here, the photon statistics has been described by a Gaussian due to the large number ( $\gtrsim 100$ ) of photons associated with a typical calibration light pulse. Starting from equation 6.2, the calibration of a light detector depends on the detailed detector response. In the following the calibration principle will be outlined for both linear and non-linear detector response.

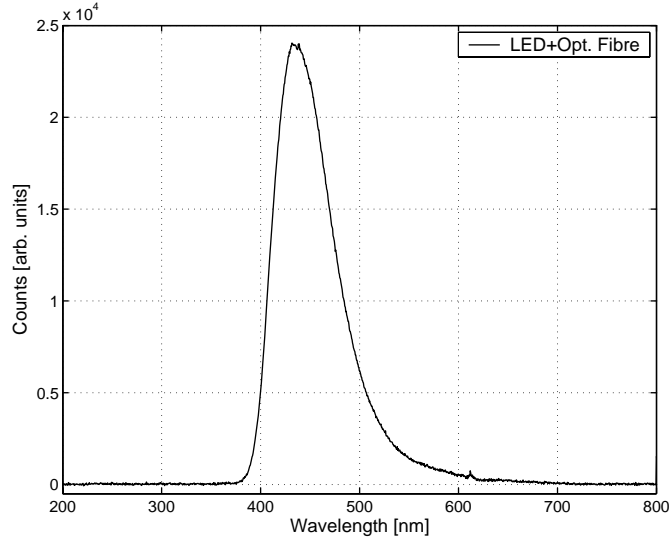


Figure 6.12: Spectral output of an InGaN LED transmitted through an optical fibre.

**6.2.2.3.1 Linear Detector Response** Assuming a linear response of the detector to the energy deposited by  $N$  photons, the measured pulse height  $x$  and the corresponding peak width  $\sigma_{ph}$  scale as

$$x = aN \quad (6.3)$$

$$\sigma_{ph} = a\sigma_N = a\sqrt{N}, \quad (6.4)$$

where  $a$  denotes the scaling factor and  $\sigma_N$  the standard deviation of the fluctuating number of absorbed photons which equals  $\sqrt{N}$  according to Poisson counting statistics. The relationship between the measured pulse height  $x$  and the peak width  $\sigma$  can now be written as

$$\sigma = \sqrt{\sigma_0^2 + a^2\sigma_N^2} = \sqrt{\sigma_0^2 + a^2N} = \sqrt{\sigma_0^2 + ax}. \quad (6.5)$$

The parameters  $\sigma_0$  and  $a$  can be derived by fitting the relationship 6.5 to a measured  $(x, \sigma)$ -set. For this measurement a blue LED ( $\lambda \sim 430$  nm) pulsed at a frequency of 50 Hz has been employed. The width of the current pulses the LED was operated with, has been chosen to be 500 ns which is one order of magnitude less than the time base of 5  $\mu$ s given by the sampling frequency. Thus the light emission can be considered as an instantaneous process.

Fig. 6.13 shows the measured  $1\sigma$  width of the light peaks versus their position. Fitting the relationship 6.5 to the data yields:

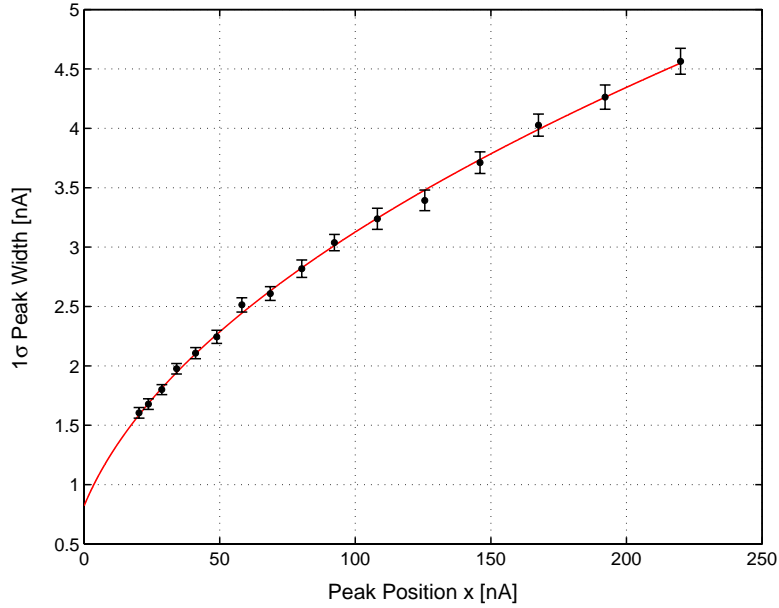


Figure 6.13: Measured  $1\sigma$  width of the light peaks versus peak position fitted by the function given in equation 6.5. The error bars correspond to the  $2\sigma$  error (95% C.L.).

$$a = (9.1 \pm 0.2) \cdot 10^{-2} \text{ nA} \quad (6.6)$$

$$\sigma_0 = 0.82 \pm 0.14 \text{ nA}. \quad (6.7)$$

The excellent agreement between the data and the theoretical model (eq. 6.5) is a strong hint for the linearity of the detector in this working point. The fitted values for  $a$  and  $\sigma_0$  imply that the energy resolution of the light detector is dominated by photon statistics (i.e.,  $ax \gg \sigma_0^2$ ) at energies in the keV regime. Both contributions,  $\sigma_{ph}$  and  $\sigma_0$ , to the measured peak width, are equal for a photon number of  $\sim 86$  (equation 6.4) corresponding to a light energy of  $\sim 249$  eV. Below this energy, the resolution of the light detector is dominated by  $\sigma_0$ .

The region of interest for WIMP searches of the CRESST experiment ranges between  $\sim 10$ - $40$  keV. Only about 1% of this energy is detected as light for electron recoils in a typical  $\text{CaWO}_4$  crystal. This fraction is further reduced by a factor of  $\sim 10$  for oxygen (O) recoils,  $\sim 18$  for calcium (Ca) recoils and  $\sim 35$  for tungsten (W) recoils [154]. For this reason, the energy detected as light from nuclear recoils in the region of interest is less than 100 eV. Therefore, the width of the nuclear recoil band which is determined by the energy resolution of the light detector is dominated by  $\sigma_0$  in this energy region. It can therefore be expected that an amplification of the light signal as provided by the Neganov-Luke effect will improve the energy

resolution in this energy region. This will help identifying the individual nuclei (O, Ca, W) in the nuclear recoil band. In this way, a better discrimination of the background induced by neutrons could be achieved since neutrons predominantly induce oxygen and calcium recoils, whereas WIMPs are expected to scatter mainly off tungsten due to the  $A^2$  dependence of the spin-independent scattering cross section in the limit of zero-momentum transfer (s. chapt. 2).

The  $5\sigma$  energy threshold can be derived in analogy to the procedure described in section 6.2.2.2. Here again noise samples have been acquired by a random trigger provided by a waveform generator. A histogram of the noise samples has been derived by fitting these noise samples with a template pulse obtained by averaging several light pulses. The  $5\sigma$  width can then be calculated from the FWHM width (eq. 6.1) which has been obtained from a Gaussian fit to the amplitude histogram of the noise samples. With the scaling factor  $a$  (eq. 6.6), the  $5\sigma$  width of the baseline noise can then be related to a photon number (eq. 6.3) and with a photon energy of  $\sim 2.9$  eV to an energy threshold  $\Delta E_{5\sigma} = 116 \pm 3$  eV (eq. 6.1).

In this measurement a  $^{55}\text{Fe}$  source was also used for calibration. The corresponding result obtained from the Mn- $K_\alpha$  line is  $\Delta E_{5\sigma} = 104 \pm 3$  eV as compared to  $\Delta E_{5\sigma} = 80 \pm 3$  eV obtained previously (Fig. 6.11). The energy thresholds estimated with both methods are in reasonable agreement.

**6.2.2.3.2 Non-Linear Detector Response** Up to now the detector response has been considered to be linear up to 7 keV. The energy content of a pulse, however, can be estimated even without knowing the functional relationship between the measured pulse height  $x$  and the number of absorbed photons  $N$ , provided the additional contribution  $\sigma_0$  to the measured peak width is known. This conclusion is based on the fact that the peak width associated with the fluctuation  $\sigma_{ph}$  of the number of absorbed photons and the pulse height  $x$  only depend on  $N$  (s. eqs. 6.3 and 6.4). Therefore, if  $\sigma_0$  is known, the number of photons  $N$  can be derived from

$$N = \left( \frac{x}{\sigma_{ph}} \right)^2 = \frac{x^2}{\sigma^2 - \sigma_0^2}. \quad (6.8)$$

$\sigma_0$  can be calculated from eq. 6.8 if the photon number  $N$ , the peak position  $x$  and the peak width  $\sigma$  are known:

$$\sigma_0 = \sqrt{\sigma^2 - \frac{x^2}{N}}. \quad (6.9)$$

The energy associated with a certain light peak, however, is not known initially. Using very short light pulses (500 ns) provides a nearly instantaneous energy deposition in the light detector. Therefore, the pulse shapes of light and X-ray events do not differ significantly. Fig. 6.14 shows the template pulses obtained by taking

the average of 3000  $^{55}\text{Fe}$  and light pulses, respectively. Both templates were normalized to have the same amplitude. Since the trigger information used to record the light pulses was provided by the pulse generator, the template pulses depicted in Fig. 6.14 slightly differ in their onset position.

Due to the nearly identical pulse shapes of light and X-ray events, the position of the  $\text{Mn-K}_\alpha$  line can be used to calibrate the pulse height spectrum in the high-energy regime where the detector response is assumed to be linear in a small energy range around 6 keV. For the calculation of  $\sigma_0$  four light peaks in the energy region between  $\sim 4.5$  and  $\sim 7$  keV have been used. For each of these lines  $\sigma_0$  was derived from eq. 6.9 yielding an average value of  $\sigma_0 = (0.5 \pm 0.2)$  nA. Assuming this value to be constant down to the lowest energies, the number of photons associated with the peak positions can be estimated from eq. 6.8.

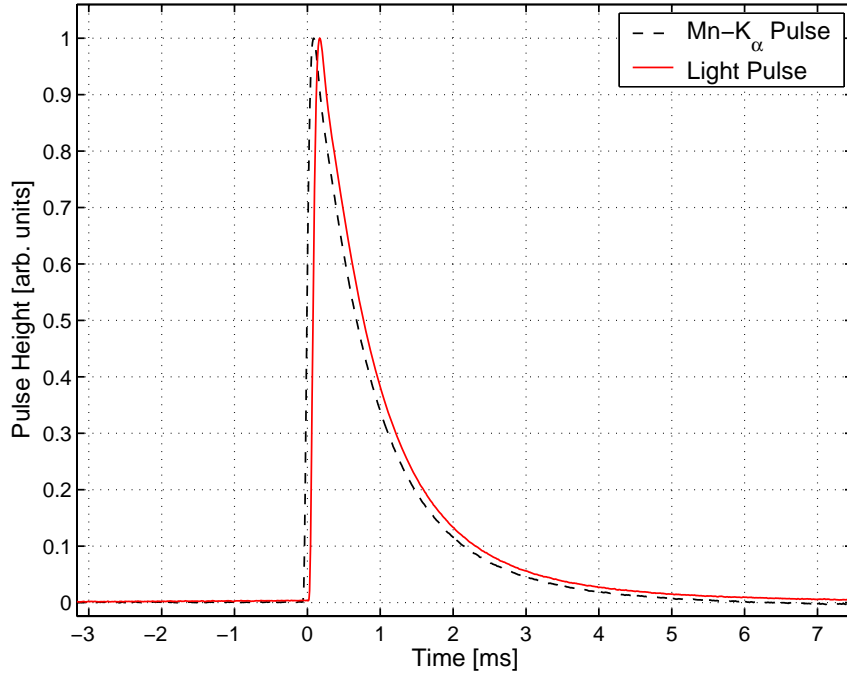


Figure 6.14: Template pulses from a  $^{55}\text{Fe}$  source (dashed line) and from light events (full line).

The numbers of photons associated with the pulse height of different light peaks are depicted in Fig. 6.15. The assumption of a non-linear (see eq. 6.8) detector response (see red squares in Fig. 6.15) does not reveal a significantly different functional relationship between pulse height and energy as compared to a linear detector response (see black circles in Fig. 6.15). This means that the non-linear

relationship (eq. 6.8) between measured pulse height  $x$  and the photon number  $N$  can be considered to be nearly linear in this energy region.

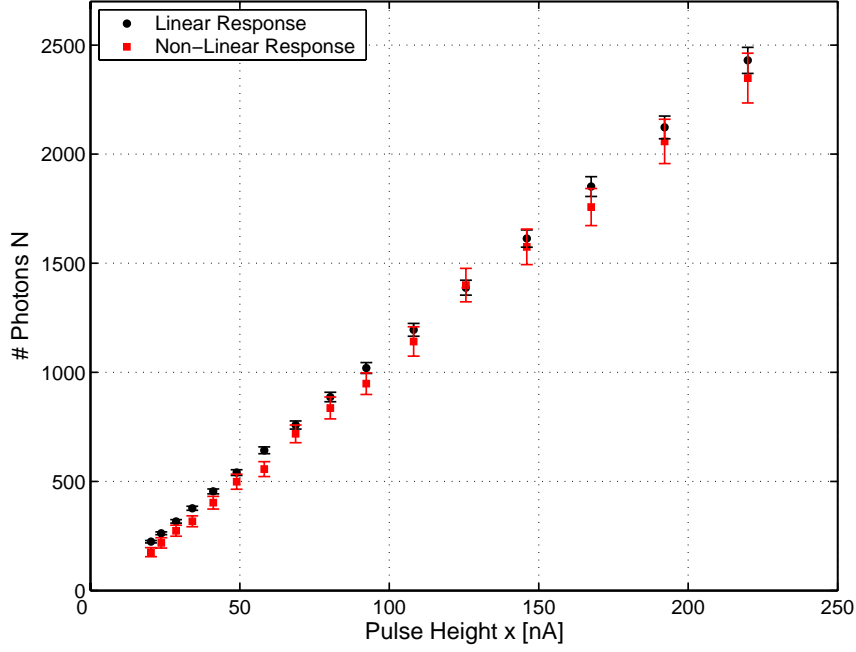


Figure 6.15: Number of photons corresponding to different light peaks assuming a linear (black circles) and a non-linear (red squares) detector response (see text).

### 6.2.3 Neganov-Luke Amplification

One of the major drawbacks of the phonon-light technique is the small fraction of the energy of incident particles detected as light. This fraction is at the percent level and for nuclear recoils it is further reduced by the quenching factor. Thus presently the discrimination threshold between the electron and nuclear recoil bands of a typical detector module in the CRESST experiment is limited to  $\gtrsim 10$  keV [139]. Due to the low light yields it is furthermore expected that the energy resolution of the light channel is mainly dominated by noise limiting the discrimination capability of the background induced by neutrons that mainly scatter off oxygen and calcium from possible events of WIMPs which are expected to mainly scatter off tungsten [140]. For these reasons, light detectors with higher sensitivities might provide substantial improvements with respect to both aspects.

Following Neganov and Trofimov [6] and Luke [7], the threshold of the light detectors can be improved by drifting the light-induced electron-hole pairs by an applied electric field (see section 4.2.1). Due to the heat dissipated in the crystal

by the drifting electron-hole pairs the phonon signal is amplified. If the generated charge is completely collected, the resulting thermal gain  $G_t$  is given by

$$G_t = 1 + \frac{eV}{\epsilon}, \quad (6.10)$$

where  $V$  denotes the bias voltage,  $e$  the electron charge and  $\epsilon$  the energy needed to create an electron-hole pair. For X-rays,  $\epsilon=3.64$  eV in silicon [1]. For light  $\epsilon$  is given by [199]

$$\epsilon_{Light} = \frac{E_{Light}}{\eta}, \quad (6.11)$$

where  $\eta$  denotes the quantum efficiency for electron-hole pair production. The emission spectrum of  $\text{CaWO}_4$  has a peak wavelength of  $\sim 420$  nm corresponding to a photon energy  $E_{Light}=2.9$  eV. For this energy, the quantum efficiency for electron-hole pair production is close to unity [200].

As discussed in the next section, in real detectors the achieved thermal gain can be reduced by space charges that build up with time in the detector leading to a reduced voltage  $V_{eff}(t)$ . Additionally, charge carriers can be trapped before reaching the electrode resulting in a reduced drift distance  $l$ . The measured thermal gain  $G_{eff}(t)$  is then given by [199]

$$G_{eff}(t) = 1 + \frac{eV_{eff}(t) l}{\epsilon d}, \quad (6.12)$$

where  $d$  is the distance between the electrical contacts.

### 6.2.3.1 Detector Response to X-Rays and Light

The response of the light detector depicted in Fig. 6.1 (left panel) with an applied Neganov-Luke voltage was calibrated with both X-rays from a  $^{55}\text{Fe}$  source and light from a pulsed blue LED irradiating the side of the Si absorber opposite to the glued TES. Fig. 6.16 shows the time dependence of the pulse height corresponding to 6 keV X-rays at 0 V, at 30 V and directly after switching off the voltage. Immediately after switching on the voltage a clear amplification which is not stable with time is visible whereas the energy resolution is heavily degraded. This degradation is further highly dependent on the effective amplification. After a slight increase during the first  $\sim 200$  s, the pulse height decreases to the initial (not amplified) value. After switching off the voltage, the pulse height rises again before it finally decreases to the initial value.

The fast decrease of the pulse height as well as the highly degraded energy resolution for X-rays have not been observed for light (Fig. 6.17) proving thus the feasibility of this device for light detection. For both X-rays and light an additional

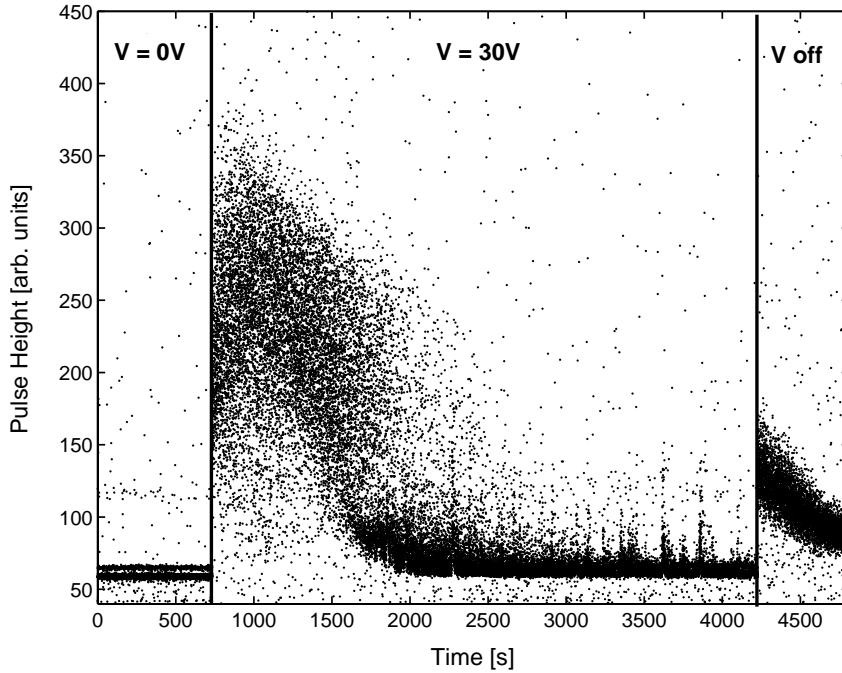


Figure 6.16: Detector response to 6 keV X-rays at 0 V, at 30 V and after switching off the voltage.

noise immediately after applying a voltage appears. This additional noise limits the achievable improvement of the signal-to-noise ratio due to the Neganov-Luke effect (see section 6.2.3.2). In the present thesis it was found that these shortcomings can be overcome by a new method of applying the Neganov-Luke voltage as described in section 6.2.3.3. This new method is based on a better physical understanding of the detector response as discussed in the present and the next section. In the following the various features observed in Fig. 6.16 as well as the different detector response to light will be discussed.

**1. Initial rise of pulse height:** A slight increase of the pulse height is observed directly after applying a voltage to the detector. This effect is strongly related to the equilibrium conditions in a semiconductor at the low operating temperatures ( $< 100$  mK) of our detectors. Here, the low thermal energy of  $\sim 1$   $\mu\text{eV}$  that is orders of magnitude smaller than the band gap ( $\sim 1.7$  eV) and the ionization energy of donor and acceptor impurities ( $\sim 30$  meV) impedes the thermal generation of charge carriers.

At low temperatures the state of the semiconductor is determined by the impurities present in the crystal. It turns out that for a donor impurity it is ener-

getically favorable to give its electron to a nearby acceptor leaving both impurities ionized: the donor is empty ( $D^+$ ) and the acceptor is occupied ( $A^-$ ). As long as no additional charge carriers are excited, these impurities will remain ionized being therefore efficient trapping sites for drifting charge carriers. When an electron or a hole is trapped by an ionized impurity of opposite sign this impurity will remain electrically neutral reducing the number of ionized traps in this way.

This mechanism can explain the initial rise of the pulse height immediately after applying a voltage since drifted photon-induced electron-hole pairs can be trapped on these ionized impurities. Reducing the number of ionized impurities makes trapping less efficient and therefore improves the measured thermal gain (see eq. 6.12).

**2. Degradation of energy resolution:** When irradiating the light detector with X-rays a substantial degradation of the energy resolution is observed when a Neganov-Luke voltage is applied. This effect might be explained by the highly localized electron-hole cloud present in a semiconductor immediately after the absorption of an X-ray. Here, the primary electron is excited high above the conduction band edge and in the subsequent deexcitation processes the initial energy is divided among several generations of electron-hole pairs until the energies of these excited free charge carriers fall below the threshold for further ionization (see chapter 4). With an electron-hole pair creation energy of 3.64 eV in silicon [1], a 6 keV X-ray creates  $\sim 1600$  electron-hole pairs in this way.

For 6 keV depositions in Si at  $T \sim 2$  K, the average total track length of the primary electron is less than  $1 \mu\text{m}$  [201]. Ignoring the drift distance of the secondary charge carriers, the resulting electron-hole cloud can be assumed to be spherical with a radius of  $\sim 500$  nm. With a density of  $\sim 10^{12}$  electron-hole pairs  $\text{cm}^{-3}$  the cloud can be considered as a plasma since the Debye shielding length is roughly 300 nm [202] at  $\sim 2$  K. Even though the interior of the cloud is not field free, an attenuation of the applied electric field is present inside the cloud as compared to its outer boundary. This effect leads to a non-homogeneous trapping probability throughout the cloud altering therefore the charge-collection efficiency. This in turn introduces an additional variation of the pulse height leading to the observed degradation of the energy resolution. Such an effect might be even more serious for X-rays absorbed close to the surface due to the higher trap density.

Another reason for the degraded energy resolution might be a position dependence of the detector response when operated in Neganov-Luke mode. Since, however, a small aperture ( $\sim 1 \mu\text{m}$  in diameter) was used in this measurement, it is unlikely that the position dependence can account for this huge effect.

**3. Decrease of pulse height with time:** A critical issue of a cryogenic light detector with Neganov-Luke amplification is the long-term stability of the amplified

signal. As shown in Fig. 6.16 the amplification of this detector is not stable with time. The signal decreases and reaches the initial not amplified value after about 1 hour. The main reason for this effect are the contacts. The aluminum electrodes have been directly evaporated onto the silicon substrate. They are therefore not well defined and with regard to the low operating temperatures they might behave rather like Schottky than Ohmic contacts providing not enough conductivity. This in turn leads to the generation of space charges inside the absorber compensating the applied voltage (see eq. 6.12).

**4. Final rise of pulse height:** With the accumulated charge carriers inside the absorber and at the electrodes an electric field is still present even without an applied voltage. This leads to the observed rise of the signal after switching off the Neganov-Luke voltage since the electron-hole pairs generated by the X-ray source are now drifted in the opposite direction by the accumulated charge carriers. Since this built-in potential is generated by accumulated electrons and holes, the field inside the absorber is now gradually reduced by the recombination of these charge carriers with the photon-induced electron-hole pairs. Therefore, this final amplification is again not stable with time. The regeneration scheme presented in subsection 6.2.3.4 is based on this effect: After having operated the detector in Neganov-Luke mode for a longer period, the voltage is switched off and the detector is then flushed with light for a few seconds. In this way, a large number of electron-hole pairs is generated. These additional charge carriers recombine with and therefore efficiently remove the accumulated space charges.

**5. Different detector response to light:** Besides the problems arising from the long-term stability of the signal, the most serious issue results from the degraded energy resolution when operating such a device as an X-ray detector in Neganov-Luke mode. In case of light, however, the situation is different. Fig. 6.17 shows the detector response to the light from a pulsed blue LED. The energy of a light pulse corresponds to few keV. The voltage applied to the detector was 50 V.

As for X-rays, a slight increase of the pulse height directly after applying the voltage is observed. Furthermore, the amplification is not stable with time since here again space charges are accumulated compensating the applied voltage. The most important difference with respect to X-rays, however, is the energy resolution. For light, the relative energy resolution is not degraded when operating the detector in Neganov-Luke mode even though the energy of each light pulse was of several keV, too. In contrast to an X-ray, the energy of a light pulse containing many photons is not deposited in one point. Each photon is absorbed by a primary electron at different positions in the detector. Therefore, no localized electron-hole clouds emerge that compensate the applied field locally.

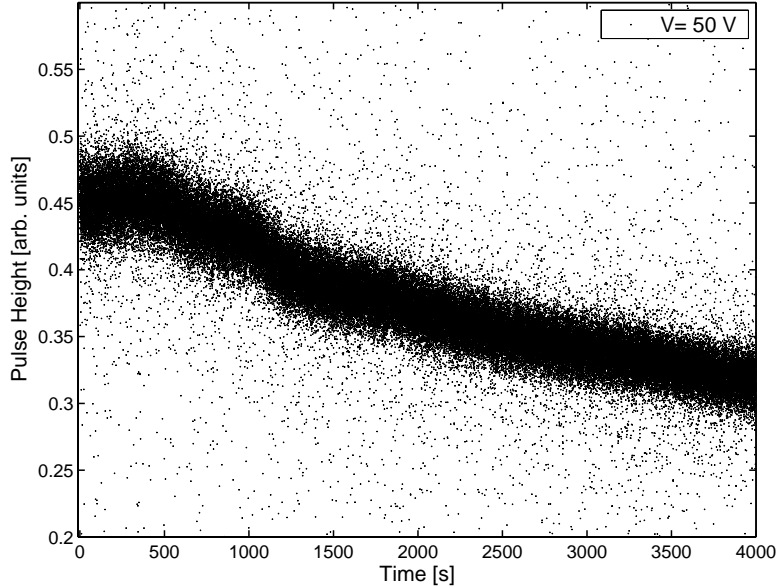


Figure 6.17: Detector response to the light from a pulsed blue LED. The Neganov-Luke voltage in this case was 50 V.

### 6.2.3.2 Performance

For a first rough characterization of the light detector with an applied Neganov-Luke voltage, the light induced by an external  $^{137}\text{Cs}$  gamma source in a  $\text{CaWO}_4$  crystal has been used to irradiate the detector. Here, the  $\text{CaWO}_4$  crystal was positioned on the back side of the light detector, i.e. the crystal was facing the side of the absorber of the light detector opposite to the glued TES. In this way, the active area of the light detector is enlarged as compared to the front side where a substantial fraction of the light is absorbed in the TES substrate. This fraction of light, however, does not contribute to the amplified signal since the  $3 \times 5 \text{ mm}^2$  TES substrate can be considered field free.

To monitor the amplification and the improved sensitivity 10000 events have been recorded for voltages in the range between 0 and 100 V. Here, a voltage of 100 V has been first applied which was then reduced to 0 V in decimal steps. For each voltage step two different spectra have been acquired for each polarity. In this way, the effect resulting from the accumulation of space charges should be reduced. The amplification for each voltage has been determined from the position of the  $^{137}\text{Cs}$  photopeak relative to the position at 0 V which has been arbitrarily set equal to unity. The results together with the expected theoretical amplification (see eq. 6.10) are depicted in Fig. 6.18.

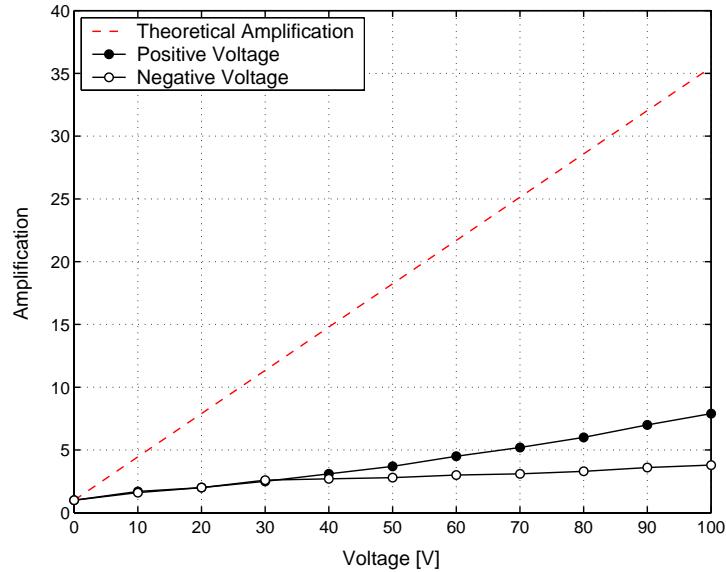


Figure 6.18: Amplification of the light signal excited by a  $^{137}\text{Cs}$  source in a  $\text{CaWO}_4$  crystal measured for both polarities of the Neganov-Luke voltage in the range between 0 and 100 V in decimal steps. The dashed (red) curve indicates the expected theoretical amplification.

From this measurement it becomes obvious that the measured amplifications are lower than expected from eq. 6.10. In addition, a clear asymmetry is present between the two polarities. Here, the higher amplification is addressed to a voltage labelled positive. This convention, however, is arbitrary since no physical difference between the aluminum electrodes should exist.

These results are consistent with those obtained by M. Stark [194, 199]. The lower amplification as compared to the theoretical value can again be explained in terms of accumulating space charges and trapping (see eq. 6.12). The asymmetry between both polarities might result from the rather undefined contacts which are of Schottky rather than Ohmic type. This in turn results in different conductivities with respect to electrons and holes leading to different opposite field strengths induced by accumulating electrons and holes in the proximity of the electrodes.

To determine the improvement of the signal-to-noise ratio (S/N) for a given voltage, pretrigger samples are used to calculate the ratio of peak position to the baseline width. This ratio has been set equal to unity for both polarities at a voltage of 0 V. The results for the different polarities are depicted in Fig. 6.19. Even though the amplification is monotonically increasing with the applied voltage, the S/N breaks down at higher voltages. A maximum improvement of the signal-to-noise ratio by a factor of 6 is achieved at a voltage of +90 V. The break-down of

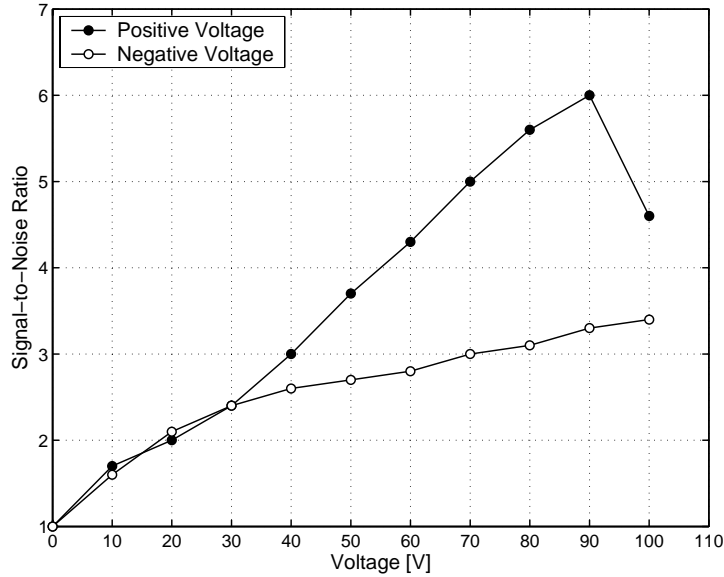


Figure 6.19: Improvement of the signal-to-noise ratio (S/N) for different Neganov-Luke voltages. At 100 V, the S/N decreases again due to the occurrence of additional noise. A maximum improvement of the S/N by a factor of 6 is achieved at +90 V.

the S/N at high voltages has also been observed by M. Stark [194, 199]. Its origin has been ascribed to shallow traps that become ionized at high field strengths. The charge carriers generated in this way also induce small phonon signals as they are drifted by the applied field. These additional small pulses, however, are not correlated with the light pulses leading therefore to an increased noise level.

### 6.2.3.3 New Method of Applying the Neganov-Luke Voltage

To investigate the origin of the additional noise observed at high voltages a pulsed blue LED was used to irradiate the detector. The LED with a peak at a wavelength of  $\sim 430$  nm was chosen to match the spectral output of a  $\text{CaWO}_4$  crystal. Using the LED further offers the opportunity to regenerate the light detector within few seconds while the regeneration with the light induced in the crystal by external sources took several hours. In this way, results become much better reproducible since space charges could be quickly removed by flushing the light detector with the LED light (see subsect. 6.2.3.4).

For a more accurate characterization of the additional noise, a voltage of 100 V has been applied to the detector for  $\sim 30$  min while acquiring noise samples by a random trigger provided by a pulse generator. In Fig. 6.20 noise samples acquired at 0V, at 100 V directly after applying the voltage, and at 100 V after  $\sim 30$  min can

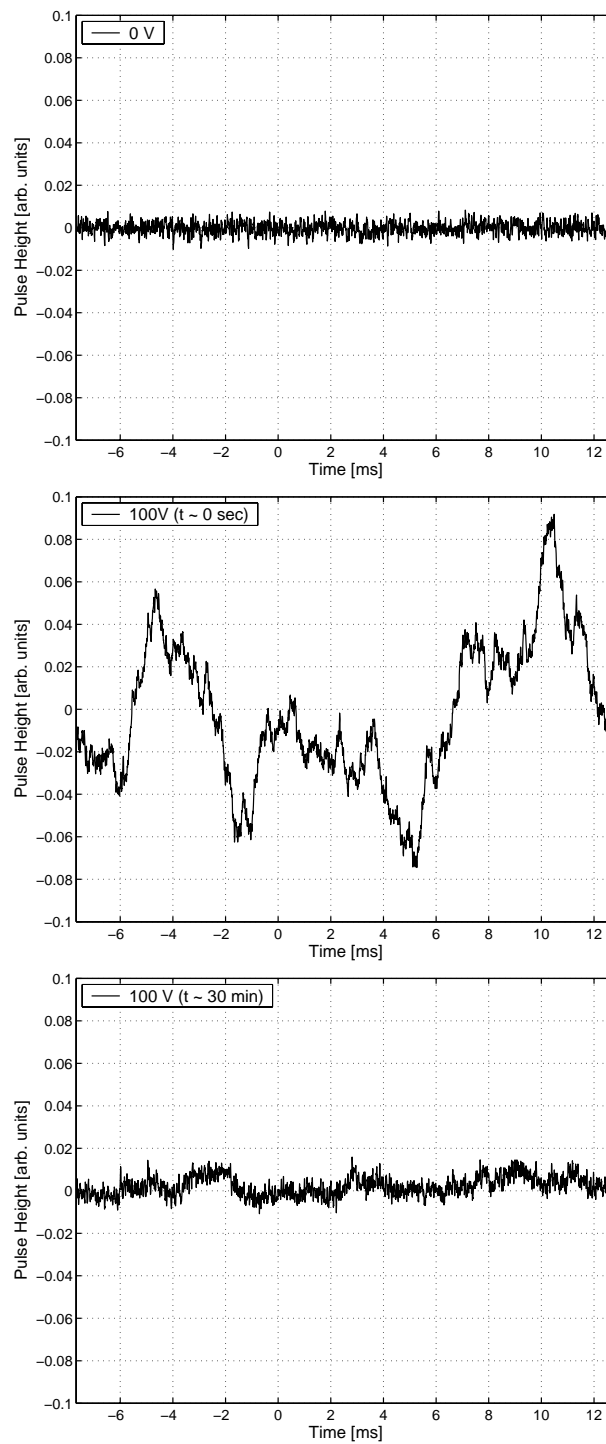


Figure 6.20: Noise samples acquired at 0 V (*top*), at 100 V directly after applying the voltage (*middle*) and at 100 V after  $\sim 30$  min (*bottom*). The level of the additional noise decreases with time and reaches almost the initial level after  $\sim 30$  min.

be seen. From these samples it becomes obvious that the level of the additional noise observed at high voltages is decreasing with time. After  $\sim 30$  min the noise almost reaches its initial level at 0 V.

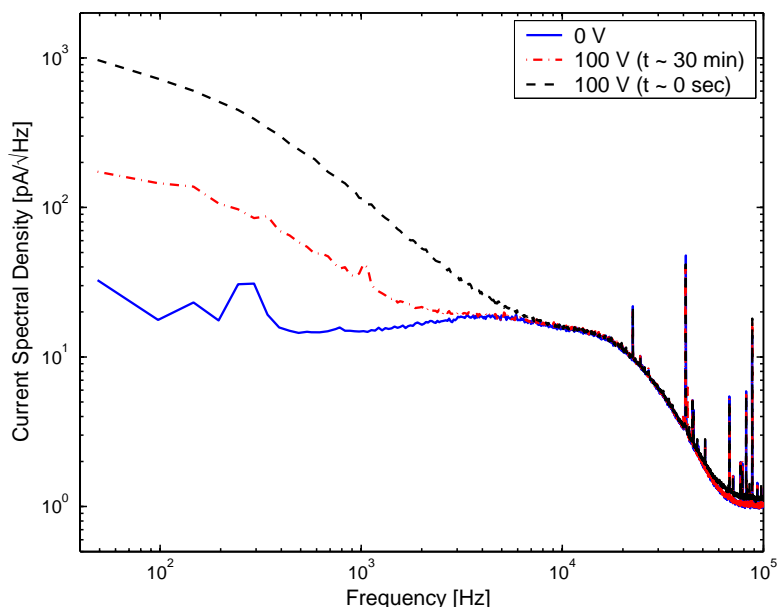


Figure 6.21: Averaged current spectral densities calculated from noise samples at 0 V (solid blue line), at 100 V directly after applying the voltage (dashed black line) and at 100 V after  $\sim 30$  min (dashed-dotted red line). The additional noise is entirely contained in the frequency region below 10 kHz. It is therefore very likely that the additional noise originates from charge carriers escaping from shallow traps.

The origin of this additional noise can be better understood in the frequency domain representation. Fig. 6.21 shows the averaged current spectral densities calculated from noise samples acquired at 0 V, at 100 V directly after applying the voltage and at 100 V after  $\sim 30$  min. From this plot it becomes obvious that the additional noise is contained in the frequency region below 10 kHz. This, however, is exactly the frequency region expected from phonon signals (see Fig. 6.9). It is therefore very likely that the additional noise originates from loosely bound electrons and holes that escape from their shallow trapping sites at higher voltages. In this way, they can be drifted by the applied voltage inducing a small phonon signal. Since the number of these traps is finite most of them can be eroded in this way after a certain period of time leading to a decreased noise level. This in turn might explain the lower measured amplification as compared to the theoretical gain since these charge carriers might accumulate in the proximity of the electrodes.

Based on these observations a new method for applying the Neganov-Luke voltage has been adopted for further measurements. In order to efficiently erode the shallow traps a voltage higher by 30 V than the nominal Neganov-Luke voltage to be used is first applied to the detector. After  $\sim 30$  min the voltage is decreased to the nominal value. For a voltage of 100 V, e.g., 130 V are first applied for 30 min and then reduced to 100 V. This procedure further reduces the noise level as compared to Fig. 6.21. The averaged current spectral densities calculated from noise samples acquired at voltages between 0 and 200 V applied in this way are depicted in Fig. 6.22. The shape of the current spectral density is slightly different than that depicted in Fig. 6.21 since in this measurement a different shunt resistor was used. Although the noise level below 10 kHz is still higher than at 0 V, an improvement of S/N up to a factor of  $\sim 10$  can be achieved at a Neganov-Luke voltage of 100 V.

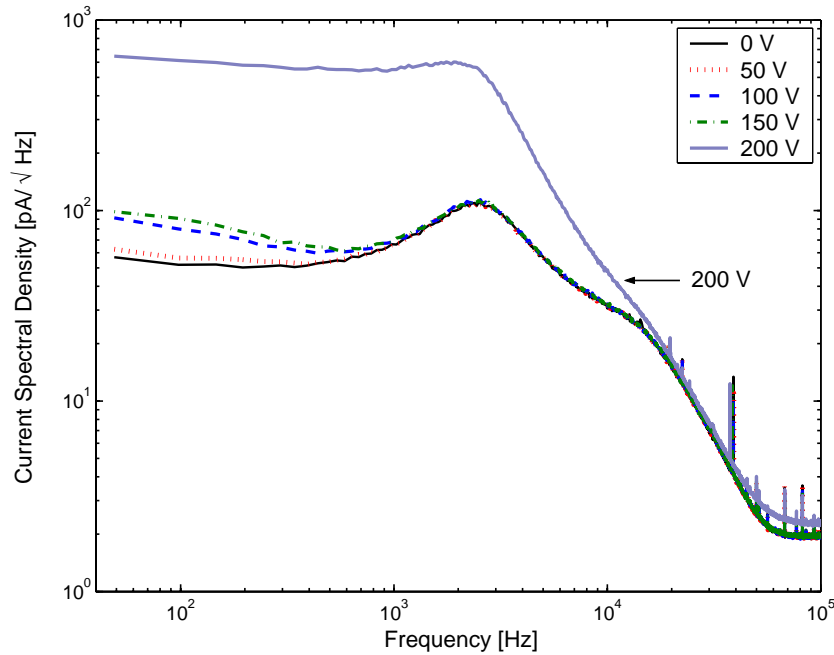


Figure 6.22: Averaged current spectral densities calculated from noise samples acquired at voltages between 0 and 200 V applied by the procedure described in the main text.

Fig. 6.23 shows the amplification and the improvement of the signal-to-noise ratio relative to 0 V for voltages in the range between 0 and 150 V applied by the new method. At voltages higher than 50 V the improved S/N is less than the amplification due to the additional noise. At higher voltages a saturation of both the amplification and the S/N is observed.

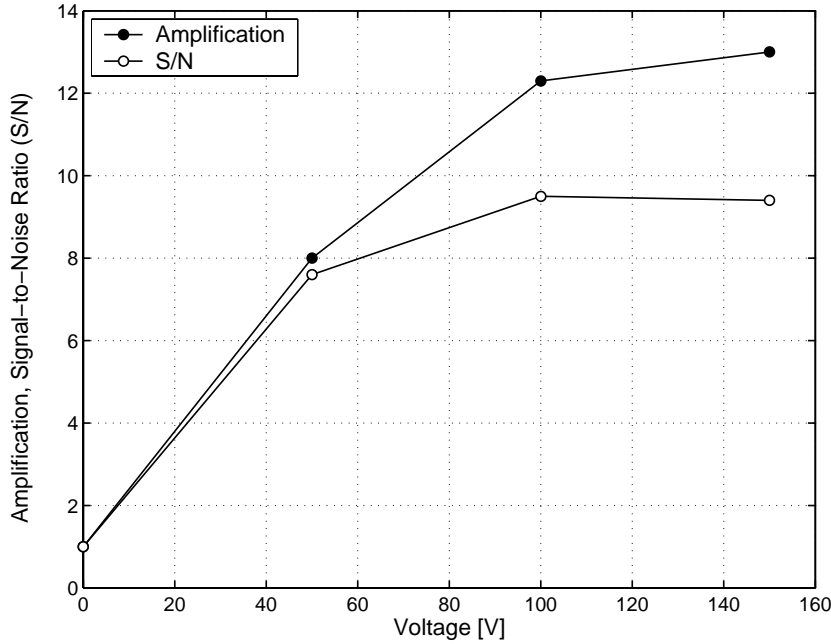


Figure 6.23: Amplification and improvement of the signal-to-noise ratio relative to 0 V for voltages in the range between 0 and 150 V applied by the procedure described in the main text. At 100 V an improvement of the S/N by a factor of 10 is achieved.

This saturation behaviour might be explained in terms of higher trap densities created by eroding the shallow traps by the higher than nominal voltage. When the voltage is decreased to the nominal value, the number of drifting charge carriers is reduced by these additional traps. An optimal voltage is found at a Neganov-Luke voltage of  $\sim 100$  V. Judging from the relative resolution of the light peak, a  $5\sigma$  energy threshold of  $\sim 10$  eV is achieved at this voltage. Without Neganov-Luke voltage the threshold was about a factor of 10 higher.

In the top panel of Fig. 6.24 a typical light pulse recorded for the characterization of the light detector is depicted. The energy of the pulse is a few 100 eV. The bottom panel shows the amplified signal at a Neganov-Luke voltage of 100 V. An amplification by a factor of  $\sim 10$  is achieved without significantly increasing the noise.

At voltages higher than 150 V the signal becomes heavily distorted (see Figs. 6.25 and 6.22). A pulse acquired at 200 V is depicted in Fig. 6.25. Here additional shot-noise like distortions appear that drastically increase the energy threshold. These spikes do not disappear even after longer periods of time. Therefore they have to be of a different origin than the additional noise observed at lower voltages. They might therefore be associated with a break-down of the electrode contacts.

At this voltage, charge carriers trapped in the proximity of the electrodes might escape and gain sufficient energy in the electric field to pass through the Schottky barrier at the silicon-aluminum interface.

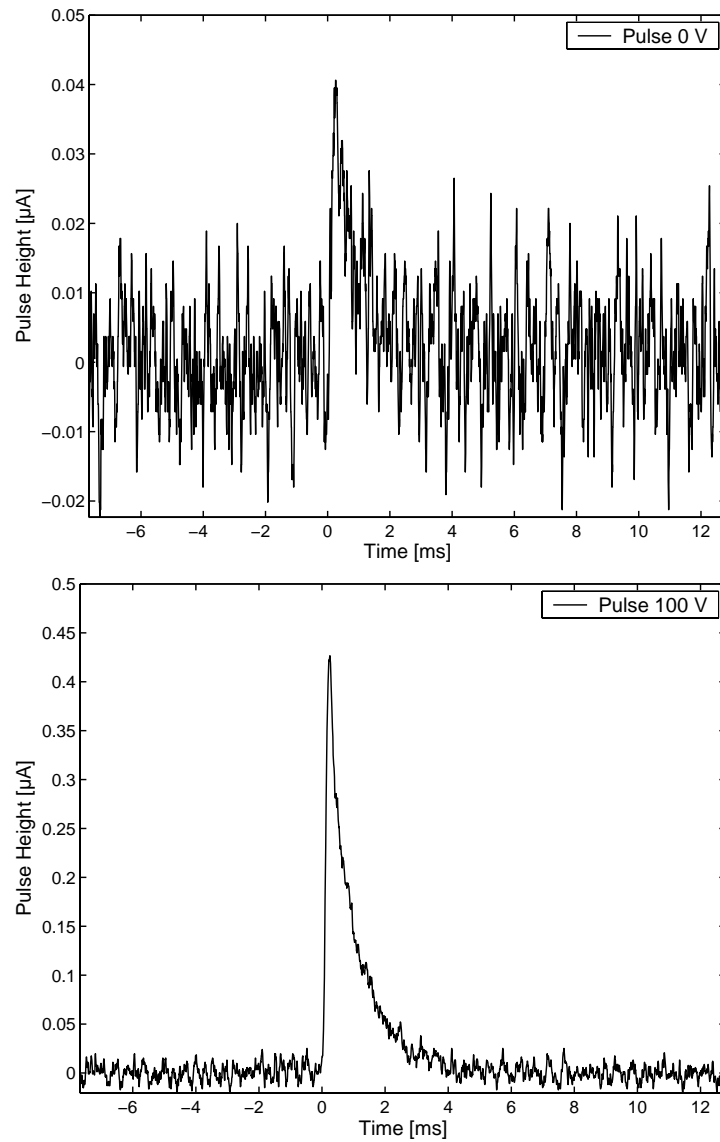


Figure 6.24: *Top Panel:* Light pulse of few 100 eV injected by the pulsed LED recorded by the light detector with no applied voltage. *Bottom Panel:* Corresponding pulse at a Neganov-Luke voltage of 100 V. An amplification by a factor of  $\sim 10$  is visible. The noise level stays practically the same.

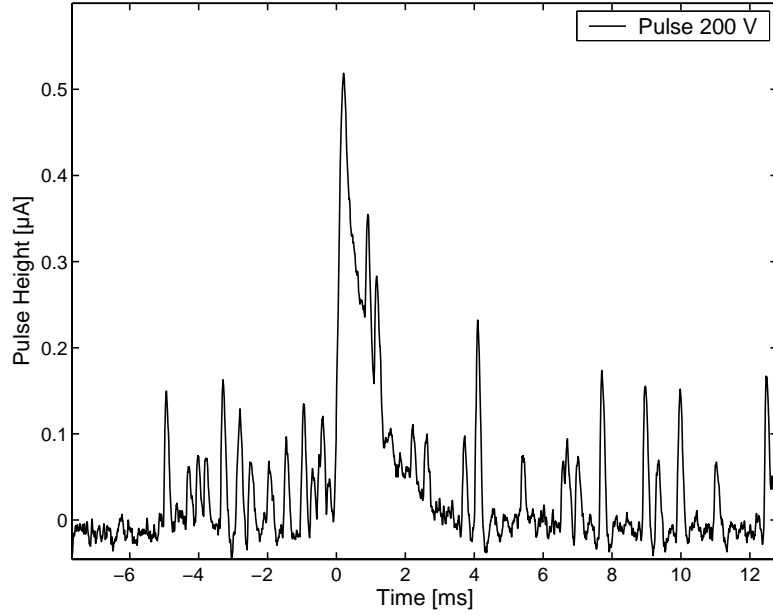


Figure 6.25: Typical pulse recorded at a voltage of 200 V. The signal is heavily distorted by large spikes that might be caused by a sudden break down at the electrodes.

#### 6.2.3.4 Regeneration

The cryogenic light detectors based on the design presented in this work suffer from space charges that build up with time compensating the applied voltage which in turn leads to a decreasing pulse height with time. It is therefore necessary to remove these space charges in order to provide a sufficiently high amplification. Such a regeneration procedure is indicated in Fig. 6.16 where the pulse height rises again after switching off the voltage. This is a strong evidence for the presence of space charges in the substrate causing the observed amplification of the phonon signal after the voltage has been turned off. This amplification is not constant either, showing that the charge carriers accumulated in the substrate are gradually removed by recombination due to the electron-hole pairs excited by the  $^{55}\text{Fe}$  source. Based on this observation, a regeneration procedure using a LED has been developed. A LED has the advantage that a significant number of electron-hole pairs can be injected into the substrate keeping the time needed to regenerate the detector very short. In order to remove the space charges, the voltage has been switched off and the detector was flushed with the light from the LED by increasing the pulse width to  $5 \mu\text{s}$  for  $\sim 10\text{s}$ . After this procedure the initial pulse height was reestablished clearly demonstrating the effectiveness of this method. After  $\sim 4000\text{s}$  the detector was again regenerated using the same procedure. Two such regeneration

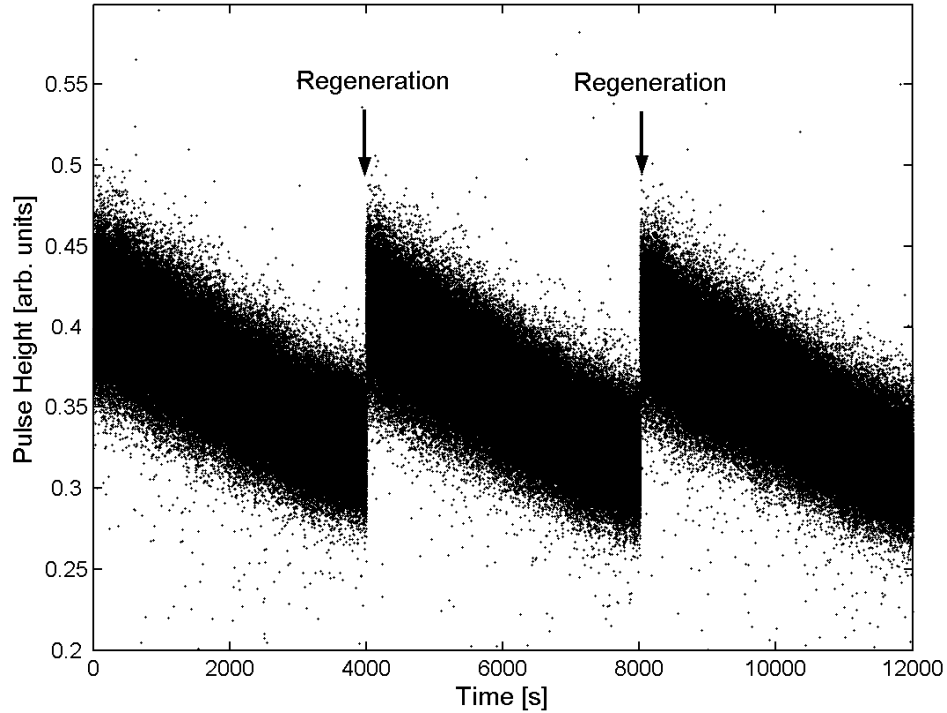


Figure 6.26: Regeneration principle of a cryogenic light detector with Neganov-Luke amplification. Space charges can be removed by switching off the voltage and flushing the detector with light for  $\sim 10$  s. Here two regeneration cycles are depicted.

cycles are shown in Fig. 6.26.

Here, the light detector was illuminated by a pulsed blue LED ( $\lambda \sim 430$  nm) with rectangular pulses of a width of 500 ns at a frequency of 50 Hz. A Neganov-Luke voltage of 50 V was applied. Assuming the width of the light peaks to be dominated by photon statistics the energy deposited per pulse can be derived from the relative peak width. In this way, an energy of  $\sim 1$  keV is obtained for a light pulse. With a resulting light energy of  $\sim 50$  keV deposited per second in the light detector the pulse height decreased by  $\sim 20\%$  after  $\sim 4000$  s (Fig. 6.26).

In this measurement, the decrease in pulse height becomes significant after one hour. Here, however, the energy deposited per second is at least one order of magnitude higher than in a low-background environment. Therefore, a light detector with Neganov-Luke amplification based on this design is expected to show a nearly constant amplification in a low-background environment in a detector module where the light is provided by a scintillating crystal. Since a 10 s regeneration is sufficient, the detector can therefore be regenerated about every 5 hours without making too long interruptions of data taking necessary.

### 6.2.3.5 Pulse-Height Correction

When employing a light detector with Neganov-Luke amplification in a detector module at the surface of the earth, due to the higher count rate a decrease of the pulse heights with time will be observed between two consecutive regeneration cycles. This in turn deteriorates the energy resolution partially compensating the advantages gained from an amplified light signal. It is therefore mandatory to monitor the time dependence of the drifting pulse heights using a reference light source. In this way the drift of the Neganov-Luke amplification can be corrected offline. It is very convenient to use a pulsed LED as a reference light source since these pulses can be made significantly shorter than the light pulses originating from the scintillating  $\text{CaWO}_4$  crystal. In this way, the reference signal can easily be discriminated from the data. Figure 6.27 shows the templates for LED and scintillation-light events. Here, the LED was biased with rectangular 500 ns current pulses making the resulting light pulses significantly shorter than typical scintillation light events from a  $\text{CaWO}_4$  crystal.

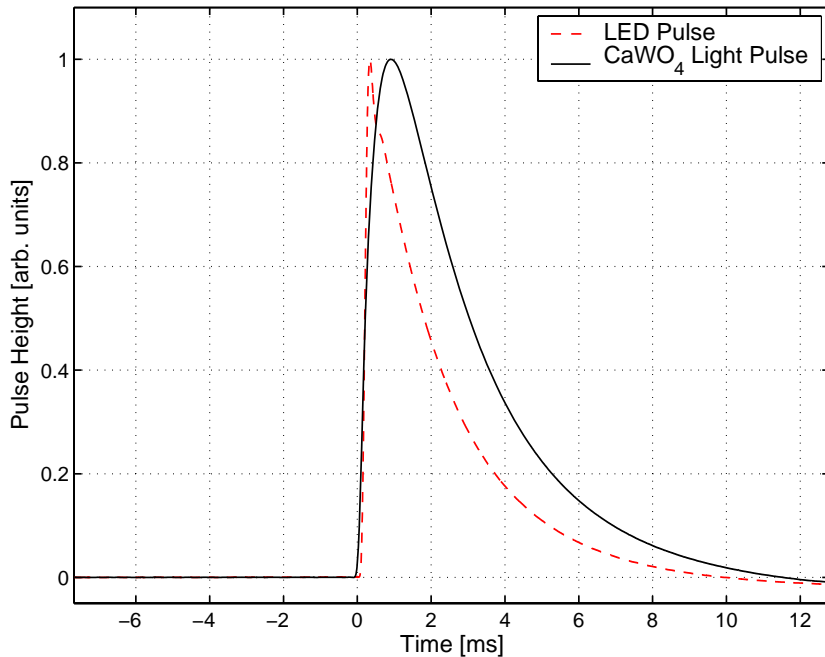


Figure 6.27: Template pulses originating from the pulsed LED (dashed line) as a reference and from the  $\text{CaWO}_4$  crystal (full line). The reference pulses can be easily identified due to the significantly different pulse shape.

The typical time dependence of the drifting pulse heights of the reference signal is depicted in the top panel of Fig. 6.28. Here, a Neganov-Luke voltage of 50 V was

applied and the LED pulses were injected every 2 seconds. It is important to keep the energy of the reference signal as small as possible since it contributes itself to the decreasing amplification. Therefore the LED pulses should be injected at low rates ( $\lesssim 1$  Hz) and the energy of the reference signal should not exceed that of a typical light event from the crystal. The time dependence of the drifting pulse heights is obtained by fitting the data with two exponentials:

$$F_{Drift}(t) = a \exp(bt) + c \exp(dt). \quad (6.13)$$

Here  $t$  is the time stamp of a pulse and  $a$ ,  $b$ ,  $c$  and  $d$  are fit parameters (with 95 % confidence bounds):

$$a = 46.33 \pm 0.36 \text{ nA} \quad (6.14)$$

$$b = (-1,122 \pm 0.099) \cdot 10^{-5} \text{ 1/s} \quad (6.15)$$

$$c = -2.478 \pm 0.427 \text{ nA} \quad (6.16)$$

$$d = (-8.6 \pm 3.3) \cdot 10^{-4} \text{ 1/s}. \quad (6.17)$$

With this function, the initial increase of the pulse height discussed in section 6.2.3.1 was also taken into account.

With  $F_{Drift}(t)$  the corrected pulse heights  $P_1(t)$  are obtained from the drifting pulse heights  $P_0(t)$  via:

$$P_1(t) = \frac{F_{Drift}(0) \cdot P_0(t)}{F_{Drift}(t)}. \quad (6.18)$$

The corrected pulse heights are depicted in the bottom panel of Fig. 6.28. Now, the drift of the pulse heights is eliminated. The fit function  $F_{Drift}(t)$  used here is arbitrarily chosen to also match the initial increase of the pulse height. After regenerating the detector the initial rise of the pulse height is usually not present. Therefore the time dependence of the pulse heights can in principle be also fitted by a linear function.

To see the effect of the pulse height drift with time on the energy resolution, the light detector was simultaneously irradiated by the light induced in the  $\text{CaWO}_4$  crystal by an external  $^{137}\text{Cs}$  source. The uncorrected pulse height spectrum is depicted in the top panel of Fig. 6.29. After correcting the pulse heights using the fit function  $F_{Drift}(t)$  the resolution of the photopeak is significantly improved (see bottom panel in Fig. 6.29).

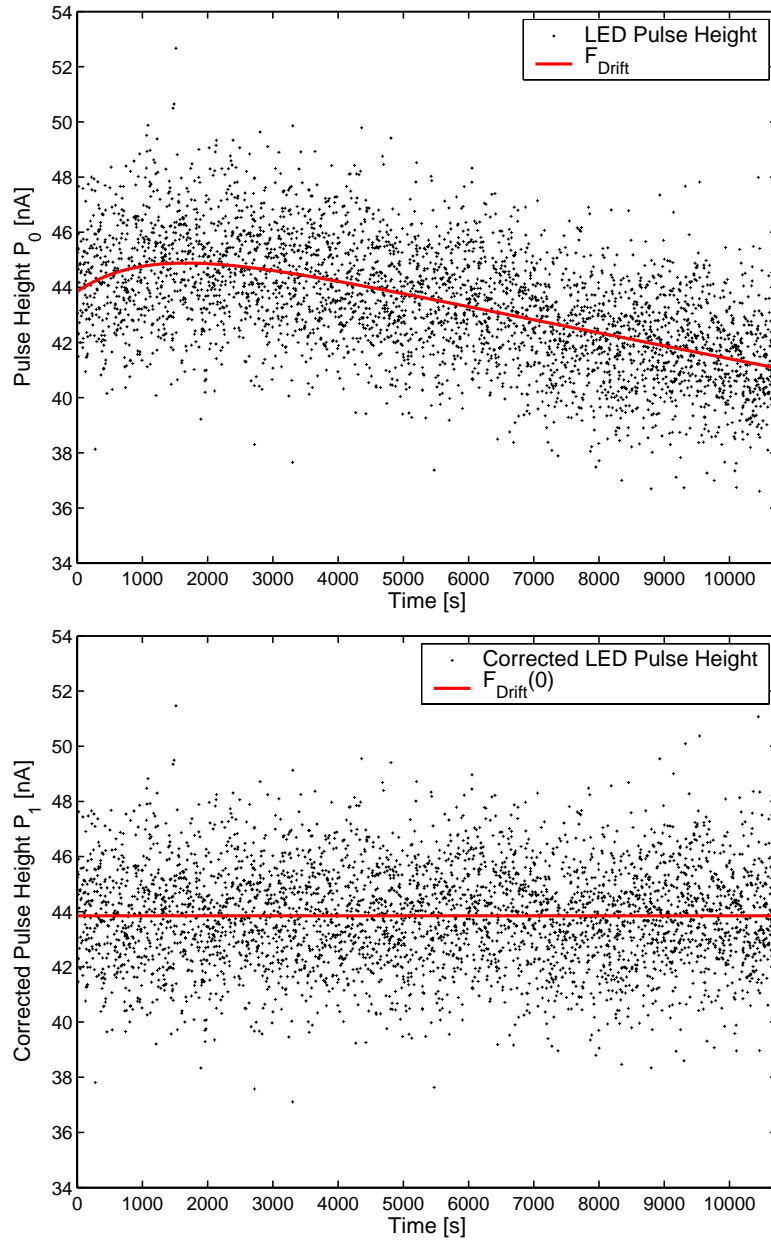


Figure 6.28: *Top Panel:* Uncorrected pulse heights  $P_0(t)$  of the reference signal injected at a frequency of 0.5 Hz. The drift of the reference signal is fitted by two exponentials indicated by the full (red) curve. *Bottom Panel:* Corrected pulse heights  $P_1(t)$  using the fit function  $F_{Drift}(t)$ .

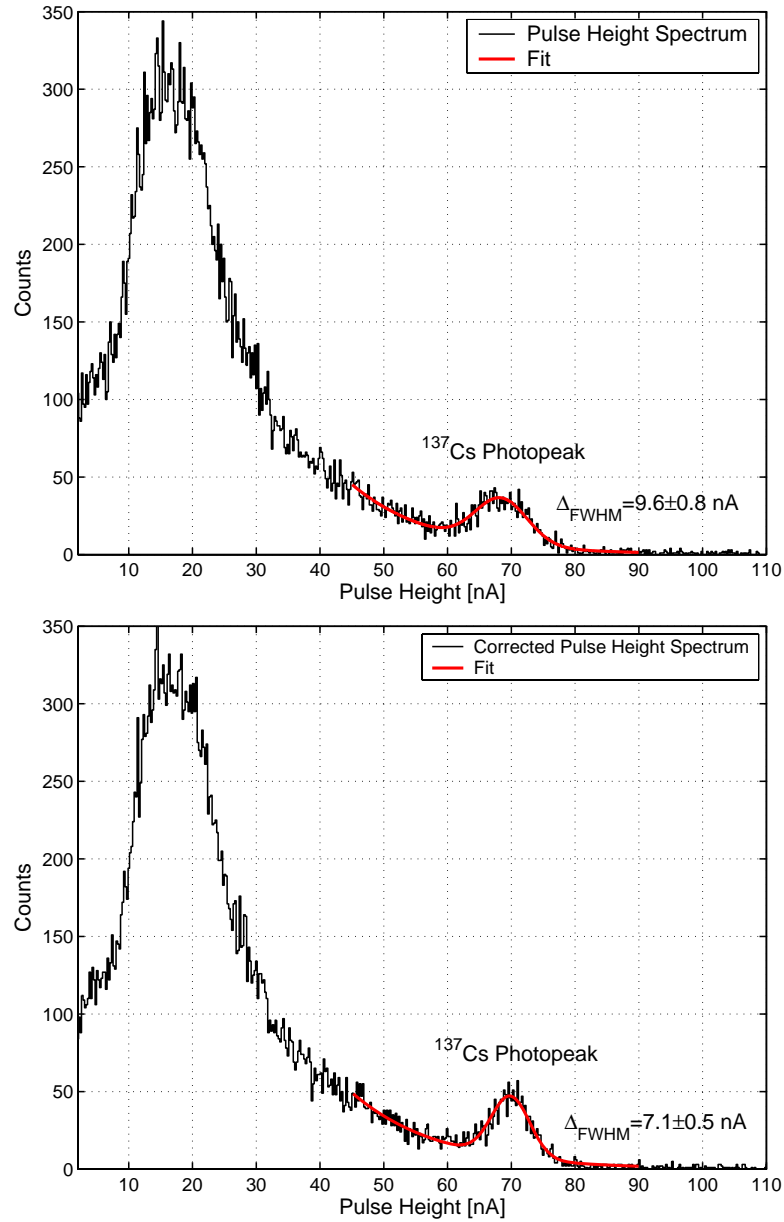


Figure 6.29: *Top Panel:* Uncorrected pulse height spectrum of the light detector with an applied voltage of 50 V. Clearly visible are the <sup>137</sup>Cs photopeak and the muon-induced events at low energies. *Bottom Panel:* Corrected pulse height spectrum with the fit function  $F_{drift}(t)$  (see main text). The resolution of the photopeak is significantly improved.

### 6.2.4 Relevance of the Neganov-Luke Effect for the Phonon-Light Technique

In the calibration scheme based on photon statistics the energy resolution  $\sigma$  was assumed to be determined by an energy-independent term  $\sigma_0$  and by the photon statistics  $\sigma_{ph}$  (see equation 6.2 in section 6.2.2.3).  $\sigma_0$  is governed by trapping, a position dependent response of the detector or by electronic noise. The latter is usually the dominant contribution and is the only parameter whose relative magnitude can be reduced by Neganov-Luke amplification. The contribution of the electronic noise  $\sigma_{el}$  can be obtained by fitting a template pulse to noise samples.  $\sigma_0$  can be determined by fitting the relationship 6.5 to a measured  $x - \sigma$  set using a pulsed LED. This fit further yields the scaling factor  $a$  needed to relate a given pulse height to a photon number and thus to an energy (eq. 6.3). The parameters obtained in this way for the light detector Si518 are:

$$\sigma_0 = 0.82 \pm 0.14 \text{ nA} \quad (6.19)$$

$$\sigma_{el} = 0.73 \pm 0.02 \text{ nA} \quad (6.20)$$

$$a = (9.1 \pm 0.2) \cdot 10^{-2} \text{ nA}. \quad (6.21)$$

With these values the improved signal-to-noise ratio provided by the Neganov-Luke effect for the nuclear recoil band measured by a  $\text{CaWO}_4$  detector module employing the phonon-light technique can be calculated as follows:

1. The energy  $E_e$  detected as light for electron recoils in a typical  $\text{CaWO}_4$  crystal is only a small fraction  $\eta \sim 1\text{-}2\%$  of the energy  $E_{crystal}$  deposited in the crystal:

$$E_e = \eta E_{crystal}. \quad (6.22)$$

2. For nuclear recoils this fraction is further reduced by the quenching factors ( $QFs$ ) associated with the different nuclei in  $\text{CaWO}_4$ :  $QF(O) \sim 10$  for oxygen,  $QF(Ca) \sim 18$  for calcium and  $QF(W) \sim 35$  for tungsten (W) [154]. The light energy deposited in the light detector for a particular nuclear recoil in the  $\text{CaWO}_4$  crystal is therefore given by

$$E_O = \frac{E_e}{QF(O)} \text{ for Oxygen Recoils} \quad (6.23)$$

$$E_{Ca} = \frac{E_e}{QF(Ca)} \text{ for Calcium Recoils} \quad (6.24)$$

$$E_W = \frac{E_e}{QF(W)} \text{ for Tungsten Recoils.} \quad (6.25)$$

3. The emission spectrum of  $\text{CaWO}_4$  has a peak wavelength of  $\sim 420$  nm corresponding to a photon energy of  $E_{ph} \sim 2.9$  eV. The average number of photons  $N$  related to a given energy input  $E_r$  ( $r = O, Ca, W$ ) in the light detector is therefore given by

$$N = \frac{E_r}{2.9 \text{ eV}}. \quad (6.26)$$

4. In the calibration scheme with light, the photon statistics could be considered by a Gaussian since the number of photons related to the calibration pulses was large. Due to the high quenching factors associated with the nuclei in  $\text{CaWO}_4$  leading to a strongly suppressed light output, the statistics of the photons in the nuclear recoil band for a given recoil energy has to be described by Poisson statistics. According to the Poisson distribution, the probability  $P_N(k)$  of detecting  $k$  photons for a given recoil energy associated with an average number  $N$  of photons is given by [203]

$$P_N(k) = \frac{N^k}{k!} e^{-N}. \quad (6.27)$$

5. With the Poisson distribution, the spectrum  $S_r(E)$  ( $r = O, Ca, W$ ) of a particular nuclear recoil band can now be calculated via convolution with the detector response described by a Gaussian:

$$S_r(E) = \exp\left(-\frac{E^2}{2(\Delta E_{el})^2}\right) \cdot e^{-N} + \sum_{k>0} \frac{N^k}{k!} e^{-N} \cdot \exp\left(-\frac{(E - kE_{ph})^2}{2(\Delta E_0)^2}\right), \quad (6.28)$$

with

$$\Delta E_{el} = \frac{\sigma_{el}}{a} E_{ph} \quad (6.29)$$

$$\Delta E_0 = \frac{\sigma_0}{a} E_{ph}. \quad (6.30)$$

The first term in eq. 6.28 is related to no-light events that can be recorded by a detector module, since the trigger information is provided by the phonon channel. Here, only the electronic noise is relevant which has been considered by  $\Delta E_{el}$ .

6. In Neganov-Luke mode the relative magnitude of the electronic noise is reduced by a factor of 10:

$$\Delta E_{el}^{NL} = \frac{\sigma_{el}}{10a} E_{ph} \quad (6.31)$$

$$\Delta E_0^{NL} = \sqrt{\Delta E_0^2 - \Delta E_{el}^2 + (\Delta E_{el}^{NL})^2}. \quad (6.32)$$

With these values the spectrum  $S_r^{NL}(E)$  ( $r = O, Ca, W$ ) of a given nuclear recoil band can be calculated using eq. 6.28 for the Neganov-Luke mode:

$$S_r^{NL}(E) = \exp\left(-\frac{E^2}{2(\Delta E_{el}^{NL})^2}\right) \cdot e^{-N} + \sum_{k>0} \frac{N^k}{k!} e^{-N} \cdot \exp\left(-\frac{(E - kE_{ph})^2}{2(\Delta E_0^{NL})^2}\right). \quad (6.33)$$

7. To obtain the spectrum of the entire nuclear recoil band, the relative count rates related to the different nuclei in  $\text{CaWO}_4$  are required. The calculated count rates for events in the energy interval 50-100 keV obtained for 11 MeV neutrons of the tandem accelerator at the Maier-Leibnitz-Laboratorium (MLL) are summerized in table 6.1 [154]. Here, the contributions of Ca and W are given relative to O which is normalized to 1000.

Nucleus	O	Ca	W
Relative count rates	1000	302	140

Table 6.1: Calculated count rates to the recoil spectrum of the different nuclei in the energy interval 50-100 keV for 11 MeV neutrons. The contributions of Ca and W are given relative to that of O which is normalized to 1000 [154].

With these count rates, the spectra calculated for the different nuclei in  $\text{CaWO}_4$  can be normalized relative to the oxygen spectrum:

$$A_O \int S_O(E) dE = 1000 \quad (6.34)$$

$$A_{Ca} \int S_{Ca}(E) dE = 302 \quad (6.35)$$

$$A_W \int S_W(E) dE = 140. \quad (6.36)$$

Here,  $A_O$ ,  $A_{Ca}$  and  $A_W$  are the normalization factors,  $S_O(E)$ ,  $S_{Ca}(E)$ ,  $S_W(E)$  the spectra of the three nuclei oxygen (O), calcium (Ca) and tungsten (W) in  $\text{CaWO}_4$ .

8. The spectrum  $S_n(E)$  of the entire nuclear recoil band for a given recoil energy is the sum of the spectra of the individual nuclei:

$$S_n(E) = \sum_{r=O, Ca, W} S_r(E) \quad (6.37)$$

$$S_n^{NL}(E) = \sum_{r=O, Ca, W} S_r^{NL}(E). \quad (6.38)$$

Here,  $S_n^{NL}(E)$  denotes the spectrum of the recoil band obtained with a light detector in Neganov-Luke mode.

With these equations, the light spectra for the different nuclear recoil bands at a recoil energy of 50 keV for two different values for  $\eta$ , which is the fraction of the recoil energy detected as light for electron recoils, have been calculated considering both a conventional and a light detector operated in Neganov-Luke mode.

The top panel of Fig. 6.30 shows the contributions of the different nuclei to the nuclear recoil band as detected by the light detector for a recoil energy of 50 keV at a Neganov-Luke voltage of 0 V ( $S_r(E)$ , dashed lines) and of 100 V ( $S_r^{NL}(E)$ , full lines). Here, 1.5 % of the energy deposited in the crystal is detected as light. The sum peaks  $S_n(E)$  (dashed line) and  $S_n^{NL}(E)$  (full line) are depicted in the bottom panel. The corresponding plots for 50 keV recoil energy and 3 % of this energy detected as light are depicted in Fig. 6.31.

In each case the Neganov-Luke amplification provides a significant improvement of the energy resolution. For small fractions of the deposited energy (recoil energy) detected as light, however, a limitation of the improved resolution becomes apparent. Here, the photon statistics becomes the limiting factor since for nuclear recoils only few photons are detected. It is therefore mandatory to improve the light yield of the crystals as well as the light collection efficiency in addition to a Neganov-Luke amplified light detector. In this section, only the improvement of the energy resolution of the light detector by a Neganov-Luke amplification has been shown. The effect on the discrimination threshold between the electron and nuclear recoil bands will be discussed in section 6.4.

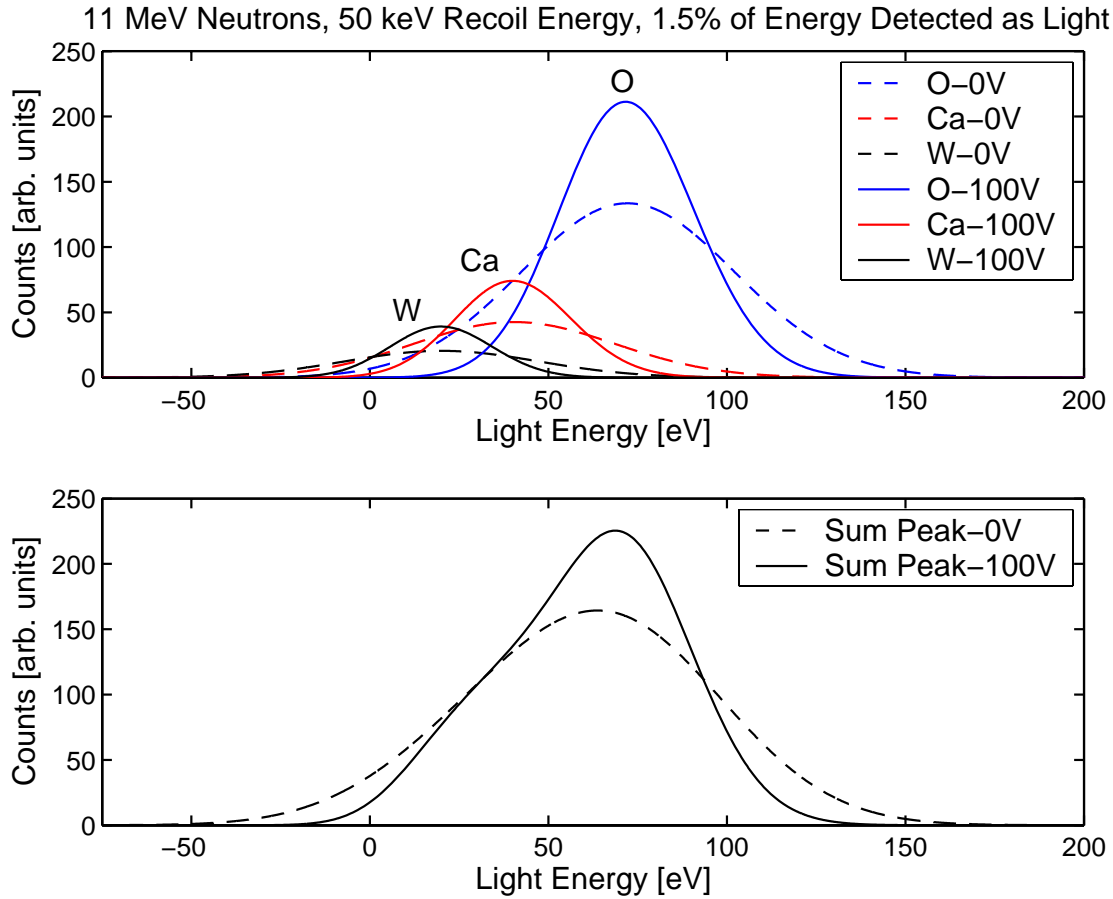


Figure 6.30: *Top Panel:* Calculated spectrum of the nuclear recoil band as detected by the light detector for a recoil energy of 50 keV assuming a fraction of 1.5 % of the energy deposited in the crystal detected as light. The dashed lines correspond to a Neganov-Luke voltage of 0 V. The full lines indicate the spectra recorded at a Neganov-Luke voltage of 100 V corresponding to an improvement of the signal-to-noise ratio by a factor of 10. *Bottom Panel:* The corresponding sum peak acquired at 0 V (dashed line) and at 100 V (full line). The different contributions by O, Ca and W recoils cannot be separated in the sum peak.

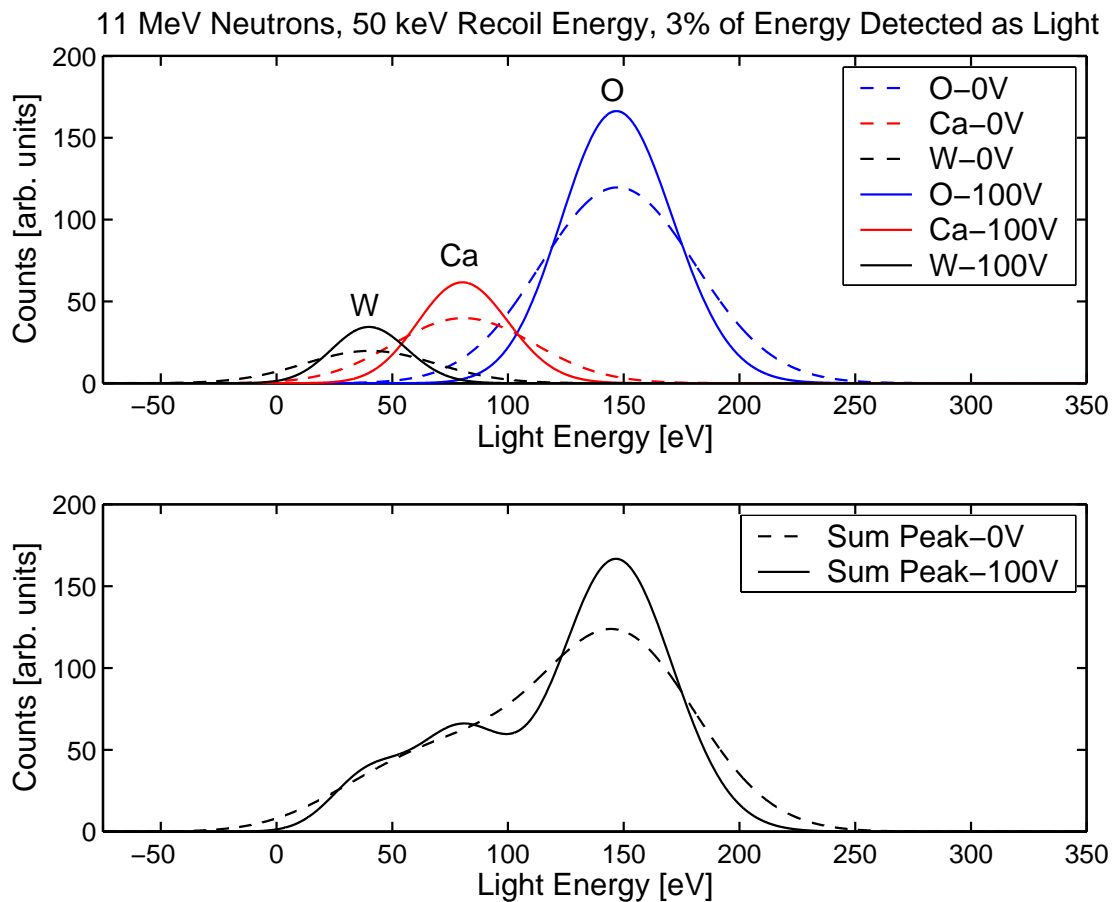


Figure 6.31: *Top Panel:* Calculated spectrum of the nuclear recoil band as detected by the light detector for a recoil energy of 50 keV assuming a fraction of 3 % of the energy deposited in the crystal detected as light. The dashed lines correspond to a Neganov-Luke voltage of 0 V. The full lines indicate the spectrum recorded at a Neganov-Luke voltage of 100 V corresponding to an improvement of the signal-to-noise ratio by a factor of 10. *Bottom Panel:* The corresponding sum peak acquired at 0 V (dashed line) and at 100 V (full line). The different contributions by O, Ca and W recoils can be separated in the sum peak.

## 6.3 Light Detector Si519

### 6.3.1 Setup

The light detector Si519 was designed to test a new drift geometry. Photographs of the front and back side of this detector are depicted in Fig. 6.32. The corresponding schematic drawings are shown in Fig. 6.33.

This detector is based on the composite design. The light absorber consists of a  $20 \times 20 \times 0.25$  mm<sup>3</sup> silicon disk with a room-temperature resistivity of 2-5 k $\Omega$ cm. The Ir/Au TES is evaporated onto a small  $3 \times 5 \times 0.25$  mm<sup>3</sup> Si substrate (thermometer). The Si disks have been bought from *CrysTec* [196]. The thermometer is coupled to the absorber by a small *EPO-TEK* [197] glue spot. The detector is mounted in a copper holder and electrically and thermally coupled via 25  $\mu$ m aluminum and gold bond wires, respectively.

For the application of the Neganov-Luke voltage four aluminum electrodes ( $19 \times 0.5$  mm<sup>2</sup>) with a thickness of  $\sim 2$  k $\text{\AA}$  have been directly evaporated onto the Si absorber on the side opposite to the TES (back side). To reduce the number of traps at the aluminum-silicon interface beneath the electrodes, the Si absorber has not been cleaned in an Ar plasma prior to the aluminum deposition in contrast to the light detector Si518. The electrodes are electrically connected via 25  $\mu$ m aluminum bond wires.

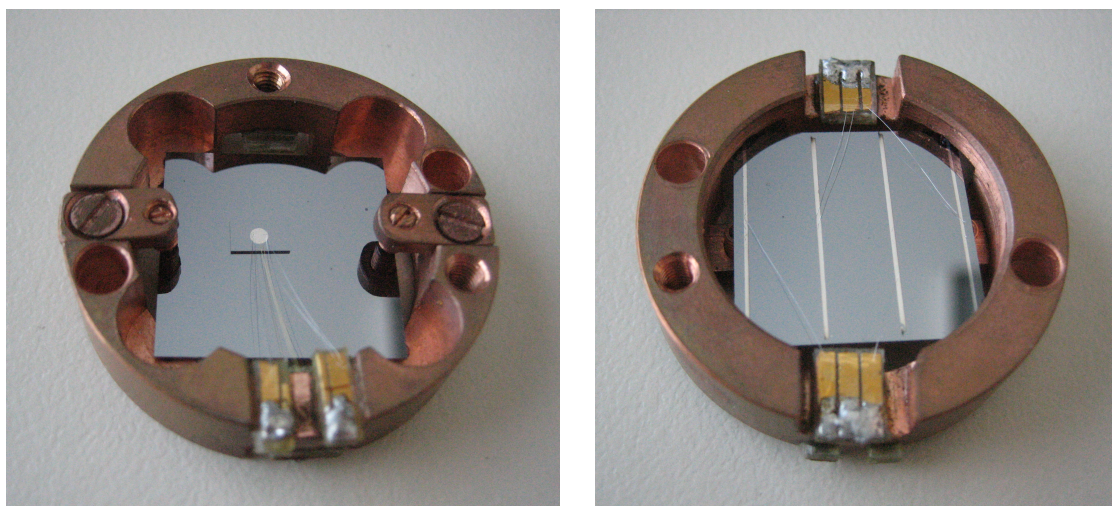


Figure 6.32: *Left panel:* Photograph of the front side of the composite light detector Si519 mounted in a copper holder. *Right panel:* Photograph of the back side of the light detector equipped with four aluminum electrodes for the application of a Neganov-Luke voltage. This side is facing the light source, i. e. the CaWO<sub>4</sub> crystal or the LED.

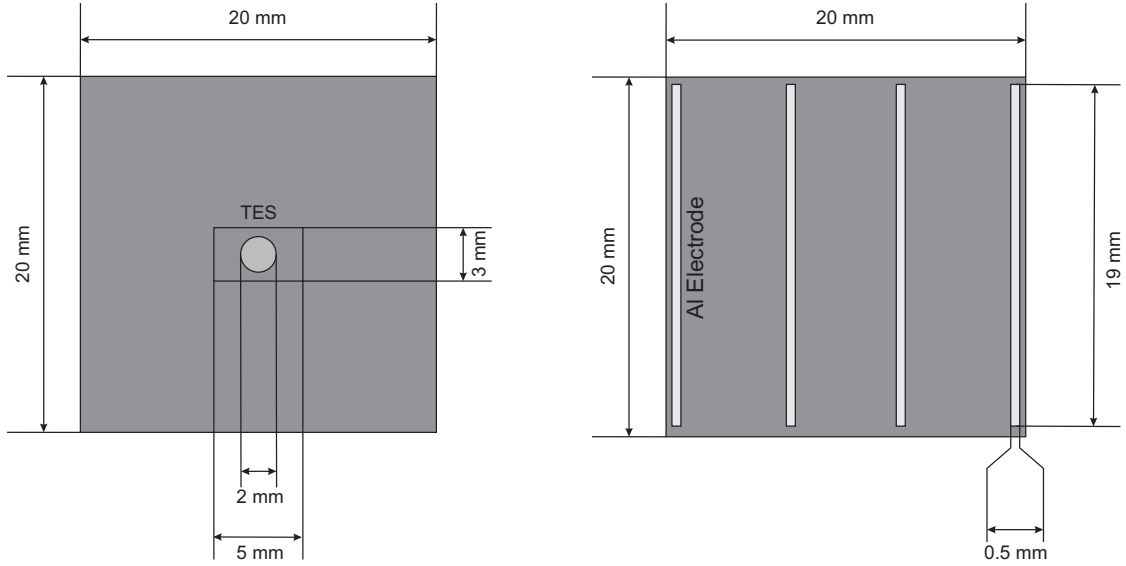


Figure 6.33: *Left panel:* Schematic view of the front side of the composite light detector Si519. It consists of a  $20 \times 20 \times 0.25 \text{ mm}^3$  Si absorber equipped with a glued Si substrate ( $3 \times 5 \times 0.25 \text{ mm}^3$ ) carrying the Ir/Au TES. *Right panel:* Schematic view of the back side of the light detector Si519. On this side, four ( $19 \times 0.5 \text{ mm}^2$ ) aluminum electrodes have been evaporated using a shadow mask.

With this electrode configuration, the back side of the detector is facing the light source ( $\text{CaWO}_4$  crystal, LED). In this way, the light-induced electron-hole pairs are drifted across the surface in contrast to the light detector Si518 where the charge carriers have been drifted through the bulk (see section 6.2). Due to the lower distance between two adjacent electrodes the local field strength is higher than for the light detector Si518. This might reduce the trapping probability at the surface. In addition, a more homogeneous field is achieved in this way. A possible drawback of this setup might arise from the large electrode surface leading to an enhanced phonon absorption in the electrodes that might reduce the sensitivity. Furthermore, photons might be absorbed in the electrodes themselves introducing an additional position dependency of the response as compared to the light detector Si518. With an applied voltage, however, this position dependency might be negligible since this signal is not amplified by the applied Neganov-Luke voltage.

### 6.3.2 Calibration

Prior to calibrating the detector the superconducting transition curve has been recorded with a bias current of  $1 \mu\text{A}$ . This transition curve is depicted in Fig. 6.34.

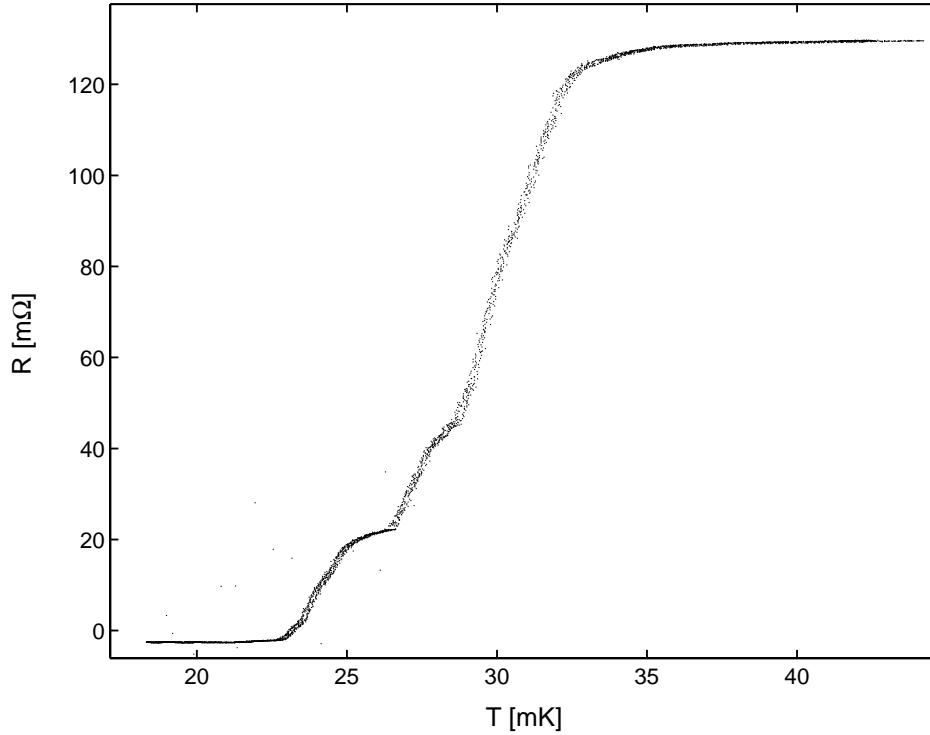


Figure 6.34: Superconducting transition curve of the composite light detector Si519 recorded with a bias current of  $I_{\text{Bias}}=1 \mu\text{A}$ . The transition temperature  $T_c$  is at  $\sim 30$  mK. The transition width is  $\sim 7$  mK.

To find a good working point, the bath temperature  $T_{\text{Bath}}$  was stabilized at  $\sim 14$  mK. At this temperature the bias current  $I_{\text{Bias}}$  was varied between 120 and 190  $\mu\text{A}$  in decimal steps. For each bias current 2500 light pulses and 2500 noise samples have been recorded. The light pulses have been injected via an optical fibre by a pulsed blue InGaN LED operated at 4K (see Fig. 5.8 in section 5.2.3) whereas the noise samples have been provided by a random trigger from a waveform generator. In this way (in analogy to section 6.2.2.2), the signal-to-noise ratio for each bias current could be determined yielding an optimal value for  $I_{\text{Bias}}=180 \mu\text{A}$ .

At this working point the light detector was calibrated with the light injected from the pulsed blue LED using the procedure described in section 6.2.2.3 assuming a linear detector response. For this purpose the rectangular current pulses the LED was biased with have been varied between 750-910 ns in decimal steps. For each current pulse width 2500 light pulses have been recorded with the light detector providing a  $x - \sigma$  set, where  $x$  denotes the peak position and  $\sigma$  the  $1\sigma$  width of the recorded light peaks.

For detector calibration, the measured  $x - \sigma$  set was fitted by the function given in equation 6.5:

$$\sigma = \sqrt{\sigma_0^2 + ax}. \quad (6.39)$$

Here,  $a$  denotes a scaling factor and  $\sigma_0$  all the contributions to the measured  $1\sigma$  width of the light peak besides the photon statistics.

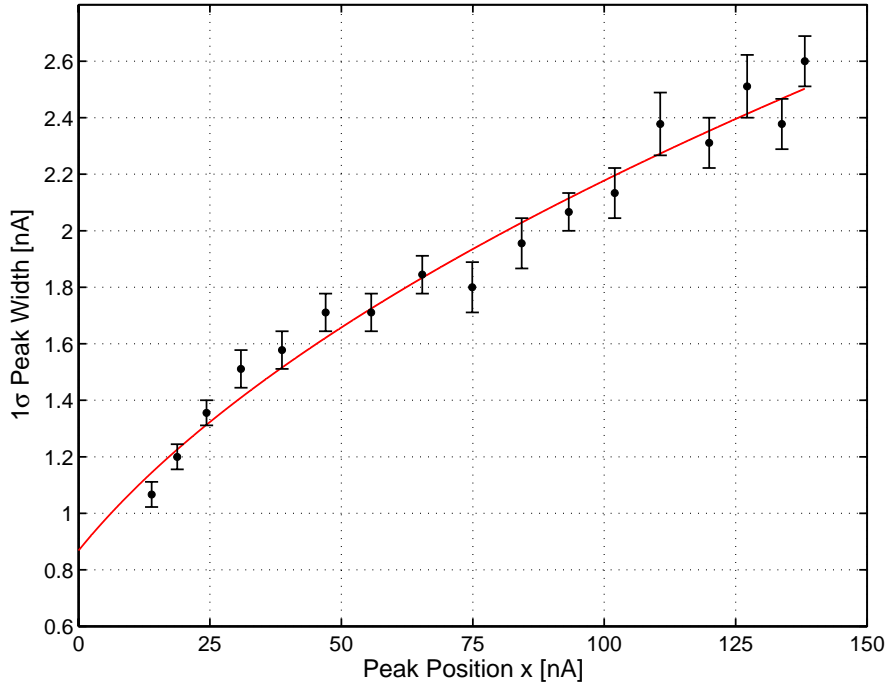


Figure 6.35: Measured  $1\sigma$  width of the light peaks versus their position fitted by the function given in equation 6.5 (full (red) curve). The error bars correspond to the  $2\sigma$  error (95% C.L.).

The measured  $1\sigma$  width of the light peaks versus their position  $x$  is depicted in Fig. 6.35. Fitting the relationship 6.5 to this  $x - \sigma$  set yields:

$$a = (3.99 \pm 0.36) \cdot 10^{-2} \text{ nA} \quad (6.40)$$

$$\sigma_0 = 0.87 \pm 0.12 \text{ nA}. \quad (6.41)$$

With these parameters a  $5\sigma$  energy threshold of  $200 \pm 4$  eV was derived by fitting a template pulse to noise samples. The corresponding width of the baseline is

$\sigma_{el}=0.55 \pm 0.02$  nA due to electronic noise. The threshold is significantly higher than that of the light detector Si518 which is consistent with the lower scaling factor  $a$  (see eq. 6.3). The value for  $\sigma_0$  obtained here, however, is comparable to that derived for the light detector Si518 (see eq. 6.7). Since the contribution of the electronic noise  $\sigma_{el}$  is smaller than for the light detector Si518 ( $\sigma_{el}=0.73 \pm 0.02$  nA) the other energy-independent contributions to  $\sigma_0$  (except  $\sigma_{el}$ ), like a position-dependent response, are more significant here. This might be related to the large Al electrodes on the Si absorber facing the  $\text{CaWO}_4$  crystal in contrast to the light detector Si518 where the electrodes were deposited on the Si absorber side opposite to the crystal. This might increase the position dependency of the response of this light detector since the pulse height associated with photons absorbed in the electrodes can be assumed to be significantly different from that of photons absorbed in the Si substrate.

### 6.3.3 Neganov-Luke Amplification

For the characterization of the light detector in Neganov-Luke mode, voltages between 0 and 90 V have been applied to the detector in the way discussed in section 6.2.3.3. In contrast to the light detector Si518 a voltage 20 V higher than the nominal one has been applied for  $\sim 30$  min. This was sufficient since due to the lower distance between two adjacent electrodes the local field strength was higher as compared to the light detector Si518 providing a more efficient erosion of the shallow traps. Due to the higher local field strength the detector was more unstable against break down when applying voltages higher than  $\sim 50$  V. This led to a short warm-up of the cryostat immediately after applying a higher voltage to the substrate. The temperature of the mixing chamber, however, recovered within few seconds providing thereafter stable operation conditions for one polarity. This behaviour impeded, however, the application of voltages higher than  $\sim 100$  V. For the other polarity, the application of the Neganov-Luke voltage led to a permanent increase of the base temperature. The measured amplification and improvement of S/N are depicted in Fig. 6.36.

The achieved amplification is slightly higher than for the light detector Si518. In addition, there is no saturation of the amplified signal. This might be explained in terms of the higher local field strength that makes trapping less probable providing therefore a higher amplification. Similar to the light detector Si518, the achieved improvement of S/N is less than the amplification at voltages higher than  $\sim 30$  V and S/N starts to saturate. A maximum increase of S/N by a factor of  $\sim 10$  is achieved at 90 V which is comparable to the performance of the light detector Si518.

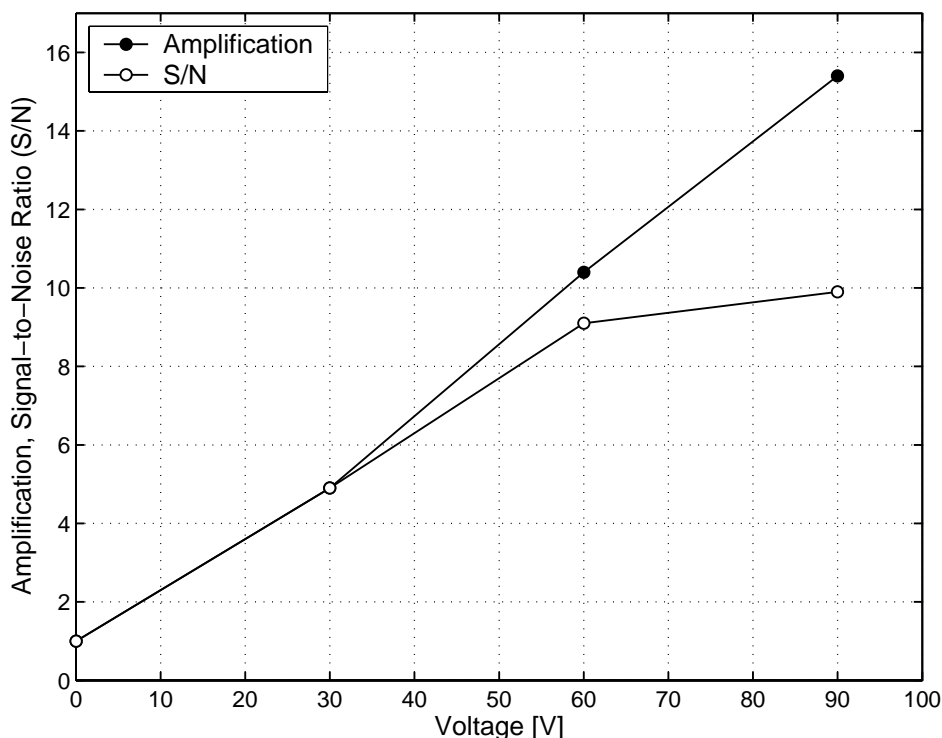


Figure 6.36: Amplification and improvement of the signal-to-noise ratio (S/N) relative to 0 V for voltages in the range between 0 and 90 V. At 90 V an improvement of S/N by a factor of  $\sim 10$  is achieved.

## 6.4 Light Detector Si521 - Measurements at the Maier-Leibnitz-Laboratorium (MLL) with a Neganov-Luke Detector

### 6.4.1 Setup

A new light detector has been fabricated to investigate the effect of the Neganov-Luke amplification on the discrimination threshold of the electron and nuclear recoil bands of a *detector module* based on the phonon-light technique. It has been installed in the dilution refrigerator of the neutron-scattering facility at the Maier-Leibnitz-Laboratorium (MLL) for the measurement of quenching factors at cryogenic temperature (see chapter 3). It was the first time that a light detector with Neganov-Luke amplification was used here. The cryostat used at the MLL is a  $^3\text{He}/^4\text{He}$  dilution refrigerator with a base temperature of  $\sim 15$  mK from Oxford Instruments (model Kelvinox 400) [186]. The cooling power is  $400 \mu\text{W}$  at 100 mK.

The cryostat is equipped with 2 Supracon SQUIDs [191] for the read out of both the phonon and the light detector. More details on the setup at the MLL can be found in [154, 155, 156].

A dedicated phonon detector was developed by W. Westphal [151]. A photograph of the detector is shown in Fig. 6.37.

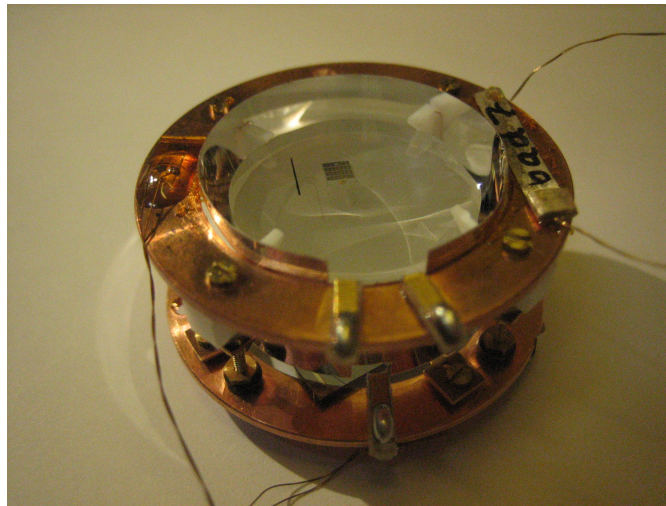


Figure 6.37: Photograph of the phonon detector mounted in the holder presently used in the neutron-scattering facility. The cylindrical CaWO<sub>4</sub> crystal has a diameter of 20 mm and a height of 5 mm. The Ir/Au TES is directly evaporated onto the crystal. A reflective foil provides the reflective housing needed for an efficient light collection. Figure from [204].

It is based on a CaWO<sub>4</sub> cylindrical crystal of 20 mm diameter and 5 mm height. This relatively small size was chosen to provide an efficient collection of non-thermal phonons generated by incident particles in the crystal since this detector is operated above ground and it has to sustain count rates up to  $\sim 10$  Hz. In addition, the double scattering rate of neutrons is reduced in this way which is mandatory for an accurate determination of quenching factors [151]. The Ir/Au TES has been directly evaporated onto the crystal and has been equipped with phonon collectors to reduce the heat capacity maintaining a large collection area of non-thermal phonons in order to provide a high sensitivity. The TES exhibits a steep superconducting transition (width  $\sim 2$  mK) at  $\sim 60$  mK [151]. The  $5\sigma$  energy threshold of this detector is  $\sim 270$  eV and the dynamic range is  $\sim 1.5$  MeV. To operate the detector in calorimetric mode (see chapter 4) the thermal link is provided by Au bond wires connected to a gold pad separated from the TES.

The light detector is again based on the composite design. The absorber is a

6.4. Light Detector Si521 - Measurements at the Maier-Leibnitz-Laboratorium (MLL) with a Neganov-Luke Detector

$20 \times 20 \times 0.25 \text{ mm}^3$  Si disk with a room-temperature resistivity of 2-5  $\text{k}\Omega\text{cm}$  bought from *CrysTec* [196]. The thermometer used here is the same as for the light detector Ge521 (see Appendix A). The thermometer has been removed from the Ge substrate and then coupled to the Si absorber by a small *EPO-TEK* [197] glue spot. For the application of the Neganov-Luke voltage, two Al electrodes ( $19 \times 0.5 \text{ mm}^2$ ) with a thickness of  $\sim 4 \text{ k}\text{\AA}$  have been directly evaporated on each side of the absorber using a shadow mask. A schematic view of the light detector is depicted in Fig. 6.38.

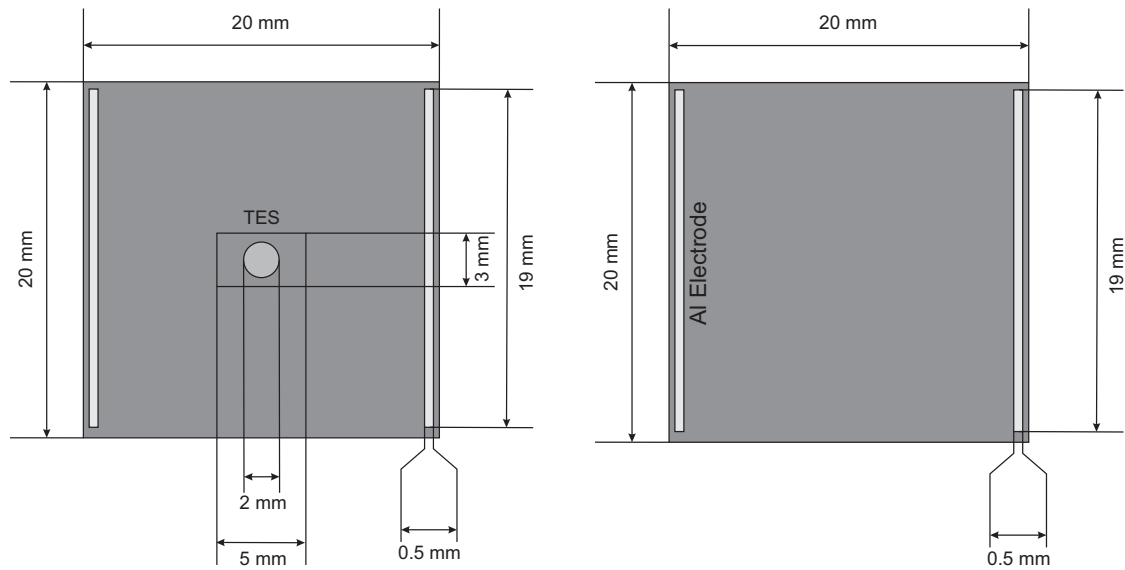


Figure 6.38: *Left panel:* Schematic view of the front side of the composite light detector Si521. It consists of a  $20 \times 20 \times 0.25 \text{ mm}^3$  Si absorber equipped with a glued Si substrate ( $3 \times 5 \times 0.25 \text{ mm}^3$ ) carrying the Ir/Au TES. This side of the absorber is equipped with two ( $19 \times 0.5 \text{ mm}^2$ ) aluminum electrodes for the application of the Neganov-Luke voltage. *Right panel:* Schematic view of the back side of the light detector Si519. Also on this side two ( $19 \times 0.5 \text{ mm}^2$ ) aluminum electrodes have been evaporated using a shadow mask. In this experiment a Neganov-Luke voltage was applied to these electrodes on the back side.

For this detector module a new holder as compared to previous runs at the MLL [154] has been adopted to minimize the neutron scattering rate in the proximity of the  $\text{CaWO}_4$  crystal by reducing the overall mass of the holder [155, 204]. A schematic view is shown in Fig. 6.39.

The light detector and the phonon detector holder consist of two annealed copper rings decoupled from each other thermally. The  $\text{CaWO}_4$  crystal is fixed by teflon supports (bottom) and bronze clamps (top). For the light detector, sintimid clamps are used. The module is enclosed by a reflective foil to improve the light-collection efficiency. The holder is thermally decoupled from the mixing chamber

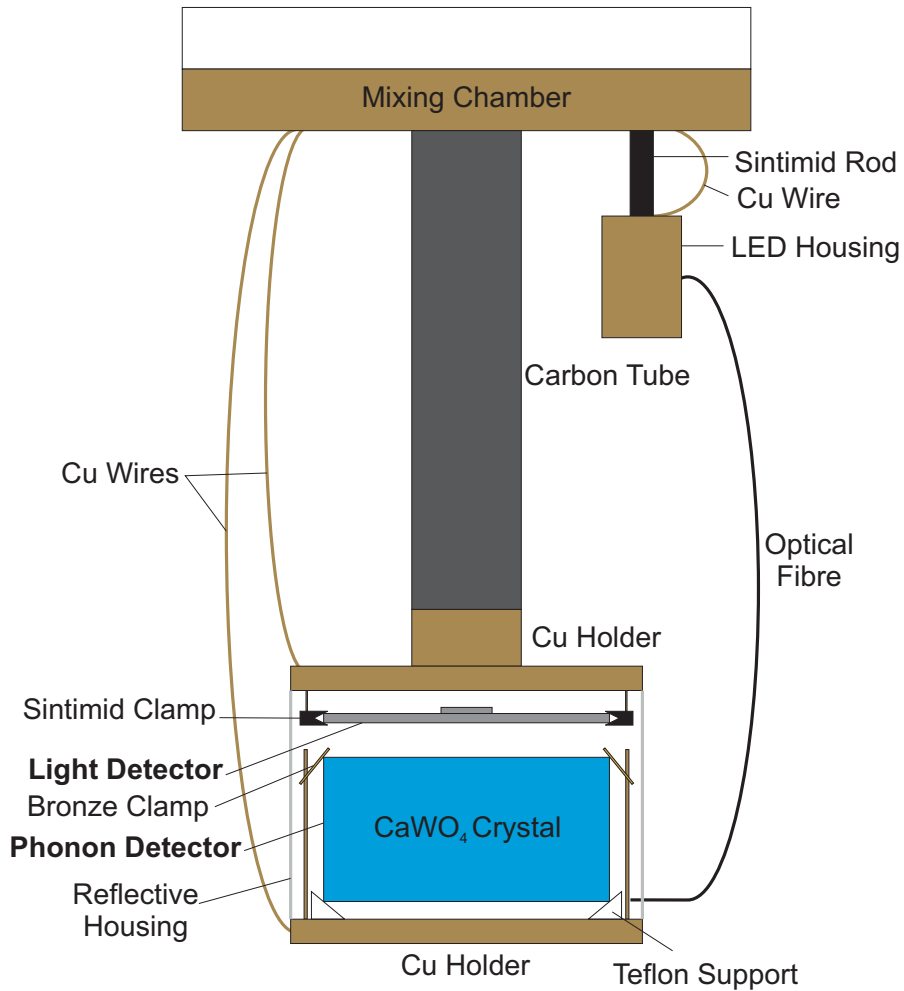


Figure 6.39: Detector setup presently used in the neutron scattering facility at the MLL [155, 204]. The detector module is decoupled from the mixing chamber by a carbon tube. Weak thermal links to both the light detector and the phonon detector holder are provided by thin ( $\sim 0.5$  mm) copper wires. The  $\text{CaWO}_4$  crystal is fixed by teflon supports (bottom) and by bronze clamps (top). For the light detector sintimid clamps are used. The module is enclosed by a reflective housing. The blue InGaN LED needed for light detector calibration and regeneration is mounted in a copper housing decoupled from the mixing chamber by a sintimid rod. A weak thermal coupling is provided by a thin ( $\sim 0.5$  mm) copper wire. The light pulses are injected via an optical fibre through a small hole at the bottom of the reflective housing.

by a carbon tube. Weak thermal links are provided by thin ( $\sim 0.5$  mm) copper wires. The blue InGaN LED needed for the calibration and the regeneration of the light detector is mounted in a light-tight copper housing thermally decoupled from the mixing chamber by a sintimid rod. A weak thermal link is provided by a thin ( $\sim 0.5$  mm) copper wire. The light pulses are injected via an optical fibre into the reflective housing of the detector module.

### 6.4.2 Calibration of the Light Detector

The transition of the light detector was measured in the dilution refrigerator TLE200 (see section 5.2.1). The superconducting transition curve is depicted in Fig. 6.40.

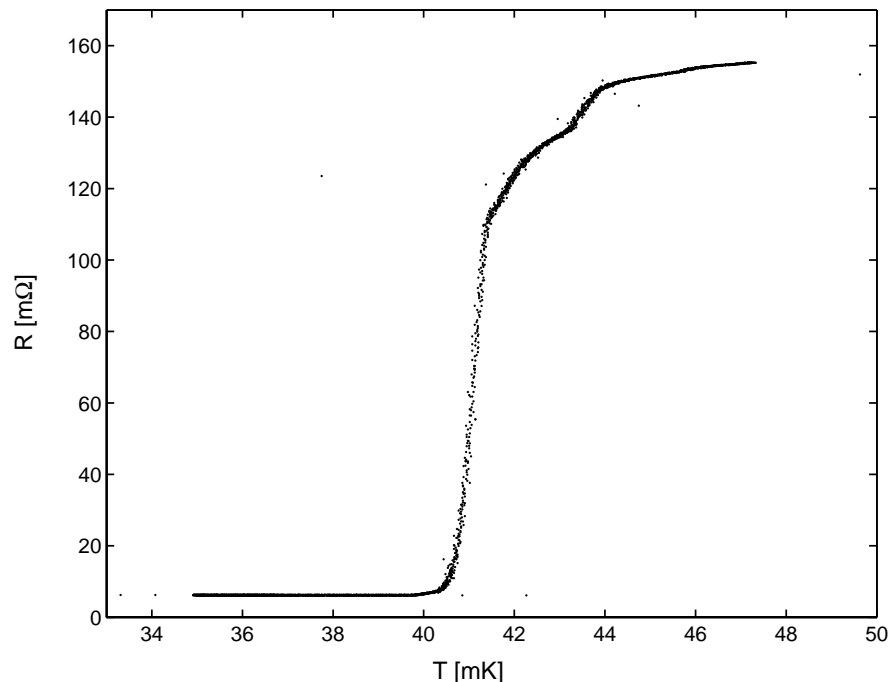


Figure 6.40: Superconducting transition curve of the light detector Si521 measured with a bias current of  $1\mu\text{A}$ . The transition temperature  $T_c$  is at  $\sim 42$  mK. The transition width is  $\sim 4$  mK.

The TES exhibits a transition temperature of  $\sim 42$  mK. In the new setup at the MLL this sensor did not sustain bias currents of the order of  $\gtrsim 100\mu\text{A}$ . Stabilizing the bath temperature well below the transition temperature and biasing the TES with relatively high currents is, however, crucial for the operation of the TES in electrothermal feedback (see chapter 4). Here, the bath temperature was therefore

stabilized only few mK below the transition temperature where an optimal working point was found at a bias current of 30  $\mu\text{A}$ .

At this working point, the detector was calibrated with light. The light pulses needed for recording the  $x - \sigma$  set ( $x$ =peak position,  $\sigma=1\sigma$  peak width, see section 6.2.2.3) have been provided by a pulsed blue InGaN LED operated at base temperature (see Fig. 6.39). Fitting the relationship

$$\sigma = \sqrt{\sigma_0^2 + ax} \quad (6.42)$$

to the  $x - \sigma$  set yields:

$$\sigma_0 = 0.65 \pm 0.13 \text{ nA} \quad (6.43)$$

$$a = (10.6 \pm 0.4) \cdot 10^{-2} \text{ nA}. \quad (6.44)$$

The measured  $x - \sigma$  set together with the fitted function are depicted in Fig. 6.41.

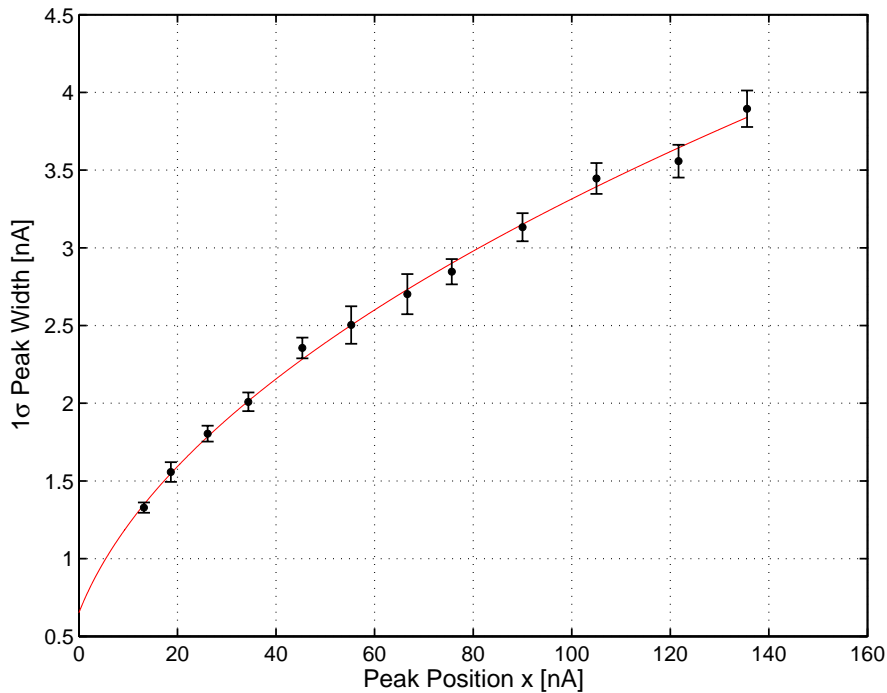


Figure 6.41: Measured  $1\sigma$  width of the light peaks versus peak position fitted by the relationship 6.42. The error bars correspond to the  $2\sigma$  error (95% C.L.).

With a  $1\sigma$  width of the baseline of  $0.54 \pm 0.02$  nA obtained by fitting a template pulse to noise samples, a  $5\sigma$  energy threshold of  $74 \pm 4$  eV is reached. The

calibration of the light detector has been performed after the beam time at the MLL. When comparing the current spectral densities (see Fig. 6.42) calculated from noise samples recorded for calibration and during the beam time, it becomes evident that the detector performance was worse during the beam time. Especially in the low-frequency region the noise level was higher by a factor of  $\sim 2$ . The energy threshold can therefore be assumed to have been  $\sim 150$ - $200$  eV during the beam time. The reason for this increased noise level is not yet clarified. However, there exist strong indications that electronic interference as well as mechanical vibrations caused by various parts of the experimental setup were the main reasons.

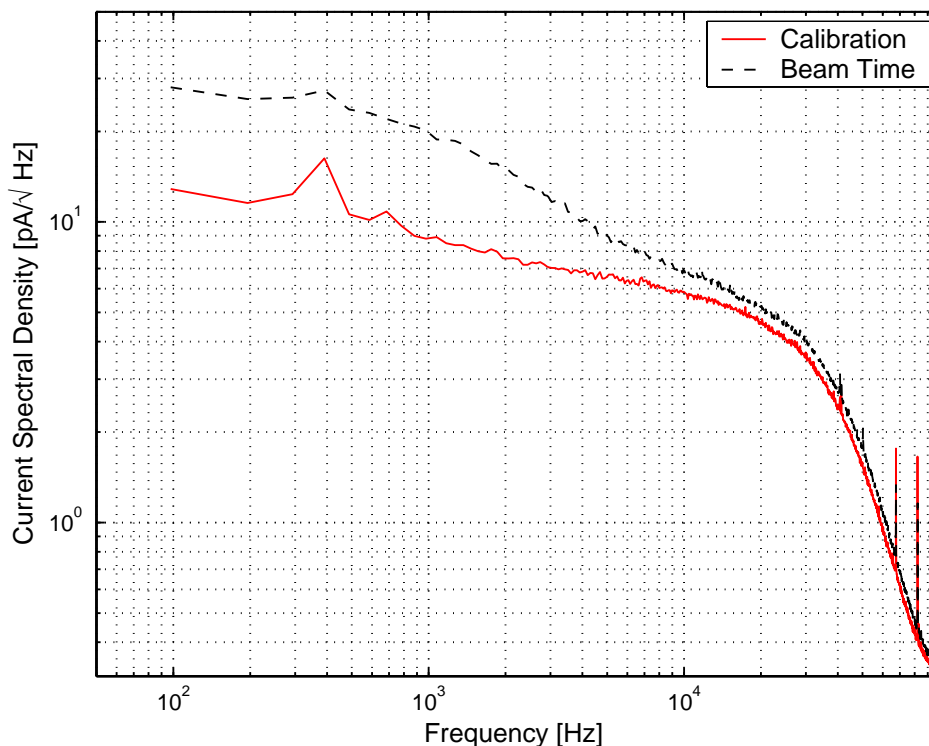


Figure 6.42: Current spectral densities calculated from noise samples recorded during the beam time and for calibration. During the beam time the noise level was considerably higher indicating a higher threshold of  $\sim 150$ - $200$  eV.

### 6.4.3 Performance of the Light Detector in Neganov-Luke Mode

To investigate the effect of the Neganov-Luke amplification on the discrimination threshold of the electron and nuclear recoil bands the light detector was operated

## 6. Results and Discussion

in Neganov-Luke mode. In this setup the back side of the light detector Si521 was facing the  $\text{CaWO}_4$  crystal (see Fig. 6.38) and only the electrodes on this side have been connected to the HV supply.

In operation, the detector also showed the additional noise discussed in section 6.2.3.2. By applying a voltage 30 V higher than the nominal NL voltage for  $\sim 30$  min, however, did not remove this noise in contrast to the detectors operated in the dilution refrigerator TLE 200. Although this behaviour has not yet been clarified it is very likely that it is related to the different setup especially with the new holder based on sintimid clamps rather than sapphire spheres. This conclusion can be drawn from measurements performed with the light detector Si519 (see section 6.3) at the MLL in the same setup showing the same behaviour as this light detector Si521.

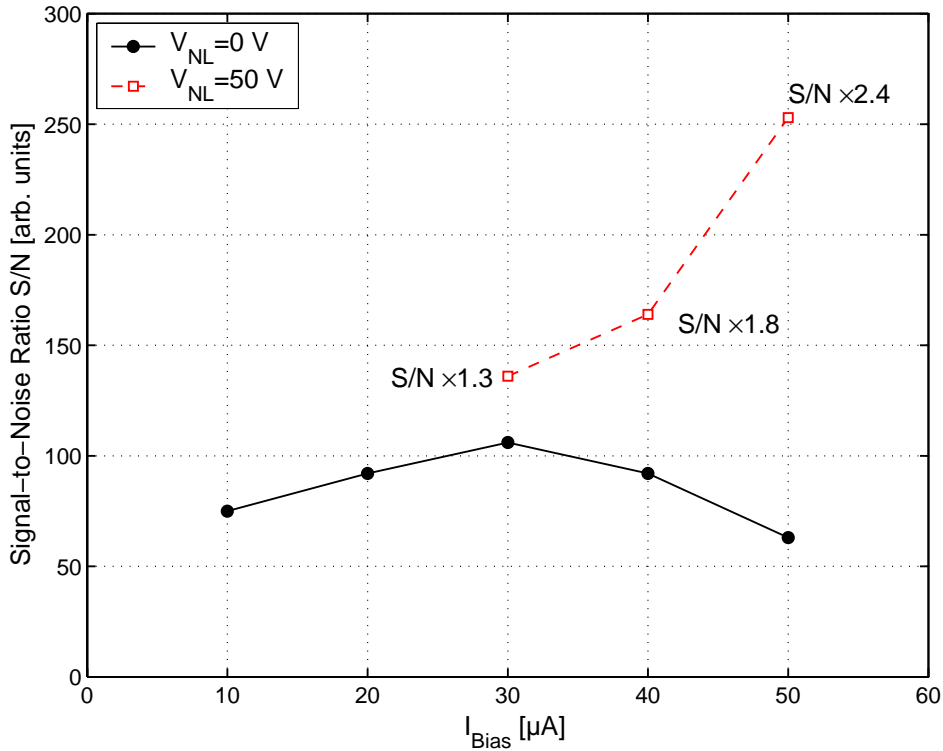


Figure 6.43: Signal-to-noise ratios (S/N) of the light detector for bias currents  $I_{\text{Bias}}$  between 10-50  $\mu\text{A}$  at 0 V (full circles). The squares indicate the S/N achieved at a Neganov-Luke voltage of 50 V between 30-50  $\mu\text{A}$ . For each bias current at 50 V the improvement of the S/N relative to the S/N at 30  $\mu\text{A}$  and 0 V is also shown. At a bias current of 50  $\mu\text{A}$  the S/N was improved by a factor of 2.4.

Prior to applying a voltage to the detector the S/N was optimized using the pulsed

blue LED operated at base temperature (see Fig. 6.39). The bias current was varied between 10 and 50  $\mu\text{A}$  in decimal steps. The resulting signal-to-noise ratios are shown in Fig. 6.43 (full circles). An optimal value has been obtained at a bias current of 30  $\mu\text{A}$ .

At this working point the S/N was only improved by a factor of  $\sim 1.3$  at a voltage of 50 V applied by the method discussed in section 6.2.3.3. It turned out, however, that by increasing the bias current the S/N could be further improved reaching an optimal value of 2.4 at  $I_{\text{Bias}}=50 \mu\text{A}$  (see squares in Fig. 6.43). This effect can be explained in terms of electrothermal feedback. By increasing the bias current the voltage-bias conditions for the TES discussed in chapter 4 are better fulfilled leading to a suppression of the low-frequency noise providing an improvement of the signal-to-noise ratio. Since neither for still higher voltages nor for the reverse Neganov-Luke voltage a significant improvement could be observed the detector was operated at a bias current of 50  $\mu\text{A}$  and at 50 V for the neutron calibration of the detector module.

To see the effect of the Neganov-Luke voltage a first calibration measurement at a Neganov-Luke voltage of 0 V of the detector module has been performed using an AmBe neutron source as well as a  $^{133}\text{Ba}$   $\gamma$  source for the calibration of the phonon channel. The amplitude of the light signal (electron equivalent energy) as measured by the light detector versus the phonon energy is depicted in Fig. 6.44 (top panel). Here, the discrimination threshold of the electron and nuclear recoil bands is at  $\sim 30$  keV.

The neutron calibration of the detector module with an applied Neganov-Luke voltage of 50 V was performed with the 11 MeV neutrons provided by the tandem accelerator at the MLL [154]. In addition, the  $^{133}\text{Ba}$   $\gamma$  source has again been used for the calibration of the phonon channel. The light versus phonon amplitude (recoil energy) is depicted in Fig. 6.44 (bottom panel).

Due to the higher sensitivity of the light detector provided by the Neganov-Luke effect the discrimination threshold of the electron and nuclear recoil bands is  $\sim 10$  keV. This corresponds to an enormous improvement as compared to the reference measurement at 0 V. This discrimination threshold is the best ever achieved at our institute even though the improvement of the signal-to-noise ratio is still much smaller as compared to the light detectors Si518 and Si519 (see sections 6.2 and 6.3) operated in the dilution refrigerator TLE 200. The same performance as with the detectors Si518 and Si519 might be achieved with a holder similar to that employed in the dilution refrigerator TLE200 (see Fig. 5.5). This includes the small sapphire spheres the detector absorber was placed on as well as a more elaborate and massive copper holder to provide similar configurations of the electric field as for the Si518 and Si519 detectors when operating the light detector in Neganov-Luke mode.

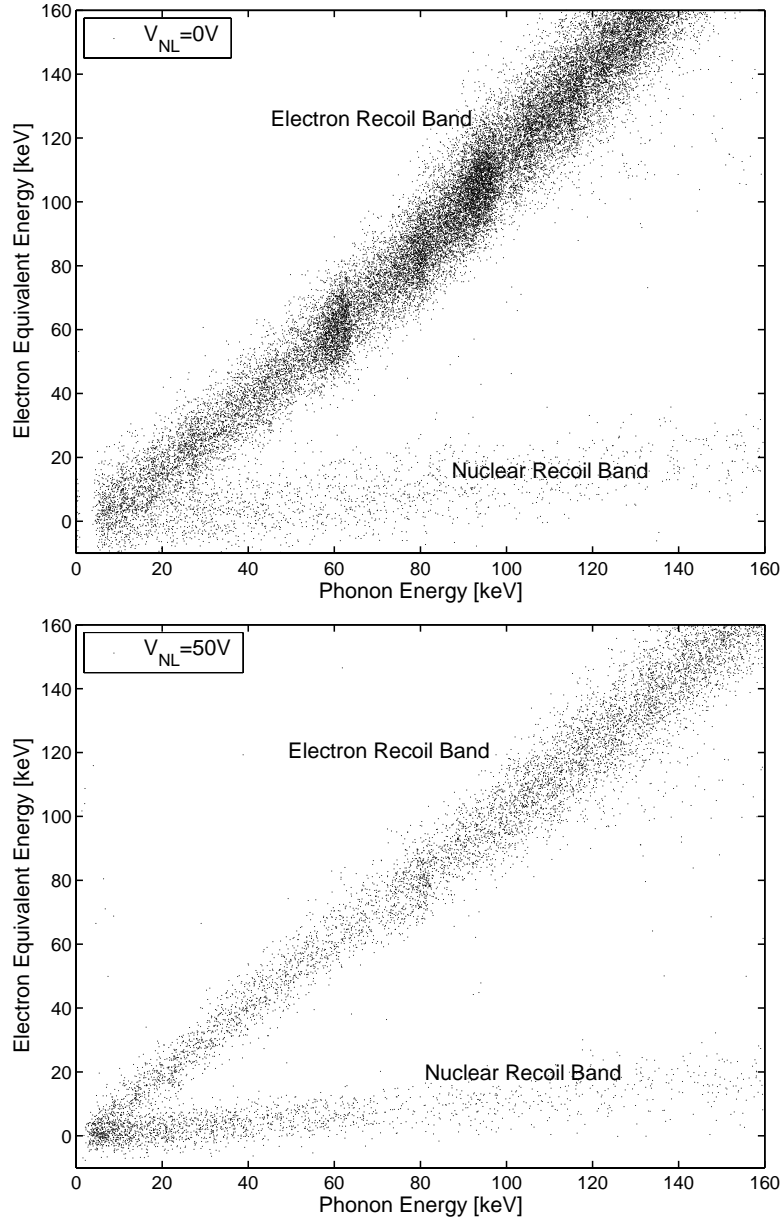


Figure 6.44: Light amplitude (electron equivalent energy) versus phonon amplitude (recoil energy) measured by the detector module installed in the neutron-scattering facility at the MLL. *Top Panel:* Detector response with no Neganov-Luke voltage applied (0 V). The phonon channel has been calibrated by a  $^{133}\text{Ba}$   $\gamma$  source and an AmBe neutron source. The discrimination threshold between the electron and nuclear recoil bands is at  $\sim 30$  keV. *Bottom Panel:* Detector response with an applied Neganov-Luke voltage of 50 V. The phonon channel has been calibrated by a  $^{133}\text{Ba}$  source. The 11 MeV neutrons have been provided by the tandem accelerator at the MLL. Due to the lower threshold of the light detector provided by the Neganov-Luke amplification at a voltage of 50 V the discrimination threshold has been reduced to  $\sim 10$  keV.

# Chapter 7

## Conclusions and Outlook

The CRESST (Cryogenic Rare Event Search with Superconducting Thermometers) experiment searches for particle Dark Matter (WIMPs) via the coherent scattering off the nuclei in terrestrial  $\text{CaWO}_4$  target crystals operated at mK temperatures. The simultaneous measurement of the phonons and the scintillation light induced by particles in the  $\text{CaWO}_4$  crystals provides an efficient technique for the discrimination of the background induced by electron recoils. This detection scheme, also referred to as phonon-light technique, will play a crucial role in the future ton-scale EURECA (European Underground Rare Event Calorimeter Array) experiment since it is the only cryogenic detection scheme allowing the use of a multi-element target to probe the  $A^2$  dependence of the WIMP-nucleon cross section. Considering the large number of detectors needed for EURECA which have to be fabricated on a short time scale a simple and reproducible way for detector fabrication is required. This aim seems to become feasible by the composite detector design (CDD) developed at our institute. Here, the transition edge sensor (TES) needed for the measurement of the phonon energy is evaporated onto a separate small crystalline substrate which is then coupled to the absorber by gluing. This technique offers the opportunity to produce a large number of TESs in one step and to test them prior to their coupling to the main absorber. It further reduces the introduction of impurities into the absorber crystal and minimizes the degradation of the light output of scintillating crystals due to the high temperatures involved in the fabrication processes of the TES.

In this thesis cryogenic light detectors based on the CDD have been developed. The TESs consisting of Ir/Au bilayers have been evaporated onto small ( $3 \times 5 \text{ mm}^2$ ) silicon substrates using a shadow mask carrying eight of the small substrates. Without further structuring processes of the thin film as employed in earlier schemes the substrates have then been coupled to  $20 \times 20 \text{ mm}^2$  high-purity silicon or germanium absorbers by gluing. For detector characterization a new method based on photon statistics has been developed. The light used for detec-

tor calibration has been provided by pulsed blue LEDs operated either at room temperature or at 4K and was injected into the detector via optical fibres installed in the cryostat. With energy thresholds ranging between  $\sim 100$ - $200$  eV, the light detectors based on the CDD exhibit a similar performance as those with directly evaporated TESs.

The major drawback of the phonon-light technique arises from the small fraction ( $\sim 1\%$ ) of the energy deposited in the  $\text{CaWO}_4$  crystal detected as light. Since this fraction is further reduced for nuclear recoils ( $\gtrsim 10$ ), the small amount of detected scintillation light is the limiting factor with respect to the discrimination threshold of the detectors currently employed in CRESST. In addition, it further reduces the resolving power of the light channel and impedes the separation of the individual nuclei (O, Ca, W) in the nuclear recoil band. Such a separation would even enable a discrimination of the neutron background since neutrons in the energy region of interest for the Dark Matter search (10-40 keV) mainly scatter off oxygen and calcium whereas WIMPs are expected to mainly induce tungsten recoils. This drawback can be overcome with more sensitive light detectors. Following Neganov, Trofimov and Luke, the sensitivity of a cryogenic detector based on a semiconducting absorber can be improved by drifting the photon-induced electron-hole pairs by an applied electric field. The drifting charge carriers produce additional phonons and amplify the signal in this way.

For the application of a voltage to the absorber, aluminum electrodes have been directly evaporated onto the silicon absorber of the light detector. To avoid most of the additional noise that is usually observed when the light detectors are operated in Neganov-Luke mode a new method for the application of the Neganov-Luke voltage has been developed. Here, prior to applying the nominal voltage to the absorber, a 20-30 V higher voltage is first applied for  $\sim 30$  min to erode the shallow traps present in the absorber which otherwise would cause the additional noise. An improvement of the signal-to-noise ratio by a factor of  $\sim 10$  can be achieved in this way. The voltage needed for this improvement depends on the geometry of the electrodes. With four equidistant electrodes evaporated on one side of the absorber this increase by an order of magnitude has been achieved with 60 V, whereas the corresponding voltage for a light detector with only two electrodes was 100 V. With four electrodes, the local field strength, however, is higher and the detector can become unstable against a sudden break-down.

A major drawback of light detectors with Neganov-Luke amplification is the decreasing pulse height with time due to space charges building up presumably at the aluminum-silicon interface of the electrodes. Therefore an efficient technique for the regeneration of the light detector has been developed, i.e., for the removal of the accumulated space charges: After turning off the voltage the detector is flashed by light provided by a LED for  $\sim 10$  s. This technique provides an efficient way to reestablish the initial uncompensated amplification. To improve the resolution of

---

the light detector when operated in Neganov-Luke mode, a pulsed LED has been used to monitor the decreasing pulse height which enabled an offline correction of the pulse heights. The decrease of the amplification strongly depends on the deposited energy per unit of time. Therefore, in the low-background environments of the direct Dark Matter experiments, this effect should not be a limiting factor and the detector has to be regenerated only after several hours of operation.

Although the light detectors with Neganov-Luke amplification show a very satisfactory performance, there are still several improvements needed, concerning mainly the electrodes. Up to now, the electrodes consist of thin aluminum layers directly evaporated onto the silicon absorber. For this reason they are poorly defined and behave rather as Schottky than Ohmic contacts and become unstable against sudden break-down at higher field strengths. A possible solution might be provided by degenerately doped p-type ( $p^{++}$ ) and n-type ( $n^{--}$ ) contacts. Here, the Fermi level is shifted into the valence and the conduction band, respectively, providing a high conductivity even at mK temperatures. A reverse-bias operation should further impede the electrode break-down.

Even with highly-doped contacts, the method developed for the application of the voltage will still be needed, since the different electrode design would not reduce the presence of the shallow traps in the absorber. The solution to this drawback might be imbedded degenerately-doped electrodes between a sapphire substrate and a thin silicon layer as provided by silicon-on-sapphire (SOS) substrates.

To see the effect of the Neganov-Luke amplification on the discrimination threshold of a detector module, a neutron calibration has been performed at the neutron-scattering facility at the Maier-Leibnitz-Laboratorium (MLL). Here, an improvement by a factor of  $\sim 2.4$  of the signal-to-noise ratio of the light detector could be achieved due to the Neganov-Luke effect. It helped reducing the discrimination threshold of the detector module from  $\sim 30$  keV to  $\sim 10$  keV which is the best result ever achieved at our institute as compared to detector modules employing light detectors without Neganov-Luke amplification. Even though these results are highly satisfying a performance of the light detectors with an improvement of the sensitivity by a factor of  $\sim 10$  should provide even better results as long as there is no limitation by photon statistics. For this reason, it is mandatory to improve the light output of the  $\text{CaWO}_4$  crystals in addition to the employment of light detectors with Neganov-Luke amplification.

The results obtained in this thesis clearly indicate the enormous relevance of the light detectors with Neganov-Luke amplification for the Dark Matter experiments CRESST and EURECA. Due to the greatly improved discrimination threshold of the electron and nuclear recoil bands the overall sensitivity is drastically enhanced by such a detector. In addition, the improved energy resolution of the light channel will help discriminating the background induced by neutrons which is the limiting factor of the sensitivity at present.

## *7. Conclusions and Outlook*

---

# Appendix A

## Light Detector Ge521

Up to now the electrical and thermal links of the transition edge sensors have been provided by thin ( $25\ \mu\text{m}$  in diameter) aluminum and gold wires connected via ultrasonic bonding. This well-proven technique allows the electrical connection even of very small structures as well as defined thermal links of the sensor to the heat sink. However, the connection of the TES via bond wires turns out to be very fragile and they are very likely to induce noise due to vibrations of the wires.

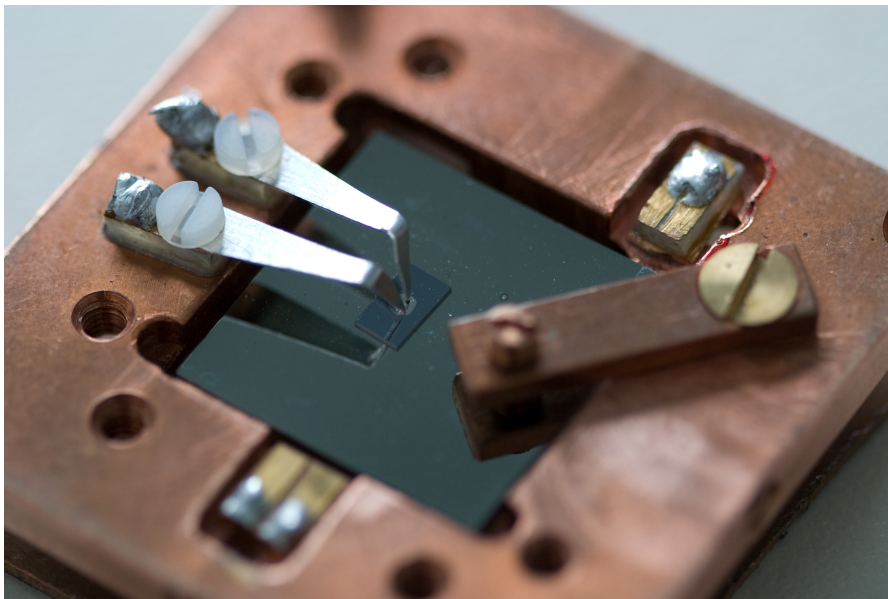


Figure 7.1: Photograph of the light detector Ge521 mounted in a copper holder. The bond wires have been replaced by two aluminum clamps.

These shortcomings can be eliminated by replacing the bond wires by mechanically more stable connections. Such a detector which is also based on the composite

design is depicted in Fig. 7.1. It consists of a  $20 \times 20 \times 0.25$  mm<sup>3</sup> germanium absorber with a room-temperature resistivity of  $>30$   $\Omega$ cm. The TES is evaporated onto a  $3 \times 5 \times 0.25$  mm<sup>3</sup> silicon substrate coupled to the absorber by gluing. Both the germanium and the silicon substrate have been provided by *CrysTec* [196]. The electrical connections consist of thin ( $\sim 250$   $\mu$ m) aluminum clamps with a short tip at one end in order to provide point-like connections to the TES. For this first test, no additional thermal link of the TES to the copper holder (heat sink) has been employed. Therefore, the thermal coupling of the TES to the heat sink is weak since Al is superconducting at the low operating temperatures of the TES. This effect can be clearly seen in Fig. 7.2. Here, the transition curves of the sensor measured with different currents ranging from 0.1 to 1  $\mu$ A are depicted. At high currents, the TES could no longer reach the superconducting state completely which can be mainly ascribed to the weak thermal coupling to the heat sink. This in turn influences the operation of the TES since it strongly curtails the  $T_{\text{Bath}}-I_{\text{Bias}}$  parameter set (see section 6.2.2.1).

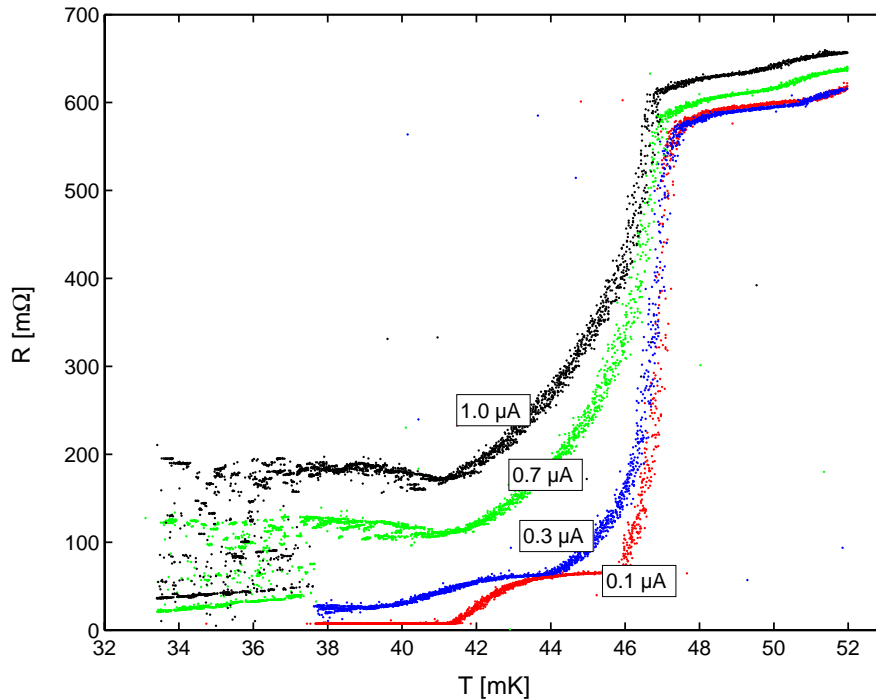


Figure 7.2: Transition curves of the light detector Ge521 (see Fig. 7.1) recorded with different currents. The transition temperature  $T_c$  is at  $\sim 47$  mK and the widths vary according to the applied bias current (0.1-1  $\mu$ A).

Nevertheless, a working point could be found where the detector shows a perfor-

mance comparable to detectors with electrical and thermal links provided by bond wires. A histogram of the Mn-K $_{\alpha}$  (5.9 keV) and the Mn-K $_{\beta}$  (6.4 keV) lines is depicted in Fig. 7.3. The FWHM energy resolution at 5.9 keV is  $\Delta E_{\text{FWHM}}=128$  eV. The  $5\sigma$  energy threshold derived from noise samples by template fitting is  $\Delta E_{5\sigma}=106$  eV.

Still, despite of these satisfying results, for an operation of the detector in the optimal working point an additional thermal link is needed. Such a link can be provided by an additional gold-coated Al clamp coupled to the Cu holder.

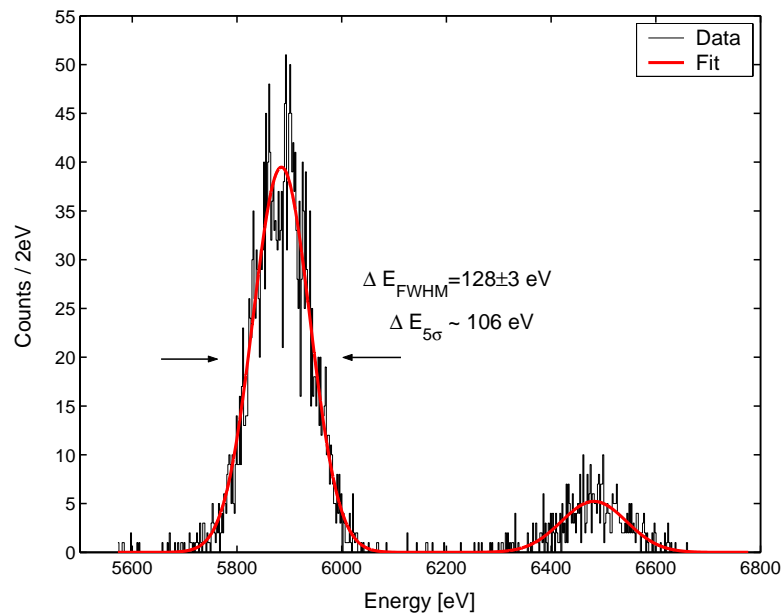


Figure 7.3: Histogram of the Mn-K $_{\alpha}$  (5.9 keV) and Mn-K $_{\beta}$  (6.4 keV) lines obtained from a  $^{55}\text{Fe}$  source.



# Appendix B

## Current Spectral Density

A very powerful tool for the analysis of discrete time-domain signals as acquired by an analog-to-digital converter (ADC) is the decomposition into its frequency components which is based on the discrete Fourier transform (DFT). In practice the DFT of a signal can be efficiently calculated using a fast Fourier transform (FFT) algorithm. The FFT is equivalent to a set of parallel filters of bandwidth  $\Delta f$  centered at each frequency increment from [198]

$$\text{DC to } \left( \frac{F_S}{2} - \frac{F_S}{N} \right). \quad (7.1)$$

Here,  $F_S$  denotes the sampling frequency and  $N$  the number of acquired samples. According to the Nyquist theorem, the highest frequency that can be sampled at a sampling frequency  $F_S$  is  $F_S/2$ . Since, however, the number of samples that can be acquired with the DAQ system used in this thesis are powers of 2 ranging from  $N = 128$  to 524288, the highest frequency for a selected  $N$  is  $(F_S/2) - (F_S/N)$ . The bandwidth  $\Delta f$  is given by

$$\Delta f = \frac{F_S}{N} = \frac{1}{N\Delta t}, \quad (7.2)$$

where  $\Delta t = 1/F_S$  is the sampling period (time base) and  $N\Delta t$  the duration of the recorded time-domain signal [198].

For a time-domain signal  $x[n]$  ( $n = 0 \dots N - 1$ ) consisting of  $N$  samples the FFT yields a complex vector  $X[k]$  ( $k = 0 \dots N - 1$ ) of length  $N$ . The amplitude  $Amp(k)$  of each component  $X(k)$  of the frequency-domain signal can be calculated from the corresponding magnitude  $|X(k)|$  and the number of acquired samples  $N$ :

$$Amp(k) = \frac{|X(k)|}{N} = \frac{\sqrt{X(k) \cdot X^*(k)}}{N} \text{ for } k = 0 \dots N - 1, \quad (7.3)$$

where  $X^*(k)$  denotes the complex conjugate of  $X(k)$ . The amplitude spectrum is given in the units of the time-domain signal. For cryogenic detectors based on

transition edge sensors a typical unit is pA.

The FFT returns a so-called two-sided spectrum since according to the Nyquist theorem the highest frequency that can be acquired at a sampling frequency  $F_S$  is  $F_S/2$ - $F_S/N$  taking an even-number length of the samples into account, as mentioned above. Therefore, the frequency information contained in the second half of the frequency-domain signal is redundant. In the two-sided form the amplitude spectrum contains only half the peak amplitude in the frequency range up to  $(F_S/2)$ - $(F_S/N)$ . To convert to the single-sided form each amplitude in the first half has to be multiplied by two (except for the DC component) whereas the second half is discarded [198].

In electrical engineering it is common to use the root mean square (RMS) amplitude. To convert the amplitude spectrum into RMS units each non-DC component has to be divided by  $\sqrt{2}$ . A single-sided RMS amplitude spectrum is then given by

$$Amp(0) = \frac{|X(0)|}{N} \text{ (DC)} \quad (7.4)$$

$$Amp(k) = \sqrt{2} \cdot \frac{|X(k)|}{N} \text{ for } k = 1 \dots N/2 - 1. \quad (7.5)$$

In this representation, however, the amplitudes are arbitrary since they depend on the sampling frequency  $F_S$  and the number of acquired samples  $N$ . It is therefore common to use a normalized representation related to a frequency increment of 1 Hz. The amplitude spectrum in normalized form is referred to as amplitude spectral density (ASD) and is given by

$$ASD = \frac{Amp}{\sqrt{\Delta f}}. \quad (7.6)$$

In practice the ASD is determined by averaging the ASDs of several thousand pulses or noise samples for a more accurate representation. For cryogenic detectors based on transition edge sensors the amplitude spectral density corresponds to a current spectral density and is typically given in units of pA/ $\sqrt{\text{Hz}}$ . More details on FFT-based signal analysis can be found in [198].

# Bibliography

- [1] R. C. Alig, Phys. Rev. B **27**, 968 (1983).
- [2] E. Simon *et al.*, Nucl. Instrum. and Meth. in Phys. Res. A **507**, 643 (2003).
- [3] U. Fano, Phys. Rev. **72**, 26 (1947).
- [4] G. Lutz, *Semiconductor Radiation Detectors* (Springer-Verlag, Berlin, 1999).
- [5] S. H. Moseley, J. C. Mather, and D. McCammon, J. Appl. Phys. **56**, 1257 (1984).
- [6] B. Neganov and V. Trofimov, Otkrytia i izobreneniya **146**, 215 (1985).
- [7] P. N. Luke, J. Appl. Phys. **64**, 6858 (1988).
- [8] G. Jungmann, M. Kamionkowski, and K. Griest, Phys. Rep. **267**, 195 (1996).
- [9] M. Persic, P. Salucci, and F. Stel, Mon. Not. R. Astron. Soc. **281**, 27 (1996).
- [10] K. G. Begeman, A. H. Broeils, and R. H. Sanders, Mon. Not. R. Astron. Soc. **249**, 439 (1991).
- [11] K. C. Freeman, Astrophys. J. **160**, 811 (1970).
- [12] F. Zwicky, Helv. Phys. Acta **6**, 110 (1933).
- [13] C. L. Sarazin, Rev. Mod. Phys. **58**, 1 (1986).
- [14] J. N. Hewitt *et al.*, Nature **333**, 537 (1988).
- [15] N. Ota, K. Mitsuda, and Y. Fukazawa, Astrophys. J. **495**, 170 (1998).
- [16] D. Clowe, A. Gonzalez, and M. Markevitch, Astrophys. J. **604**, 596 (2004).
- [17] D. Clowe, M. Bradac, A. H. Gonzalez, and M. Markevitch, Astrophys. J. Lett. **648**, 109 (2006).

- [18] L. Bergström and A. Goobar, *Cosmology and Particle Astrophysics*, 2nd ed. (Springer, Berlin, 2004).
- [19] E. Hubble, Proc. Nat. Acad. Sci **15**, 168 (1929).
- [20] G. Hinshaw *et al.*, arXiv:astro-ph/0803.0732v1, 2008.
- [21] W.-M. Yao *et al.*, J. Phys. G **33**, 1 (2006).
- [22] D. Tytler, J. M. O’Meara, N. Suzuki, and D. Lubin, Phys. Scr. **T85**, 12 (2000).
- [23] M. Fukugita, C. J. Hogan, and P. J. E. Peebles, Astrophys. J. **503**, 518 (1998).
- [24] G. Gamow, Phys. Rev. **70**, 572 (1946).
- [25] R. A. Alpher and R. C. Herman, Nature **162**, 774 (1948).
- [26] A. A. Penzias and R. W. Wilson, Astrophys. J. **142**, 419 (1965).
- [27] E. Gawiser and J. Silk, Phys. Rept. **333**, 245 (2000).
- [28] J. C. Mather *et al.*, Astrophys. J. **512**, 511 (1999).
- [29] G. Smoot, arXiv:astro-ph/9705101v2, 1997.
- [30] G. F. Smoot *et al.*, Astrophys. J. Lett. **396**, 1 (1992).
- [31] G. Hinshaw *et al.*, Astrophys. J. Suppl. **170**, 288 (2007).
- [32] J. Silk, Astrophys. J. **151**, 459 (1968).
- [33] M. R.olta *et al.*, arXiv:astro-ph/0803.0593v1, 2008.
- [34] C. Alcock *et al.*, Astrophys. J. **542**, 281 (2000).
- [35] C. Afonso *et al.*, Astron. Astrophys. **400**, 951 (2003).
- [36] J. R. Primack, arXiv:astro-ph/9707285v2, 1997.
- [37] G. Bertone, D. Hooper, and J. Silk, Phys. Rept. **405**, 279 (2005).
- [38] V. M. Lobashev *et al.*, Nucl. Phys. B (Proc. Suppl.) **91**, 280 (2001).
- [39] C. Kraus *et al.*, Eur. Phys. J. C **40**, 447 (2005).
- [40] R. D. Peccei and H. R. Quinn, Phys. Rev. Lett **38**, 1440 (1977).

- 
- [41] L. Bergström, Rep. Prog. Phys. **63**, 793 (2000).
- [42] S. Andriamonje *et al.*, arXiv:hep-ex/0702006v3, 2007.
- [43] J. Ellis, A. Ferstl, and K. A. Olive, Phys. Rev. D **63**, 065016 (2001).
- [44] L. Serin, arXiv:hep-ex/0010049v1, 2000.
- [45] D. G. Cerdeno *et al.*, arXiv:hep-ph/0509275v2, 2007.
- [46] H. Pagels and J. R. Primack, Phys. Rev. Lett. **48**, 223 (1982).
- [47] M. Bolz, A. Brandenburg, and W. Buchmüller, Nucl. Phys. B **606**, 518 (2001).
- [48] W. Buchmüller *et al.*, JHEP **0703**, 037 (2007).
- [49] F. Takayama and M. Yamaguchi, Phys. Lett. B **485**, 388 (2000).
- [50] A. Ibarra and D. Tran, Phys. Rev. Lett. **100**, 061301 (2008).
- [51] A. Ibarra and D. Tran, JCAP **0807**, 002 (2006).
- [52] K. Ishivata, S. Matsumoto, and T. Moroi, arXiv:hep-ph/0805.1133v2, 2008.
- [53] A. Ibarra, arXiv:hep-ph/0809.2067v1, 2008.
- [54] M. Milgrom, Ann. Phys. **229**, 384 (1994).
- [55] M. Milgrom, Astrophys. J. **455**, 439 (1995).
- [56] M. Milgrom, Astrophys. J. **478**, 7 (1997).
- [57] R. H. Sanders, Astrophys. J. **473**, 117 (1996).
- [58] W. H. Press and D. N. Spergel, Astrophys. J. **296**, 679 (1985).
- [59] L. M. Krauss, M. Srednicki, and F. Wilczek, Phys. Rev. D **33**, 2079 (1986).
- [60] O. Suvorova, arXiv:hep-ph/9911415v1, 1999.
- [61] M. Ambrosio *et al.*, Phys. Rev. D **60**, 082002 (1999).
- [62] S. Desai *et al.*, Phys. Rev. D **70**, 083523 (2004).
- [63] I. A. Belolaptikov *et al.*, Astropart. Phys. **7**, 263 (1997).
- [64] V. Aynutdinov *et al.*, arXiv:astro-ph/0507709v1, 2005.

- [65] E. Andres *et al.*, *Nature* **410**, 441 (2001).
- [66] M. Ackermann *et al.*, *Astropart. Phys.* **24**, 459 (2006).
- [67] P. Amram *et al.*, *Nucl. Instrum. and Meth. in Phys. Res. A* **484**, 369 (2002).
- [68] S. E. Tzamarias, *Nucl. Instrum. and Meth. in Phys. Res. A* **502**, 150 (2003).
- [69] J. Ahrens *et al.*, *Astropart. Phys.* **20**, 507 (2004).
- [70] L. Bergström and P. Ullio, *Nucl. Phys. B* **504**, 27 (1997).
- [71] P. Ullio and L. Bergström, *Phys. Rev. D* **57**, 1962 (1998).
- [72] W. de Boer *et al.*, *Phys. Lett. B* **636**, 13 (2006).
- [73] D. Elsaesser and K. Mannheim, *Phys. Rev. Lett* **94**, 171303 (2005).
- [74] P. Ullio, L. Bergström, J. Edsjo, and C. G. Lacey, *Phys. Rev. D* **66**, 123502 (2002).
- [75] A. Ibarra and D. Tran, arXiv:astro-ph/0804.4596v1, 2008.
- [76] P. Jean *et al.*, *Astron. Astrophys. Lett.* **407**, 55 (2003).
- [77] C. Boehm *et al.*, *Phys. Rev. Lett* **92**, 101301 (2004).
- [78] P. Fayet, *Phys. Rev. D* **70**, 023514 (2004).
- [79] O. Adriani *et al.*, *Nature* **458**, 607 (2009).
- [80] S. W. Barwick *et al.*, *Astrophys. J. Lett.* **482**, 191 (1997).
- [81] J. Chang *et al.*, *Nature* **456**, 362 (2008).
- [82] D. Hooper, P. Blasi, and P. D. Serpico, arXiv:astro-ph/0810.1527v2, 2009.
- [83] L. Bergström, T. Bringmann, and J. Edsjo, *Phys. Rev. D* **78**, 103520 (2008).
- [84] I. Cholis *et al.*, arXiv:hep-ph/0809.1683v1, 2008.
- [85] G. Dobler and D. P. Finkbeiner, *Astrophys. J.* **680**, 1222 (2008).
- [86] D. Hooper, D. P. Finkbeiner, and G. Dobler, *Phys. Rev. D* **76**, 083012 (2007).
- [87] D. Hooper, G. Zaharijas, D. P. Finkbeiner, and G. Dobler, *Phys. Rev. D* **77**, 043511 (2008).

- 
- [88] M. W. Goodman and E. Witten, Phys. Rev. D **31**, 3059 (1985).
- [89] J. Binney and S. Tremaine, *Galactic Dynamics* (Princeton University Press, Princeton, 1987).
- [90] F. J. Kerr and D. Lynden-Bell, Mon. Not. R. Astron. Soc. **221**, 1023 (1986).
- [91] K. Freese, J. Frieman, and A. Gould, Phys. Rev. D **37**, 3388 (1988).
- [92] A. Bottino *et al.*, Phys. Lett. B **402**, 113 (1997).
- [93] R. H. Helm, Phys. Rev. **104**, 1466 (1956).
- [94] J. D. Lewin and P. F. Smith, Astropart. Phys. **6**, 87 (1996).
- [95] G. Heusser, Annu. Rev. Nucl. Part. Sci. **45**, 543 (1995).
- [96] G. Chardin, arXiv:astro-ph/0411503v2, 2005.
- [97] W. Westphal *et al.*, J. Low Temp. Phys. **151**, 824 (2008).
- [98] A. Drukier, K. Freese, and D. Spergel, Phys. Rev. D **33**, 3495 (1986).
- [99] K. Freese, J. Friedman, and A. Gould, Phys. Rev. D **37**, 3388 (1988).
- [100] D. Spergel, Phys. Rev. D **37**, 1353 (1988).
- [101] C. J. Copi, J. Heo, and L. M. Krauss, Phys. Lett. B **461**, 43 (1999).
- [102] D. P. Snowden-Ifft, T. Ohnuki, E. S. Rykoff, and C. J. Martoff, Nucl. Instrum. and Meth. in Phys. Res. A **498**, 155 (2003).
- [103] R. Bernabei *et al.*, arXiv:astro-ph/0804.2741v1, 2008.
- [104] R. Bernabei *et al.*, Riv. Nuovo Cim. **26N1**, 1 (2003).
- [105] E. M. Drobyshevski, arXiv:physics.ins-det/0706.3095, 2008.
- [106] R. Bernabei *et al.*, arXiv:astro-ph/0710.0288v1, 2007.
- [107] C. Savage, G. Gelmini, P. Gondolo, and K. Freese, arXiv:astro-ph/0808.3607v2, 2008.
- [108] A. Bottino, F. Donato, N. Fornengo, and S. Scopel, arXiv:hep-ph/0806.4099v2, 2008.
- [109] S. Chang, A. Pierce, and N. Weiner, arXiv:hep-ph/0808.0196v1, 2008.

- [110] M. Fairbairn and T. Schwetz, arXiv:hep-ph/0808.0704v1, 2008.
- [111] D. Hooper, F. Petriello, K. M. Zurek, and M. Kamionkowski, arXiv:hep-ph/0808.2464v1, 2008.
- [112] D. N. McKinsey and K. J. Coakley, *Astropart. Phys.* **22**, 355 (2005).
- [113] M. Laffranchi and A. Rubbia, *J. Phys.: Conf. Ser.* **65**, 012014 (2007).
- [114] P. Benetti *et al.*, *Astropart. Phys.* **28**, 495 (2008).
- [115] M. G. Boulay and A. Hime, *Astropart. Phys.* **25**, 179 (2006).
- [116] J. Angle *et al.*, *Phys. Rev. Lett* **100**, 021303 (2008).
- [117] D. Y. Akimov *et al.*, *Astropart. Phys.* **27**, 46 (2007).
- [118] K. Abe *et al.*, arXiv:physics.ins-det/0809.4413v3, 2009.
- [119] E. Aprile, A. E. Bolotnikov, A. I. Bolozdyna, and T. Doke, *Noble Gas Detectors* (Wiley-VCH, Weinheim, 2006).
- [120] E. Aprile *et al.*, *Phys. Rev. C* **79**, 045807 (2009).
- [121] E. Aprile and L. Baudis, arXiv:astro-ph.IM/0902.4253v1, 2009.
- [122] T. Shutt *et al.*, *Phys. Rev. Lett* **69**, 3425 (1992).
- [123] T. Shutt *et al.*, *Phys. Rev. Lett* **69**, 3531 (1992).
- [124] O. Martineau *et al.*, arXiv:astro-ph/0310657v1, 2003.
- [125] T. Shutt *et al.*, *Nucl. Instrum. and Meth. in Phys. Res. A* **444**, 340 (2000).
- [126] D. S. Akerib *et al.*, *Phys. Rev. D* **72**, 052009 (2005).
- [127] Z. Ahmed *et al.*, arXiv:astro-ph.CO/0912.3592v1, 2009.
- [128] D. S. Akerib *et al.*, *J. Low Temp. Phys.* **151**, 818 (2008).
- [129] <http://cdms.berkeley.edu/>.
- [130] <http://edelweiss2.in2p3.fr/>.
- [131] V. Sanglard *et al.*, *Phys. Rev. D* **71**, 122002 (2005).
- [132] S. Marnieros *et al.*, *J. Low Temp. Phys.* **151**, 835 (2008).

- 
- [133] A. Broniatowski *et al.*, J. Low Temp. Phys. **151**, 830 (2008).
- [134] E. Armengaud *et al.*, arXiv:astro-ph.CO/0912.0805v1, 2009.
- [135] J. Ninkovic *et al.*, Nucl. Instrum. and Meth. in Phys. Res. A **564**, 567 (2006).
- [136] S. Cebrián *et al.*, Phys. Lett. B **563**, 48 (2003).
- [137] S. Cebrián *et al.*, Astropart. Phys. **21**, 23 (2004).
- [138] A. Calleja *et al.*, J. Low Temp. Phys. **151**, 848 (2008).
- [139] G. Angloher *et al.*, Astropart. Phys. **23**, 325 (2005).
- [140] G. Angloher *et al.*, Astropart. Phys. **31**, 261 (2009).
- [141] G. Angloher *et al.*, Astropart. Phys. **18**, 43 (2002).
- [142] M. Cribier *et al.*, Astropart. Phys. **6**, 129 (1997).
- [143] R. Lang, Ph.D. thesis, Technische Universität München, 2008.
- [144] P. F. Smith, Astropart. Phys. **8**, 27 (1997).
- [145] P. Meunier *et al.*, Appl. Phys. Lett. **75**, 1335 (1999).
- [146] K. D. Irwin *et al.*, Rev. Sci. Instrum. **66**, 5322 (1995).
- [147] C. Arpesella, Nucl. Phys. B (Proc. Suppl.) **28**, 420 (1992).
- [148] E. Bellotti, M. Buraschi, E. Fiorini, and C. Liguori, INFN/TC-85/19, 1985.
- [149] H. Wulandari, J. Jochum, W. Rau, and F. v. Feilitzsch, Astropart. Phys. **22**, 313 (2004).
- [150] H. Wulandari, Ph.D. thesis, Technische Universität München, 2003.
- [151] W. Westphal, Development and Characterization of Cryogenic Detectors for the CRESST Experiment, [http://www.e15.physik.tu-muenchen.de/research\\_and\\_projects/cresst/](http://www.e15.physik.tu-muenchen.de/research_and_projects/cresst/), 2008.
- [152] T. Jagemann, Ph.D. thesis, Technische Universität München, 2004.
- [153] T. Jagemann *et al.*, Astropart. Phys. **26**, 269 (2006).
- [154] C. Coppi, Ph.D. thesis, Technische Universität München, 2009.

- [155] C. Ciemniak, Ph.D. thesis - In Preparation, Technische Universität München, 2010.
- [156] R. Strauss, Diploma thesis, Technische Universität München, 2010.
- [157] V. N. Lebedenko *et al.*, Phys. Rev. D **80**, 052010 (2009).
- [158] E. A. Baltz and P. Gondolo, Phys. Rev. D **67**, 063503 (2003).
- [159] <http://dmtools.brown.edu/>.
- [160] J.-C. Lanfranchi, T. Lachenmaier, W. Potzel, and F. v. Feilitzsch, Nucl. Instrum. and Meth. in Phys. Res. A **520**, 135 (2004).
- [161] J.-C. Lanfranchi, Ph.D. thesis, Technische Universität München, 2005.
- [162] H. Kraus *et al.*, J. Phys.: Conf. Ser. **39**, 139 (2006).
- [163] H. J. Maris and S. Tamura, Phys. Rev. B **47**, 727 (1993).
- [164] R. C. Alig and S. Bloom, Phys. Rev. Lett **35**, 1522 (1975).
- [165] R. S. Markiewicz, Phys. Rev. B **21**, 4674 (1980).
- [166] P. Norton, T. Braggins, and H. Levinstein, Phys. Rev. B **8**, 5632 (1973).
- [167] S. Tamura, Phys. Rev. B **31**, 2574 (1985).
- [168] R. Orbach and L. A. Vredevoe, Physics (N.Y.) **1**, 91 (1964).
- [169] S. Tamura and H. J. Maris, Phys. Rev. B **31**, 2595 (1985).
- [170] H. J. Maris, Phys. Rev. B **41**, 9736 (1990).
- [171] F. Pröbst *et al.*, J. Low Temp. Phys. **100**, 69 (1995).
- [172] W. Knaak, T. Hauß, M. Kummrow, and M. Meißner, in *Phonon Scattering in Condensed Matter 5*, edited by A. C. Anderson and J. P. Wolfe (Springer, Berlin, 1986).
- [173] C. Kittel, *Einführung in die Festkörperphysik*, 10. ed. (Oldenbourg, München, 1993).
- [174] M. Tinkham, *Introduction to Superconductivity*, 2nd ed. (Dover Publications, Mineola, N.Y., 1996).
- [175] M. A. Lindeman *et al.*, Rev. Sci. Instrum. **75**, 1283 (2004).

- [176] S. Roth, Diploma thesis, Technische Universität München, 2007.
- [177] S. Roth *et al.*, Opt. Mat. **31**, 1415 (2009).
- [178] W. Seidel, Ph.D. thesis, Technische Universität München, 1990.
- [179] K. D. Irwin, Appl. Phys. Lett. **66**, 1998 (1995).
- [180] K. D. Irwin, G. C. Hilton, D. A. Wollman, and J. M. Martinis, J. Appl. Phys. **83**, 3978 (1998).
- [181] J. Schnagl, Ph.D. thesis, Technische Universität München, 2001.
- [182] F. Pobell, *Matter and Methods at Low Temperatures*, 3rd ed. (Springer, Berlin, 2007).
- [183] N. R. Werthammer, Phys. Rev. **132**, 2440 (1963).
- [184] <http://www.telemark.com/>.
- [185] <http://www.microresist.com/>.
- [186] <http://www.oxford-instruments.com/>.
- [187] <http://www.picowatt.fi/>.
- [188] <http://www.vishay.com/>.
- [189] <http://www.iseg-hv.de/>.
- [190] <http://www.rohde-schwarz.de/>.
- [191] <http://www.supracon.com/>.
- [192] <http://www.appliedphysics.com/>.
- [193] <http://www.ni.com/>.
- [194] M. Stark, Ph.D. thesis, Technische Universität München, 2005.
- [195] R. H. Geballe, in *Semiconductor*, edited by R. B. Hannay (Reinhold, New York, 1959).
- [196] <http://www.crystec.de/>.
- [197] <http://www.epotek.com/>.

- [198] M. Cerna and A. F. Harvey, National Instruments - Application Note 041, 2000.
- [199] M. Stark *et al.*, Nucl. Instrum. and Meth. in Phys. Res. A **545**, 738 (2005).
- [200] V. S. Vavilov, Phys. Chem Solids **8**, 223 (1959).
- [201] L. Pages, E. Bertel, H. Joffre, and L. Sklavenitis, At. Data **4**, 1 (1972).
- [202] M. J. Penn *et al.*, J. Appl. Phys. **79**, 8179 (1996).
- [203] W. R. Leo, *Techniques for Nuclear and Particle Physics Experiments*, 2nd ed. (Springer, Berlin, 1994).
- [204] R. Strauss, Ph.D. thesis - In Preparation, Technische Universität München, 2010.

# Danksagung

Zum Abschluss ist es nun an der Zeit mich bei all denjenigen zu bedanken, die zum Gelingen dieser Arbeit beigetragen haben.

Prof. Dr. Franz von Feilitzsch möchte ich für die Möglichkeit dieser spannenden Doktorarbeit an seinem Lehrstuhl danken. Er erwies sich überdies in sehr vielen schwierigen Situationen als großer Motivationskünstler und ließ mich nie den Glauben daran verlieren, dass man den Kampf Mensch gegen Maschine gewinnen kann.

Dr. Walter Potzel war der perfekte Betreuer. Er führte nicht nur unzählige physikalische Diskussionen mit mir, die zur Klärung der wichtigsten Sachverhalte im Zusammenhang mit dem Neganov-Luke-Effekt führten, sondern kümmerte sich auch stets um die sonstigen Probleme, die im Verlauf dieser Doktorarbeit auftraten.

Dr. Jean-Côme Lanfranchi danke ich für die unglaublich vielen Tipps und Ratschläge zu Kryophysik und Detektorentwicklung aber auch darüber hinaus. Ich möchte mich außerdem insbesondere dafür bei ihm bedanken, dass er mir während meiner Doktorarbeit stets als Freund begegnet ist.

Prof. Dr. Tobias Lachenmaier danke ich für einige sehr wertvolle Beiträge zu meiner Arbeit. Für sein großes Interesse am Neganov-Luke-Effekt danke ich ihm genauso wie Prof. Dr. Lothar Oberauer.

Die Mitarbeiter der Firma *KETEK*, insbesondere Dr. Josef Kemmer, Dr. Oliver Boslau und Dr. Florian Wiest waren in den ersten Jahren meiner Promotion eine große Hilfe, wenn es um Fragen zu Halbleiterdetektoren ging. Die zahlreichen Diskussionen mit ihnen haben wesentlich zum Verständnis der Lichtdetektoren mit Neganov-Luke-Verstärkung beigetragen.

Sabine Roth danke ich nicht nur für unsere tolle gemeinsame WG-Zeit, sondern auch dafür, dass sie mir in manch einer schwierigen Situation eine große Hilfe war. Darüber hinaus waren wir ein ziemlich gutes Kryo-Gespann.

Meine letzte Messung während der letzten Strahlzeit am MLL wäre ohne die Unterstützung von Christian Ciemniak und Raimund Strauss nahezu undenkbar gewesen. Unsere gemeinsamen Nachtschichten werden mir immer in Erinnerung bleiben. Überdies möchte ich ihnen aber insbesondere dafür danken, dass sie unglaublich tolle Kollegen gewesen sind.

Meinen langjährigen Bürokollegen Dr. Chiara Coppi und Wolfgang Westphal danke ich für die angenehme Atmosphäre und gute Kollegialität. Wolfgang Westphal verdanke ich überdies viele grundlegende Kenntnisse sowohl zum Kryostatenbetrieb als auch zur Detektorentwicklung. Ich bedauere es zutiefst, dass ich ihm diesen Dank nicht mehr persönlich ausdrücken kann.

Meine ehemalige Fußballmannschaft bescherte mir als Trainer leider keinen einzigen Sieg oder Unentschieden. Einigen von ihnen, u.a. Achim Gütlein, Martin Hofmann und Jürgen Winter verdanke ich aber immerhin einige sehr heiß geführte Fußballdebatten über den FC Bayern.

Den anderen Cryonisten/Ölpanschern Sebastian Pfister, Moritz v. Sivers, Nils Haag, Patrick Pfahler, Quirin Meindl, Michael Willers, Timo Lewke, Dr. Michael Wurm usw. danke ich für die tolle Stimmung, für die sie am Institut gesorgt haben.

Unserem Werkstatt-Team bestehend aus Harald Hess, Erich Seitz und Thomas Richter danke ich dafür, dass sie unsere Aufträge stets pünktlich und in hervorragender Qualität ausgeführt haben.

Mein ganz besonderer Dank gilt Hermann Hagn. Er war stets zur Stelle, wenn Störungen oder sonstige Elektronikprobleme beseitigt werden mussten. Norbert Gärtner war immer erster Ansprechpartner, wenn es um Pumpen, Interlock-Probleme oder Strahlenschutz ging.

Unseren Sekretärinnen Beatrice van Bellen, Alexandra Földner, Sonja Kraus und Maria Bremberger danke ich dafür, dass sie unseren bürokratischen Alltag sehr gut im Griff hatten und uns sehr viele administrative Lasten abnahmen.

Abschließend möchte ich mich noch bei meinen Eltern für ihre große finanzielle und moralische Unterstützung während dieser Arbeit bedanken.